Structural engineering on specific organic-solar cells and transistors

from materials synthesis to device fabrication

Xu, Wei

DOI (link to publication from Publisher):
10.54337/aau528219032

Publication date:
2023

Document Version
Publisher's PDF, also known as Version of record

STRUCTURAL ENGINEERING ON SPECIFIC ORGANIC-SOLAR CELLS AND TRANSISTORS: FROM MATERIALS SYNTHESIS TO DEVICE FABRICATION

BY
WEI XU

DISSERTATION SUBMITTED 2023

AALBORG UNIVERSITY
DENMARK

STRUCTURAL ENGINEERING ON SPECIFIC ORGANIC-SOLAR CELLS AND TRANSISTORS: FROM MATERIALS SYNTHESIS TO DEVICE FABRICATION

by

Wei Xu

AALBORG UNIVERSITY
DENMARK

Dissertation submitted 2023

Dissertation submitted: January 2023

PhD supervisor: Prof. Donghong Yu
Aalborg University

PhD committee: Associate Professor Vittorio Boffa (chair)
Aalborg University, Denmark

Professor Lluis F. Marsal
University Rovira I Virgili, Spain

Professor Federico Bella
Politecnico di Torino, Italy

PhD Series: Faculty of Engineering and Science, Aalborg University

Department: Department of Chemistry and Bioscience

ISSN (online): 2446-1636
ISBN (online): 978-87-7573-766-6

Published by:
Aalborg University Press
Kroghstræde 3
DK – 9220 Aalborg Ø
Phone: +45 99407140
aauf@forlag.aau.dk
forlag.aau.dk

Printed in Denmark by Stibo Complete, 2023

CV

Mr. Wei Xu was born on December 1th, 1992 in Tianfu New Area, Chengdu City, Sichuan Province, China. He obtained his Bachelor degree in Chemistry and Master degree in Organic Chemistry at Sichuan University, P.R. China in 2015 and 2018, respectively. And he was successfully granted the China Scholarship Council (CSC) scholarship in June 2019, and then began his Ph.D. study with focuses on organic solar cells at the Department of Chemistry and Bioscience, Faculty of Engineering and Science, at Aalborg Unversity.

ENGLISH SUMMARY

Comparing with other types of solar cells that are currently popular, organic solar cells have the advantages of light weight, solution processability, translucency, low cost, and the ability to fabricate large-area flexible devices, and are currently a hot research direction in solar cell technology. Due to the limitations of most organic photovoltaic materials with complex structures, numerous synthesis steps, low yields, and high purification costs, research on non-fullerene acceptors (NFAs) has been well performed. Such materials are relatively simple to synthesize, easy to purify, and can overcome the disadvantages of limited absorption performance, nonadjustable molecular energy levels, and easy aggregation in the active layer of their counterpart, i.e., the fullerene receptors. With the continuous optimization and improvement of material structure and device technology, new non-fullerene acceptor materials have developed rapidly in the field of solar cells.

Specifically, being halogen-free and therefore more environmentally friendly, these works selected the current novel non-fullerene BTP-eC9 as the acceptor to study the relationship between BDT-based organic polymer donor materials with different structures and their PV performance. Through the structural design and synthesis of organic molecules, the corresponding materials were obtained, and then the molecular structure properties, physical properties, optical properties, electrochemical properties, photovoltaic performance and semiconductor properties of these materials were characterized. All these bring an urgent need for developing more suitable donor materials for pairing them in the active layer of organic solar cells (OSCs). This thesis mainly investigates the effects of organic photovoltaic by adjusting the molecular structure of BDT-based organic polymer donor materials. Using a series of molecular structure design strategies, such as fused core-modified engineering, bridge engineering, end-group engineering, functional group engineering or side-chain engineering, etc., to reveal the relationship between these strategies and the photovoltaic performance in OSCs. Besides, the fused-ring small molecule acceptors as the precursor materials of photovoltaic devices are studied to illustrate the relationship between the end-group engineering and the semiconductor properties.

Based on the above studies, the relationship between photovoltaic performance and BDT-based molecular structure was revealed. Copolymers substituted with alkylthio-phenyl side chains exhibit better photovoltaic performance than alkoxy-phenyl alternatives. In addition to the lower lying HOMO energy levels, alkylthio-phenyl side-chain substituents also exhibit higher carrier mobility, better charge dissociation ability, and smaller exciton recombination. Furthermore, unlike fullerene systems, excess fluorine substitution hinders the formation of efficient phase separation in NFA-based organic active layers, impairing the π-π stacking interactions of adjacent polymer backbones, the carrier transport ability and charge dissociation properties. Meanwhile, one BDT-based homopolymer with asymmetric structure has achieved

the highest PCE among recent analogous homopolymer donor materials. The asymmetric strategy has unique advantages in controlling the morphology of homopolymer molecular donor materials, reducing unfavorable factors such as excessive phase separation and hole/charge transport imbalance caused by strong aggregation effects and strong crystallinity. Finally, the bromo-anthryl end groups substituted DPP organic small molecules are found as one excellent candidate for small molecule photovoltaic acceptor materials.

DANSK RESUME

Sammenlignet med andre typer solceller, der i øjeblikket er populære, har organiske solceller fordelene ved let vægt, opløsnings processerbarhed, gennemskinnelighed, lave omkostninger og evnen til at fremstille fleksible enheder med stort område og er i øjeblikket en hot forskningsretning inden for solenergi. celleteknologi. På grund af begrænsningerne for de fleste organiske fotovoltaiske materialer med komplekse strukturer, talrige syntesetrin, lave udbytter og høje oprensningsomkostninger er forskning i ikke-fulleren receptorers (NFAs) begyndt. Sådanne materialer er relativt enkle at syntetisere, nemme at rense og kan overvinde ulemperne ved begrænset absorptionsevne af fulleren receptorer, ujusterbare molekylære energiniveauer og let aggregering i det aktive lag. Med den løbende optimering og forbedring af materialestruktur og enhedsteknologi har nye ikke-fulleren receptorers materialer udviklet sig hurtigt inden for solceller.

Specifikt valgte disse værker den nuværende nye ikke-fulleren BTP-eC9 som acceptor til at studere forholdet mellem BDT-baseret organiske polymerdonormaterialer med forskellige strukturer og deres PV-ydeevne. Gennem det strukturelle design og syntese af organiske molekyler blev de tilsvarende materialer opnået, og derefter blev disse materialers molekylære strukturegenskaber, fysiske egenskaber, optiske egenskaber, elektrokemiske egenskaber, fotovoltaisk ydeevne og halvlederegenskaber karakteriseret. Denne afhandling undersøger hovedsageligt virkningerne af BDT-baseret organisk fotovoltaik ved at justere den molekylære struktur af organiske polymerdonormaterialer. Ved at bruge en række molekylære strukturdesignstrategier, såsom smeltet kerne-modificeret engineering, bridge engineering, end-group engineering, funktionel gruppe engineering eller side-chain engineering osv., afslører virkningerne af forskellige modifikationsstrategier på den fotovoltaiske ydeevne af organisk solcelle. enheder. Ydermere studeres de fusionerede små molekyle-acceptorer som forløbermaterialer for OPV-enheder forholdet mellem slutgruppekonstruktion og halvlederegenskaberne.

Baseret på ovenstående undersøgelser blev sammenhængen mellem fotovoltaisk ydeevne og BDT-baseret molekylær struktur afsløret. Copolymerer substitueret med alkylthio-phenyl sidekæder udviser bedre fotovoltaisk ydeevne end alkoxy-phenyl alternativer. Ud over de lavere HOMO-energiniveauer udviser alkylthio-phenyl sidekæde substituenter også højere bærermobilitet, bedre ladningsdissociationsevne og mindre exciton rekombination. I modsætning til fulleren systemer hindrer overskydende fluorsubstitution dannelsen af effektiv faseadskillelse i NFA-baserede organiske aktive lag, hvilket forringer π-π-stablingsinteraktionerne af tilstødende

polymerskeletter, bærertransportevnen og ladningsdissociationsegenskaberne. Og en BDT-baseret homopolymer med asymmetrisk struktur har opnået den højeste PCE blandt nyere analoge homopolymer donor materialer. Den asymmetriske strategi har unikke fordele ved at kontrollere morfologien af homopolymere molekylære donormaterialer, hvilket reducerer ugunstige faktorer såsom overdreven faseadskillelse og hul/ladningstransportubalance forårsaget af stærke aggregeringseffekter og stærk krystallinitet. Endelig findes de brom-anthryl ende grupper substituerede DPP organiske små molekyler som en fremragende kandidat til små molekyle fotovoltaiske acceptor materialer.

ACKNOWLEDGEMENTS

During my three-year Ph.D study., I would like to express my deepest gratitude to those who have helped me. First of all, I would like to thank my supervisor, Professor Donghong Yu. After one failure, we won our first CSC fellowship together and started my PhD career. Thus, I went to Denmark to study alone in 2019, and then, with his help and support, I successfully completed my research task. His enthusiasm for research, meticulous attitude and many constructive comments have inspired me a lot, motivated me to conduct experiments and overcome challenges in research, and learn to write high-level scientific papers. At the same time, he also gave me a lot of effective advice on life, helping me to quickly adapt to life in Aalborg, and also quickly understand the Danish culture.

I would also like to appreciate all my collaborators, whose rich experience and creative ideas have facilitated the realization of my research goals. Dr. Um Kanta Aryal from University of Southern Denmark is knowledgeable and experienced in the fabrication process of organic semiconductor transistors. During the collaborative research, he actively taught me how to design and make a complete transistor on my own. At the same time, I would also like to thank his colleagues, Prof. Morten Madsen and Prof. Jakob Kjelstrup-Hansen. They frequently provided me with discourse and guidance on the transistor fabrication process, and patiently assisted in the subsequent characterization of electrical properties and manuscript review. In addition, Prof. Leonid and Professor Wang Deyong provided a lot of assistance and helpful discussions on morphology characterization via AFM and SEM measurements. And Prof. Reinhard Wimmer is a kind person who helped me a lot in NMR measurements.

I am also very grateful to Prof. Cheng Yang from the College of Chemistry of Sichuan University (SCU). He led me into the field of scientific research. After my master's degree, he suggested me to study in Denmark and gave me a lot of assistance in applying for CSC scholarships. Later, during my stay abroad, he also provided me with a month-long experimental site assistance and a lot of experimental characterization support. Sincere thanks should go to him from me. Then, I would also like to thank my friends and colleagues in the College of Chemistry of SCU, Ting, Xingke, Chunying, Ming, Jiecheng, Lingling and Jingyu, who gave me a lot of advice on experiments during my study-abroad period. Besides, I would like to thank the funding of AAU Doctoral School, which allowed me to successfully complete the remaining part of the experiment of my doctoral research project in SCU after 5 months. I am very grateful to Professor Pei Cheng (College of Polymer Science & Engineering, SCU) for his kindness and help, providing me with the working environment and experimental guidance for OPV device fabrication, allowing me to successfully complete the device fabrication and characterization experiments. I also sincerely thank my colleagues in the polymer group: Wei He, Yuanhao Li, Hailing Yu, Songtao Wei, Yinyue Hu, Jiayu Wang and Hongxiang Li. They taught me a lot

about device process optimization and thin film topography characterization. Here, I wish everyone a fruitful academic career and a bright future.

The shared experience of these three years with all my colleagues in the chemistry department has become an integral part of my PhD studies and life. Most sincere thanks to following everyone: Prof. Kim L. Larsen, Prof. Yuanzheng Yue, Prof. Morten Mattrup Smedskjær, Assoc. Prof. Vittorio Boffa, Assoc. Prof. Thorbjørn Nielsen, Dr. Ang Qiao, Dr. Martin Østergaard, Dr. Fengchao Li, Dr. Rasmus Peterson, Dr. Zhencai Li, Dr. Aamer Ali, Dr. Qi Zhang, Dr. Tao Du, Dr. Pengfei Liu, Dr. Chengwei Gao, Rasmus Madsen, Søren Sørensen, Anne Sophie Jødal, Rasmus Christensen, Jingnan Wu, Jing Gao, Xianzheng Ma, Xiangting Ren, Wei Fan, Jiajia Yan, Xinxin Chen, Daming Sun, Zhimin Chen, Annemarie Davidsen, Anne Flensborg. Moreover, my sincere regards to my wonderful friends and neighbors in Aalborg, Wenyuan Cao, Yuan Si, Wenqiang Xie, Hanchi Zhang, Kai Yin, Zhenfa Zhang, Yue Guan, Fengsheng Li, Zekun Li, Zhaoxin Wang, Tianbao Gu, Min Liu, Weiheng Zhang, Yucheng Fang and Yi Xu, who help me leave unforgettable memories in Denmark.

Finally, I would like to thank my lovely girlfriend Juan, who has been with me for many years, for her great support and love during my studies. Leaves leave marks, the river remains. Although scientific research and life have been quite difficult in the past few years of Covid-19, the endless love of my parents, the encouragement of friends and the unconditional support of my girlfriend have helped me to successfully complete my Ph.D. study abroad career. It's great to have them around.

TABLE OF CONTENTS

CHAPTER 1. INTRODUCTION

1.1. BACKGROUND AND CHALLENGES

Under the world situation of rapid consumption of fossil energy, the development and utilization of new energy and renewable energy has become an unavoidable topic at present. Solar energy as a huge potential energy plays a pivotal role in many forms of new energy. According to statistics, the solar energy reaching the earth's surface annually is twice the total energy of all non-renewable resources, since acquired and utilized by human beings on earth, such as coal, oil, natural gas and nuclear energy (1-5). Photovoltaic (PV) power generation has been gradually entered the mature stage up to now, many country countries, such as Germany, have established energy supply models with PV. At present, the conversion efficiency of monocrystalline silicon solar cells is undoubtedly the highest, so it still occupies a dominant position in large-scale applications and industrial production. However, the large demand of high-purity silicon materials, complex production process, high cost and greatly power consumption in cell process purge us to find better alternatives to monocrystalline silicon cells. Therefore, thin film solar cells have become a new generation of promising PV products, among which polycrystalline silicon thin film solar cells and amorphous silicon thin film solar cells are typical representatives (6-10).

Thin-film solar cells are new PV devices to alleviate the energy crisis, which can be manufactured as the products with a microns thin film thickness on inexpensive substrates of different materials such as ceramics, graphite, and glass (9, 11-15). Owing to the flexibility, thin-film solar cells have a wide range of applications in manufacturing products with non-planar structures, even they could be combined with buildings or become part of buildings (11, 12, 16). As one kind of Thin-film solar cells, organic solar cells (OSCs) possess cheaper, easily mass-produce and more flexible properties, which makes it attract the attention of current scholars. Moreover, except for above mentioned, OSCs based on organic polymer materials as the photosensitive active layer have the characters of diverse material structures, large area, low-cost printing, flexibility, semitransparency and even transparency, which has huge application potential in field of energy efficient building integration and wearable equipment (16-23). This is all attributed to the new opportunities provided by the research progress in the field of organic semiconductor, organic electronics and organic (polymer) functional materials in recent years.

Although the history of emerging OSCs is less than a century, the development of photoelectric conversion efficiency is rapidly improved. After several generations of innovations in organic photovoltaic materials, the power conversion efficiency (PCE) of PV devices based on organic polymer materials has grown to over 18% from initial

less than 1%. As donor materials, the polymers based on benzodithiophene (BDT) unit has an extend and symmetrical planar structure, which can optimize the π-π stacking of the material by increasing the conjugation plane and conjugation length to improve the charge mobility. Compared with other earlier polymer donor materials, such as poly(p-phenylene vinylene) (PPVs) and Poly(3-hexylthiophene-2,5-diyl) (P3HT),(24-26) it has a higher extinction coefficient and a broader absorption spectrum, it also has bicontinuous network film morphology with nanoscale phase separation and tunable highest occupied molecular orbital (HOMO) and lowest unoccupied molecular orbital (LUMO) levels. Then, 2D-conjugated structure design strategy of BDT moiety, whose has stronger light-harvesting ability and better film morphology, replaces 1D structure to achieve a further improvement of PV performance, and it also proves a bright future for the design strategy of alternating push-pull type copolymers, consisting of electron-rich (D) and electron-deficient (A) units.(27) Thence, the D-A alternating copolymer donor materials based on BDT moiety always has a huge potential and attracts much attention in PSC devices. Precisely attributing to the emerging of D-A alternating strategy of bulk heterojunction (BHJ) structure, organic solar cells based on promising molecule acceptors, fullerene, had gradually confirmed the research of mainstream direction and entered a period of rapid development. And with the continuous improvement of manufacturing technology in organic solar cells based on fullerene electron acceptor materials, the PCE had exceeded 10% (28-31).

Although fullerene and its derivatives have dominated organic solar cell acceptor materials for over 20 years, the molecular structure determines that fullerene acceptors have insurmountable shortcomings, such as difficult molecular structure tailoring, difficult energy level regulation, weak visible light absorption, poor morphology and device stability, etc. These defects make the improvement of PV efficiency and the industrialization encounter a bottleneck, which has seriously restricted the sustainable development in the field of organic photovoltaic devices (28, 31, 32). In 2007, Xiaowei Zhan and his co-workers took the lead in conducting study on non-fullerene accepters (NFAs), perylene imide polymer (33), which led the beginning of the development of NFAs materials in this field. And few years later, the popular molecule ITIC, second generation of NFAs, was synthesized (34), then the concept of fused-ring electron acceptor (FREA) was proposed. Afterwards, they developed a series of molecular design strategies for fused-ring electron acceptors based on ITIC structure to modulate molecular optical and electrochemical properties, revealing the relationship between molecular structure and PCE. Such as fused core-modified engineering, bridging engineering, end-group engineering, functional group engineering and side-chain engineering, etc., were also suitable for polymer donors. And the significant differences between novel FREAs and traditional fullerene acceptors in terms of structural characteristics, optical characters, physical property and device PV/semiconductor performance were also expounded. In the past five years, due to the invention of fused-ring electron acceptors, the energy conversion efficiency of organic solar cells based on the third generation NFAs, Y6 and

corresponding Y6 derivatives, exhibited better PV performance without exception, which has achieved a historic breakthrough, PCE of now exceeded 18%, in single-junction BHJ photovoltaic devices (35-39). In short, the fused-ring electron acceptor is a novel electron acceptor system, which solves the key scientific issues of traditional electron acceptors represented by fullerenes, subverts the classic fullerene mechanism, and leads organic photovoltaic devices into a new era.

Nonetheless, due to the short research history of NFAs solar cells, especially BDT-based polymer solar cells (PSCs), the field of NFAs organic photovoltaic devices still lacks a theoretical foundation, thus more experimental studies are needed to perfect the theoretical knowledge framework. Firstly, the polymer donor molecule based on the BDT unit has a rigid plane and can form a strong π-π stacking with the adjacent polymer backbone, while the fullerene acceptor has a spherical structure, which cannot form a closed π-conjugated interaction with the polymer backbone. On the other side, NFAs also have the good rigid planes to form strong π-π stacking with polymer backbones, inducing to form different film morphologies of the active layers comparing with fullerene acceptors. Therefore, the mechanisms of exciton generation, transport and dissociation are quite different in two kinds of blending films, which means that experience generalized from past experiments in fullerene-based PSCs can no longer be accurately applied into the NFAs-based PSCs. (40-43). Besides, due to the liable degradation of organic polymers and organic fused-ring small molecules at high temperature, the significant defects of NFAs-based PSCs in stability and lifetime also are waiting to be optimized. Thirdly, although the PCEs of NFAs-based PSCs are still rising, how to maintain the balance between the increase of open circuit voltage and the decrease of short circuit current still needed to be given a relatively complete research conclusion.

In fact, when the power conversion efficiency of PSCs reaches a sufficient height while maintaining a suitable stability and intensity, these flaws can no longer be obstacle when they are employed as commercial products, even if their service life is only half a year. The scrapped PSCs device can be easily replaced by another new one because of the simplicity of the manufacturing process and the low cost. Therefore, improving efficiency is the primary consideration for the application of current organic photovoltaic technology, which means that we should concentrate on previous three questions. However, in these years most researchers just focused on the development of NFAs, they are dedicated to improving PCE through structural manipulation or design of novel molecular structures. But few people discussed organic polymer donor materials, which was the interdependent partners of NFAs. Thence, this Ph.D. thesis mainly focuses on the effect of the organic photovoltaic/semiconductor performance by modulating the molecular structure of BDT-based organic polymer donor materials and fused-ring small molecule acceptor materials. Utilizing above mentioned molecular structural design strategies, fused core-modified engineering, bridging engineering, end-group engineering , functional group engineering or side-chain engineering, to reveal the effect on photovoltaic and

semiconductor performances of organic photovoltaic devices through different modification-methods.

1.2. OBJECTIVES

The Ph.D. project mainly aims to provide the idea and experience to choose the appropriate modulated approach when designing the molecular structure in the field of NFAs-based OSCs. Therefore, to investigate the effect of several structural modifications of organic polymers, as the electron donors based on benzo[1,2-b:4,5-b′]dithiophene (BDT) unit, on PV performance in NFAs-based photovoltaic devices, the study program is designed in three sections. Firstly, to study the effect of alkylthio and alkoxy side-chain engineering on PV performance in BDT-based polymer donor solar devices. Secondly, to study the effect of fluorinated functional group engineering on PV performance in BDT-based polymer donor solar devices. Last, to study the effect of donor-donor strategy fused core-modified engineering on PV performance in BDT-based polymer donor solar devices. Additionally, another section is the study of the effect of anthryl end-group engineering on semiconductor performance in diketopyrrolopyrrole (DPP)-based small molecular FREA solar devices. Thus, this research project consists of four sections, and each section is an integral research processes, including molecular structure design, synthesis, characterization and application. This thesis focuses on illuminating the following aspects:

- Study of the effect on side-chain engineering for PV performance in NFAs-based OSCs.
- Study of the effect on fluorinated functional group engineering for PV performance in NFAs-based OSCs.
- Study of the effect on fused core-modified engineering for PV performance in NFAs-based OSCs.
- Study of the effect on end-group engineering for semiconductor performance in NFAs-based OSCs.

Synthesis is the base of organic chemistry. Therefore, this thesis aims to deliver ways of organic molecular structure design for improving PV/semiconductor performance and reveal the relationship between structural modulation and optimized mechanism. Above mentioned four design concepts are the mainly means in organic field to study different novel functional organic molecules of applying to the organic photovoltaic/semiconductor devices. Aiming to reveal and complete the theory of the modification engineering. In Chapter 2, side-chain engineering is principally discussed modulation method, but it also contains some discussions of bridging engineering modulation method. And the discussions of functional group engineering, fused core-modified engineering and end-group engineering are summarized in

following contents, Chapter 3, Chapter 4 and Chapter 5, respectively. Then the overall discussions and conclusions are summarized in Chapter 6.

1.3. THESIS CONTENT

The project experiments of molecular structure design, synthesis and characterization in this thesis are carried out at Aalborg University (AAU), and rest experiment of molecular application is accomplished at Sichuan University (SCU) and University of Southern Denmark (SDU), respectively. This thesis includes four articles, of which one has been published in peer-reviewed SCI journal, and three has been submitted in three different peer-reviewed journals. These articles constitute the main body of the thesis, and will be cited by their roman numerals throughout the thesis:

I. **W. Xu**, U. K. Aryal, J. Wu, M. Madsen, J. Kjelstrup-Hansen, Z. Cao, D. H. Yu*, Effects of bromination on anthryl-capped DPP-based semiconductor materials: Improved electrical characteristics of organic field-effect transistors, *Synthetic Metals* (2022), 290, 117153.

II. **W. Xu**, W. He, G. Li, J. Wu, C. Yang, Z. Cao, P. Cheng, H. Li*, Z. Du*, D. H. Yu*, Challenging PM6-alike donor polymers for paring a Y-type state-of-art acceptor in binary blends for bulk heterojunction solar cells, *Physical Chemistry Chemical Physics*, 2022, DOI: 10.1039/D2CP05414K.

III. **W. Xu**, L. Du, G. Li, W. He, C. Yang, H. Li, Z. Cao, Z. Du*, P. Cheng *, D. H. Yu*, Revisiting benzodithiophene-based donor polymers via thiolalkylation for enhanced photovoltaic performance, *to be submitted*.

IV. **W. Xu**, W. He, G. Li, C. Yang, Z. Cao, H. Li, Z. Du*, P. Cheng*, D. H. Yu*, The impact of position-sensitive fluorination on photovoltaic performance of donor-acceptor polymer/Y-type small molecule based organic solar cells, *in preparation*.

CHAPTER 2. SIDE-CHAIN ENGINEERING IN ORGANIC POLYMER MATERIALS

With the joint efforts of scientific researchers from academia and industry, the power conversion efficiency (PCE) of BHJ-OPVs has been rapidly improved so far. Matching with acceptor was primary objective for the polymer donor design in the past, because fullerene derivatives had been dominant as electron acceptor materials during the development of organic photovoltaic (OPV) technology. However, OSCs based on non-fullerene organic acceptors (NFAs) have been developed rapidly recently, which gradually substitute for fullerene OSCs and play an increasingly important role in this field. Comparing with the classical fullerene OPVs, NFA-OPVs put forward new requirements on polymer-donor structures to achieve desirable physical and optoelectronic properties.

Besides, solution processability is the outstanding feature of the photovoltaic active layer in OPVs devices and has great potential in reducing the cost of cell fabrication to realize highly flexible large-area OPVs. And side-chain modification undoubtedly is the primary consideration for optimizing solution processability. Therefore, this chapter focuses on the discussions of the molecular structural design of NFA-OPV polymer donor materials by side-chain engineering.

2.1. RELEVANT PROGRESS AND CHALLENGE

Modulating the flexible side chains, i.e., side-chain engineering, on conjugated backbone of organic polymer molecule is one easiest mean to optimize solution processability of OPVs. Normally, long and branched side chains can improve the solubility of polymers in common organic solvents but can weaken intermolecular π-π interactions to negatively impact carrier transport. Therefore, the solubility and the π-π interactions of polymers should be balanced by choosing suitable length and branches. Side-chain engineering could be utilized in any one or more moieties of donor (D), acceptor (A) or bridging moieties. Shown in the following Figure 2-1 (left), the D-A strategy structure of organic polymer donor materials are the most popular and most potential molecular structure design idea in recent research field of OSCs (44-46). Generally, benzo[1,2-b:4,5-b']dithiophene (BDT) unit is the fundamental core of the polymer molecule as D moiety due to its structural plasticity and large π-conjugated planes (47-50). The alternative A moiety has many choices, such as 2-(1-oxoaklxyl)thieno[3,4-b]thiophene (TT), thieno[3,4-c]pyrrole-4,6-dione (TPD), benzothiadiazole (BT), benzotriazole (BTA), diketopyrrolopyrrole (DPP) and benzo[1',2'-c:4',5'-c']dithiophene-4,8-dione (BDD) (51-53). And the bridge moiety

can be composed of thiophene or dithiophene, and even be removed (54-59). Moreover, side chain also has various options (Figure 2-1.right), such alkyl chain, alkyl-phenyl chain, alkyl-thienyl chain, alkyl-furanyl chain or alkyl- pyrrolyl chain. For D moiety, phenyl, thienyl or alkyl all are common side chains in recent research of organic polymer donor materials. While A moiety or bridge is common substituted with alkyl side chains (60-66).

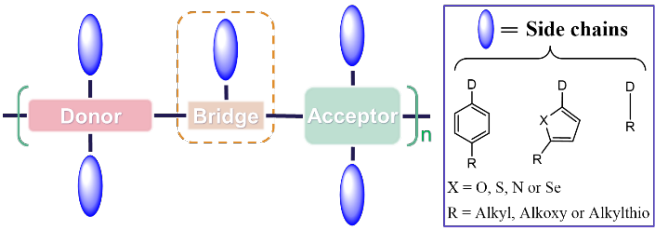

Figure 2-1. Schematic diagram of molecular structure modification idea of polymer donor (left) and alternative type of side chains (right).

As so far, plentiful attempts have been achieved to optimize the PV performance via side-chain engineering of organic polymer donors. Following (Figure 2-2) is the reported polymer donor materials with the effect of different side-chain engineering on PV performance. Series A of copolymers were synthesized by Yu. and co-workers, BDT unit as D moiety, TT unit as A moiety and alkoxy as side chains, to investigate the effect of PV performance by changing side chains (67). The HOMO levels of these polymers changed from -4.90 to -5.01 eV, but their optical bandgaps (E_g) were approximately same. It was obviously that there was no specific rules for optoelectronic properties with the changing length and branches of alkoxy side chain. But the OPV devices based on series A proved that overlong and excessively branched side chains had a negative impact on short circuit current (J_{SC}) and fill factor (FF). And according to the measurement results of grazing incident wide-angle X-ray scattering (GIWAXs), the biggest π-π stacking spacing (3.65Å) for A1 was smaller than ones (3.89Å) for A4, which was attributed to greater steric hindrance of A4 inducing by overlong and excessively branched alkyl side chains (68). Besides, Hou. et al. draw a similar conclusion when they synthesized the series C copolymers by introducing three different types of alkyl side chains on BDT unit. C1 exhibited closest π-π stacking interaction in the series C copolymers, because the side chain (octyl) of C1 is linear to induce the minimal steric hindrance. Thence, the OPV devices based on C1 had the best PV performance with a J_{SC} of 17.55 mA/cm^2 and an FF of 67.2%, affording a highest PCE of 9.52% (69). In addition, Beaujuge. et al. synthesized the series B copolymers to investigate the influence of the alkyl side chains of A moiety on PV performance, which indicated that different alkyl side chains had no apparent effect on V_{OC} but a notable change on J_{SC}. Concretely, B1-based OPV device had a best J_{SC} of 11.5 mA/cm^2, comparing with other two series B devices, owing to its smallest π-π interaction spacing of 3.6 Å. They suggested that the branched side chain would decrease the π-π interaction distance due to the strong steric hindrance, which

caused a lower carrier mobility, higher bimolecular recombination. Therefore, the rules of alkyl side chain in general also applied to the case of A moiety modification, which meant that side chains in A moiety had a great influence on the intermolecular arrangement (70). Ma. and co-workers obtained the series D polymers by incorporating different alkyl side chains on the thienyl of BDT unit. D1-based OPV device performed the best PCE of 6.17% with a surprising V_{OC} of 1.00 V. 2-ethylhexyl as the shortest side chains in group D, which had influence on the solubility, energy levels, and stacking spacing of polymers. Thence they believed that moderate size and topology of the side chains had a positive effect on PV performance (71).

Polymer	Eg (eV)	HOMO (eV)	Voc (V)	Jsc (mA/cm²)	FF (%)	PCE (%)	ref
A1	1.58	−4.90	0.58	12.5	65.4	4.76	63,64
A2	1.59	−4.94	0.6	12.8	66.3	5.1	63,64
A3	1.62	−5.01	0.68	10.3	43.1	3.02	63,64
A4	1.61	−5.01	0.62	7.74	47	2.26	63,64
B1	1.8	−5.56	0.85	9.81	66	5.5	65
B2	1.75	−5.48	0.87	8.1	56	3.9	65
B3	1.7	−5.57	0.81	9.7	67	5.4	65
C1	1.6	−5.29	0.81	17.55	67.2	9.52	66
C2	1.59	−5.29	0.81	16.52	62.3	8.37	66
C3	1.61	−5.29	0.81	16.22	56	7.36	66
D1	1.85	−5.61	1	9.79	63	6.17	67
D2	1.8	−5.47	0.92	8.92	55	4.51	67
D3	1.82	−5.56	0.95	8.94	53.2	4.5	67

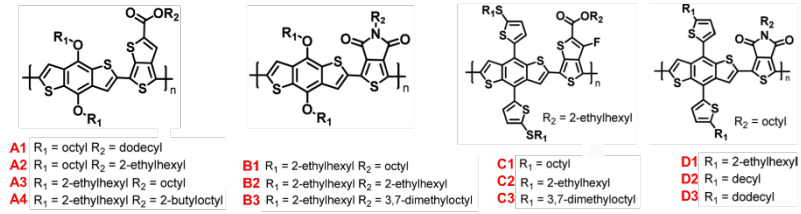

Figure 2-2. Table (top) of photovoltaic performance of abovementioned organic polymer donor materials, and schematic diagram (bottom) of corresponding polymer molecular structures.

However, these studies of alkyl side chains are all based on fullerene OPV devices, because the rise of OSCs based on NFAs are too short to be explored. The PV system of NFAs-based devices have a fundamental difference from fullerene-based OPV devices, thus the effect of the side chain engineering of organic polymer donor materials on PV performance of NFAs-based OSCs still needs to be investigated. Especially, some special side chains are more necessary to be studied, such alkyl-phenyl or alkyl-pyrrolyl, which could fill the fractional study vacancy in the field of NFAs-based OSCs.

2.2. DESIGN OF ORGANIC POLYMER DONOR MATERIALS

Well known, the properties of bulk-heterojunction layers, such as optical absorption bandgap, carrier mobility, crystallization, and film morphology, are all closely related

to short circuit current (J_{SC}) and fill factor (FF). And the molecular energy levels difference between highest occupied molecular orbital (HOMO) of donor and lowest unoccupied molecular orbital (LUMO) of acceptor corresponds to the open circuit voltage (V_{OC}) of the corresponding PV devices. J_{SC}, FF and V_{OC} are all the vital parameters to acquire the PCE of OSCs. The V_{OC} is the most easily predictable one among these PV properties of polymers, when concepting the molecular structure of polymer donors. Thence, for D-A copolymers, the choice of A units with strong electron-withdrawing effect was the most efficient pathway to tune the HOMO. In general, the high V_{OC} came at the expense of weak J_{SC}, resulting to hinder reaching higher PCE of the OPVs. Because high-bandgap OPV couples with weak absorption in near infrared region induce the lower J_{SC}. Thus, rational energy-level adjustment, maintaining moderate balance of J_{SC} and V_{OC}, was the proper optimization mentality. Recently, the reported TPD unit as the electron-acceptor moiety of D-A copolymers afforded deeper HOMO and more appropriate bandgap for absorption complementing typical low-bandgap non-fullerene small molecular acceptors when coupling with BDT (72, 73). Besides, side-chains modification on BDT moiety also could reach the same purpose as abovementioned. So far, many reported works on thiophene-flanked modification of BDT units had been confirmed, which successfully increased the V_{OC} and improved the PCE (65, 74-76). Whereafter, the co-polymer donor materials, containing BDT units with phenyl flanking, were demonstrated to be a deeper HOMO and a higher V_{OC} in corresponding photovoltaic devices than thiophene substitutes, because of the weaker electron-donor ability and the higher ionization potential of phenyl-flanked BDT moiety (62, 75, 77, 78). However, few papers discussed the specific influence of alkyl side-chain modification in the phenyl-modified BDT unit on the PV performance of NFAs-based OSCs till now.

In this chapter, we mainly focused on the impact of specific side chains on PV performance of NFAs-based OSCs. Thus, we presented the BDT- and TPD-based conjugated polymer donors to affording high V_{OC} of OSCs. For avoiding the dilemma of the overregulated HOMO, we inserted the thieno[3,2-b]thiophene as the π-bridge between BDT and TPD moieties, which could tune the absorption bandgap, HOMO/LUMO, crystallinity of active layers and π-π conjugated structure of the polymer backbone to improve carrier mobility, FF and J_{SC} (79, 80). To investigate the effect of different specific side chains on PV performance of NFAs-based OSCs. Thence, two copolymers with structure of PBDT-PX-ttTPD, named PBDT-PS-ttTPD (P10) and PBDT-PO-ttTPD (P11), were successfully synthesized as depicted in following picture (Figure 2-3). After further studied, we found that two polymers exhibited excellent PV performance in single-junction NFAs-based OPV devices.

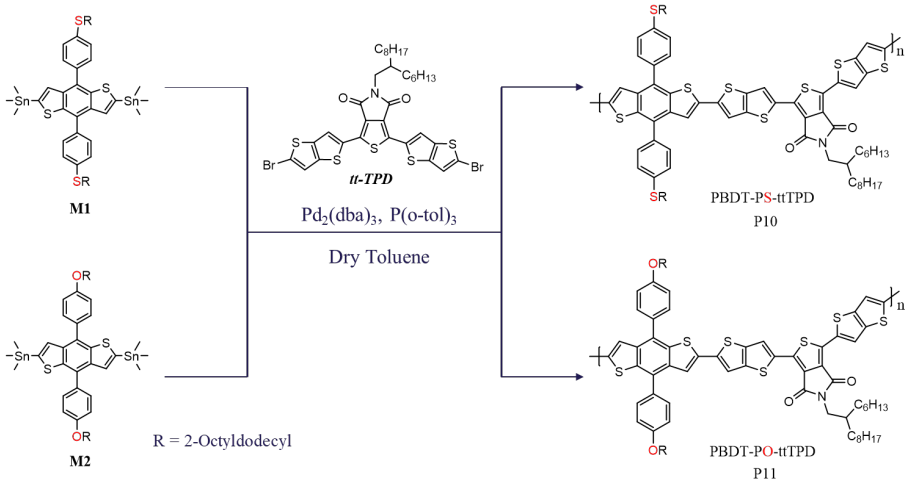

Figure 2-3. The synthetic pathway of PBDT-PS-ttTPD (P10) and PBDT-PO-ttTPD (P11).

2.3. THIN-FILM PROPERITES AND PV PERFORMANCE

Characterized by thermogravimetric analysis (TGA), two polymers exhibited good thermal stability for OSC applications, whose decomposition temperatures (T_d) for 5% weight loss were 353 °C for P10 and 419 °C for P11, respectively. Comparing with P10, obviously P11 could more easily dissolve into many organic solvents, which implied that the solution processability of P11 was better than P10 although P10 had a good solution processability. And the optical band gaps (E_g^{opt}) of two copolymers were 1.87eV for P10 and 1.89 eV for P11, respectively, which meant that two polymers belonged mid-bandgap donor materials. Moreover, the electrochemical bandgap of two were measured by cyclic voltammetry (CV), obtaining the HOMO levels of -5.33 eV for P10 and -5.30 eV for P11, respectively. The HOMO of P10 was ~0.03 eV deeper than P11, which indicated that alkylthio-phenyl side-chain modifications had a more significant electron-drawing effect on the HOMO than alkoxy-phenyl side-chain substituents. Thence, P10-based OPV devices with lower lying HOMO were expected to achieve higher V_{OC}. Because sulfur atom has an empty *d* orbital, it could generate π electron-withdrawing effect when coupling with phenyl. Meanwhile, the electronegativity of the sulfur atom is also greater than that of carbon, which would induce σ electron-withdrawing effect. Thus, the alkylthio side chain is the superposition of the two above effects. Despite, oxygen is more electronegative than carbon which would induce σ electron-withdrawing effect, oxygen has a lone pair of p electrons which would form p-π conjugation with adjacent delocalized π bond of benzene to emerge electron-donating effect (p-π conjugation electron-donating effect is much greater than σ electron-withdrawing effect).

Although the electron-donating effect of alkoxy side chains would make the HOMO higher lying than alkyl and alkylthio side chains when coupling with the thienyl

flanking (64, 81), the difference between three types of side chains became small when coupling with phenyl flanking. And we attributed this phenomenon to the large π electron delocalization bond of benzene, which possessed strong resistance of inductive effect. Compared with the analogous structure of copolymers with thienyl side chains (64, 77, 82, 83), the HOMO of polymers with phenyl side chains seemed to be deeper. Additionally, according to density-functional theory (DFT) calculations (Figure 2-4), a large torsion angle (ca. ~58°) was formed between phenyl side chains and benzodithiophene moiety, hindering π-conjugation expansion on vertical orientation of polymer backbone, owing to the intense intramolecular repulsion of the hydrogen atoms between side-phenyl and benzodithiophene. And it also made the polymer form a three-dimensional conformation to induce better side-chains accumulations. All the digital values of optical and electrochemical properties were listed together in Figure 2-4.

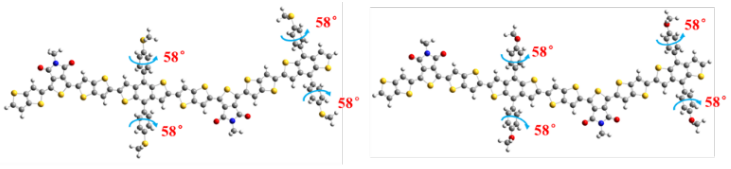

Polymers	λ_{edge} [nm]	HOMO [eV][a]	LUMO [eV][b]	E_g^{opt} [eV][c]	HOMO [eV][d]	LUMO [eV][d]
P10	663	-5.33	-3.46	1.87	-5.11	-2.18
P11	656	-5.60	-3.41	1.89	-5.27	-2.14

[a] Calculated from the equation $E_{HOMO} = -(E_{OX} + 4.8 - |Fc/Fc^+|)$ eV; [b] $E_{LUMO} = E_{HOMO} + E_g^{opt}$; [c] Evaluated from the absorption band edge of the polymer films and determined by the equation $E_g^{opt} = 1240/(\text{onset band edge of absorption})$; [d] Calculated via DTF.

Figure 2-4. Schematic diagram (top) of optimized molecular structure of two polymers, and table (bottom) of optical and electrochemical properties of two synthetic polymers.

2.3.1. PV PERFORMANCE OF POLYMERS

Then we fabricated two polymers, blending with NFAs (BTP-eC9), into the conventional devices to characterize their PV performance. The device configuration is ITO/PEDOT:PSS/Active layer/PFN-Br/Ag, where ITO is the anode, PEDOT:PSS is the hole transport layer (HTL), PFN-Br is the electron transport layer (ETL), Ag is the cathode, and the active layer is the bulk-heterojunction of donor and acceptor. After optimizing the manufactured conditions, the dosage of DIO additive and the weight ratio of D/A, the best PV performance for P10-based OSC devices (0.3 vol% DIO, 1:1 of D/A) were obtained with a V_{OC} of 0.89 V, a J_{SC} of 22.71 mA·cm^{-2}, and an FF of 63.81%, affording a high PCE of 12.93%. For P11-based OPV devices (0.7 vol% DIO, 1:1 of D/A) were achieved the best PV performance of 0.87 V for V_{OC}, 54.07% for FF and 19.96 mA·cm^{-2} for J_{SC}, respectively, resulting a moderate PCE of

9.37% (Figure 2-5.A). Obviously, the changing of experimental V_{OC} (~0.02 V) between P10 (alkylthio-phenyl side chains) and P11 (alkoxy-phenyl side chains) was consistent with the predicted trend of HOMO levels. Furthermore, the external quantum efficiency (EQE, Figure 2-5.B) curves indicated that the integrated J_{SC} was calculated of 22.65 mA·cm^{-2} for P10-based devices and 19.14 mA·cm^{-2} for P11-based devices, respectively, which were similar to the values of J-V measurement. Apparently, the PV performance of P10-based OPVs was better than P11. Except for the difference of V_{OC} between two polymers, the difference of J_{SC} was also worth investigating, which was closely associated with the semiconductor characteristics of OPV devices.

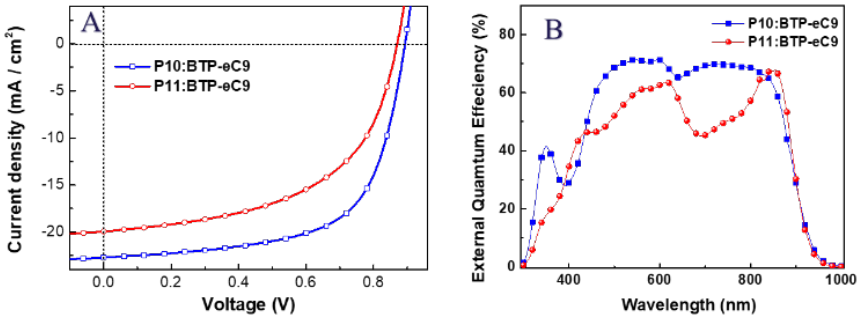

Polymer/ BTP-eC9	DIO (vol%)	FF (%)	V_{oc} (V)	J_{sc} (mA cm^{-2})	PCE (%) Best/Ave [a]
P10	0	57.33	0.89	23.00	11.75/11.08
	0.3	63.81	0.89	22.71	12.93/12.24
P11	0	49.08	0.87	19.55	8.35/8.06
	0.7	54.07	0.87	19.96	9.37/9.04

[a] Average PCE is calculated from 10 parallel devices.

Figure 2-5. J-V (top A) and EQE (top B) curves of OPV devices under optimal manufactured conditions. And table (bottom) of corresponding PV performance.

2.3.2. SEMICONDUTOR PERFORMANCE OF POLYMERS

Therefore, we performed the further study of semiconductor characteristics, exciton recombination abilities, carrier mobility properties and charge dissociation abilities (P_{diss}), to understand the effect of side-chain engineering on PV performance of OPV devices based on two polymers. As shown in Figure 2-6.A, the relationship of J_{SC} and the light intensity (I) is $J_{SC} \propto I^{\alpha}$, where α is the degree of biomolecular recombination. When $\alpha = 1$, dissociated free charges do not recombine during the movement process, and are all collected by the electrode, implying the recombination can be ignored. If

α is less than 1, the bimolecular recombination will be present in the devices, and the smaller the value of α indicates the stronger bimolecular recombination. Moreover, as shown in Figure 2-6.B, $V_{OC} \propto (nkT/q)\cdot\ln(I)$, where K represents the Boltzmann constant, T is the Kelvin temperature, and q is the elementary charge. If the slope is close to 2kT/q, the trap-assisted recombination will be inside the devices (84, 85). For P10-baesd devices with α value of 1.01 and slope of 1.24 KT/q and for P11-based devices with α value of 0.98 and slope of 1.08 KT/q, which indicated that little trap-assisted recombination was in two kinds of devices and the bimolecular recombination also could nearly be ignored.

The charge dissociation probability was obtained from the function of photogenerated current density (J_{ph}) *versus* effective applied voltage (V_{eff}). The J_{ph} is defined as the difference between J_L and J_D, where J_L and J_D are the current density of devices under light (100 mW/cm^2) and dark, respectively. $V_{eff} = V_0 - V$, where V_0 is the voltage when $J_{ph} = 0$ and V is the applied voltage during the measurement. When the reverse voltage is greater than 2 V, the recombination is suppressed by a high internal electric field. Thus, J_{ph} will reach the saturated current density (J_{sat}). Consequently, $P_{diss} = J_{ph}/J_{sat}$ could be used to describe the charge dissociation probability (86, 87). And the higher P_{diss} is indicated the more effective charge dissociation. Obviously, two polymer-based OPV devices both possessed high effective charge dissociation abilities. Nonetheless, the charge dissociation ability of P10-based OPV devices were still slightly higher than P11.

The carrier mobility properties could be investigated by fabricating the corresponding diode devices based on two polymers. Then they could be determined by applying the space charge limited current (SCLC) method to the J-V measurements of the devices. And the hole/electron mobilities could be calculated using the following equation:

$$J_{SCLC} = (9/8)\varepsilon_r\varepsilon_0\mu(V^2/L^3)$$

where J is the current density, ε_r is the dielectric constant of the polymers, ε_0 is the permittivity of the vacuum, μ is the hole mobility, L is the thickness of the blend films, $V = V_{appl} - V_{bi}$, where V_{appl} is the applied potential, and V_{bi} is the built-in voltage which results from the difference in the work function of the anode and cathode (88). As shown in Figure 2-6 from D to F, following the formula of SCLC method, the hole mobilities were found of 3.60×10^{-4} cm^2 V^{-1} s^{-1} for P10/eC9-based diode devices and 3.46×10^{-4} cm^2 V^{-1} s^{-1} for P11/eC9-based diode devices, respectively. And the electron mobilities were obtained of 2.49×10^{-4} cm^2 V^{-1} s^{-1} for P10/eC9-based diode devices and 1.81×10^{-4} cm^2 V^{-1} s^{-1} for P11/eC9-based diode devices, respectively. Besides, the polymer-only diode devices were fabricated as the comparison, obtaining the hole mobilities of 3.80×10^{-4} cm^2 V^{-1} s^{-1} for P10 and 3.48×10^{-4} cm^2 V^{-1} s^{-1} for P11, respectively. The measurement results of polymer-only devices were similar to D-A blending devices, which indicated that these results were persuasive. Overall, when alkylthio-phenyl side chains substituted alkoxy-phenyl side chains, the carrier

mobility and charge dissociation ability were improved and the exciton recombination was reduced, which afforded a higher J_{SC}. Thus, we believed that OPV devices with alkylthio-phenyl side chains had better PV performance than ones with alkoxy-phenyl side chains.

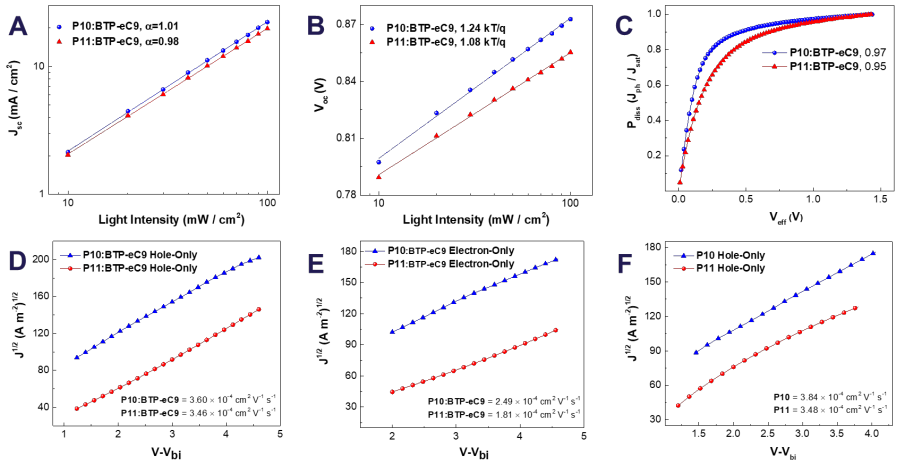

Figure 2-6. Dependence diagram of J_{SC} (A) and V_{OC} (B) as a function of light intensity in the polymer:BTP-eC9 OPV devices. Schematic diagram (C) of charge dissociation probabilities (P_{diss}) vs effective voltage (V_{eff}) in the polymer:BTP-eC9 OPV devices. $J^{1/2}$-V plots of Polymer:BTP-eC9 hole-only devices (D), Polymer:BTP-eC9 electron-only devices (E), and polymer hole-only devices (F).

2.3.3. PHASE MORPHOLOGY OF POLYMER FILMS

According to UV-vis absorption spectrum (Figure 2-7.A), comparing with structurally analogous polymers (71, 89), two polymers showed the distinct shoulder absorption peaks next to their maximum absorption peaks, which indicated that the strong π-π stacking behavior was in both solution and film. And alkylthio side chains had strong effect of electron-withdrawing, while alkoxy side chains were the electron-donating group. Therefore, due to the electron could of alkoxy-phenyl side chain substituted polymer was denser than that of alkylthio-phenyl side chain, there was a higher intermolecular repulsion potential between the backbones of two adjacent polymers with alkoxy-phenyl side chains, which demonstrated that the polymer with alkylthio-phenyl side chains had more highly effective aggregation behavior. As shown in the temperature-dependence UV-vis absorption spectrum (Figure 2-7.B), the shoulder absorption peak of P10 decreased slightly with the increase of temperature, indicating that the potential energy provided by high temperature cannot destroy the strong π-π stacking behavior of P10 in chlorobenzene. On the contrast, because of the weak π-π stacking behavior of P11, the disaggregation of π-π stacking could be promoted when the appropriate potential energy was provided at high temperature, thus the shoulder absorption peak of P11 (Figure 2-7.C) gradually disappeared with the increase of

temperature. These results also were proved from the side that the alkylthio-phenyl side chains promoted the π-π stacking behavior of the polymer backbone.

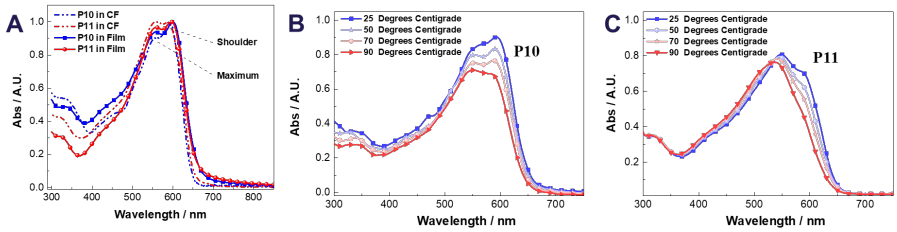

Figure 2-7. Normalized UV-vis absorption curves of two polymers (A) and temperature dependent UV-vis absorption plots of P10 (B) and P11 (C) in chlorobenzene.

Additionally, we investigated the surface morphology and the phase morphology of binary (donor and acceptor) blending films by utilizing two analytical methods, atomic force microscopy (AFM) and grazing-incidence wide-angle X-ray scattering (GIWAXs). As depicted in AFM images (Figure 2-8.top), except for few large-sized nanoparticles in P10-based blending films, the good miscibility of two polymer-based blending thin films could be observed, which provided the desirable phase separation in microscopic scale. From the overall surface morphology of two polymers, the phase distribution of BHJ in the film was relatively uniform. GIWAXs analysis method was used to charactered for distinguishing the molecular crystalline, arranged orientation and π-stacking in these films of two polymers. As Shown in Figure 2-8.A, the films of P10 and P10:BTP-eC9 both preferentially formed face-on orientation, and obviously P10:BTP-eC9 blending films exhibited increased molecular arrangements of face-on orientation, implying the enhanced π-π stacking interaction. Besides, the films of P11 and P11:BTP-eC9 also formed face-on orientation. The signal positions along q_z axis in the P11-only film indicated that the arrangement of polymer backbones was loose and disordered. Notably, when P11 was blended with BTP-eC9, the random and inhomogeneous arrangement turned to regularly and uniformly face-on orientation immediately. Shown in Figure 2-8.B, the main alkyl side-chain stacking (100) diffraction pattern of four blending films were almost same. But there were two emerging diffraction peaks of P10 along the q_{xy} axis (next to the 100) after blending with BTP-eC9, which indicated that the closer ordered lamellar packing of side chains was formed in different phases. In the Figure 2-8.C, a (010) diffraction peak along the q_z axis of 1.832, 1.756, 1.932 and 1.827 $Å^{-1}$ for P10, P11, P10/BTP-eC9 and P11/BTP-eC9, respectively, which correspond to the d-spacing of 3.43, 3.58, 3.25 and 3.44 Å, respectively. The results revealed that two polymers formed enhanced π-π stacking interactions along the polymer backbone when blended with BTP-eC9. Besides, a weak and broad diffraction peak of P10 at about 1.54 $Å^{-1}$, corresponding to the d-spacing of 4.06 Å, emerged after blending the NFAs, which was considered to be the π-π stacking between two different phases. And it also implied that the P10/BTP-eC9 binary blending films showed obvious D-A phase separation, which meant that the exciton diffusion interface increased. Thus, the BHJ blending films

with alkylthio-phenyl side chains substitutes had the denser π-π stacking behavior, the more ordered molecular orientation and the larger area of phase separation.

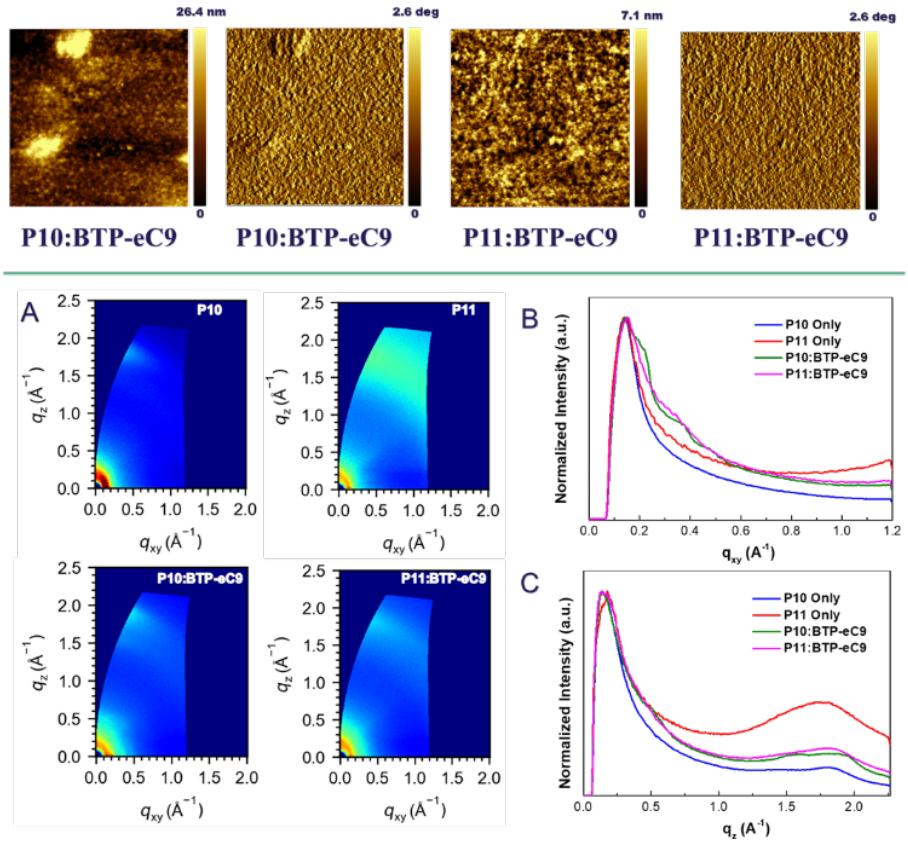

Figure 2-8. AFM height and phase diagrams (top) of blending thin films, 4 μm × 4 μm. GIWAXs images (bottom A) of polymer-only and blending films, corresponding out-of-plane direction (bottom B) pattern and in-plane direction (bottom C) pattern.

2.4. SUMMARY

Through synthesis of two novel polymer donor materials with special side chains, alkylthio- and alkoxy-phenyl flanks, we investigated the effect of side-chain engineering on PV performance in single-heterojunction NFAs-based OSCs. And two polymers showed excellent PV performance pairing with BTP-eC9. The alkylthio-phenyl side chains substituted OPV devices had a higher V_{OC}, J_{SC} and FF, which reached higher PCE than that of alkoxy-phenyl substitutes. Because the alkylthio-phenyl side chains have a stronger electron-withdrawing effect, which deepens the HOMO levels of polymer molecules to achieve higher V_{OC}. And by substituting of

alkoxy-phenyl with alkylthio-phenyl, the carrier mobility and the charge dissociation ability are improved, and the exciton recombination is reduced. Besides, alkylthio-phenyl side chains also induce denser π-π stacking behavior of polymer backbones, form more ordered molecular orientation and increase the area of D-A phase separation. The synergistic effect of these improvements is reflected in the increase of J_{SC} and FF in corresponding OPV devices. Besides, this result fills the research vacancy on side chain engineering modification of polymer donor materials and provides new ideas and experimental basis for improving PV performance of NFAs-based OPV devices.

CHAPTER 3. FUNCTIONAL GROUP ENGINEERING IN ORGANIC POLYMER MATERIALS

As abovementioned in Chapter 2, the inductive effect, a molecular polarization effect of shifting the density of the bonding electron cloud to a certain direction causing by the influence of substituents (atoms or atomic groups) with different electronegativity, can modulate the optical and electrochemical characterizations of polymer donor materials. Obviously, different substituents have different effects, thus we refer to the studies based on this theory as functional group engineering in the field of OSCs. Commonly, the strategy of functional group engineering is to introduce electron-withdrawing or electron-donating substitutions into backbone and/or the flanks, such as fluorine, oxygen, sulfur, ester, carbonyl, sulfonyl or cyano, etc. This chapter will introduce the reader to several common functional atoms or groups, and a practical experimental case based on fluorination modification in detail.

3.1. FOUNDATION AND MOTIVATION

Compared with side-chain engineering, functional group engineering focuses more on modulating the electron cloud distribution of the molecular orbital of the polymer, which will have a greater impact on molecular energy levels, optical absorption bandgaps and carrier transports of polymer donor materials. More importantly, the preliminary conclusion of structural modulations with these atoms or groups can be easily predicted by the basic theory of atomic orbital or molecular orbital before experiment. When the polymers are replaced by electron-withdrawing functional groups, the molecular energy levels (HOMO and LUMO) of the polymers will decrease, and when it is an electron-donating group, the result is opposite. Additionally, the relative inductive effects of these functional groups have been measured experimentally with reference to hydrogen, and then the ranking is listed in the order of decreasing intensity of induced effect by researchers, as follows: $-NO_2$ > $-SO_2R$ > -CN > $-SO_3H$ > -CHO > -CO > -COOR > -COCl > $-CONH_2$ > -F> -Cl> -Br> -I> -SR> -C≡CR> -OR> -OH> $-NR_2$> $-C_6H_5$> $-CH=CH_2$> -H> $-CR_3$ (90). It is notable that there are some special groups need to be illustrated, i.e., SR, OR and NR_2. In terms of atomic electronegativity, S, O and N atoms are all stronger than C atom (C<S<O<N), but SR groups are electron-withdrawing effect while OR and NR_2 groups are electron-donating effect. As described in Chapter 2 (page 19), same as oxygen, nitrogen also has a lone pair of p electrons which would form p-π conjugation with adjacent delocalized π bond of aromatic hydrocarbons to generate the electron-donating effect (p-π conjugation electron-donating effect is much greater than σ electron-withdrawing effect). Thus, combined with the requirement of steric

hindrance size of atoms or groups, a wise choice can be made about functional group engineering.

As functional group, fluorine atom is excellent to modulate the electronic properties of the conjugated polymers, due to its advantages of strong electron-withdrawing ability and small size. When fluorine atoms are introduced into polymer molecules, the HOMO and LUMO energy levels are lowered without causing considerable steric hindrance. As shown in Figure 3-1, in 2013 Andrew et al. developed a series of PBnDT-DTBT-based polymer donor materials to investigate the relationship between the degree of fluorination and PV performance. They found that the HOMO levels decreased from -5.42 to -5.53 eV, the V_{OC} improved from 0.78 to 0.90 V and PCE achieved 7.16% from 4.53% with increased fluorine content (91). And the polymers, E1-E3, were designed and synthesized by Hou. and co-workers to study the effect of different fluorinated moiety on PV performance. The result demonstrated that the fluorinated D moiety had lower lying HOMO and higher V_{OC}, affording a better PCE of 7.2, than the fluorinated A moiety. And polymer donor materials with the fluorinated D and A moieties had the lowest HOMO level of -5.20 eV, the highest V_{OC} of 0.78 V and the best PCE of 8.6% among three (92).

Polymer	HOMO (eV)	Voc (V)	Jsc (mA/cm²)	FF (%)	PCE (%)	ref
PBnDT-DTBT	−5.42	0.78	11.7	47.6	4.53	87
PBnDT-DTfBT	−5.48	0.84	11.5	52.2	5.52	87
PBnDT-DTffBT	−5.53	0.90	12.2	62.3	7.16	87
E1	−4.95	0.6	14.3	65.7	5.6	88
E2	−5.15	0.74	14.4	67.7	7.2	88
E3	−5.20	0.78	15.2	72.4	8.6	88

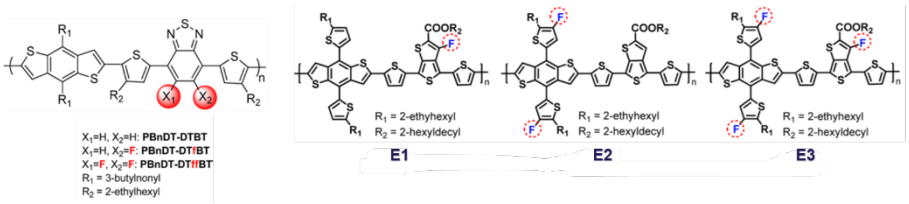

Figure 3-1. Table (top) of photovoltaic performance of abovementioned organic polymer donor materials, and schematic diagram (bottom) of corresponding polymer molecular structures.

Moreover, there are some reported polymer donor materials with other functional groups, shown in Figure 3-2, revealing the different effects on PV performance in their corresponding OSC devices. Yu et al. synthesized the polymer with stronger electron-withdrawing substitution, cyano group, to discuss the difference of PV performance between it and H or F substituents. It was obviously that the HOMO levels and V_{OC} changed after modifications, reducing of HOMO from -5.29 to -5.67 eV and increased of V_{OC} from 0.7 to 0.97 V, respectively. But the difference of PCE

between cyano and fluorine substituted polymers was very small, because the large steric hindrance of the cyano group weakened the J_{SC} of the OPV devices (93). Alkylthio, alkoxy, sulfone, carbon and ester groups substituted polymer donor materials were also reported in recent papers. E7-E9 were modified on D moieties with functional groups, and despite of the high V_{OC}, the OPV devices of P8 with sulfone groups exhibited extremely worse PV performance owing to the terribly large steric hindrance reducing the J_{SC} and FF (94). For E10-E12, the polymers, substituted with sulfone, carbon and ester groups on A moieties, were designed and synthesized to discuss their PV performance. The carbonyl substituted polymer had moderate V_{OC} and higher J_{SC}, achieving the best PCE of 7.59% among them, due to its lower lying HOMO and smallest steric hinderance. Comparing with the sulfone substituted polymer in D moiety (P8), P12-based OPV devices performed pretty good without drastic decrease of J_{SC}, and this result indicated that the large-size functional groups with large steric hindrance had a small effect on PV performance when they were modified in A moiety (95).

Polymer	HOMO (eV)	Voc (V)	Jsc (mA/cm²)	FF (%)	PCE (%)	ref
E4	−5.29	0.7	11.14	55.2	4.3	89
E5	−5.36	0.79	11.83	72.9	6.81	89
E6	−5.67	0.97	10.92	71.4	7.52	89
E7	−5.01	0.64	14.9	70.3	6.7	90
E8	−5.16	0.81	5.95	37.9	1.85	90
E9	−5.17	0.78	13.4	71.8	7.5	90
E10	−5.09	0.68	14.59	62.6	6.21	91
E11	−5.11	0.74	17.48	58.7	7.59	91
E12	−5.29	0.81	12.27	61.98	5.93	91

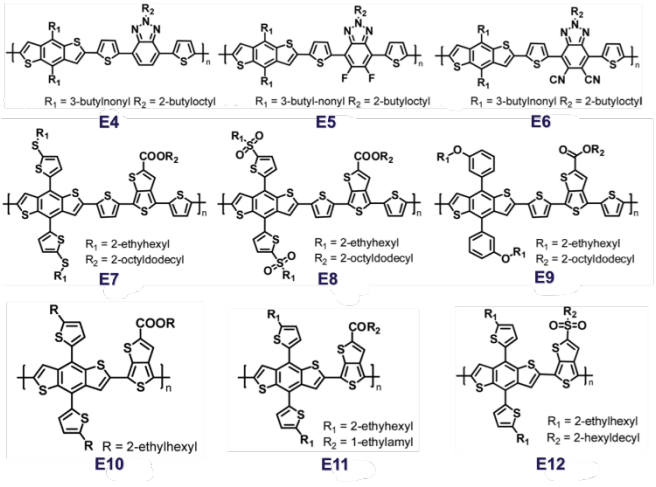

Figure 3-2. Table (top) of photovoltaic performance of abovementioned E4-E12 polymers, and schematic diagram (bottom) of corresponding polymer molecular structures.

Thus, we can conclude that the functional groups with stronger electron-withdrawing effect performs lower lying HOMO levels and higher V_{OC}, and they achieves better PCE if the steric hindrance of them is small. And fluorine atom is undoubtedly one of the most ideal functional groups, which has a good balance between the properties of electron-withdrawing ability and steric hindrance. Additionally, the steric hindrance effect of functional groups is a smaller influence when they are modified in A moiety of the copolymers. However, systematic studies discussed above are the OPV devices based on fullerene acceptors, but it is still feasible to achieve high V_{OC} by introducing strong electron-withdrawing groups to modulate the HOMO energy levels in NFAs system. Therefore, next part of this chapter, we focus on the effect of functional groups on J_{SC} in NFAs-based OPV devices and present a practical example to discuss these details about functional group engineering.

3.2. STRUCTURES AND MOLECULAR PROPERTIES

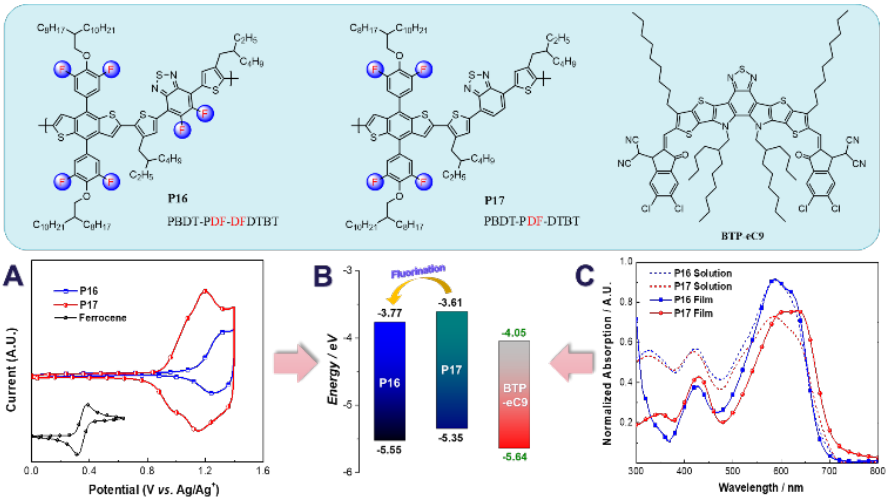

Figure 3-3. Structures (top) of polymers and BTP-eC9, cyclic voltammetry curves (A) of two polymers and Fc/Fc$^+$, respectively, HOMO-LUMO energy levels (B) of polymers and acceptor, and UV-vis absorption spectrum (C) of two polymers in chloroform and film.

We developed a synthetic pathway for fluorinated polymer donor (Figure 3-3.top), named PBDT-PDF-DFDTBT (P16), the BDT unit 4,8-bis(3,5-difluro-4-(2-octyldodecyl)phenyl)-benzo[1,2-b:4,5-b']dithiophene as the D moiety and DTBT unit 4,7-di(4-(2-ethylhexyl)-2-thienyl)-2,1,3-benzothiadiazole as the A moiety. For comparing with P16, we designed another difluorinated A moiety , which was modified with two more fluorine on DTBT, and copolymerized with BDT units to obtain PBDT-PDF-DTBT (P17). Two polymers had the excellent solution processability and were readily dissolving in most common organic solvent, such as chloroform (CF), chlorobenzene (CB), and o-dichlorobenzene (o-DCB), etc. The

number-average molecular weight (M_n) and the polydispersity index (PDI) of two polymers were measured with calibration against polystyrene standards by gel permeation chromatography (GPC), resulting M_n for P16 of 12.1 KDa and for P17 of 15.3 KDa and PDI for P16 for 1.77 and for P17 of 1.92, respectively. And two polymers exhibited good thermal stability in thermogravimetric analysis (TGA, Figure 3-4.B), where the decomposition temperatures (T_d) for 5% weight loss of P16 and P17 were 406 °C and 420 °C, respectively. As shown in Figure 3-4.C, the UV-vis absorption spectrum of P16 and P17 in solution was similar, which meant that the modification of fluorine in A moiety had little effect on optical bandgap. However, there was 18 nm bathochromic shift of maximum absorption peak in thin films after fluorination, which indicated that P17 had the tighter π-π stacking interaction along the polymer backbone. Obviously, more fluorine atoms hinder the better formation of π-conjugation effect, instead. And the thin-films electrochemical characteristics of P16 and P17 were studied by cyclic voltammetry (Figure 3-4.A). The onset oxidation potentials (E_{OX}) were 1.1 V for P16 and 0.9 V for P17, respectively, corresponding to the highest occupied molecular orbital (HOMO) of -5.55 for P16 and -5.35 eV for P17, respectively. The HOMO level of P16 was ~0.2 eV lower than one of P17, which indicated that the fluorine atoms in A moiety had a significant electron-withdrawing effect on the polymer backbone to induce the deepener HOMO. Thus, the P16-based OSC devices would have a larger V_{OC} than P17. On the other hand, lower unoccupied molecular orbital (LUMO) was determined from the difference of E_{HOMO} and E_g^{opt}, obtaining of -3.77 eV for P16 and -3.61 eV for P17, respectively.

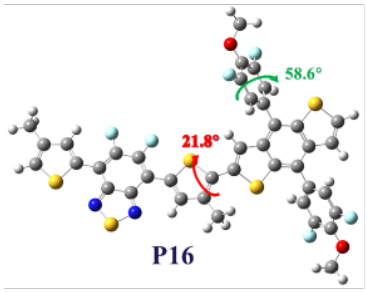

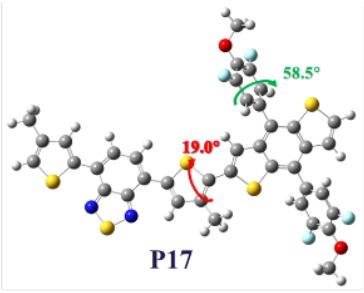

Polymers	λ_{edge} [nm]	E_g^{opt} [eV][c]	HOMO [eV][a]	LUMO [eV][b]	HOMO [eV][d]	LUMO [eV][d]
P16	698	1.78	-5.55	-3.77	-5.16	-2.79
P17	712	1.74	-5.35	-3.61	-5.09	-2.70

[a] Calculated from the equation $E_{HOMO} = -(E_{OX} + 4.8 - |Fc/Fc^+|)$ eV; [b] $E_{LUMO} = E_{HOMO} + E_g^{opt}$; [c] Evaluated from the absorption band edge of the polymer films and determined by the equation $E_g^{opt} = 1240/(\text{onset band edge of absorption})$; [d] Calculated via DTF

Figure 3-4. Schematic diagram of optimized molecular structure (top) of two polymers by DFT, and table (bottom) of optical and electrochemical properties of two polymers.

For further investigation of molecular structure property of two polymers, density-functional theory (DFT) was used to simulate and calculate the thermodynamically optimal structure and corresponding energy levels. As shown in Figure 3-4.top, the intramolecular intense repulsion of side-phenyl o-Hydron and benzodithiophene 3-b-Hydron induced a large torsion angle (ca. 58°) between phenyl side chains and BDT moiety, which implied that polymer molecular backbone preferred 3D three-dimensional structure rather than 2D planar structures in thermodynamics. And 3D structure was more beneficial for forming of C–F···H band interaction between the adjacent polymer conjugated backbones. And the dihedral angles between D moiety and A moiety unit are 21.8° for P16 and 19.0° for P17, respectively, which indicates that the D-A structure of P17 is flatter than that of P16. Thus, we believe that the molecular arrangement of P16 will be better than that of P17 in thin films.

3.3. SURFACE MORPHOLOGY AND PHASE SEPERATION

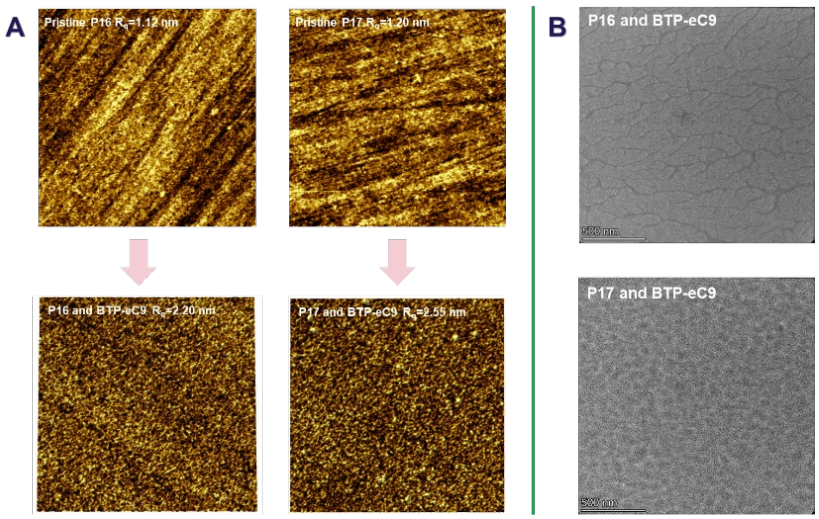

Figure 3-5. AFM height diagrams (A) of pristine P16, pristine P17, P16:BTP-eC9 and P17:BTP-eC9 thin films, 10 μm × 10 μm. And TEM images (B) of P16:BTP-eC9 and P17:BTP-eC9 thin films, 2 μm × 2 μm.

Firstly, for further understanding the difference between two polymer donor materials in NFAs-based OPV devices, atomic force microscopy (AFM) and transmission electron microscope (TEM) were used to investigate the nanoscale morphologies and molecular arrangement. As shown in Figure 3-5.A, the surface morphologies of pristine P16 thin film clearly exhibited deep and straight through linear dark ravines, while that of P17 was shallow and intermittent. We believed that P16 had sufficient sites of C-F···H bonds along the polymer backbone, which linked and fixed the surrounding adjacent polymer chains to make them align in parallel. However, since

P17 lacked such sites, the staggered arrangement between polymer chains increased. When blended with the BTP-eC9, the orientated linear ravines of P16 disappears but the shallow straight ravines were still faintly visible. The linear ravines of P17 blending film completely disappeared and formed staggered mesh topography instead. And P16 showed similar surface roughness (R_q) as P17, so two polymers had the good miscibility. But the phase separation of P17 was better than P16 because of the network interpenetrating structure. Moreover, according to the TEM images (Figure 3-5.B), same as present in AFM, P17 exhibited better polymer phase separation and formed a well-developed nanoscale bicontinuous interpenetrating network fibrous structure, which implied better exciton dissociation ability.

Then the polymers materials were characterized by grazing-incidence wide-angle X-ray scattering (GIWAXs). As shown in Figure 3-6.A, the heterojunction morphologies of pristine P16 and pristine P17 films were both face-on orientation, and the content of face-on orientation in pristine P17 film was more than that in P16. After blending with BTP-eC9, the orientation of the face-on morphology in P16 and P17 blending films were enhanced comparing with pristine ones. In addition, P16-based blend film also had obviously partly edge-on morphology orientation, which indicated that the π-conjugated structure of polymer backbone in P16 blended film not aligned in a parallel direction. Thus, P16-based OPV devices had worse carrier transport property. The out-of-plane and in-plane cut pattern of blended films were presented in the Figure 3-6.B and C, a (010) diffraction peak along the q_z axis of 1.82 and 1.85 $Å^{-1}$ for P16/BTP-eC9 and P17/BTP-eC9, respectively, which correspond to the d-spacing of 3.45 and 3.40 Å, respectively, which revealed that P17 blending film had closer π-π stacking structure along the polymer backbone.

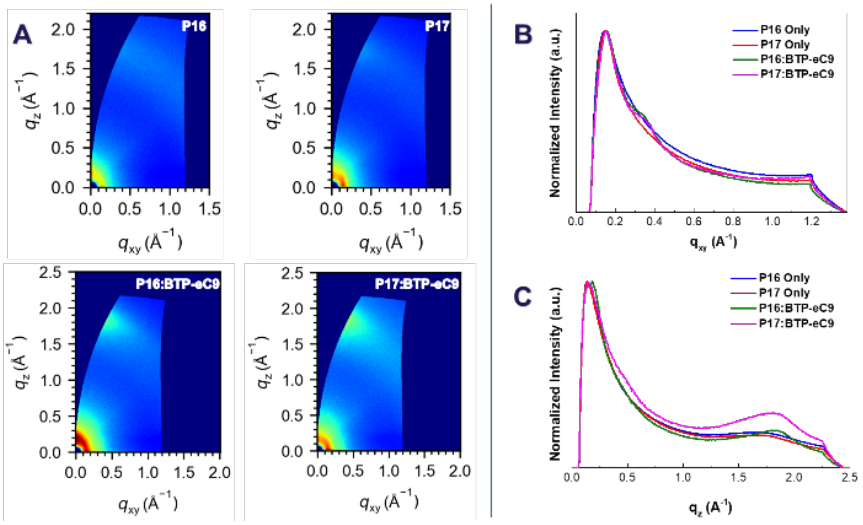

Figure 3-6. GIWAXs images (A) of polymer-only and blending films, corresponding out-of-plane direction (B) pattern and in-plane direction (C) pattern.

3.4. PV PERFORMANCE AND SEMICONDUTOR PROPERTIES

To evaluate the photovoltaic potentials of two novel donor polymer materials were fabricated as conventional structure, blending with BTP-eC9. The configuration of OSC device is ITO/PEDOT:PSS/polymer:BTP-eC9/PFN-Br/Ag. Through optimizing the fabrication conditions, weight ratio of donor and acceptor, content of solvent additive and spin-coating speed of active layer, the best photovoltaic performance of PSC devices were obtained. As shown in Figure 3-7.bottom, P17-based OPV devices achieved the best PCE of 12.71% with FF of 69.9%, J_{SC} of 21.08 mA·cm^{-2} and V_{OC} of 0.86 V, under conditions of 10:12 (w/w) of donor-to-acceptor weight ratio, non-additive and spin-coating of 2000 rpm. Unexpectedly, in Figure3-7.A, P16-based OPV devices showed a worse PCE of 6.46% with FF of 51.83%, J_{SC} of 13.78 mA·cm^{-2} and V_{OC} of 0.90 V. Obviously, the PCE of P16-based device was much lower than that of P17, in spite of the higher V_{OC}. And corresponding current density-voltage (J-V) curves and external quantum efficiency (EQE) spectra of the solar cells are illustrated in Figure 3-7.B, which indicated that the integrated J_{SC} was calculated of 13.58 mA·cm^{-2} for P16 and 20.82 mA·cm^{-2} for P17, which were consistent to their J-V experimental results.

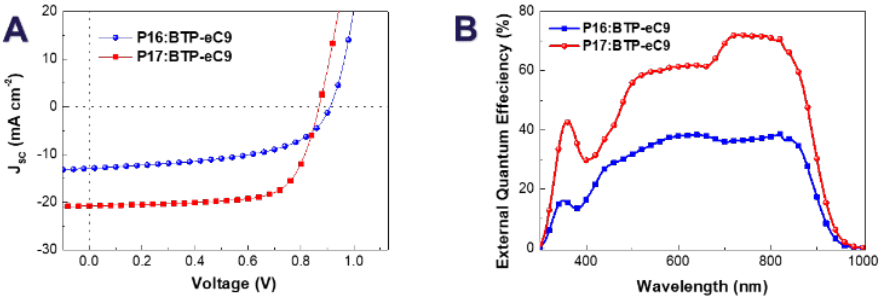

Polymer/ BTP-eC9	FF (%)	V_{OC} (V)	J_{SC} (mA cm^{-2})	PCE (%) Best/Ave [a]
P16	51.83	0.90	13.78	6.46
P17	69.90	0.86	21.08	12.71

[a] Average PCE is calculated from 15 parallel devices.

Figure 3-7. J-V (top A) and EQE (top B) curves of the OPV devices under optimal manufactured conditions. Table (bottom) of corresponding PV performance.

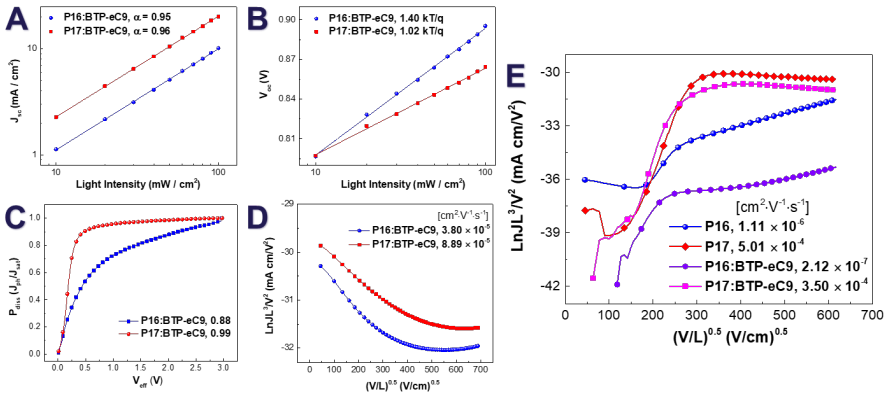

Figure 3-8. Dependence diagram of J_{SC} (A) and V_{OC} (B) as a function of light intensity in OPV devices. Plots (C) of P_{diss} vs V_{eff} in OPV devices. $J^{1/2}$-V plots of hole-only devices (D) and electron-only devices (E).

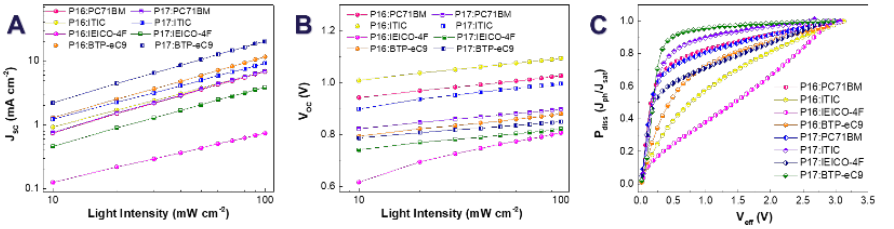

Polymer / Acceptor	D:A (w/w) [a]	PCE Best/Ave(%) [b]	FF (%)	V_{OC} (V)	J_{SC} (mA cm^{-2})	J_{SC} (mA cm^{-2}) [c]	α	KT/q	P_{diss} (J_{ph}/J_{sat})
P16:PC71BM	1:1.5	4.42/4.22	62.87	1.03	6.83	6.21	0.96	1.39	0.92
P16:ITIC	1:1.2	3.21/3.04	46.05	1.10	6.31	5.12	0.87	1.39	0.81
P16:IEICO-4F	1:1.2	0.22/0.20	35.39	0.81	0.75	0.58	0.77	3.04	0.67
P16:BTP-eC9	10:12	6.46/6.15	51.83	0.90	13.78	12.58	0.95	1.40	0.88
P17:PC71BM	1:1.5	3.92/3.83	63.01	0.90	6.89	6.68	0.96	1.35	0.92
P17:ITIC	1:1.2	6.51/6.27	60.06	0.99	10.91	10.73	0.87	1.38	0.97
P17:IEICO-4F	1:1.2	1.87/1.81	59.64	0.83	3.77	2.96	0.92	1.29	0.87
P17:BTP-eC9	10:12	12.71/12.37	69.90	0.86	21.08	20.42	0.96	1.02	0.99

[a] The total concentrations of BTP-eC9-based devices are 22 mg/mL, others are 20 mg/mL, [b] average PCE is calculated from 8 parallel devices, [c] Calculated from EQE integrated short circuit density.

Figure 3-8. Dependence diagram of J_{SC} (A) and V_{OC} (B) as a function of light intensity in D:A blending OPV devices. Schematic diagram (C) of charge dissociation probabilities (P_{diss}) vs effective voltage (V_{eff}) in D:A blending OPV devices. The corresponding table (bottom) with anaylized resultes of PV performance.

Furthermore, carrier mobilities and charge dissociation abilities were characterized as described in Chapter 2 (page 21). Firstly, the carrier mobilities of two materials were studied by SCLC method (Figure 3-8.D and E), where the hole mobility properties were found of 2.12×10^{-7} cm^2 V^{-1} s^{-1} for P16 and 3.50×10^{-4} cm^2 V^{-1} s^{-1} for P17, respectively. Comparing with the polymer-only devices, the hole mobility of P17 was approximate, while mobility of P16 was unexpectedly much lower. Because after blending with BTP-eC9, the different orientations of molecular arrangements increase in the organic active layer of P16. Meanwhile, the electron mobilities were obtained of 3.80×10^{-5} cm^2 V^{-1} s^{-1} for P16 and 8.89×10^{-5} cm^2 V^{-1} s^{-1} for P17, respectively. The P_{diss} of P17-based OPVs were much higher than that of P16 due to the excellent phase separation of P17 blending film. Besides, the charge recombination in Figure 3-8.A and B, α values were obtained of 0.95 for P16 and 0.96 for P17 and slopes of KT/q were obtained of 1.40 for P16 and 1.02 for P17, respectively, indicated that the bimolecular recombination of two could nearly be ignored and there was more trap-assisted recombination inside of P16-based device.

Interestingly, the photovoltaic performance of two polymer materials were opposite when they were applied into the fullerene PSCs. As shown in Figure 3-9, P16-based devices exhibited better PCE of 4.42% with FF of 62.87%, J_{SC} of 6.83 $mA \cdot cm^{-2}$ and V_{OC} of 1.02 V than P17, affording a PCE of 3.92% with FF of 63.01%, J_{SC} of 6.89 $mA \cdot cm^{-2}$ and V_{OC} of 0.90 V, in OPVs blending with $PC_{71}BM$. Except for the higher V_{OC}, other characterizations of P16-based PSC were similar to P17, and finally affording higher PCE. Moreover, two donor materials presented identical charge recombination and charge dissociation ability, where the α and KT/q value of two polymers were almost equal. However, other different SM-NFAs were paired with P16 and P17 in PSCs, which indicated that photovoltaic performance of P17-based solar cells were more excellent than P16-based devices, which was in accord with former result in BTP-eC9-blending OPVs. Obviously, donor materials modifying with fluorine atoms on A moiety performed worse charge separation, weaker charge mobility ability and more charge recombination in SM-NFA PSCs.

3.5. SUMMARY

Through the practical experiment that we present illustrates the different effect of functional groups engineering between fullerene and non-fullerene OPVs. From this, we can preliminarily draw a conclusion that excessive fluorine substitution, especially in A moiety, could reduce the formation of efficient phase separation to hinder the improvement of PV performance in NFAs-based OPVs. And the fluorine atoms increase the dihedral angle between D and A moieties, which weakens the π-π stacking interaction of adjacent polymer backbone. Meanwhile, it also impedes the formations of efficient nanoscale bicontinuous interpenetrating network fibrous structure and phase separation, impairing the improvement of carrier transport ability and charge dissociation ability. Thus, the P16-based NFAs OPV devices perform worse J_{SC} and FF than that of P17, affording a worse PCE.

The difference between fullerene and non-fullerene is mainly due to the difference in structure. The polymer blending films with NFAs can induce the formation of better morphology and phase separation than that of fullerene. Introducing of functional groups, such as fluorine, hinders this promoting process because of the steric hinderance and redundant non-covalent bond sites, despite the improvement of the HOMO levels and V_{OC} benefitting from the electron-withdrawing effect. For fullerene system, there is no promoting effect, which means that the introduction of functional groups have no such problems. Thus, this conclusion provides a strategy in the future molecular design of polymer donor materials in NFAs-based OPVs.

CHAPTER 4. FUSED CORE-MODIFIED ENGINEERING IN ORGANIC POLYMER MATERIALS

The development of polymer molecular structure design plays an important role in improving the energy conversion efficiency of polymer solar cell (PSC). A high-performance PSC usually has an excellent active layer, which is closely related to the π-electron properties of polymer donor materials. Recently, the copolymers with a strategy of D-A structure were proposed owing to their superior π-electron properties, and they could be given better optical and electrochemical properties by adopting the fused core-modified engineering with different combinations of D-A units. However, the copolymer with two or more different types of monomers naturally demanded multiple synthetic steps, which indicated that the synthesis cost more time and raw materials. Thus, the homopolymers, such as polythiophenes, can serve as the ideal alternative polymer donor materials to solve the above dilemma. This chapter aims to synthesize and investigate some low-cost and high-performance homopolymers.

4.1. DEVELOPMENT OF HOMOPOLYMERS

So far, there were many reported homopolymers in high-performance PSCs, among which poly(3-hexylthiophene) (P3HT) was one of the most successful homopolymers for PSC applications. Due to its low cost, simple synthesis and high yield, P3HT was always regarded as the most ideal commercial polymer donor material. Since P3HT has a narrow absorption in the visible light region and its HOMO energy level was relatively high, the PSC devices based on P3HT usually had lower J_{SC} and V_{OC}. Thus, two pathways was put forward to achieve highly efficient PSCs based on P3HT, modulating the molecular structure of P3HT (PCBM as acceptor) or synthesizing the matching acceptor materials. And now, as show in Figure 4-1, two pathway had achieved the best PCE of 7.2% and 9.1%, respectively (96, 97).

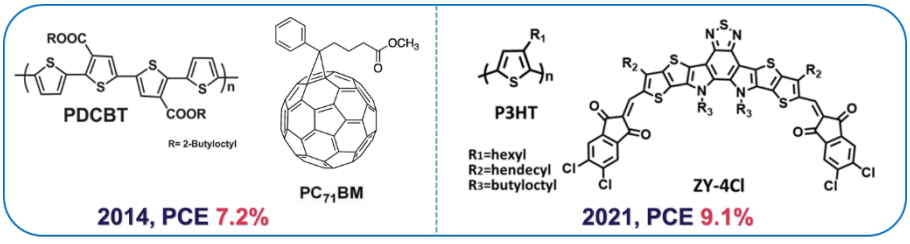

Figure 4-1. Reported high-efficiency PSCs based on P3HT homopolymers.

Compared with recent D-A strategy of copolymer materials, which had achieved the outstanding PCE of 18%, P3HT-based OPV device still had a huge gap due to its structural limitations of poor spectral absorption and higher HOMO level (98). Therefore, another alternative homopolymer with benzodithiophene (BDT) unit had emerged to attempt overcoming the above difficulties. In 2015, J. Kim and colleagues designed and synthesized the homopolymer with BDT units (PBDTT, Figure 4-1) to obtain PCE of 6.1% in $PC_{71}BM$-based PSCs, which had more potential of tuned optical and electronic properties to improve the corresponding PSC devices (99). Then Hwang et al. reported novel homopolymer and analogous homopolymer on the basis of PBDTT, and they found that T-S substituted BDT polymer had the deeper HOMO level of -5.58 eV and performed a high V_{OC} of 0.98 V, affording a high PCE of 7.1% (100). Recently, Wong et al. further studied a fluorine substituted analogous BDT-based homopolymer (PBBF) and applied it into the IDIC-based PSCs, which reached a higher PCE of 8.5%. Compared with PBDTT-BDTT-S, PBBF had the same HOMO level, which indicated that 2-postion alkylthio substituents had similar electron-withdrawing effect as the synergy of 2-postion alkyl and 3-postion fluorine substituents (101). And these results also demonstrated that combining the modulation of polymer structure and the choice of more matching acceptor was a new pathway for further improving PV performance in BDT-based homopolymer solar cells. Thus, this chapter will follow this idea to further improve the photovoltaic performance of BDT-based homopolymer in NFA-based OPV devices.

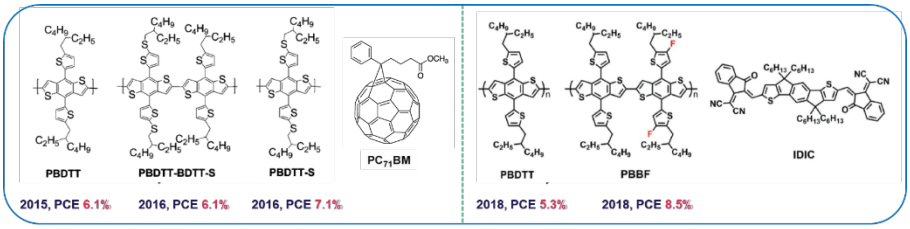

Figure 4-2. Reported recent PSCs based on BDT homopolymers or analogous homopolymers.

4.2. STRUCTURE DESIGN AND POLYMER CHARACTERISTIC

For further study of improving the PV performance of BDT-based homopolymers, as shown in Figure 4-3, we designed and synthesized the BDT-based analogous homopolymer PBDTT-Cl-BDT-S (P13) to investigate the synergistic effect of 2-postion alkylthio and 3-postion chloroform substituents. Furthermore, homopolymer PBDTT-S (P14) and analogous homopolymer PBDTT-BDT-S (P15) were also synthesized for comparison. Three polymers had the excellent solution processability, which could easily dissolve in most common organic solvent. And the average molecular weight were found of 3.43 KDa with PDI 2.58 for P13, 2.89 KDa with PDI 2.20 for P14 and 2.79 KDa with PDI 2.16 for P15, respectively, charactered by GPC. As the organic semiconductor materials, all polymer materials were thermally stable

with the decomposition temperatures for 5% weight loss of 348 °C for P13, 315 °C for P14 and 341 °C for P15, respectively.

Then, the optical property was charactered by ultraviolet-visible spectroscopy, as shown in Figure 4-4.A, the UV-vis absorption spectrum of three polymers in thin films indicated that P15 exhibited the best optical property with broadest absorption edge. The optical absorption edges of these polymer donors were 630 nm for P13, 635 nm for P14 and 640 nm for P15, which corresponded the optical bandgaps of 1.97 eV for P13, 1.95 eV for P14 and 1.94 eV for P15, respectively. And three polymers were moderately complementary to the absorbance of acceptor BTP-eC9. Besides, the thin-films electrochemical characteristics of three were studied by CV (Figure 4-4.B), whose onset oxidation potentials (E_{OX}) were found of 1.13 V for P13, 1.20 V for P14, and 1.10 V for P15, corresponding to HOMO levels of -5.51 eV for P13, -5.58 eV for P14 and -5.48 eV for P15, respectively. The HOMO level of P14 was undoubtably lowest lying than others, and we attributed it to the strongest electron-withdrawing effect of alkylthio side chains. The electronic bandgaps of three were shown in Figure 4-4.C, which approximated to their optical bandgaps. And the optimization and calculation by DTF, energy-levels schematic diagram these homopolymers were present in Figure 4-4.D. It was obviously that the HOMO levels of three were all evenly distributed along the molecular π-conjugation backbone, which indicated that the polymers had all flat rigid conjugated backbone planes. And all electronic and optical characters were exhibited in the Table 4-1.

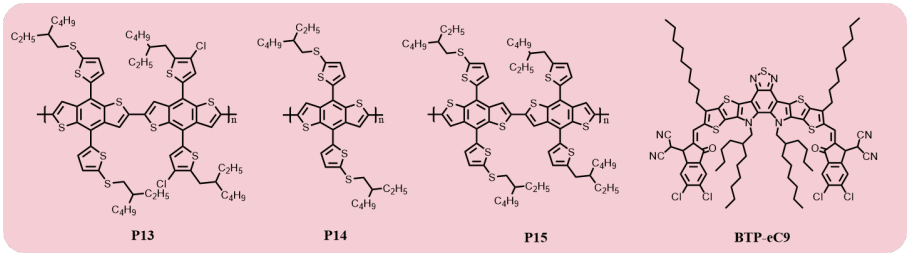

Figure 4-3. Schematic diagram of the molecular structures of synthetic polymers and acceptor.

Sample	HOMO [eV][a]	LUMO [eV][a]	E_g [eV][b]	λ_{edge} [nm]	E_g^{opt} [eV][c]	HOMO [eV][d]	LUMO [eV][d]
P13	-5.51	-3.63	1.88	630	1.97	-5.32	-2.18
P14	-5.58	-3.60	1.98	635	1.95	-5.27	-2.14
P15	-5.48	-3.61	1.87	640	1.94	-5.15	-2.05

[a] Calculated from the equation $E_{HOMO} / E_{LUMO} = - (E_{OX} / E_{RED} + 4.8 - |Fc/Fc^+|)$ eV; [b] Calculated from the equation $E_g = E_{LUMO} - E_{HOMO}$; [c] Evaluated from the absorption band edge of the polymer films and determined by the equation $E_g^{opt} = 1240/(\text{onset band edge of absorption})$; [d] Calculated via DTF.

Table 4-1. The electronic and optical properties of P13-P15.

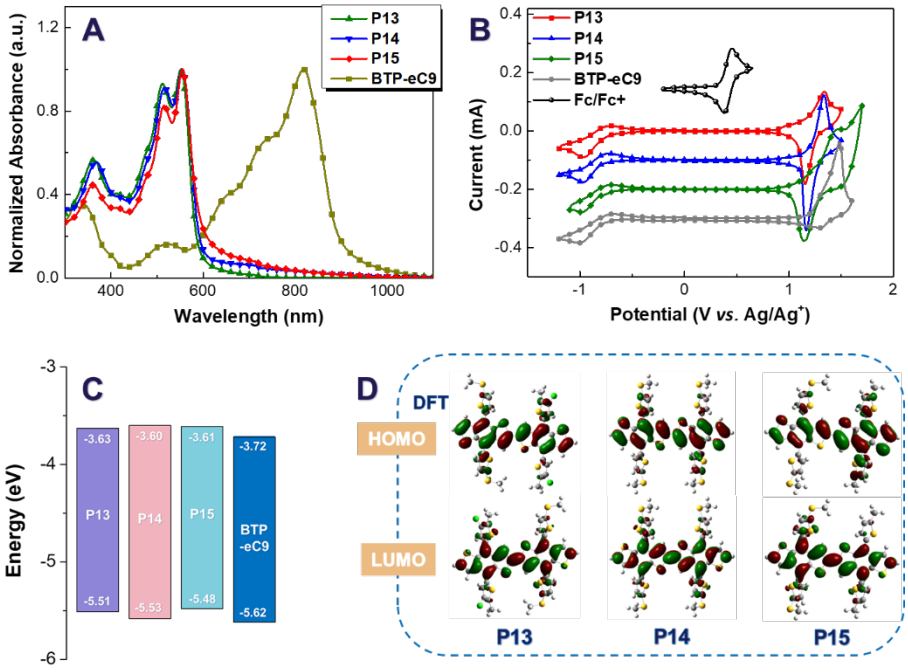

Figure 4-4. UV-vis absorption spectrum (A), CV chart (B), molecular energy levels (C) and the calculated electron distributions at HOMO/LUMO orbitals (D) of polymers and acceptor.

4.3. PV PERFORMANCE

To study the PV performance of these homopolymer donor materials, we applied them into practical OPV devices with the conventional structure, same as mentioned in Chapter 2 (page 20). Through many-times attempts in blending weight ratio of donor and acceptor, we confirmed the optimal blending weight ratio (1:1, w/w) of active layer based on these homopolymers. And on the basis of the optimal weight ratio, we went further optimization by tuning the content of solvent additive, DIO. The optimal processes of the content of solvent additive in active layers based on three homopolymers were present in following Figure 4-5.A, B and C. Both P13 and P15 had the same optimal content of solvent additive of 0.1% volume ratio, and P14-based OPV devices performed optimally at the pristine blending condition, which means that P14-based OPV devices were strongly negatively sensitive to DIO. For P13, the content of solvent additive in active layer increased from 0 to 0.1%, FF had an increasement of 7.9%, J_{SC} had a decrease of 4.8% and V_{OC} kept content. When from 0 to 0.3%, FF had an increasement of 10.0%, while J_{SC} had a decrease of 13.9%, which indicated that DIO had a moderate effect on P13-based active layers. For P15, content of additive increased from 0 to 0.1%, FF had an increasement of 6.8%, J_{SC} had an increasement of 0.3% and V_{OC} had an increasement of 1.3%. And from 0 to

0.3%, FF had an increasement of 4.5%, J_{SC} had an increasement of 0.6%, and V_{OC} maintained the increasement of 1.3%. This result implied that DIO exhibited the positive effect in P15-based active layer. We believed that the additive had a close relationship with thin-film morphology, which could be discussed in following text.

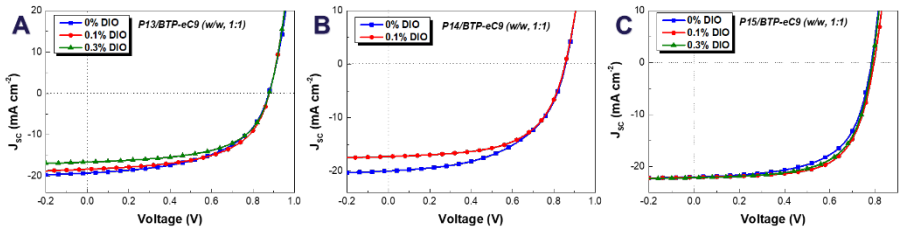

Polymer/ BTP-eC9	D:A	DIO (vol%)	PCE (%)	FF (%)	V_{oc} (V)	J_{sc} (mA cm^{-2})
P13	1:1	0	8.92	52.90	0.88	19.25
		0.1	9.18	57.10	0.88	18.33
		0.3	8.46	58.24	0.88	16.58
P14	1:1	0	9.07	53.15	0.86	19.94
		0.1	8.76	59.54	0.85	17.26
P15	1:1	0	10.61	61.69	0.78	21.97
		0.1	11.53	65.87	0.79	22.04
		0.3	11.20	64.46	0.79	22.10

Figure 4-5. J-V curves of P13- (A), P14- (B) and P15-based (C) OPV devices (weight ratio, 1:1, w/w) with different content of DIO at spin-coating speed of 2000 rpm under an illumination of AM 1.5 G, 100 mW cm^{-2}. Corresponding table (bottom) of PV performance properties.

Thence, we obtained the optimal PV performance in OPV devices based on these homopolymers. As shown in Figure 4-6, although the V_{OC} was the lowest among three, P15-based OPV devices performed the best PCE of 11.53% (the average PCE was 11.08%, obtaining from 10 parallel devices), which had the highest FF of 65.87% and the highest J_{SC} of 22.04 mA/cm^{-2}. It was no doubt that P15-based devices had the lowest V_{OC} due to the highest lying HOMO level among three. Compared with P14, P13-based OPV devices occupied the higher FF of 57.1% and V_{OC} of 0.88 V, resulting them to perform a higher PCE of 9.18% (Ave. 8.63%). P14-based OPV devices performed the worst PCE of 9.07% (Ave. 8.49%) owing to its lowest FF although they had moderate the J_{SC} and V_{OC}. Overall, three homopolymers had the excellent J_{SC}, comparing with abovementioned analogous homopolymers, and also achieved the better PCE. Especially, the P15-based OPV devices had an astonishing PCE of 11.53%, which was even better than the PBBF-based OPVs with the best performance of PCE in 2018. Moreover, P15 had surpassed the current most efficient homopolymer-based OPV devices, abovementioned P3HT-based NFA OPV devices. Although P3HT-based OPVs had the higher V_{OC} and FF, P15-based OPVs had an extremely high J_{SC}, affording the better PCE. In generally, coupling with BTP-eC9, the OPV devices based on P13, P14 and P15 all had the excellent PV performance.

As well known, FF is also related to the thin-film morphology. Thence, the following part, we will focus on the study of thin-film morphology of active layers to understand the effect of different polymer structure on PV performance by fused core-modified engineering modifications. More importantly, aiming to find a pathway for further improvement of PV performance in homopolymer-based OPVs.

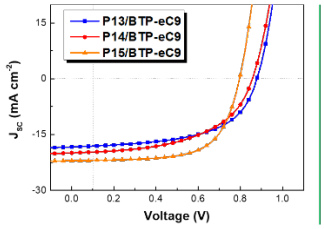

Polymer/ BTP-eC9	PCE (%) [a]	FF (%)	V_{oc} (V)	J_{sc} (mA cm^{-2})
P13	9.18 (8.63)	57.10	0.88	18.33
P14	9.07 (8.49)	53.15	0.86	19.94
P15	11.53 (11.08)	65.87	0.79	22.04

[a] Average PCE is calculated from 10 parallel devices.

Figure 4-6. J-V curves (left) and Table (right) of the optimal OPV devices based on three homopolymers.

4.4. MORPHOLOGY OF ACTICE LAYERS

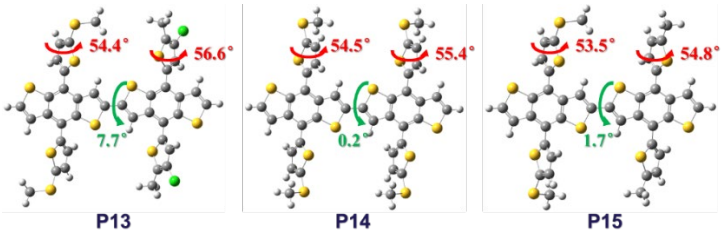

Figure 4-7. The optimized molecular structure of dimer moieties of three polymers

For further investigating the thin-film properties of the organic active layers based on three homopolymers, DFT method was used to simulate the optimal thermodynamic structure of three. And the dihedral angles of three polymer backbones were calculated and present in Figure 4-7. These homopolymers had the similar dihedral angles between thiophene side chains and BDT units. However, P14 exhibited the minimum dihedral angle between two adjacent BDT units, which was attributed to the symmetrical structure of the polymer backbone. And another result also proved above inference, P13, substituted with chloride thiophene side chains, had the largest dihedral angle due to its most analogous structure. As far as the theoretical results are concerned, the smaller the dihedral angle between the polymer backbones corresponded the flatter the molecular conjugated planes, which could induce the polymer to form closer π-π stacking in thin film. But the actual morphology of these thin films still required more characterizations to investigate by atomic force microscopy (AFM) or grazing-incidence wide-angle X-ray scattering (GIWAXs).

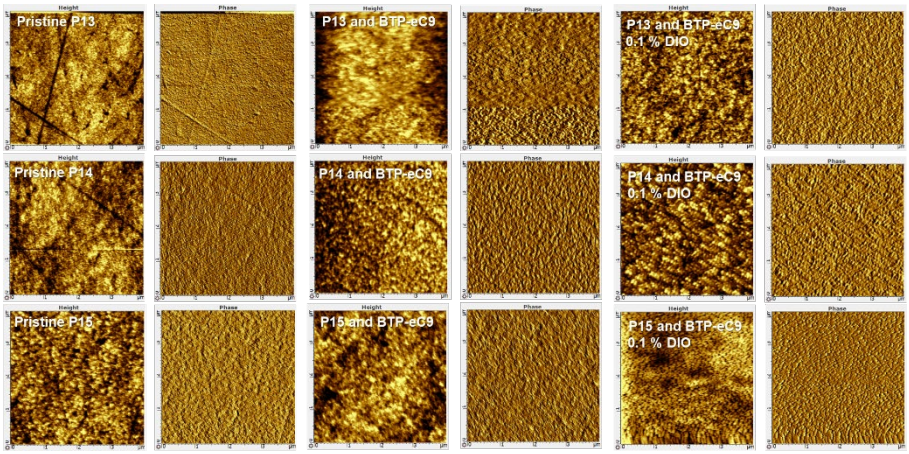

Figure 4-8. AFM height and phase diagrams of the thin films of pristine P13, pristine P14, pristine P15, P13:BTP-eC9, P14:BTP-eC9, P15:BTP-eC9, P13:BTP-eC9 with 0.1% DIO, P14:BTP-eC9 with 0.1% DIO and P15:BTP-eC9 with 0.1% DIO, 4 μm × 4 μm.

Therefore, we firstly charactered the morphologies of three homopolymer thin films and their corresponding blending thin films by AFM, see Figure 4-8. Totally, the surface morphologies of these thin films were less roughness, uniform particles and good miscibility. And all pristine homopolymer thin films showed oriented, parallel and thin-lines like fibers in the phase diagrams, which demonstrated that all the homopolymer chains were ordered and closed arrangement by π-π stacking along the polymer backbone. After blending with BTP-eC9, the size of the particles of three in thin films were bigger, and all the oriented and parallel arrangement of polymer backbones became a well-developed nanoscale bicontinuous interpenetrating network fibrous structure. We attributed this to the assistance of the acceptor BTP-eC9, which enhanced the crystalline of polymer/BTP-eC9 particles and stimulate the dense π-π stacking interaction between donors and acceptors. Besides, according to the height and phase diagrams of blending thin films, three homopolymers all exhibited the excellent surface phase separation, which was beneficial for the charge separation and recombination. Obviously, the blending thin films of P13 and P14 both changed from the densely arranged morphology to the loose and porous morphology, although they formed the larger crystalline particles, which indicated that intense aggregation effect and strong crystallinity resulted the unfavorable factors for corresponding OPVs such as excessive phase separation and unbalanced charge transport. Thence, these blending OPV devices with DIO additive had higher FF and lower J_{SC}, comparing with pristine blending OPVs. While P15-based blending OPV device present contrary results, because its thin-film morphology became smaller crystalline morphology and denser morphology. These results of the surface morphologies in active layers all conformed to the variation of PV performance when the DIO was incorporated into the organic active layers.

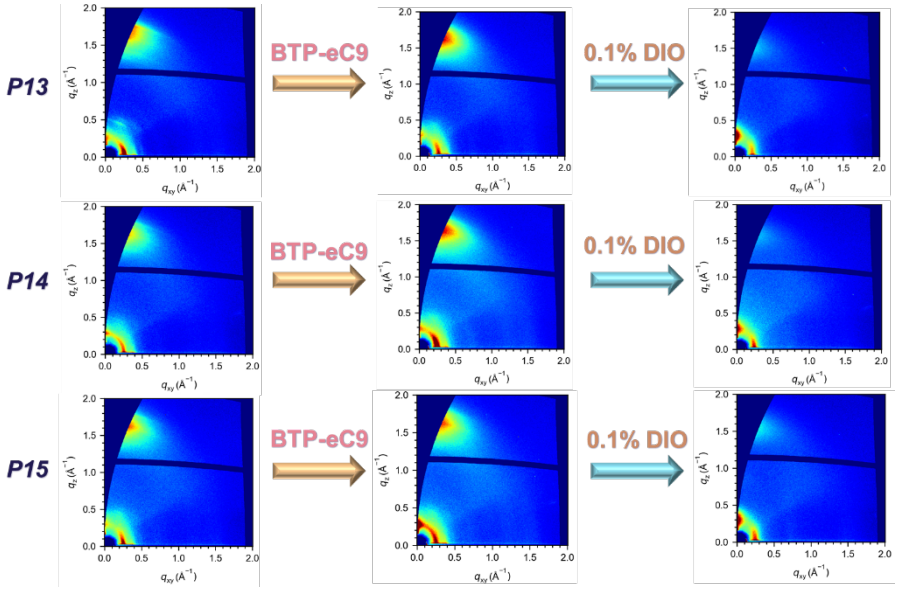

Figure 4-9. GIWAXs diagrams of the homopolymers-only (left), blending homopolymers/BTP-eC9 (middle) and blending homopolymers/BTP-eC9 with 0.1% DIO (right) thin films.

Furthermore, to investigate in-plane morphologies of the thin films based on three homopolymers, GIWAXs analysis was used to characterized, which revealed more detailed information of molecular arrangement in active layers. Shown in Figure 4-9, three homopolymer-only thin films mainly formed in the face-on orientation stacking arrangement, while they also had part edge-on orientation molecular arrangement. After blending with BTP-eC9, all homopolymers had undergone significant changes. For P13 and P14, the blending thin films both showed an obvious enhancement of face-on orientation stacking arrangement. And P15-based blending thin film had a significant increasement of edge-on orientation stacking arrangement, and the face-on orientation stacking arrangement of it also had a slight enhancement. After incorporating with 0.1% DIO, the blending thin films of three all changed to dominate by edge-on orientation stacking arrangement. Except for P15, the face-on orientation arrangements of others almost totally disappeared, which indicated the increase of electron transport properties and the decrease of hole transport properties in their OPV. However, an excellent organic semiconductor device demanded a balance of hole and electron transport properties. Obviously, P13 and P14 blending thin films had the worse balances and the practical J_{SC} of their corresponding OPV devices decreased after adding the additive. While P15-based blending thin film showed a better balance, so that the J_{SC} of its OPV device exhibited a slight increasement with the incorporation of DIO.

4.5. SUMMARY

In this chapter, we successfully designed and synthesized high PV performance BDT-based homopolymer donor materials, named P13, P14 and P15, which achieved the highest PCE among the reported analogous homopolymer donor materials recently. Meanwhile, we found that the solvent additive, DIO, induced the variation of three homopolymers of the surface and in-plane morphologies in NFA-based blending thin films, such as crystallinity, phase separation and arrangement orientation. And the analogous structure of homopolymer P15 exhibited best PCE of 11.5% with an astonishing J_{SC} in corresponding OPV devices, which indicated that the asymmetric strategy had its unique advantages in controlling the energy level and morphology of polymer molecular donor materials (reducing the unfavorable factors such as excessive phase separation and unbalanced carrier transport, caused by strong crystallinity and strong aggregation effect). P13-based symmetrical homopolymer had a moderate PV performance owing to its large steric hindrance caused by the large-size chloroform atoms. Besides, we also develop a design idea of homopolymer structure based on BDT units to improve the PV performance in their NFA-based OPVs. Thence, we believe that the future BDT-based homopolymer could achieve higher PV performance through suitable modulation of polymer structure.

CHAPTER 5. END-GROUP ENGINEERING IN ORGANIC SMALL MOLECULAR MATERIALS

Organic solar cells are the devices that directly or indirectly convert solar energy into electrical energy by using organic semiconductor materials as photoelectric conversion materials. Thus, the essence of organic photovoltaic material is organic semiconductor material, which means that the semiconductor properties of organic photovoltaic materials are closely related to their photovoltaic performance. In other words, more outstanding conductivity provides the organic photovoltaic devices a better exciton diffusion environment, which is more benefit for the PV performance.

In general, the carrier mobility, the general term for the electrical conductivity of semiconductor materials including electron mobility and hole mobility, is always used to evaluate the pros and cons of the organic semiconductor materials. And the carrier mobility capability can be characterized by fabricating the target materials into semiconductor devices, field-effect transistor or specific diode. The former one is the basic building blocks of modern electronic circuits, which has the mature electrochemical theoretical basis and possesses the characterization method of fast responses and accurate results. The latter one, SCLC method that mentioned in chapter 2, is an emerging and convenient conductivity characterization method in recent years, which is not as accurate as the former. This chapter mainly focuses on the former method to discuss the semiconductor properties of the end-group engineering modification of organic small molecular materials without further discussion of PV performance, due to lack of suitable donor materials.

5.1. FUNDAMENTALS OF ORGANIC FIELD-EFFECT TRANSISTOR

Field-Effect Transistors (FET) are electronic components that control current through electric field effects and one of the most basic electronic device structures. It relies on the electric field to control the polarization state of the conductive channel, and therefore the conductivity of the channel of a certain type of carrier in the semiconductor material. Just as the name implies, organic field-effect transistors (OFETs) are one kind of FETs that uses organic semiconductor materials. According to the position of the source, drain and semiconductor layer, OFETs have two structures (Figure 5-1): top contact and bottom contact. According to the carriers transport properties, they can also be divided into two types: one is the p-channel field effect transistor with holes as the main carriers, and the other is the n-channel field effect transistor with electrons as the main carriers in the semiconductor layer. And

the former are generally organic molecules with electron-rich fused-ring aromatic hydrocarbons as their cores, while the latter are mainly organic molecules with electron-deficient fused-ring aromatic hydrocarbons as their cores. The working principle of OFETs is to control the source-drain current I_{DS} through the gate electrode V_{GS}. When a voltage is applied to the gate, the carrier concentration at the interface between the semiconductor and the insulating layer increases, the I_{DS} increases, and then the transistors are in the "on" state. When the gate voltage is zero, I_{DS} is small, and the transistors are in the "off" state. The source-drain current ratio I_{ON}/I_{OFF} in the “on” and “off” states is defined as the on/off ratio. Together with the field-effect mobility μ, which reflects the carrier mobility, they are two key indicators for evaluating the performance of OFETs, which means that the higher these two , the better.

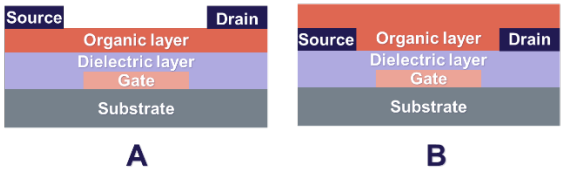

*Figure 5-1. Schematic diagram of two typical OFET structures, **A** top contact and **B** bottom contact.*

OFET semiconductor materials should meet the following requirements: the lowest vacant molecular orbital LUMO energy level or the highest occupied molecular orbital HOMO energy level of a single molecule is conducive to electron or hole injection (102-104). The solid-state crystal structure should provide sufficient molecular orbital overlap to ensure that the adjacent charges do not have excessive energy barrier during intermolecular migration (105-107). The size range of the semiconductor single crystal should continuously span the contact points of source and drain, and the orientation of the single crystal, i.e., the direction of carrier migration, should be parallel to the current direction. The ideal single crystal film should be larger than the device size (108-112). Besides, it should have low intrinsic conductivity, the conductivity of a semiconductor in which impurities and structural defects are absent or where the concentration is very low, less off-state leakage current and high device current on/off ratio. In recent years, after research, we have realized that different organic semiconductor materials have different performances on OFET devices, which are introduced below: High polymer, the solution viscosity and the solid-phase entanglement are best, which is conducive to the formation of continuous film formation, but the overall order is poor. The poor intermolecular π-π stacking is not conducive to the formation of channels parallel to hole transport, so the field effect mobility decreases. If the polymer is to form a highly three-dimensionally ordered polymer molecular chain to improve its field effect, the solvent selected for film formation is very critical (113, 114). Oligomer, it tunes molecular orbital energy levels by flexibly changing molecular chain lengths and introducing functional groups to

control and improve carrier transport, but their film-forming ability is not as good as polymers (115-118). Small molecule, it is easier to purify, lower molecular barrier, easier to form self-assembled polycrystalline film to improv effective overlap and easier to obtain single crystals. However, the viscosity of the organic small molecule solution is too low to be processed into a film by the solution method, and most organic small molecule semiconductors are more sensitive to the processed environment (108, 119-121).

5.2. END-GROUP ENGINEERING IN ORGANIC SMALL MOLECULAR MATERIALS

The quality of OFET performance depends on the effective overlapping structural area of large π bonds of ordered organic conjugated molecules, the thin-film morphology of organic semiconductor materials, and the matching source and drain electrode materials. Therefore, this chapter focuses on the effect of end-group engineering in π-π conjugated structure and thin-film morphology of organic small molecular materials.

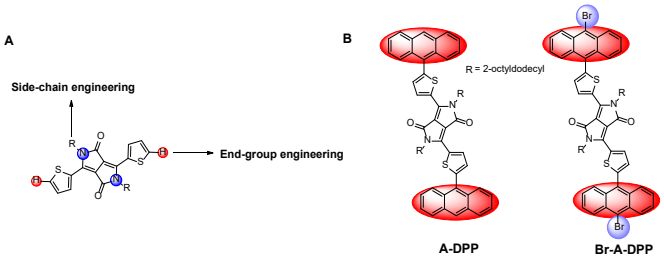

Figure 5-2. Schematic diagram of molecular structure modification idea of DPP core (A), and structural diagram of novel organic small molecular materials based on DPP core(B).

The side-chain engineering by introducing alkyl on organic molecules can improve the solubility of the materials, which means that the materials are easier to process in solution. but will severely impair the π-π stacking behaviors between molecules. End-group engineering can increase the rigid conjugation area of organic molecules and can also tune molecular energy levels, thereby improving the carrier transport properties of materials (122-125). Therefore, under the premise of ensuring the good solubility of the material, we would like to optimize the electrical conductivity of the material through end-group engineering. Diketopyrrolopyrrole (DPP) derivatives have attracted more and more attention in the field of organic semiconductor materials, and have also achieved remarkable results in the research of organic field effect transistors (OFETs) (126-128). The structure of DPP molecules (Figure 5-2.A), amino and active H, provide more flexible design ideas of molecular modifications. Solubility, micromorphology, and molecular energy levels can be greatly optimized for their respective purposes through molecular modification. Solubility, molecular energy levels and thin-film morphology can be multiply optimized for the respective

purposes through molecular modification, thereby improving the electrochemical properties of DPP derivatives (129-132). Small organic molecules have poor solubility, so long alkyl chains are required to improve the solubility of them in low polarity solutions. However, as mentioned above, long alkyl chains would also give small-molecule thin film materials serious defects. Therefore, the coordination of end-group engineering is particularly important, and the selection of appropriate end groups is a very important part of molecular design.

Anthracene was chosen as the end group because of its good rigid coplanar structure and high crystalline properties, which could promote the formation of close π-π stacking interactions between molecules and form an ordered molecular arrangement in thin film, thereby improving the electrical transport performance of semiconductor transistors (133-136). Importantly, the structure design of combining DPP core and anthryl group has not been discussed yet in application of organic small molecular semiconductor transistors. Based on this design idea, shown in Figure 5-2.B, we synthesized two novel organic small molecular materials, named A-DPP and Br-A-DPP, with 2-octyldodecyl group as the side chain, diketopyrrolopyrrole (DPP) as the core of the rigid conjugated structure and anthracene group as the end group, which improved the film-forming properties of organic materials, π extension of the conjugated structure and crystallinity of the molecule. Besides, A-DPP was brominated to synthesize Br-A-DPP, because halogen-modified DPP has better hole mobility on OFETs than unmodified DPP materials (137). Obviously, as shown in Figure 5-3, the UV absorption band of the end-grouped DPP derivative had a bathochromic-shift, and the UV absorption band of the end-group-anthracene group was also red-shifted compared to the unmodified anthracene group. This phenomenon showed that the rigid conjugated π plane has been significantly enlarged after end-group engineering. And the CV voltammograms of A-DPP and Br-A-DPP indicated that the HOMO/LUMO of these two were -5.53/-3.50 eV and -5.59 /-3.53 eV, respectively, which were closed to recently reported DPP molecules with HOMO of ~ -5.6 to -5.3 eV and LUMO of ~ -3.6 to -3.5 eV. This experimental data showed that the synthesized DPP derivative materials met the single-molecule energy level conditions for OFET semiconductor materials that were conducive to hole injection.

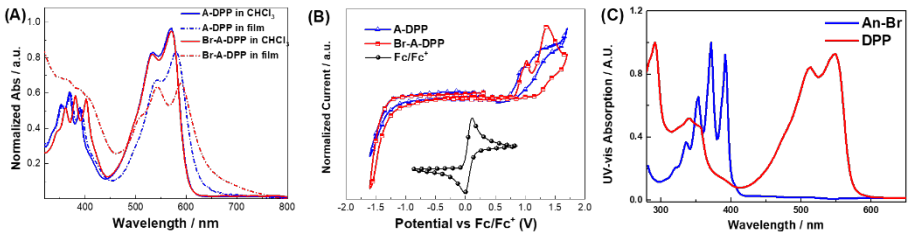

Figure 5-3. UV-vis absorption spectrum of A-DPP and Br-A-DPP in solution and film (A), CV voltammograms of A -DPP and Br-A-DPP with ferrocene (inset of b, black) as an internal standard (B), and UV-vis absorption spectrum of 9-bromoanthracene (An-Br) and 2,5-Bis(2-octyldodecyl)-3,6-di(thiophen-2-yl)pyrrolo[3,4-c]pyrrole-1,4-dione (DPP) in solution (C).

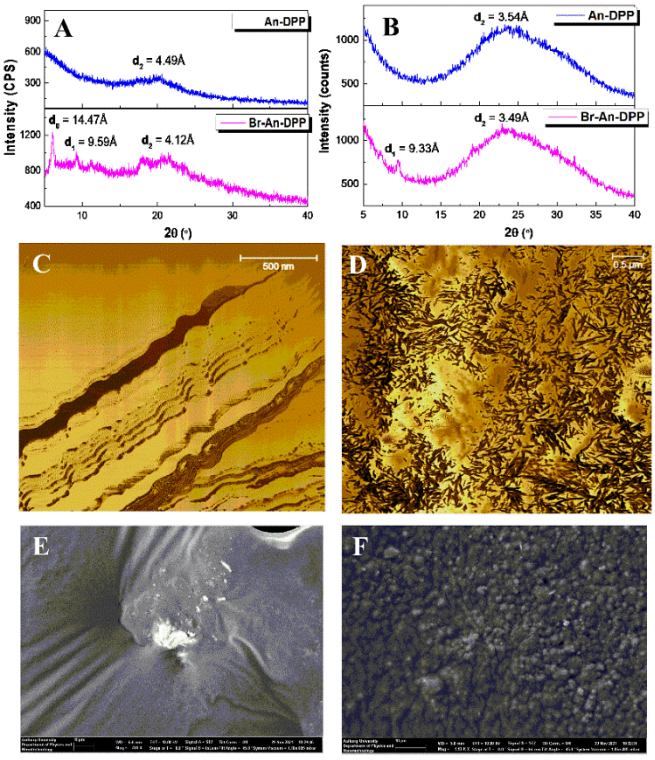

Figure 5-4. The out-of-plane (A) and in-plane (B) XRD patterns the An-DPP and Br-An-DPP in thin films, AFM phase images of A-PP (C) and Br-A-DPP (D) in thin films , and SEM pictures of An-DPP (E) and Br-An-DPP (F) thin films in scale of 120 ×100 μm area.

Besides, both end-group-modified DPP derivatives had good solubility in many low-polarity organic solvents and were easy to form films under spin-coating. But according to the color shades of the thin films, A-DPP possessed deeper dark color under the same processes of solution process which meant that the solution viscosity of this material was much higher than that of Br-A-DPP. We attributed this result to the amorphous phase morphology and weak crystallinity of the A-DPP thin films.

Depicted in Figure 5-4.A, two materials exhibited the broad d_2-spacing peaks of above 20° in out-of-plane X-ray diffractogram, indicating the intermolecular π-π stacking distances of 4.49 Å and 4.12 Å for A-DPP and Br-A-DPP, respectively. While Br-A-DPP exhibited some sharp diffraction peaks in the low-angle range around 6° and 9°, which indicated that the spacing between the top-bottom and left-right side alkyl chains was 9.59 Å and 14.47 Å, respectively. From this, it could be seen that thin films of Br-A-DPP material were superior to A-DPP in both crystallinity and stacking spacing of conjugated π planes. And according to the in-plane patterns (Figure 5-4.B), grazing incidence XRD, the crystalline size (D), i.e., crystalline particle size, of Br-A-DPP could be obtained of 531 Å (53.1 nm) by using the Debye-Scherrer equation

D=(K·λ/β·cos θ), where K is the Scherrer's constant (K=0.94), λ is the X-ray wavelength (1.54178 Å), β is full width at half maximum (FWHM) of the diffraction peak (0.367°), and θ is diffraction angle (9.51°). The thin films of A-DPP were amorphous structure without crystalline property. At the same time, as shown in the SEM image (Figure 5-4.E), A-DPP thin film looked like a soft cloth spread on the substrate with a few unoriented aggregated particles. And AFM image of A-DPP (Fig. 5-4.C) showed the soft cloth is formed by non-uniform, layer-by-layer laminations with different thicknesses. Therefore, we considered the A-DPP thin films to be amorphous structures. In contrast, AFM diagram (Figure 5-4.D) of Br-A-DPP thin films exhibited interlaced strips of fibers with a width of about 25 nm and a length of about 200 nm. And these fibers stacked to form oriented crystalline particles with a transverse diameter of about 1 μm (Figure 5-4.F). Therefore, we concluded that end-group engineering with brominated anthracene groups could enable long alkyl-chains DPP cores with better crystalline properties and tighter π-π stacking.

5.3. CONDUCTIVITY OF ORGANIC SMALL MOLECULAR MATERIALS

According to the method reported by Kjelstrup-Hansen et al., we adopted the high sensitivity and easy fabrication of OFET devices with interdigitated array (IDA) structure, and thus fabricated a batch of A-DPP-based and Br-A-DPP-based OFET devices as depicted in Figure 5-5 (138). The OFET substrate was bottom-gate bottom-contact (BGBC) structure, which was fabricated on a highly N-doped single-sided polished silicon wafer as the gate electrode with gold-plated contacts, SiO_2 (200 nm thick, thermally grown) as the gate dielectric layer and the optical patterned gold electrodes serve as source and drain. The interdigitated source and drain electrode design provided a channel width of 40,000 μm (20 interdigitated electrode gaps × 2000 μm). And experimental transistor devices based on two small molecular materials both were obtained on transistor substrates by a simple solution-processing method, spin-coating at 2000 rpm for 60 sec.

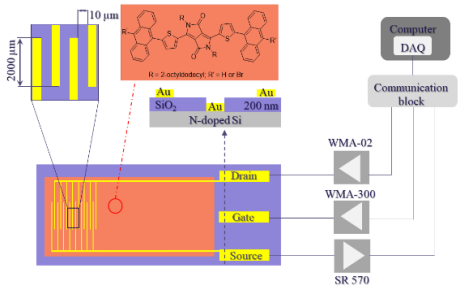

Figure 5-5. Design of the bottom-contact bottom-gate OFET and schematic drawing of the setup for electrical characterization. Inset of the figure presents the molecular structure of produced DPP derivatives thin films herein.

Then we characterized the conductive performance of these organic small molecular field-effect transistors using the LabVIEW-based measurement system, which was illustrated in Figure 5-5. Scanning the gate voltage at range of 0 to -5 V with keeping constant drain-source voltage (V_{DS}) at -5 V provided saturated transfer characteristics, resulting the volt-ampere characteristic curves of drain current (I_{DS}) versus gate voltage (V_G). And above measured plots were plotted with square root of I_{DS} (absolute value) versus V_G, obtaining corresponding transfer curves, which could be used to calculate the saturated hole mobility (μ_{sat}) by linear fitting (Figure 5-6.A). In the saturation regime, the square root of I_{DS} is proportional to V_G (139), and the eq.1 assumes that the mobility is independent of V_G. Thence, μ_{sat} could be extracted from the equation as following eq.2:

$$I_{DS} = \frac{W}{2 \cdot L} \cdot \mu_{sat} \cdot C_i \cdot (V_G - V_{TH})^2 \qquad \text{(eq.1)}$$

$$\mu_{sat} = \left(\frac{d\sqrt{I_{DS}}}{d_{Vg}} \right)^2 \cdot \frac{2 \cdot L}{W \cdot C_i} \qquad \text{(eq.2)}$$

where I_{DS} is the drain-to-source saturated current, W and L is the channel width (40 mm) and length (10 μm), respectively, C_i is the capacitance per unit area of the gate dielectric SiO_2 (C_i = 11.5 nF·m^{-2}), V_G is gate voltage, and V_{TH} is threshold voltage. According to this equation, highest μ_{sat} and V_{TH} of Br-A-DPP transistor were obtained of 0.20 cm^2 V^{-1} s^{-1} and -2.5 V, and the corresponding leakage current on/off ratio was 240. The average μ_{sat} of the four independent Br-A-DPP transistor devices was 0.13 cm^2 V^{-1} s^{-1} with V_{TH} of -2.3 V. However, the conductive performance of the upstream product A-DPP with many optimizations was still extremely poor. With same fabricated process, the best μ_{sat} was obtained of 5 × 10^{-8} cm^2 V^{-1} s^{-1} with a higher input drain-source voltage (-20 V), although most signals of DPP-A were almost covered by noise (Figure 5-6.C). Therefore, there was no useful data for output curves of A-DPP transistor devices, unlike Br-A-DPP (Figure 5-6.B). It could be seen that the conductive properties of OFET devices based on Br-A-DPP were quite excellent. Because the highly ordered crystalline structure in Br-A-DPP thin films with the formation of efficient building blocks improved semiconductor properties, which was more superior than A-DPP. And this intriguing phenomenon also contributes to a better understanding of the effect of highly ordered crystalline layers on charge carrier transport in transistor devices.

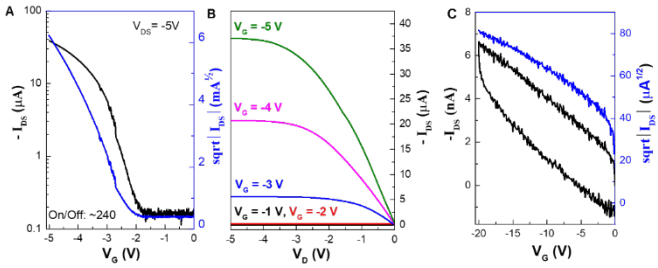

Figure 5-6. Transfer curve (A) and output curves (B) of spin-coated thin-film OFET based on Br-A-DPP, and transfer curves (C) of spin-coated thin-film OFET based on A-DPP.

5.4. SUMMARY

In this chapter, one example of end-group engineering is represented to investigate the effect of this modified method on organic small molecular semiconductor materials. Two novel organic small-molecule materials, namely A-DPP and Br-A-DPP, were synthesized by modifying 5- and 5'-positions flanking thiophenes of bis(thiophen-2-yl)-diketopyrrolopyrrole (DPP) with natural anthryl or brominated anthryl groups. Due to their crystallinity and stacking spacing of conjugation plane, the conductive properties on interdigitated organic field-effect transistor (OFET) devices of two materials showed huge differences, and Br-A-DPP-based OFETs showed excellent carrier mobility, which is 10^7 times of A-DPP. Therefore, we believe that bromination on aromatics end group can improve the crystallinity and molecular π-π stacking behavior of long alkyl chain substituted DPPs. Furthermore, for organic small molecule semiconductor materials, the choice of end-group engineering substituents is particularly important, because even individual molecular differences can have a large impact.

CHAPTER 6. CONCLUSIONS AND PERSPECTIVES

This chapter, we mainly highlight the consequences in our recent research and discuss the relationship between these consequences and current research dilemma in OPVs field. And we present our concerning perspectives and suggestions for future research.

6.1. CONCLUSION

Organic solar cells are one emerging PV technology in new energy field. And the organic semiconductor materials are expected to inherit the characters of current commercial PV materials with respect to achieving high PV performance and low-cost produce, which possess the properties of flexible structure modulation. Besides, as a novel PV material, they also have the unique properties of flexibility and semi-transparency, which implies that these materials enable many incapable applications of previous PV materials, such as wearable, building-integrated or biocompatible PV devices. Whereas the PV performance of OSCs still demands further improvement, to realize stable, long-lifetime and highly efficient OPV devices while maintaining their flexibility. In this thesis, the following four topics of the relationship between the modulation of organic molecular structure and the PV performance of corresponding OPV devices have been systematically promoted and developed: (i) revealing the relationships between side-chain engineering and PV performances in polymer donor materials based on NFAs OPVs (Chapters 2); (ii) exploring the effect of functional group engineering of polymer donor materials on PV performance based on NFAs OPVs (Chapter 3); (iii) developing the homopolymer donor materials with high PV performance in NFA-based OPVs through fused core-modified engineering (Chapter 4); (iv) investigating the effect of end-group engineering on semiconductor properties based on organic non-fullerene small molecular FET (Chapter 5). And the highlights of our Ph.D. program are summarized in following sections:

Modifying with alkylthio- and alkoxy-phenyl side chains, the BDT-based polymer donor materials exhibit excellent photovoltaic performance in single-heterojunction NFA-based OPVs. The consequence is that the copolymer substituted with alkylthio-phenyl side chains has better PV performance than alkoxy-phenyl alternative. Alkylthio-phenyl side chain has stronger electron-withdrawing effect, which deepens the HOMO energy level of the polymer molecule. The alkylthio-phenyl side chains substituents have higher carrier mobility, better charge dissociation ability and smaller exciton recombination. In addition, the polymers with alkylthio-phenyl side chains have denser π-π stacking behavior along the polymer backbone, which induces more ordered molecular orientation and large-area phase separation. Thence, alkylthio-phenyl side chains substituted polymers have higher V_{OC}, J_{SC} and FF, achieving higher

PCE than alkoxy-phenyl alternatives in OPV devices. And this achievement fills the research gap of side-chain engineering in polymer donor materials for improving the NFAs-based OPVs, and provides a new idea and experimental basis for the design of high PV performance polymer donor materials.

Moreover, excess fluorine substitutions on the A moieties reduces the formation of effective phase separation in NFAs-based organic active layers, and increases the dihedral angle between the D and A moieties thereby weakening the π-π stacking interaction of the adjacent polymer backbones. It also hinders the formation of efficient phase separation, i.e., the formation of nanoscale bicontinuous interpenetrating network fibrous structures, which impairs the enhancement of the carrier transport ability and charge dissociation ability. Because the polymer blend films can form better in-plane morphology and phase separation after incorporating BTP-eC9, while the functional groups such as fluorine atoms break this promotion effect due to steric hindrance and redundant non-covalent bond sites induced by fluorine. In the fullerene system, since the fullerene acceptors have no same promoting effect, the hindering effect of fluorine does not have either. Therefore, we conclude that the excess fluorine atoms have a negative effect on the PV performance enhancement of polymer-donor materials, and also provide a strategy for future molecular design of polymer-donor materials in NFA-based OPVs.

Thirdly, a series of BDT-based homopolymers with high PV performance have been developed, and the highest PCE has been achieved among similar homopolymer donor materials reported in recent years. And we believe that the asymmetric strategy has unique advantages in controlling the morphologies of homopolymer molecular donor materials (reducing unfavorable factors such as excessive phase separation and unbalanced hole/charge transport induced by strong aggregation effect and strong crystallinity). Therefore, we propose a design concept for the asymmetric structure of homopolymers based on BDT units to enhance the photovoltaic performance of their NFA-based OPVs.

Finally, we believe that bromination on aromatics end groups can enhance the crystallinity and π-π stacking behavior of the organic small molecular materials (DPP with long alkyl chains), which improves the carrier transport ability of organic semiconductor devices. Meanwhile, we also believe that the bromo-anthryl end groups substituted DPP organic small molecules are one of the excellent candidates for small molecule photovoltaic acceptor materials.

6.2. PERSPECTIVE

In this thesis, we have successfully prepared a series of organic materials with high-efficiency performance from four aspects, and explored the relationship between their structural modification and device performance. However, in the large research field

of optimizing the OPV device performance through structural modification of organic molecules, there is still much potential for further investigation.

However, in addition to abovementioned points of this thesis, there are many other sites worth of further investigation. Firstly, side-chain engineering in Chapter 2 only discusses the different effect between alkylthio and alkoxy side chains, which belongs to one of the functional side chains in side-chain engineering. Besides, the alkyl chain configuration, which balances the solubility and intermolecular π-conjugation of polymers, and the position of alkyl chain, which impacts the intermolecular π-π stacking, are all important roles in determining the polymer properties, such as solubility, π-electron transport, and miscibility with acceptors. Secondly, functional group engineering in Chapter 3, fluorine-atom substitution is only one small part of this section. In addition to the exploration of other various functional groups, the substituted positions of functional groups are also an indispensable research content in this section. Thirdly, except for the development of homopolymers, in Chapter 4 there are many other research directions in the fuse core-modified engineering, i.e., hot strategy of D-A copolymerization (which is the usual strategy of the current popular high-efficiency donor materials), choice of π-bridge (which is widely used to modulate the conjugated backbones of polymers) and the strategy of ternary copolymerization (which forms the copolymers with the optical absorption in the long wavelength region to achieve deeper HOMO levels). In Chapter 5, although the experiment result of end group engineering in organic small molecular non-fullerene acceptor only exhibits the excellent carrier mobility in organic semiconductor transistors, the suitable matching donor materials have not yet been found for OPV devices.

Moreover, there are many more potential applications of OPVs that have not been investigated in this thesis, such as large-area printing processes, translucent processes, flexible photovoltaic devices (wearable or curved processes), and building integration. In conclusion, further improvement of PV performance and realization of these potential applications will always be the popular topic in further years in the field of NFAs-based OPVs.

BIOGRAPHY

1. Krumbein WE, Cohen Y, Shilo M. Solar Lake (Sinai). 4. Stromatolitic cyanobacterial mats. Limnology and Oceanography. 1977;22(4):635-56.

2. Tabor H. Solar ponds. Solar Energy. 1981;27(3):181-94.

3. Jha AR. Solar Cell Technology and Applications. New York: Auerbach Publications; 2009.

4. King RR, Bhusari D, Larrabee D, Liu XQ, Rehder E, Edmondson K, Cotal H, Jones RK, Ermer JH, Fetzer CM, Law DC, Karam NH. Solar cell generations over 40% efficiency. Progress in Photovoltaics: Research and Applications. 2012;20(6):801-15.

5. Nayak PK, Mahesh S, Snaith HJ, Cahen D. Photovoltaic solar cell technologies: analysing the state of the art. Nature Reviews Materials. 2019;4(4):269-85.

6. Shah A, Torres P, Tscharner R, Wyrsch N, Keppner H. Photovoltaic Technology: The Case for Thin-Film Solar Cells. Science. 1999;285(5428):692-8.

7. Chopra KL, Paulson PD, Dutta V. Thin-film solar cells: an overview. Progress in Photovoltaics: Research and Applications. 2004;12(2-3):69-92.

8. Jef Poortmans VA. Thin Film Solar Cells: Fabrication, Characterization and Applications. Wiley: John Wiley & Sons, Ltd 2006.

9. Green MA. Thin-film solar cells: review of materials, technologies and commercial status. Journal of Materials Science: Materials in Electronics. 2007;18(1):15-9.

10. Aberle AG. Thin-film solar cells. Thin Solid Films. 2009;517(17):4706-10.

11. Hamakawa Y. Thin-Film Solar Cells: Next Generation Photovoltaics and Its Applications. T. Kamiya BM, H. Venghaus and Y. Yamamoto editor. Springer Book Archive: Springer Berlin, Heidelberg; 2004. XV, 244 p.

12. Eser E. Polycrystalline Thin Film Solar Cells: Present Status and Future Potential. Annual Review of Materials Science. 1997;27(625):53.

13. Bergmann RB. Crystalline Si thin-film solar cells: a review. Applied Physics A. 1999;69(2):187-94.

14. Lee TD, Ebong AU. A review of thin film solar cell technologies and challenges. Renewable and Sustainable Energy Reviews. 2017;70:1286-97.

15. Kirchartz T, Rau U. Introduction to Thin-Film Photovoltaics. Advanced Characterization Techniques for Thin Film Solar Cells2011. p. 1-32.

16. Hu Y, Wang J, Yan C, Cheng P. The multifaceted potential applications of organic photovoltaics. Nature Reviews Materials. 2022.

17. Fukuda K, Yu K, Someya T. The Future of Flexible Organic Solar Cells. Advanced Energy Materials. 2020;10(25):2000765.

18. Sun Y, Liu T, Kan Y, Gao K, Tang B, Li Y. Flexible Organic Solar Cells: Progress and Challenges. Small Science. 2021;1(5):2100001.

19. Liu C, Xiao C, Xie C, Li W. Flexible organic solar cells: Materials, large-area fabrication techniques and potential applications. Nano Energy. 2021;89:106399.

20. Meng X, Zhang L, Xie Y, Hu X, Xing Z, Huang Z, Liu C, Tan L, Zhou W, Sun Y, Ma W, Chen Y. A General Approach for Lab-to-Manufacturing Translation on Flexible Organic Solar Cells. Advanced Materials. 2019;31(41):1903649.

21. Schubert MB, Werner JH. Flexible solar cells for clothing. Materials Today. 2006;9(6):42-50.

22. Pagliaro M, Ciriminna R, Palmisano G. Flexible Solar Cells. ChemSusChem. 2008;1(11):880-91.

23. Fu X, Xu L, Li J, Sun X, Peng H. Flexible solar cells based on carbon nanomaterials. Carbon. 2018;139:1063-73.

24. Sariciftci NS, Braun D, Zhang C, Srdanov VI, Heeger AJ, Stucky G, Wudl F. Semiconducting polymer - buckminsterfullerene heterojunctions: Diodes, photodiodes, and photovoltaic cells. Applied Physics Letters. 1993;62(6):585-7.

25. Zhang X, Richter LJ, DeLongchamp DM, Kline RJ, Hammond MR, McCulloch I, Heeney M, Ashraf RS, Smith JN, Anthopoulos TD, Schroeder B, Geerts YH, Fischer DA, Toney MF. Molecular Packing of High-Mobility Diketo Pyrrolo-Pyrrole Polymer Semiconductors with Branched Alkyl Side Chains. Journal of the American Chemical Society. 2011;133(38):15073-84.

26. Yaghoobi Nia N, Bonomo M, Zendehdel M, Lamanna E, Desoky MMH, Paci B, Zurlo F, Generosi A, Barolo C, Viscardi G, Quagliotto P, Di Carlo A. Impact of P3HT Regioregularity and Molecular Weight on the Efficiency and Stability of Perovskite Solar Cells. ACS Sustainable Chemistry & Engineering. 2021;9(14):5061-73.

27. Ye L, Zhang S, Huo L, Zhang M, Hou J. Molecular Design toward Highly Efficient Photovoltaic Polymers Based on Two-Dimensional Conjugated Benzodithiophene. Accounts of Chemical Research. 2014;47(5):1595-603.

28. Pivrikas A, Sariciftci NS, Juška G, Österbacka R. A review of charge transport and recombination in polymer/fullerene organic solar cells. Progress in Photovoltaics: Research and Applications. 2007;15(8):677-96.

29. Terao Y, Sasabe H, Adachi C. Correlation of hole mobility, exciton diffusion length, and solar cell characteristics in phthalocyanine/fullerene organic solar cells. Applied Physics Letters. 2007;90(10):103515.

30. Howard IA, Mauer R, Meister M, Laquai F. Effect of Morphology on Ultrafast Free Carrier Generation in Polythiophene:Fullerene Organic Solar Cells. Journal of the American Chemical Society. 2010;132(42):14866-76.

31. Günes S, Neugebauer H, Sariciftci NS. Conjugated Polymer-Based Organic Solar Cells. Chemical Reviews. 2007;107(4):1324-38.

32. Yao H, Ye L, Zhang H, Li S, Zhang S, Hou J. Molecular Design of Benzodithiophene-Based Organic Photovoltaic Materials. Chem Rev. 2016;116(12):7397-457.

33. Zhan X, Tan Za, Domercq B, An Z, Zhang X, Barlow S, Li Y, Zhu D, Kippelen B, Marder SR. A High-Mobility Electron-Transport Polymer with Broad Absorption and Its Use in Field-Effect Transistors and All-Polymer Solar Cells. Journal of the American Chemical Society. 2007;129(23):7246-7.

34. Lin Y, Wang J, Zhang Z-G, Bai H, Li Y, Zhu D, Zhan X. An Electron Acceptor Challenging Fullerenes for Efficient Polymer Solar Cells. Advanced Materials. 2015;27(7):1170-4.

35. Yu R, Wu G, Tan Za. Realization of high performance for PM6:Y6 based organic photovoltaic cells. Journal of Energy Chemistry. 2021;61:29-46.

36. Wei Q, Liu W, Leclerc M, Yuan J, Chen H, Zou Y. A-DA′ D-A non-fullerene acceptors for high-performance organic solar cells. Science China Chemistry. 2020;63(10):1352-66.

37. Fan X. Doping and Design of Flexible Transparent Electrodes for High-Performance Flexible Organic Solar Cells: Recent Advances and Perspectives. Advanced Functional Materials. 2021;31(8):2009399.

38. Wu J, Liao C-Y, Chen Y, Jacobberger RM, Huang W, Zheng D, Tsai K-W, Li W-L, Lu Z, Huang Y, Wasielewski MR, Chang Y-M, Marks TJ, Facchetti A. To Fluorinate or Not to Fluorinate in Organic Solar Cells: Achieving a Higher PCE of 15.2% when the Donor Polymer is Halogen-Free. Advanced Energy Materials. 2021;11(47):2102648.

39. Cui Y, Yao H, Zhang J, Xian K, Zhang T, Hong L, Wang Y, Xu Y, Ma K, An C, He C, Wei Z, Gao F, Hou J. Single-Junction Organic Photovoltaic Cells with Approaching 18% Efficiency. Advanced Materials. 2020;32(19):1908205.

40. Cui Y, Yao H, Hong L, Zhang T, Tang Y, Lin B, Xian K, Gao B, An C, Bi P, Ma W, Hou J. Organic photovoltaic cell with 17% efficiency and superior processability. National Science Review. 2020;7(7):1239-46.

41. Firdaus Y, Le Corre VM, Khan JI, Kan Z, Laquai F, Beaujuge PM, Anthopoulos TD. Key Parameters Requirements for Non-Fullerene-Based Organic Solar Cells with Power Conversion Efficiency >20%. Advanced Science. 2019;6(9):1802028.

42. Greenbank W, Djeddaoui N, Destouesse E, Lamminaho J, Prete M, Boukezzi L, Ebel T, Bessissa L, Rubahn H-G, Turkovic V, Madsen M. Degradation Behavior of Scalable Nonfullerene Organic Solar Cells Assessed by Outdoor and Indoor ISOS Stability Protocols. Energy Technology. 2020;8(12):2000295.

43. Li N, McCulloch I, Brabec CJ. Analyzing the efficiency, stability and cost potential for fullerene-free organic photovoltaics in one figure of merit. Energy & Environmental Science. 2018;11(6):1355-61.

44. Cui Y, Li P, Song C, Zhang H. Terminal Modulation of D−π–A Small Molecule for Organic Photovoltaic Materials: A Theoretical Molecular Design. The Journal of Physical Chemistry C. 2016;120(51):28939-50.

45. Jemison RC, McCullough RD. Techniques for the Molecular Design of Push-Pull Polymers towards Enhanced Organic Photovoltaic Performance. Polymer Composites for Energy Harvesting, Conversion, and Storage. ACS Symposium Series. 1161: American Chemical Society; 2014. p. 71-109.

46. Wan X, Li C, Zhang M, Chen Y. Acceptor–donor–acceptor type molecules for high performance organic photovoltaics – chemistry and mechanism. Chemical Society Reviews. 2020;49(9):2828-42.

47. Houston JE, Richeter S, Clément S, Evans RC. Molecular design of interfacial layers based on conjugated polythiophenes for polymer and hybrid solar cells. Polymer International. 2017;66(10):1333-48.

48. Yao H, Ye L, Zhang H, Li S, Zhang S, Hou J. Molecular Design of Benzodithiophene-Based Organic Photovoltaic Materials. Chemical Reviews. 2016;116(12):7397-457.

49. Li M, Ni W, Wan X, Zhang Q, Kan B, Chen Y. Benzo[1,2-b:4,5-b′]dithiophene (BDT)-based small molecules for solution processed organic solar cells. Journal of Materials Chemistry A. 2015;3(9):4765-76.

50. An C, Hou J. Benzo[1,2-b:4,5-b′]dithiophene-Based Conjugated Polymers for Highly Efficient Organic Photovoltaics. Accounts of Materials Research. 2022;3(5):540-51.

51. Chen Y, Wan X, Long G. High Performance Photovoltaic Applications Using Solution-Processed Small Molecules. Accounts of Chemical Research. 2013;46(11):2645-55.

52. Li Y, Xiao B, Chen R, Chen H, Dong J, Liu Y, Chang S. Single-molecule conductance investigation of BDT derivatives: an additional pattern found to induce through-space channels beyond π–π stacking. Chemical Communications. 2019;55(57):8325-8.

53. Giovannitti A, Thorley KJ, Nielsen CB, Li J, Donahue MJ, Malliaras GG, Rivnay J, McCulloch I. Redox-Stability of Alkoxy-BDT Copolymers and their Use for Organic Bioelectronic Devices. Advanced Functional Materials. 2018;28(17):1706325.

54. Du M, Chen Y, Li J, Geng Y, Ji H, Li G, Tang A, Guo Q, Zhou E. Wide-Band-Gap Phthalimide-Based D-π-A Polymers for Nonfullerene Organic Solar Cells: The Effect of Conjugated π-Bridge from Thiophene to Thieno[3,2-b]thiophene. The Journal of Physical Chemistry C. 2020;124(1):230-6.

55. Zhong T, Xiao C, Xiao B, Hu L, Li Z, Guo F, Wang X, Zhang M, Lei S, Yang R. Enhanced photovoltaic performance of donor polymers effected by asymmetric π-bridges. Polymer Chemistry. 2022;13(34):4944-52.

56. Liu J, Ren J, Zhang S, Hou J. Effects on the photovoltaic properties of copolymers with five-membered chalcogen-π-heterocycle bridges. Polymer Chemistry. 2020;11(31):5019-28.

57. Jing X, Zhao Y, Wang Q, Kang X, Zhuang T, Liu X, Wang X, Yu L, Sun M. Effects of additional π-bridges on a terpolymer based on the second acceptor unit of DTBT and the performance of organic solar cells. Polymer. 2022;254:125089.

58. Du M, Geng Y, Ji H, Li G, Xiao Y, Zuo K, Liu Y, Guo Q, Tang A, Zhou E. The optimization of π-bridge for trialkylsilyl substituted D-π-A photovoltaic polymers. Dyes and Pigments. 2021;194:109609.

59. Liao J, Zheng P, Xu G, Weng F, Zeng L, Huang Z, Chen Y, Yang Y, Chen J, Qiu Z, Zhao H, Xu Y. Fluorination of the π-bridge in a polymer skeleton enables a significant improvement in photovoltaic performance. Dyes and Pigments. 2022;197:109834.

60. Jiang J-M, Raghunath P, Lin Y-C, Lin H-K, Ko C-L, Su Y-W, Lin MC, Wei K-H. Linear solubilizing side chain substituents enhance the photovoltaic properties of two-dimensional conjugated benzodithiophene-based polymers. Polymer. 2015;79:262-70.

61. Liu Z, Bao C, Zhang G, Zhang K, Lei G, Zhang Q, Peng Q, Liu Y. Enhancement the photovoltaic performance of conjugated polymer based on simple head-to-head alkylthio side chains engineered bithiophene. Chinese Chemical Letters. 2020;31(9):2459-64.

62. Chen W, Huang G, Li X, Wang H, Li Y, Jiang H, Zheng N, Yang R. Side-Chain-Promoted Benzodithiophene-based Conjugated Polymers toward Striking Enhancement of Photovoltaic Properties for Polymer Solar Cells. ACS Applied Materials & Interfaces. 2018;10(49):42747-55.

63. Cui C, Wong W-Y. Effects of Alkylthio and Alkoxy Side Chains in Polymer Donor Materials for Organic Solar Cells. Macromolecular Rapid Communications. 2016;37(4):287-302.

64. Cui C, Wong W-Y, Li Y. Improvement of open-circuit voltage and photovoltaic properties of 2D-conjugated polymers by alkylthio substitution. Energy & Environmental Science. 2014;7(7):2276-84.

65. Chen W, Huang G, Li X, Li Y, Wang H, Jiang H, Zhao Z, Yu D, Wang E, Yang R. Revealing the Position Effect of an Alkylthio Side Chain in Phenyl-Substituted Benzodithiophene-Based Donor Polymers on the Photovoltaic Performance of Non-Fullerene Organic Solar Cells. ACS Applied Materials & Interfaces. 2019;11(36):33173-8.

66. Jiang J-M, Lin H-K, Lin Y-C, Chen H-C, Lan S-C, Chang C-K, Wei K-H. Side Chain Structure Affects the Photovoltaic Performance of Two-Dimensional Conjugated Polymers. Macromolecules. 2014;47(1):70-8.

67. Liang Y, Feng D, Wu Y, Tsai S-T, Li G, Ray C, Yu L. Highly Efficient Solar Cell Polymers Developed via Fine-Tuning of Structural and Electronic Properties. Journal of the American Chemical Society. 2009;131(22):7792-9.

68. Szarko JM, Guo J, Liang Y, Lee B, Rolczynski BS, Strzalka J, Xu T, Loser S, Marks TJ, Yu L, Chen LX. When Function Follows Form: Effects of Donor Copolymer Side Chains on Film Morphology and BHJ Solar Cell Performance. Advanced Materials. 2010;22(48):5468-72.

69. Piliego C, Holcombe TW, Douglas JD, Woo CH, Beaujuge PM, Fréchet JMJ. Synthetic Control of Structural Order in N-Alkylthieno[3,4-c]pyrrole-4,6-dione-Based Polymers for Efficient Solar Cells. Journal of the American Chemical Society. 2010;132(22):7595-7.

70. Zhang S, Uddin MA, Zhao W, Ye L, Woo HY, Liu D, Yang B, Yao H, Cui Y, Hou J. Optimization of side chains in alkylthiothiophene-substituted benzo[1,2-b:4,5-b′]dithiophene-based photovoltaic polymers. Polymer Chemistry. 2015;6(14):2752-60.

71. Yuan J, Zhai Z, Dong H, Li J, Jiang Z, Li Y, Ma W. Efficient Polymer Solar Cells with a High Open Circuit Voltage of 1 Volt. Advanced Functional Materials. 2013;23(7):885-92.

72. Liao C-Y, Chen Y, Lee C-C, Wang G, Teng N-W, Lee C-H, Li W-L, Chen Y-K, Li C-H, Ho H-L, Tan PH-S, Wang B, Huang Y-C, Young RM, Wasielewski MR, Marks TJ, Chang Y-M, Facchetti A. Processing Strategies for an Organic Photovoltaic Module with over 10% Efficiency. Joule. 2020;4(1):189-206.

73. Hadmojo WT, Wibowo FTA, Ryu DY, Jung IH, Jang S-Y. Fullerene-Free Organic Solar Cells with an Efficiency of 10.2% and an Energy Loss of 0.59 eV Based on a

Thieno[3,4-c]Pyrrole-4,6-dione-Containing Wide Band Gap Polymer Donor. ACS Applied Materials & Interfaces. 2017;9(38):32939-45.

74. Fan M, Du Z, Chen W, Liu D, Wen S, Sun M, Yang R. Benzodithiophene-Based Polymers Containing Alkylthiophenyl Side Chains with Lowered HOMO Energy Levels for Organic Solar Cells. Asian Journal of Organic Chemistry. 2016;5(10):1273-9.

75. Yuan J, Xiao L, Liu B, Li Y, He Y, Pan C, Zou Y. New alkoxylphenyl substituted benzo[1,2-b:4,5-b′] dithiophene-based polymers: synthesis and application in solar cells. Journal of Materials Chemistry A. 2013;1(36):10639-45.

76. Xiao L, Yuan J, Zou Y, Liu B, Jiang J, Wang Y, Jiang L, Li Yf. A new polymer from fluorinated benzothiadiazole and alkoxylphenyl substituted benzo[1,2-b:4,5-b′]dithiophene: Synthesis and photovoltaic applications. Synthetic Metals. 2014;187:201-8.

77. Dou L, Gao J, Richard E, You J, Chen C-C, Cha KC, He Y, Li G, Yang Y. Systematic Investigation of Benzodithiophene- and Diketopyrrolopyrrole-Based Low-Bandgap Polymers Designed for Single Junction and Tandem Polymer Solar Cells. Journal of the American Chemical Society. 2012;134(24):10071-9.

78. Fan M, Du Z, Chen W, Liu D, Wen S, Sun M, Yang R. Benzodithiophene‐Based Polymers Containing Alkylthiophenyl Side Chains with Lowered HOMO Energy Levels for Organic Solar Cells. Asian Journal of Organic Chemistry. 2016;5(10):1273-9.

79. Kim J-H, Park JB, Xu F, Kim D, Kwak J, Grimsdale AC, Hwang D-H. Effect of π-conjugated bridges of TPD-based medium bandgap conjugated copolymers for efficient tandem organic photovoltaic cells. Energy & Environmental Science. 2014;7(12):4118-31.

80. Wang X, Sun Y, Chen S, Guo X, Zhang M, Li X, Li Y, Wang H. Effects of π-Conjugated Bridges on Photovoltaic Properties of Donor-π-Acceptor Conjugated Copolymers. Macromolecules. 2012;45(3):1208-16.

81. Ye L, Zhang S, Zhao W, Yao H, Hou J. Highly Efficient 2D-Conjugated Benzodithiophene-Based Photovoltaic Polymer with Linear Alkylthio Side Chain. Chemistry of Materials. 2014;26(12):3603-5.

82. Kotturappa CG, Gopikrishna MM, Rao AD, Ramamurthy PC. Design and synthesis of thieno[3,4-c]pyrrole-4,6-dione based conjugated copolymers for organic solar cells. Polymer International. 2017;66(8):1206-13.

83. Park JB, Ha J-W, Jung IH, Hwang D-H. High-Performance Nonfullerene Organic Photovoltaic Cells Using a TPD-Based Wide Bandgap Donor Polymer. ACS Applied Energy Materials. 2019;2(8):5692-7.

84. Koster LJA, Mihailetchi VD, Ramaker R, Blom PWM. Light intensity dependence of open-circuit voltage of polymer:fullerene solar cells. Applied Physics Letters. 2005;86(12):123509.

85. Kyaw AKK, Wang DH, Wynands D, Zhang J, Nguyen T-Q, Bazan GC, Heeger AJ. Improved Light Harvesting and Improved Efficiency by Insertion of an Optical Spacer (ZnO) in Solution-Processed Small-Molecule Solar Cells. Nano Letters. 2013;13(8):3796-801.

86. Blom PWM, Mihailetchi VD, Koster LJA, Markov DE. Device Physics of Polymer:Fullerene Bulk Heterojunction Solar Cells. Advanced Materials. 2007;19(12):1551-66.

87. Huo L, Liu T, Sun X, Cai Y, Heeger AJ, Sun Y. Single-Junction Organic Solar Cells Based on a Novel Wide-Bandgap Polymer with Efficiency of 9.7%. Advanced Materials. 2015;27(18):2938-44.

88. Melzer C, Koop EJ, Mihailetchi VD, Blom PWM. Hole Transport in Poly(phenylene vinylene)/Methanofullerene Bulk-Heterojunction Solar Cells. Advanced Functional Materials. 2004;14(9):865-70.

89. Cabanetos C, El Labban A, Bartelt JA, Douglas JD, Mateker WR, Fréchet JMJ, McGehee MD, Beaujuge PM. Linear Side Chains in Benzo[1,2-b:4,5-b′]dithiophene–Thieno[3,4-c]pyrrole-4,6-dione Polymers Direct Self-Assembly and Solar Cell Performance. Journal of the American Chemical Society. 2013;135(12):4656-9.

90. Richard F. Daley SJD. Organic Chemistry, Part 1 of 32005. 395 p.

91. Stuart AC, Tumbleston JR, Zhou H, Li W, Liu S, Ade H, You W. Fluorine Substituents Reduce Charge Recombination and Drive Structure and Morphology Development in Polymer Solar Cells. Journal of the American Chemical Society. 2013;135(5):1806-15.

92. Zhang M, Guo X, Zhang S, Hou J. Synergistic Effect of Fluorination on Molecular Energy Level Modulation in Highly Efficient Photovoltaic Polymers. Advanced Materials. 2014;26(7):1118-23.

93. Price SC, Stuart AC, Yang L, Zhou H, You W. Fluorine Substituted Conjugated Polymer of Medium Band Gap Yields 7% Efficiency in Polymer−Fullerene Solar Cells. Journal of the American Chemical Society. 2011;133(12):4625-31.

94. Li S, Ye L, Wang Q, Zhang S, Zhao W, Hou J. Improving the open-circuit voltage of alkylthio-substituted photovoltaic polymers via post-oxidation. Organic Electronics. 2016;28:39-46.

95. Huo L, Zhang S, Guo X, Xu F, Li Y, Hou J. Replacing Alkoxy Groups with Alkylthienyl Groups: A Feasible Approach To Improve the Properties of Photovoltaic Polymers. Angewandte Chemie International Edition. 2011;50(41):9697-702.

96. Zhang M, Guo X, Ma W, Ade H, Hou J. A Polythiophene Derivative with Superior Properties for Practical Application in Polymer Solar Cells. Advanced Materials. 2014;26(33):5880-5.

97. Yang C, Yu R, Liu C, Li H, Zhang S, Hou J. Achieving over 10 % Efficiency in Poly(3-hexylthiophene)-Based Organic Solar Cells via Solid Additives. ChemSusChem. 2021;14(17):3607-13.

98. Xu X, Zhang G, Yu L, Li R, Peng Q. P3HT-Based Polymer Solar Cells with 8.25% Efficiency Enabled by a Matched Molecular Acceptor and Smart Green-Solvent Processing Technology. Advanced Materials. 2019;31(52):1906045.

99. Kang TE, Kim T, Wang C, Yoo S, Kim BJ. Poly(benzodithiophene) Homopolymer for High-Performance Polymer Solar Cells with Open-Circuit Voltage of Near 1 V: A Superior Candidate To Substitute for Poly(3-hexylthiophene) as Wide Bandgap Polymer. Chemistry of Materials. 2015;27(7):2653-8.

100. Kim J-H, Park JB, Yoon SC, Jung IH, Hwang D-H. Enhanced and controllable open-circuit voltage using 2D-conjugated benzodithiophene (BDT) homopolymers by alkylthio substitution. Journal of Materials Chemistry C. 2016;4(11):2170-7.

101. Li G, Xu Q, Chang C, Fan Q, Zhu X, Li W, Guo X, Zhang M, Wong W-Y. High-Performance Nonfullerene Polymer Solar Cells Based on a Wide-Bandgap Polymer without Extra Treatment. Macromolecular Rapid Communications. 2019;40(1):1800660.

102. Ishii H, Sugiyama K, Ito E, Seki K. Energy Level Alignment and Interfacial Electronic Structures at Organic/Metal and Organic/Organic Interfaces. Advanced Materials. 1999;11(8):605-25.

103. Su WP, Schrieffer JR, Heeger AJ. Solitons in Polyacetylene. Physical Review Letters. 1979;42(25):1698-701.

104. Zhu XY. Charge Transport at Metal−Molecule Interfaces: A Spectroscopic View. The Journal of Physical Chemistry B. 2004;108(26):8778-93.

105. Tanase C, Meijer EJ, Blom PWM, de Leeuw DM. Unification of the Hole Transport in Polymeric Field-Effect Transistors and Light-Emitting Diodes. Physical Review Letters. 2003;91(21):216601.

106. Pasveer WF, Cottaar J, Tanase C, Coehoorn R, Bobbert PA, Blom PWM, de Leeuw DM, Michels MAJ. Unified Description of Charge-Carrier Mobilities in Disordered Semiconducting Polymers. Physical Review Letters. 2005;94(20):206601.

107. Tanase C, Meijer EJ, Blom PWM, de Leeuw DM. Local charge carrier mobility in disordered organic field-effect transistors. Organic Electronics. 2003;4(1):33-7.

108. Singh Dhayal S, Nain A, Kumar A, Kumar A. Recent trends in selection of small molecules for OFET applications: A mini review. Materials Today: Proceedings. 2022.

109. Hiszpanski AM, Loo Y-L. Directing the film structure of organic semiconductors via post-deposition processing for transistor and solar cell applications. Energy & Environmental Science. 2014;7(2):592-608.

110. Liu S, Wang WM, Briseno AL, Mannsfeld SCB, Bao Z. Controlled Deposition of Crystalline Organic Semiconductors for Field-Effect-Transistor Applications. Advanced Materials. 2009;21(12):1217-32.

111. Yan L-H, Wu R-T, Bao D-L, Ren J-H, Zhang Y-F, Zhang H-G, Huang L, Wang Y-L, Du S-X, Huan Q, Gao H-J. Adsorption behavior of Fe atoms on a naphthalocyanine monolayer on Ag(111) surface*. Chinese Physics B. 2015;24(7):076802.

112. Jiang Z-B, Peng M-J, Li L-L, Zhou D-S, Wang R, Xue G. Unusual structural properties of polymers confined in a nanocylinder*. Chinese Physics B. 2015;24(7):076801.

113. Duan S, Wang T, Geng B, Gao X, Li C, Zhang J, Xi Y, Zhang X, Ren X, Hu W. Solution-Processed Centimeter-Scale Highly Aligned Organic Crystalline Arrays for High-Performance Organic Field-Effect Transistors. Advanced Materials. 2020;32(12):1908388.

114. Chen S, Li Z, Qiao Y, Song Y. Solution-processed organic semiconductor crystals for field-effect transistors: from crystallization mechanism towards morphology control. Journal of Materials Chemistry C. 2021;9(4):1126-49.

115. Pan H, Li Y, Wu Y, Liu P, Ong BS, Zhu S, Xu G. Low-Temperature, Solution-Processed, High-Mobility Polymer Semiconductors for Thin-Film Transistors. Journal of the American Chemical Society. 2007;129(14):4112-3.

116. Ong BS, Wu Y, Liu P, Gardner S. High-Performance Semiconducting Polythiophenes for Organic Thin-Film Transistors. Journal of the American Chemical Society. 2004;126(11):3378-9.

117. Guo X, Facchetti A, Marks TJ. Imide- and Amide-Functionalized Polymer Semiconductors. Chemical Reviews. 2014;114(18):8943-9021.

118. Wang C, Dong H, Hu W, Liu Y, Zhu D. Semiconducting π-Conjugated Systems in Field-Effect Transistors: A Material Odyssey of Organic Electronics. Chemical Reviews. 2012;112(4):2208-67.

119. Tao J, Sun W, Lu L. Organic small molecule semiconductor materials for OFET-based biosensors. Biosensors and Bioelectronics. 2022;216:114667.

120. Oh JG, Ha YH, Kim J-H, Kwon S-K, An TK, Kim Y-H, Jang J. Effect of selenophene in naphthalene-diimide-vinylene-based small molecules on n-type organic field-effect transistors. Organic Electronics. 2021;89:106032.

121. Sun M, Sun Y, Chen R, Hu Y, Zhang G. Small molecule semiconductors based on hemi-isoindigo and diketopyrrolopyrrole for solution-processed organic field-effect transistors. Synthetic Metals. 2021;278:116833.

122. Kang S-H, Lee D, Kim H, Choi W, Oh J, Oh JH, Yang C. Effects of the Polarity and Bulkiness of End-Functionalized Side Chains on the Charge Transport of Dicyanovinyl-End-Capped Diketopyrrolopyrrole-Based n-Type Small Molecules. ACS Applied Materials & Interfaces. 2021;13(44):52840-9.

123. Waliszewski W, Parr ZS, Michalska A, Halaksa R, Zajaczkowska H, Sleczkowski P, Neophytou M, Luszczynska B, Blom PWM, Nielsen CB, Marszalek T, Pisula W. Role of oxygen within end group substituents on film morphology and charge carrier transport in thiophene/phenylene small-molecule semiconductors. Organic Electronics. 2022;109:106608.

124. Kafourou P, Nugraha MI, Nikitaras A, Tan L, Firdaus Y, Aniés F, Eisner F, Ding B, Wenzel J, Holicky M, Tsetseris L, Anthopoulos TD, Heeney M. Near-IR Absorbing Molecular Semiconductors Incorporating Cyanated Benzothiadiazole Acceptors for High-Performance Semitransparent n-Type Organic Field-Effect Transistors. ACS Materials Letters. 2022;4(1):165-74.

125. Duan Y, Xu X, Yu L, Li Y, Li R, Peng Q. Molecular packing modulation enabling optimized blend morphology and efficient all small molecule organic solar cells. Dyes and Pigments. 2021;191:109387.

126. Liu Q, Sun H, Blaikie C, Caporale C, Manzhos S, Feron K, MacLeod JM, Massi M, Bottle SE, Bell J, Noh Y-Y, Sonar P. Naphthalene flanked diketopyrrolopyrrole based organic semiconductors for high performance organic field effect transistors. New Journal of Chemistry. 2018;42(15):12374-85.

127. He T, Leowanawat P, Burschka C, Stepanenko V, Stolte M, Würthner F. Impact of 2-Ethylhexyl Stereoisomers on the Electrical Performance of Single-Crystal Field-Effect Transistors. Advanced Materials. 2018;30(44):1804032.

128. Liu Q, Bottle SE, Sonar P. Developments of Diketopyrrolopyrrole-Dye-Based Organic Semiconductors for a Wide Range of Applications in Electronics. Advanced Materials. 2020;32(4):1903882.

129. Di Carlo Rasi D, Janssen RAJ. Advances in Solution-Processed Multijunction Organic Solar Cells. Advanced Materials. 2019;31(10):1806499.

130. Xie B, Chen Z, Ying L, Huang F, Cao Y. Near-infrared organic photoelectric materials for light-harvesting systems: Organic photovoltaics and organic photodiodes. InfoMat. 2020;2(1):57-91.

131. Zhang N, Chen G, Xu Y, Xu X, Yu L. Power Generation, Evaporation Mitigation, and Thermal Insulation of Semitransparent Polymer Solar Cells: A Potential for Floating Photovoltaic Applications. ACS Applied Energy Materials. 2019;2(8):6060-70.

132. Shin DH, Choi S-H. Recent Studies of Semitransparent Solar Cells. Coatings [Internet]. 2018; 8(10).

133. Back JY, An TK, Cheon YR, Cha H, Jang J, Kim Y, Baek Y, Chung DS, Kwon S-K, Park CE, Kim Y-H. Alkyl Chain Length Dependence of the Field-Effect Mobility in Novel Anthracene Derivatives. ACS Applied Materials & Interfaces. 2015;7(1):351-8.

134. Chen M, Yan L, Zhao Y, Murtaza I, Meng H, Huang W. Anthracene-based semiconductors for organic field-effect transistors. Journal of Materials Chemistry C. 2018;6(28):7416-44.

135. Irfan A, Zhang J, Chang Y. Theoretical investigations of the charge transfer properties of anthracene derivatives. Theoretical Chemistry Accounts. 2010;127(5):587-94.

136. Ito K, Suzuki T, Sakamoto Y, Kubota D, Inoue Y, Sato F, Tokito S. Oligo(2,6-anthrylene)s: Acene–Oligomer Approach for Organic Field-Effect Transistors. Angewandte Chemie International Edition. 2003;42(10):1159-62.

137. Stolte M, Suraru S-L, Diemer P, He T, Burschka C, Zschieschang U, Klauk H, Würthner F. Diketopyrrolopyrrole Organic Thin-Film Transistors: Impact of Alkyl Substituents and Tolerance of Ethylhexyl Stereoisomers. Advanced Functional Materials. 2016;26(41):7415-22.

138. Cielecki PP, Leißner T, Ahmadpour M, Madsen M, Rubahn H-G, Fiutowski J, Kjelstrup-Hansen J. Photo-induced and electrical degradation of organic field-effect transistors. Organic Electronics. 2020;82:105717.

139. Zaumseil J, Sirringhaus H. Electron and Ambipolar Transport in Organic Field-Effect Transistors. Chemical Reviews. 2007;107(4):1296-323.

LIST OF PUBLICATIONS

PUBLICATIONS IN PEER-REVIEW JOURNALS

Contributed as the first author:

I. **W Xu**., U. K. Aryal, J. N. Wu, M. Madsen, J. Kjelstrup-Hansen, Z. Cao, D. H. Yu*, Effects of bromination on anthryl-capped DPP-based semiconductor materials: Improved electrical characteristics of organic field-effect transistors, *Synthetic Metals* (2022), 290, 117153

II. **W. Xu**, W. He, G. Li, J. Wu, C. Yang, Z. Cao, P. Cheng, H. Li*, Z. Du*, D. H. Yu*, Challenging PM6-alike donor polymers for paring a Y-type state-of-art acceptor in binary blends for bulk heterojunction solar cells, *Physical Chemistry Chemical Physics*, 2022, DOI: 10.1039/D2CP05414K.

III. **W. Xu**, L. Du, G. Li, W. He, C. Yang, H. Li, Z. Cao, Z. Du*, P. Cheng *, D. H. Yu*, Revisiting benzodithiophene-based donor polymers via thiolalkylation for enhanced photovoltaic performance, *to be submitted*.

IV. **W. Xu**, W. He, G. Li, C. Yang, Z. Cao, H. Li, Z. Du*, P. Cheng*, D. H. Yu*, The impact of position-sensitive fluorination on photovoltaic performance of donor-acceptor polymer/Y-type small molecule based organic solar cells, *in preparation*.

PAPER I

Synthetic Metals 290 (2022) 117153

Contents lists available at ScienceDirect

Synthetic Metals

journal homepage: www.elsevier.com/locate/synmet

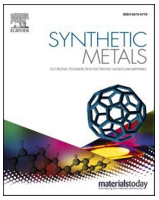

Effects of bromination on anthryl-capped DPP-based semiconductor materials: Improved electrical characteristics of organic field-effect transistors

Wei Xu [a], Um Kanta Aryal [b], Jingnan Wu [a], Morten Madsen [b], Jakob Kjelstrup-Hansen [b], Zhong Cao [c], Donghong Yu [a,d,*]

[a] Department of Chemistry and Bioscience, Aalborg University, Fredrik Bajers Vej 7H, Aalborg East DK-9220, Denmark
[b] SDU NanoSYD, Mads Clausen Institute, University of Southern Denmark, Alsion 2, Soenderborg DK-6400, Denmark
[c] Hunan Provincial Key Laboratory of Materials Protection for Electric Power & Transportation and Hunan Provincial Key Laboratory of Cytochemistry, School of Chemistry and Chemical Engineering, Changsha University of Science and Technology, Changsha 410114, China
[d] Sino-Danish Center for Education and Research, DK-8000 Aarhus, Denmark

ARTICLE INFO

Keywords:
Anthracene
Diketopyrrolopyrrole
Organic field-effect transistors
Small molecules
Semiconductor devices

ABSTRACT

Diketopyrrolopyrrole (DPP), typically flanked with thiophene rings as π-spacers, has been regarded as a promising electron-acceptor unit for constructing donor-acceptor-donor (D-A-D) type small molecule organic semiconductors. Exploring the relationships between its conjugation structure and semiconducting property is of great importance for both molecular design and device fabrication of such DPP materials. Herein we describe the synthesis, self-assembly, and transistor characteristics of two novel N- and N′– 2-octyldodecylated DPP derivatives which were modified with native anthracene (**An**) and brominated anthracene **(Br-An)** at 5-, 5′-position of the flanked thiophenes, respectively, namely **An-DPP** and **Br-An-DPP**. Attributing to the self-assembly behaviors, they exhibit enormous difference in hole transport characteristics on interdigitated-electrode based organic field-effect transistor (OFET) devices even though there is only two atoms' discrepancy in accordance with their molecular structures. The characterization of OFETs with interdigitated-electrodes based on **Br-An-DPP** reveals p-channel operation with highest field-effect mobility of 0.2 $cm^2 \cdot V^{-1} \cdot s^{-1}$, which is 10^7 times higher than that of **An-DPP** (4.8×10^{-8} $cm^2 \cdot V^{-1} \cdot s^{-1}$), and with a threshold voltage of - 2.5 V. X-ray diffraction, atomic force microscopy, scanning electron microscopy, and optical absorption studies reveal the presence of crystalline films caused by bromination on anthracene-modified alkylated DPP (i.e., **Br-An-DPP**), while **An-DPP** exhibits completely amorphous phase.

1. Introduction

Although diketopyrrolopyrrole (DPP) derivatives exhibit strong light-absorption in visible and even near infrared (NIR) range when being copolymerized into donor-acceptor (D-A) low band gap polymers, seemingly suitable for their use in organic photovoltaics (OPVs) [1–6], the resulting power conversion efficiencies (PCEs) have been limited to 9.66% for binary- and 9.0% for ternary-blends based devices, respectively [7–15]. On the contrary, significant achievements from DPP-materials based organic field-effect transistors (OFETs) have attracted great attention over the last decades [16–18]. From the viewpoint of rational design of their molecular structures, it is both the amide groups and the aromatic moiety that afford DPP-based small molecules/polymers the controlled solubility and viscosity (for polymers), more finely tuned energy levels of the molecular orbitals, degree of molecular packing in thin films, and therefore their final optical and electronic characteristics [19–22]. In OFETs devices, small molecule films with better crystallinity exhibit more excellent electrical charac- teristics [23], among which anthracene (An) and its derivatives have attracted much attention in OFETs due to their coplanar structures, prompted intramolecular π-π stacking interaction, eases of crystalliza- tion, and therefore enhanced electrical transfer properties in anthryl semiconductors [23–25]. It had been also explored that efficient π-extension of the anthracene unit (such as formation or dimers and

* Corresponding author at: Department of Chemistry and Bioscience, Aalborg University, Fredrik Bajers Vej 7H, Aalborg East DK-9220, Denmark.
E-mail address: yu@bio.aau.dk (D. Yu).

https://doi.org/10.1016/j.synthmet.2022.117153
Received 20 February 2022; Received in revised form 1 July 2022; Accepted 24 July 2022
Available online 8 August 2022

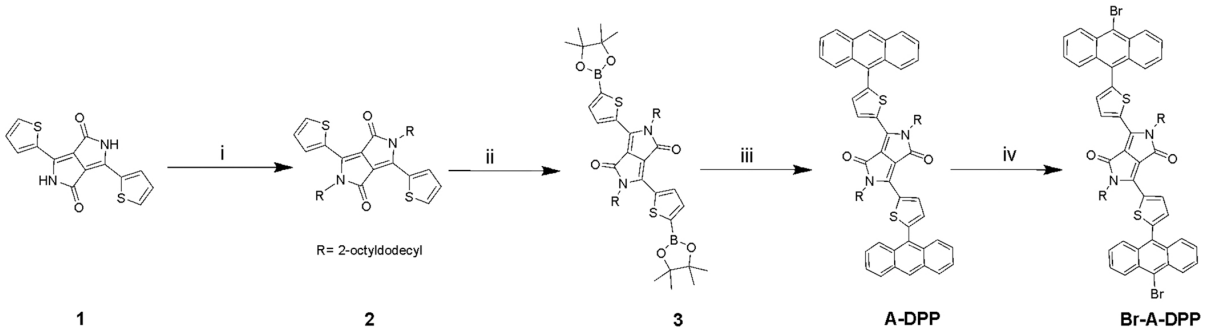

Scheme 1. Synthetic routes to **An-DPP** and **Br-An-DPP**. i.) K_2CO_3, 2-octyldodecyl bromide, DMF, 145 °C; ii.) 2-isopropoxy-4,4,5,5-tetramethyl-1,3,2-dioxaborolane, lithium diisopropylamide, THF, − 25–0 °C; iii.) K_2CO_3(aq, 2.0 M), 9-bromoanthracene, $Pd(PPh_3)_4$, toluene, 110 °C; iv.) N-Bromosuccinimide, $CHCl_3$, 0–60 °C.

trimers [26] and coupling with aryl moieties [27–31]) and introduction of halogen elements [32] would afford much improved hole mobilities. It is just these enhanced degree of orderness and densed packing maintained by π-π stacking interaction that become the most common supramolecular self-assembly behavior, which demonstrates significantly improvement of carrier transport capability on small molecular organic semiconductor materials [30–34]. In addition, the design of the inter-digitated array (IDA) structure in the OFET enables the semiconductor device to have a higher sensor and a simpler fabrication process. Being inspired by these two aspects, we successfully designed and synthesized two small molecules (An-DPP and Br-An-DPP, Scheme 1) of anthracene- and bromoanthracene-DPP via the Suzuki coupling and bromination approaches under an economical synthetic route.

Interestingly, simple bromination on anthracene-DPP reveals significant improvement of 10^7 times higher charge carrier mobility. The transistor devices based on An-DPP thin films show extremely low field-effect mobility of 5×10^{-8} $cm^2V^{-1}s^{-1}$. On the contrary, those based on Br-An-DPP films show excellent semiconducting (hole transporting) properties with a carrier mobility of up to 0.2 cm^2 $V^{-1}s^{-1}$. We attribute this to the self-assembly behavior of Br-A-DPP, which was caused by bromination as the solely structural difference, producing more ordered packing for improving the electrical performance of organic transistors from such a DPP derivative.

2. Results and discussion

2.1. Synthesis and molecular characteristics

As shown in Scheme 1, **An-DPP** was firstly prepared by classical Suzuki coupling reaction between the pinacol borate derivative of DPP (compound 3) and 9-bromoantherence (2.5 molar equivalent) in toluene at 120 °C for 24 hr. Then **Br-An-DPP** was afforded by conventional bromination of **An-DPP** in chloroform for 3 hr at room temperature in the presence of N-bromosuccinimide (NBS). Both **An-DPP** and **Br-An- DPP** were purified by means of column chromatography and obtained as dark red solid in high yields. Interestingly, such tiny difference on their molecular structures between **A-DPP** and **Br-A-DPP** (w/o two bromine atoms) led to two kinds of macroscopic morphology as shown in Fig. S11: at room temperature and atmospheric pressure, the former exhibits bitumen-like viscous oil, while the latter behaves solid granules like grits. Meanwhile, these two materials both present good solubility in most of common organic solvents as expected, especially in dichloromethane and chloroform, which is indeed beneficial for solution-processing of optoelectronic devices due to their ease of evaporation.

2.2. Optical and physicochemical properties

UV–vis absorption of the synthesized **An-DPP** and **Br-An-DPP** in both solutions and films are shown in Fig. 1a. Both compounds exhibit strong and broad absorption benefited from their D-A type molecular structures. The groups of high-energy absorption bands ranging from 354 to ca. 405 nm are attributed to the delocalized π-π * electron tran- sition of conjugated units of **An**. The shoulder peaks around 533 nm are ascribed to the intramolecular charge transfer (ICT) from the electron- rich **An** moiety as the donor (D) to the electron deficient DPP units and bromine atoms as the acceptors (A), indicating a strong electron withdrawing effects caused by bromination of An. This indeed suggest a

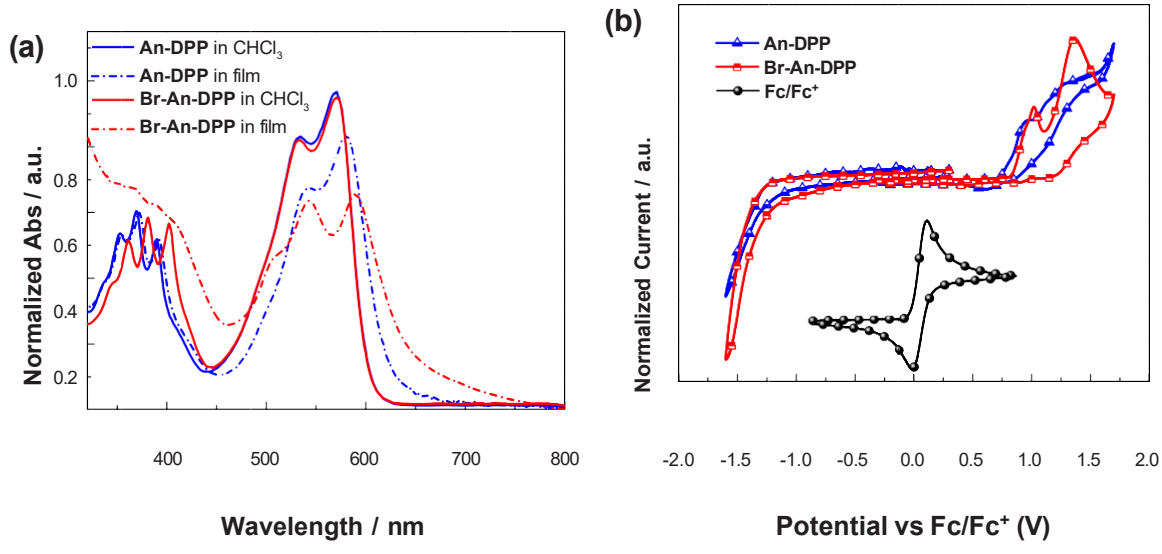

Fig. 1. (a) The UV–vis absorption spectra of **An-DPP** (blue) and **Br-An-DPP** (magenta) in $CHCl_3$ solutions and films, (b) Cyclic voltammograms of **An -DPP** (blue) and **Br-An-DPP** (magenta) with ferrocene (inset of b, black) as an internal standard.

Table 1
Summarized optical and electrochemical properties of two compounds.

Sample	λ_{max} (nm)[a]	HOMO (eV)[b]	LUMO (eV)[c]	Energy gap (E_g, eV)[d]	Optical gap (E_g', eV)[e]
A-DPP	(371) (570)	-5.86	-3.81	2.05	2.05
Br-A-DPP	(381) (570)	-5.92	-3.86	2.06	2.05

[a] In Chloroform, at room temperature.
[b] Calculated from the equation LUMO = - (E_{RE} + 5.13 - | Fc/Fc^+|).
[c] Calculated from the equation HOMO = - (E_{OX} + 5.13 - | Fc/Fc^+|).
[d] Eg = LUMO - HOMO.
[e] Determined from the equation Eg´ = 1240/(onset wavelength of absorption).

more efficient A′-D-A-D-A′ nature of the **Br-An-DPP** molecule, among which A′ refers to Br atom and A represents DPP, while D is the An moiety. The strong intermolecular π-π stacking presented as the ab- sorption maxima (λmax) at ca. 570 nm for both **An-DPP** and **Br-An-DPP** in their $CHCl_3$ solutions and as bathochromic shifts of ca. 10 and 19 nm from solution to films for **An-DPP** and **Br-An-DPP**, respectively, which can be expected to facilitate intermolecular charge transport.,Meanwhile, although **An-DPP** and **Br-An-DPP** present identical ICT band for electron transfer from **An-/Br-An-** DPP moiety, the π-π * electron transition peaks appears a red shift of ca. 10 nm, suggesting strong aggregation of **Br-An-DPP** in solutions. This is furthermore approved by both studies of temperature-dependent UV–vis absorption (c-d) as shown in Fig. S2: all absorption spectra for both **An-DPP** and **Br-An-DPP** show significant reduction and blue-shifts as temperature increases. Such changes on **Br-An-DPP** are more pronounced than those on **An-DPP**, especially reading the higher peak absorbance ratios between the absorption of stacking- and ICT-band indicating that the former has a strong temperature dependent aggregation effect in the solution. This could be attributed into the bromination effects on anthryl moiety as well. Interestingly, the absorption band of anthracene moiety based on **An-DPP** shows no difference between those in solution or film, which implies that the anthracene moiety contributes less than DPP unit does in their molecular aggregations. In contrast, the brominated anthracene moiety in Br-A-DPP film shows higher relative intensity and broader absorption band, which declares the bromo-anthryl-capping does participate the molecular self-assembled stacking of Br-A-DPP. The onset absorption at 605 nm for the two compounds are found in solu- tion, which corresponds to the optical bandgaps (E_g, in solution) of 2.05 eV for both **An-DPP** and **Br-An-DPP** (as found in Table 1).

Fluorescent (FL) property of the synthesized **A-DPP** and **Br-A-DPP** in solutions was combined to explore their molecular self-assembly behavior (Fig. S1), which is meaningful for later investigations on the thin films morphology for their OFET devices. A large overlap between the absorption and emission spectra in solution suggests self-absorption in both these two molecules (Fig. S1). Therefore, the fluorescence emission intensity of two materials significantly decreases as increasing concentration of the samples in the chloroform solution. Previously, Shian and his coworkers investigated optical properties of 9-anthryl- capped DPP-based dyes, namely ATDPP [33]. They believed that the twisted angles among thiophene, anthryl, and the DPP core were extremely small owing to the only one existing α, β-hydrogen (α closes to anthryl, β closes to DPP core), which indicated that the backbone of ATDPP owned an effectively extended molecular conjugation. Simulta- neously, the lower internal rotation barrier and larger distortion angle within the 9-anthrylthiophene moiety, rendered by the relatively weak steric hindrance and repulsion between the 1,8-hydrogens of anthra- cene, made the molecule rotate with a larger amplitude and a lower frequency. In consequence, it could activate one kind of quantum channel called the non-irradiation decay channel, which allows the quantum or other classical information transmit inside. Since the rela- tively weak steric hindrance caused by electron repulsion between the 1-, and 8-hydrogens of anthracene and 4-hydrogen in thiophene moiety

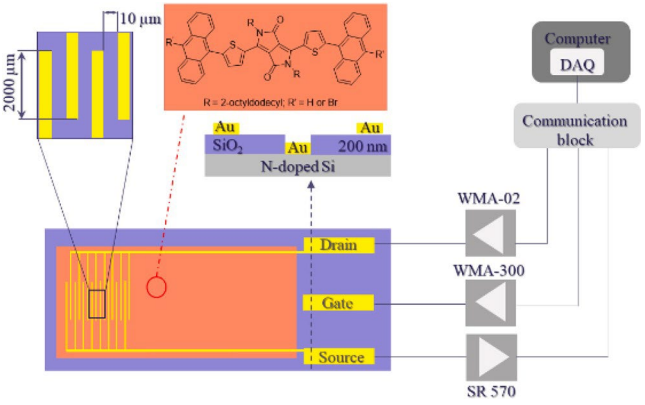

Fig. 2. Design of the bottom-contact bottom-gate OFET and the schematic drawing of the setup for electrical characterization. Inset of the figure presents the molecular structure of produced DPP derivatives herein.

render the molecules to rotate with a larger amplitude and a lower frequency, which could activate the non-irradiation decay channels and then decrease the fluorescence emission as observed in Fig. S2. Furthermore, the significant drops of the fluorescence intensity of both these two molecules with their increased concentrations prove enhanced molecular aggregation in solution phase.

Cyclic voltammograms (CVs, Fig. 1**b**) study on both two materials show irreversible oxidation peaks and sharp reduction peaks. The onset of oxidation peaks (E_{OX}) of **An-DPP** and **Br-An-DPP** are 0.77 and 0.83 V versus Fc^+/Fc, respectively, which corresponds to highest occupied molecular orbital (HOMO) energy levels of − 5.86 and − 5.92 eV, respectively, as listed in Table 1. Their onset of reduction peaks (E_{RE}) are − 1.28 and − 1.23 V, which corresponds to lowest unoccupied molecular orbital (LUMO) energy levels of − 3.81 and − 3.86 eV, respectively, resulting the energy band gaps (E_g) of **An-DPP** and **Br-An-DPP** are 2.05 and 2.06 eV, respectively, which are consistent to the optical ones. Theoretical studies on **An-DPP** and **Br-An-DPP** was performed by means of density functional theory (DFT) with B3LYP/6–31 G(d, p) using the Gaussian09 package. As shown in Fig. S4, the results indicate that the lowering of the electronic energy levels is more significant after bromination. The calculated HOMO and LUMO levels for **An-DPP** and **Br-An-DPP** reveal that they occupy relatively deep positions of energy levels. Despite the slight deviation between calculation and experiment, the role of bromination on their molecular electronic properties is clearly demonstrated, i.e., bromine atoms lower the overall energy levels of HOMO and LUMO owing to the strong electronegativity, but in "a same" degree, therefore the band gaps remain the same regardless of bromination.

2.3. Device fabrication and charge transport properties

For achieving highly sensitive and easy manufacturing of OFET devices, a batch of OFET devices based on the two small molecules of **An-DPP** and **Br-An-DPP** were obtained through a simple solution-processing method on transistor substrates with inter-digitated array (IDA) as illustrated in Fig. 2**,** which was developed by Kjelstrup-Hansen et al. [33] The OFET substrates were fabricated as bottom-gate bottom-contact (BGBC) on a highly N-doped, single-side polished silicon wafer with a SiO_2 layer (300 nm thick, thermally grown) acting as the gate dielectric, Si substrate as gate electrode, and lithographically patterned gold electrodes as source and drain. The interdigitated source and drain electrode design provided a channel width of 40,000 μm (20 interdigitated electrode gaps$_\times$ 2000 μm).

We characterized the electrical performance of the transistors using a custom-built, LabVIEW-based measurement system presented in Fig. 2. Sweeping the gate voltage between 0 and − 5 V while keeping the drain

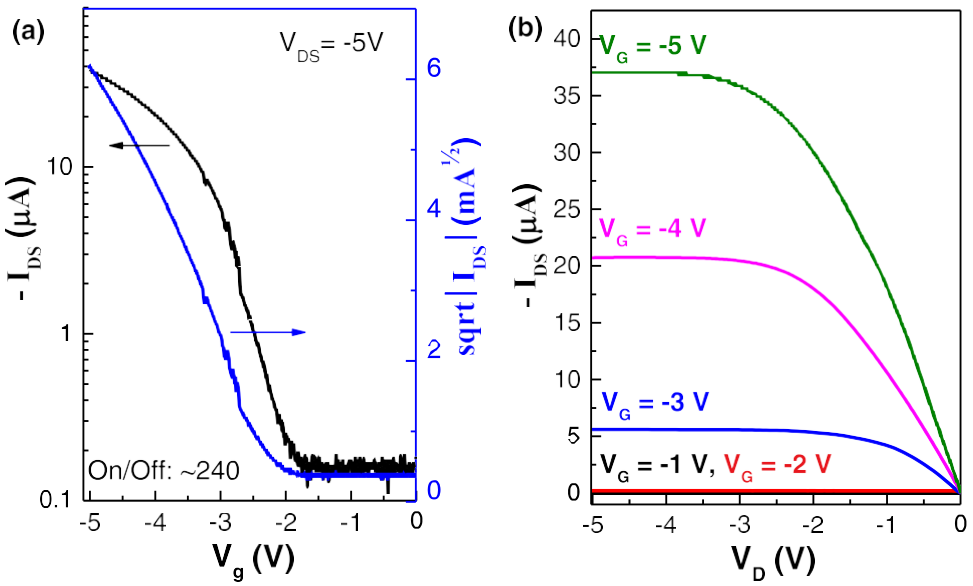

Fig. 3. Transfer curve (a) and (b) output curves of spin-coated thin-film OFET from **Br-An-DPP**.

source voltage (V_{DS}) constant at 5 V provides the transfer character- istics of the transistor devices in the saturation regime (drain current (I_{DS}) and its square-root versus gate voltage (V_G), respectively), while corresponding output curve (sweep the drain voltage from 0 to 5 V while keeping the Vg constant) demonstrated that the saturated drain voltage was 4 V, as shown in Fig. 3, with their corresponding linear fit (red line) for the **Br-An-DPP** device. The highest obtained saturation hole mobility (μ_{sat}) for **Br-An-DPP** was found to be 0.20 cm^2 V^{-1} s^{-1} with a corresponding threshold voltage (V_{th}) of – 2.5 V and current on/off ratio of 240. The averaged performance of four independent devices gave 0.13 cm^2 V^{-1} s^{-1} and a threshold voltage of – 2.3 V, which are quite attractive, considering the ease and high yield of the synthesis. On the contrary, the upstream product, **An-DPP** shows extremely poor FET performance after attempted optimization for many times. The corresponding signal of **An-DPP** almost was covered by noise under higher input drain source voltage (20 V) using the same device manufacturing conditions (Fig. S5). After fitting to the square root of I_{DS} (absolute value) versus V_G curve, a saturation mobility of 5×10^{-8} cm^2 V^{-1} s^{-1} was obtained.

2.4. Self-assembly and morphology

Thermo-gravimetric analysis (TGA) and differential scanning calorimetry (DSC) studies evidenced excellent thermo-stability of both **An-DPP** and **Br-An-DPP** with their decomposition temperature of 350 and 335 °C, respectively, based on their significant mass loss ranging 80–90% of their initial mass as shown in Fig. S6,**7.**Furthermore both DSC and TGA results display possible sublimation for **An-DPP** and **Br- An-DPP** at ca. 180 190 °C. **An-DPP** show no solid-liquid phase transitions, confirming totally amorphous structure, being agreed by its completely amorphous diffractogram from out-of-plane (OOP) X-ray diffraction (XRD) study (Fig. S8, black line). While for **Br-An-DPP**, besides an exothermic peak at around 340 °C, indicating its decomposition which well corresponds to its TGA data as just above-mentioned, it also declares a clear melting point with its endothermic peak at ca. 120 °C, which strongly suggests its crystalline characteristics. Moreover, **Br-An-DPP** emerges somehow diffracted peaks at low angle range around 5° in its film (Fig. S8, blue line), which proves certain crystalline structures resulted by possible self-assembly/π-π stacking from **Br-An-DPP** as what we have discussed in the photophysical properties above in both solutions and films.

For furthermore investigating such molecular self-assembled structure and morphology in thin films, firstly "routine" XRD on power diffraction for OOP structures was investigated. The diffractograms (Fig. S8) of both **An-DPP** and **Br-An-DPP** show the broad peaks at above 20° (d_2-spacing), indicating π-π stacking distances of 4.5 Å for **An-DPP** and 4.1 Å for **Br-An-DPP**, respectively, even though their wide broad- ness indicate large distribution of the size of crystallites as imperfect crystal structures. Whereas the latter emerges observable diffraction peaks at low angle range around 6° and 9° (14.5 and 9.6 Å), implying possible edge-on packing by flexible long alkyl sidechains. Notably, **Br-An-DPP** exhibits better crystallinity and closer face-on packing abilities than **An-DPP** in the solid state. Secondly, grazing incidence XRD for surveying the proper thin film morphology was accomplished, whereas samples were spin-coated on the SiO_2 glass substrate and scanned by X-ray starting from incident angle of 1.5° and the radius of 240 mm, respectively. The IP diffractograms of **An-DPP** and **Br-An-DPP** are shown in Fig. S8 (bottom), with a small but sharp signal as a constructive interfered peak at about 9.0° corresponded to d_1-spacing of 9.33 Å for possible edge-on sidechain packing by **Br-An-DPP**, whereas the broad peaks around 20° were characterized as reasonable face-on π-π stacking distance for d_2-spacing of 3.54 Å and 3.49 Å for **An-DPP** and **Br-An-DPP** respectively.

Attributing to the stronger interchain interactions of alkyl side chains, the molecular aligning of **Br-A-DPP** through π-π stacking was closer than that of **An-DPP**. Thence, strong π-stacking ability and crys- talline property of **Br-A-DPP** could provide a high ordered assembly for effective electron transport. Meanwhile, Scherrer equation was employed to calculate the crystal coherence lengths (CCL) of the crys- tallites. The CCL (100) in the OOP direction for Br-An-DPP in thin film was 53.1 nm, which approximately consistent with the size of the self- assembly in the AFM spectrum.

There are two twisted angles in the molecular conjugation bridge, α and β, which were named according to their neighboring hydrogens (Fig. S10). The twisted angle β is small due to few interacting units between thiophene and intermediate unit, which implies that the excellent thiophene π bridge maintains a relative flat conjunction plane of DPP core. While, the enhancement of the steric hindrance and repulsion ef- fect, between the α-hydrogen of thiophene and the 1,8-positions of anthracene, renders anthracene with a larger rotating amplitude [15].

The DFT simulation optimization (Table S1) indicates that α twisted angle slightly increases and β twisted angle decreases after bromination, which probably owing to the variation of the electron distributions in anthracene induced by the electron withdrawing effect of bromine.

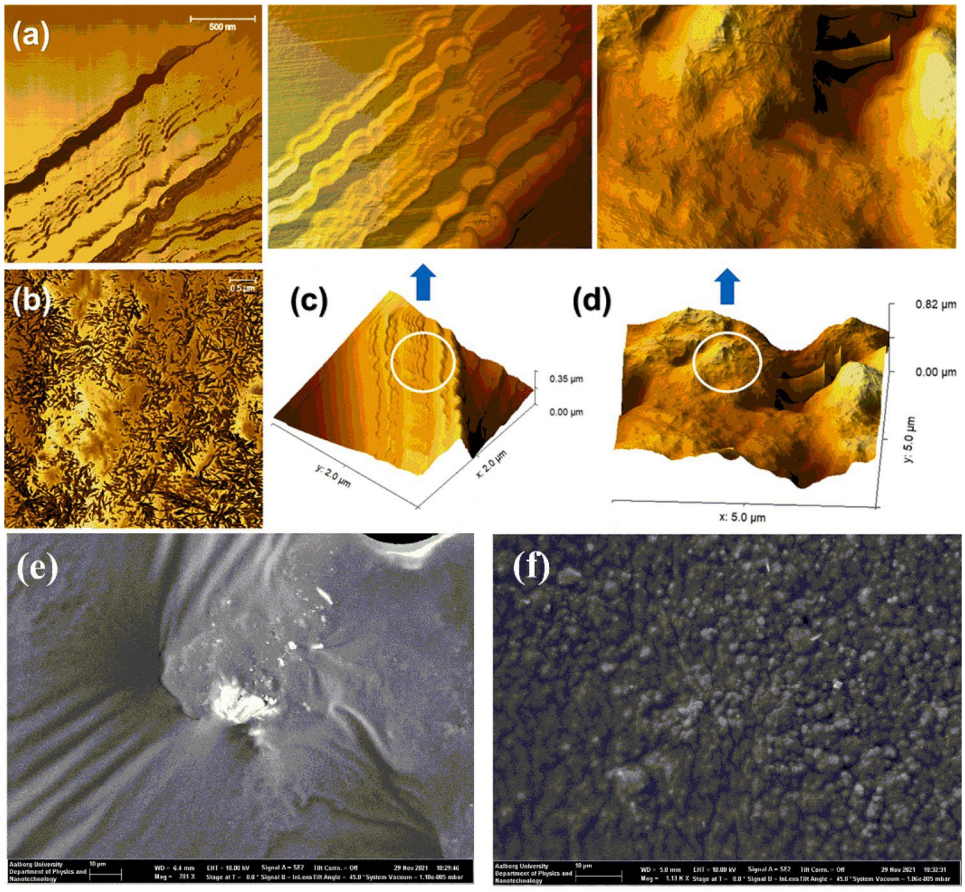

Fig. 4. AFM phase images of **An-DPP** (a) and **Br-An-DPP** (b) in thin films, and corresponding 3D height images of **An-DPP** (c) and **Br-An-DPP** (d) with zoom-in pictures on their top. SEM pictures of **An-DPP** (e) and **Br-An-DPP** (b) in scale of 120 μm × 100 μm.

Whereas the twisted angle (α_2) is close to 90°, revealing that the two planes (between anthracene and thiophene bridge) are almost vertical, the difference between two compounds (α_1 and α_2) is very small. In addition, the anthryl in the capping position is easier to rotate, so the α twisted angle could be the subordinate reason for causing the difference in morphology.

Interestingly, the β twisted angle decreases to a very small value after bromination, which implies that the conjugated planes composed of thiophene π bridge and DPP are flatter. And the hindrance of **Br-A-DPP** molecules in such conformation is greatly reduced when forming the intermolecular π-π stacking.

Thence we speculated the aggregation behaviors of **An-DPP** and **Br-An-DPP** are distinct, shown in Fig. 5, former one is spacing with disordered cross-linking of alkyl chains and relatively weak intermolecular π-π stacking to form amorphous network structure. On the contrary, the latter one forms self-assemblies by stronger intermolecular π-π stacking, and then the assemblies aggregate by cross-linking of alkyl chains. Owing to the ordered self-assembly behavior, the side alkyl chains of **Br-A-DPP** also become ordered-orientated which reflects the better crystallinity in thin film. The aggregation behavior of **A-DPP** like the polymer cross-linking, but it does not form holes as some organic polymers, because the molecular size of **A-DPP** is such small that molecules can be close together. Thence the surface of **A-DPP** thin film is flatter and the ultraviolet light does not emit significant scattering at long wavelength region (Fig. 1**a**). However, due to the self-assembly behavior of **Br-A-DPP**, high and low undulating particles are formed on the surface, so the UV absorption spectrum of the film shows relatively obvious scattering phenomenon at long wavelength region.

The microscopic morphology of the thin films of **An-DPP** and **Br-An-DPP** were investigated by means of atomic force microscopy (AFM) and scanning electron microscopy (SEM). Shown in Figs. 4**a and** 4**c**, the surface topology induced by molecular aggregation of **An-DPP** is irregular, forming terraces-like layer-by-layer surfaces, with no signs of crystallinity. On the contrary, **Br-An-DPP** presents the configuration of the crystal forms in film (Figs. 4**b and** 4**d**). After zooming in the 3D height pattern of AFM, the staggered and stacked strips -like fibers are clearly visible on the slopes of the valley, which is also self-explanatory in AFM phase graph with about 25 nm wide and 200 nm long scale of the short fibers. In their SEM images (Fig. 4**e** and **f**), **A-DPP** films claims almost shows flatter surface than **Br-An-DPP-**, although there presented a special area strong self-aggregation in **An-DPP** films. After zooming in the self-aggregation area, the layer-by-layer shape is easily to see, which is similar to the terraces-like shape in AFM phase (Fig. S9a). And it is clearly to recognize the micrometer scale of particles, which implies that there could be in presence of the geometrically shaped crystals formed by ordered self-assembly. Under smaller view of 12 × 10 μm, it is conspicuous to see the particles, with size of 1–3 μm, are relatively ordered and even one by one (Fig. S9b), and the morphology is consistent with the AFM phase diagram. Obviously, the deductive difference of molecular morphology structure in film between the two compounds displayed in AFM and SEM is qualitatively consistent with the result in the DSC and XRD analysis. There are two twisted angles in the molecular conjugation bridge, α and β, which were named according to their neighboring hydrogens (Fig. S10). The β twisted angle is very small inducing due to few interactions between thiophene and intermediate unit, which implies that the excellent thiophene π bridge maintains a relative flat conjunction plane of DPP core. While, the enhancement of the steric hindrance and repulsion effect, between the α-hydrogen of thiophene and the 1,8-positions of anthracene, renders anthracene with a larger rotating amplitude [10]. Interestingly, quantum chemical

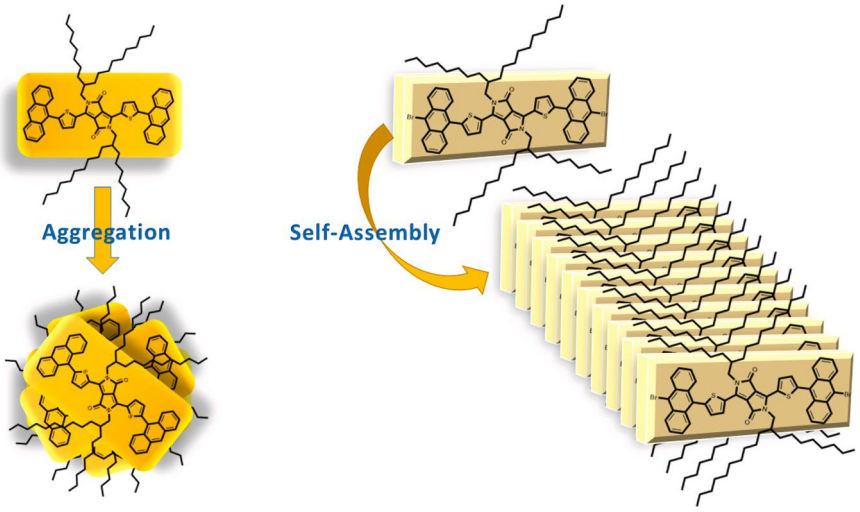

Fig. 5. Schematic diagram of aggregation of **An-DPP** (left) and self-assembly of **Br-An-PP** (right) in thin films.

calculations indicates that the angle between two planes, α twisted angle, slightly increases after bromination, which probably owing to the variation of the electron distributions in anthracene induced by the electron withdrawing effect of bromine. Comparing with those without long alkyl chains (Table S1), the simulation results are almost identical, which illustrates that there is relatively weak steric hindrance and repulsion between long alkyl and anthryl.

As the simulation results reveal that the twisted angle (α_2) is close to 90°, suggesting that the two planes (between anthracene and thiophene bridge) are almost vertical to each other after bromination. The strong steric hindrance and repulsion from the 9-bromoanthryl prevents the alkyl chains from spreading on the plane of the DPP core, which in- dicates the alkyl chains won´t hinder the molecular self-assembly in the subsequent. Thence, we could speculate that **An-DPP** and **Br-An-DPP** are different in microcosmic self-assembled structures (Fig. 5) corresponding to the results of UV and AFM analysis. The former forms the imperfect self-assembly units with weak and disordered π-π stacking on the plane of DPP core in film, due to the non-planarity between anthryl and DPP core induced by the steric hindrance and repulsion effect of alkyl chains. Then it forms amorphous layered structure by entangle- ment among the alkyl chains. Whereas the latter **Br-An-DPP** shows stronger and ordered π-π stacking units with larger molecular area on the plane of DPP core, which demonstrates the anthryl take part in the molecular self-assembly. In films, the anthryl plane could rotate to a small twisted angle against the DPP core plane without the alkyl chains' entangling, which finally form fine fibrous-like self-assemblies. More interestingly, due to the forming of highly effective building blocks, the highly ordered crystalline self-assembly in **Br-An-DPP** films show more excellent electronic properties than **An-DPP**. Furthermore, this intriguing phenomenon establishes a better understanding of the impact of highly ordered crystalline layers on charge carrier transport in tran- sistor devices.

3. Conclusions

In this paper, we have successfully synthesized 1,4-diketo-2,5-dio- ctyldodecyl-3,6-bis(thiophen)-pyrrolo[3,4-*c*]pyrrole (DPP) derivatives capping with anthryl (**An-DPP**) or 9-bromoanthrayl (**Br-An-DPP**) and investigated their optical and electronic properties. Studies on FL spectroscopy, UV–vis spectroscopy, DSC, XRD, and AFM confirmed bromination effect on inducing more ordered molecular self-assemblies for **Br-An-DPP**, leaving **An-DPP** (without bromination) amorphous in films. Furthermore, according to optimized geometric structure, combination with results of UV and AFM analysis, we declare that **Br-An-DPP** forms highly effective building blocks by molecular self-assembly in films, which drastically improved the field-effect mobility in OFETs.

Declaration of Competing Interest

The authors declare the following financial interests/personal relationships which may be considered as potential competing interests: Donghong Yu reports financial support was provided by Sino-Danish Centre for Education and Research. Wei Xu reports financial support was provided by China Scholarship Council.

Acknowledgements

This work received a financial support from China Scholarship Council, China (CSC No. 201908510136). Support from Sino-Danish Center for Education and Research is fully acknowledged.

Appendix A. Supporting information

Supplementary data associated with this article can be found in the online version at doi:10.1016/j.synthmet.2022.117153.

References

[1] H. Zhang, R. Li, Z. Deng, S. Cui, Y. Wang, M. Zheng, W. Yang, π-Conjugated oligomers based on aminobenzodifuranone and diketopyrrolopyrrole, Dyes Pigm 181 (2020), 108552-108552.
[2] Y. Yu, Q. Ma, H. Ling, W. Li, R. Ju, L. Bian, N. Shi, Y. Qian, M. Yi, L. Xie, Small-molecule-based organic field-effect transistor for nonvolatile memory and artificial synapse, Adv. Funct. Mater. 29 (2019), 1904602-1904602.
[3] D. Li, J. Zou, C. Wei, Y. Zhou, L. Wang, W. Zhang, G. Yu, Small-molecule semiconductors containing dithienylacrylonitrile for high-performance organic field-effect transistors, J. Mater. Chem. C. 7 (2019) 11457–11464.
[4] Z. Cai, H. Luo, X. Chen, G. Zhang, Z. Liu, D. Zhang, Extended conjugated donor–acceptor molecules with E-(1, 2–Difluorovinyl) and Diketopyrrolopyrrole (DPP) moieties toward high-performance ambipolar organic semiconductors, Chem. Asian J. 9 (2014) 1068–1075.
[5] C. Wang, X. Zhang, H. Dong, X. Chen, W. Hu, Challenges and emerging opportunities in high-mobility and low-energy-consumption organic field-effect transistors, Adv. Energy Mater. 10 (2020), 2000955-2000955.
[6] P. Sonar, E.L. Williams, S.P. Singh, S. Manzhos, A. Dodabalapur, A benzothiadiazole end capped donor–acceptor based small molecule for organic electronics, Phys. Chem. Chem. 15 (2013) 17064–17069.
[7] A.B. Pun, L.M. Campos, D.N. Congreve, Tunable emission from triplet fusion upconversion in diketopyrrolopyrroles, J. Am. Chem. Soc. 141 (2019) 3777–3781.
[8] J. Schmitt, V. Heitz, A. Sour, F. Bolze, P. Kessler, L. Flamigni, B. Ventura, C. S. Bonnet, E´. To´th, A theranostic agent combining a two-photon-absorbing photosensitizer for photodynamic therapy and a gadolinium (III) complex for MRI detection, Chem. Eur. J. 22 (2016) 2775–2786.
[9] A. Shukla, S.K.M. McGregor, R. Wawrzinek, S. Saggar, E.G. Moore, S.C. Lo, E. B. Namdas, Light amplification and efficient electroluminescence from a solution-

processable diketopyrrolopyrrole derivative via triplet-to-singlet upconversion, Adv. Funct. Mater. 31 (2021), 2009817-2009817.
[10] L. Bürgi, M. Turbiez, R. Pfeiffer, F. Bienewald, H.J. Kirner, C. Winnewisser, High-mobility ambipolar near-infrared light-emitting polymer field-effect transistors, Adv. Mater. 20 (2008) 2217–2224.
[11] L. Pan, T. Liu, J. Wang, L. Ye, Z. Luo, R. Ma, S. Pang, Y. Chen, H. Ade, H. Yan, Efficient organic ternary solar cells employing narrow band gap diketopyrrolopyrrole polymers and nonfullerene acceptors, Chem. Mater. 32 (2020) 7309–7317.
[12] X. Song, N. Gasparini, M.M. Nahid, S.H.K. Paleti, C. Li, W. Li, H. Ade, D. Baran, Efficient DPP donor and nonfullerene acceptor organic solar cells with high photon-to-current ratio and low energetic loss, Adv. Funct. Mater. 29 (2019), 1902441-1902441.
[13] E.Q. Guo, P.H. Ren, Y.L. Zhang, H.C. Zhang, W.J. Yang, Diphenylamine end-capped 1, 4-diketo-3, 6-diphenylpyrrolo [3, 4-c] pyrrole (DPP) derivatives with large two-photon absorption cross-sections and strong two-photon excitation red fluorescence, Chem. Commun. (2009) 5859–5861.
[14] W.W. Bao, R. Li, Z.C. Dai, J. Tang, X. Shi, J.T. Geng, Z.F. Deng, J. Hua, Diketopyrrolopyrrole (dpp)-based materials and its applications: a review, Front. Chem. 8 (2020), 679-679.
[15] S. Ying, M. Chen, Z. Liu, K. Zhang, Y. Pan, S. Xue, W. Yang, 9-Anthryl-capped DPP-based dyes: aryl spacing induced differential optical properties, J. Mater. Chem. C. 4 (2016) 8006–8013.
[16] Q. Liu, H. Sun, C. Blaikie, C. Caporale, S. Manzhos, K. Feron, J.M. MacLeod, M. Massi, S.E. Bottle, J. Bell, Naphthalene flanked diketopyrrolopyrrole based organic semiconductors for high performance organic field effect transistors, N. J. Chem. 42 (2018) 12374–12385.
[17] T. He, P. Leowanawat, C. Burschka, V. Stepanenko, M. Stolte, F. Würthner, Impact of 2–Ethylhexyl Stereoisomers on the Electrical Performance of Single-Crystal Field-Effect Transistors, Adv. Mater. 30 (2018), 1804032-1804032.
[18] Q. Liu, S.E. Bottle, P. Sonar, Developments of diketopyrrolopyrrole-dye-based organic semiconductors for a wide range of applications in electronics, Adv. Mater. 32 (2020), 1903882-1903882.
[19] D.H. Shin, S.-H. Choi, Recent studies of semitransparent solar cells, Coatings 8 (2018), 329-329.
[20] N. Zhang, G. Chen, Y. Xu, X. Xu, L. Yu, Power generation, evaporation mitigation, and thermal insulation of semitransparent polymer solar cells: a potential for floating photovoltaic applications, ACS Appl. Energy Mater. 2 (2019) 6060–6070.
[21] B. Xie, Z. Chen, L. Ying, F. Huang, Y. Cao, Near-infrared organic photoelectric materials for light-harvesting systems: organic photovoltaics and organic photodiodes, InfoMat 2 (2020) 57–91.
[22] D. Di Carlo Rasi, R.A.J. Janssen, Advances in solution-processed multijunction organic solar cells, Adv. Mater. 31 (2019), 1806499-1806499.
[23] A. Irfan, J. Zhang, Y. Chang, Theoretical investigations of the charge transfer properties of anthracene derivatives, Theor. Chem. Acc. 127 (2010) 587–594.
[24] M. Chen, L. Yan, Y. Zhao, I. Murtaza, H. Meng, W. Huang, Anthracene-based semiconductors for organic field-effect transistors, J. Mater. Chem. C. 6 (2018) 7416–7444.
[25] J.Y. Back, T.K. An, Y.R. Cheon, H. Cha, J. Jang, Y. Kim, Y. Baek, D.S. Chung, S.-K. Kwon, C.E. Park, Alkyl chain length dependence of the field-effect mobility in novel anthracene derivatives, ACS Appl. Mater. Interfaces 7 (2015) 351–358.
[26] K. Ito, T. Suzuki, Y. Sakamoto, D. Kubota, Y. Inoue, F. Sato, S. Tokito, Oligo (2, 6–anthrylene) s: acene–oligomer approach for organic field-effect transistors, Angew. Chem. Int. Ed. 42 (2003) 1159–1162.
[27] J. Liu, H. Dong, Z. Wang, D. Ji, C. Cheng, H. Geng, H. Zhang, Y. Zhen, L. Jiang, H. Fu, Thin film field-effect transistors of 2, 6-diphenyl anthracene (DPA), Chem. Commun. 51 (2015) 11777–11779.
[28] D. Sung Chung, T. Kyu An, C. Eon Park, H.-J. Yun, S.-K. Kwon, Y.-H. Kim, High-speed solution-processed organic single crystal transistors using a novel triisopropylsilylethynyl anthracene derivative, Appl. Phys. Lett. 101 (2012), 193304-193304.
[29] H. Meng, F. Sun, M.B. Goldfinger, G.D. Jaycox, Z. Li, W.J. Marshall, G.S. Blackman, High-performance, stable organic thin-film field-effect transistors based on bis-5 '-alkylthiophen-2 '-yl-2, 6-anthracene semiconductors, J. Am. Chem. Soc. 127 (2005) 2406–2407.
[30] J. Liu, H. Zhang, H. Dong, L. Meng, L. Jiang, L. Jiang, Y. Wang, J. Yu, Y. Sun, W. Hu, High mobility emissive organic semiconductor, Nat. Commun. 6 (2015) 1–8.
[31] H. Meng, F. Sun, M.B. Goldfinger, F. Gao, D.J. Londono, W.J. Marshal, G. S. Blackman, K.D. Dobbs, D.E. Keys, 2, 6-Bis [2-(4-pentylphenyl) vinyl] anthracene: a stable and high charge mobility organic semiconductor with densely packed crystal structure, J. Am. Chem. Soc. 128 (2006) 9304–9305.
[32] M. Stolte, S.L. Suraru, P. Diemer, T. He, C. Burschka, U. Zschieschang, H. Klauk, F. Würthner, Diketopyrrolopyrrole organic thin-film transistors: impact of alkyl substituents and tolerance of ethylhexyl stereoisomers, Adv. Funct. Mater. 26 (2016) 7415–7422.
[33] P.P. Cielecki, T. Leissner, M. Ahmadpour, M. Madsen, H.-G. Rubahn, J. Fiutowski, J. Kjelstrup-Hansen, Photo-induced and electrical degradation of organic field-effect transistors, Org. Electron. 82 (2020), 105717-105717.

Electronic Supplementary Information for

Bromination induces small molecular self-assembly breaking amorphous state on DPP-based semiconductor materials: improved electrical characteristics of interdigitated-electrodes organic field-effect transistors

Wei Xu[1], Ulm Kanta Aryal[2], Jingnan Wu[1], Morten Madsen[2], Jakob Kjelstrup-Hansen[2], Zhong Cao[3], Donghong Yu[1,4*]

[1]*Department of Chemistry and Bioscience, Aalborg University, Fredrik Bajers Vej 7H, Aalborg East, DK-9220, Demark*

[2]*SDU NanoSyd, Mads Clausen Institute, University of Southern Denmark, Alsion 2, Soenderborg, DK-6400, Denmark*

[3]*Hunan Provincial Key Laboratory of Materials Protection for Electric Power & Transportation and Hunan Provincial Key Laboratory of Cytochemistry, School of Chemistry and Chemical Engineering, Changsha University of Science and Technology, Changsha 410114, China*

[4]*Sino-Danish Center for Education and Research, DK-8000, Aarhus, Denmark*

1. General information

NMR spectra were recorded at room temperature on Bruker Avance III^{TM} HD–600 (operating at 600 MHz for ^{1}H NMR and 300 MHz for ^{13}C NMR) in $CDCl_3$ with TMS as internal standard. HRMS were measured in a water–Q–TOF Premier (ESI). Agilent Cary Eclipse fluorescence spectrometer and Varian Cary® 50, respectively obtained UV-vis and fluorescence spectra. Besides, the differential scanning calorimetry (DSC) and thermogravimetric analysis (TGA) both are measured by STA 449 F3 Jupiter®. X-ray diffraction (XRD) and Atomic Force Microscope (AFM) were acquired by Malvern PANalytical and NTEGRA Aura, respectively. The samples of XRD measurement were drop-coating on the single crystal silicon substrates. Besides, Grazing Incidence-XRD (GIXRD) was measured by Empyrean X-ray Diffractometer, and the samples of GIXRD measurement were spin-coating on the SiO_2 substates, incidence angle was 1.5°, incidence radius was 240mm, scan step size and time per step were 0.04° and 0.352 s, respectively. Scherrer equation was employed to calculate the crystal coherence lengths (CCL) of the crystallites. According to the Debye-Scherrer equation of $D=(K\cdot\lambda/\beta\cdot\cos\theta)$, the crystalline size (D) could be obtained, where D is the size of the crystallite, K is known as the Scherrer's constant (K=0.94), λ is the X-ray wavelength (1.542 Å), β is full width at half maximum (FWHM) of the diffraction peak (0.367°), and θ is the angle of diffraction (9.51°). All other solvents and reagents were of reagent quality, purchased commercially, and used without further purification.

The CV (cyclic voltammetry) of the two compounds were recorded on a CH-Instruments Model 650A Electrochemical Workstation. Three-electrode configuration were using in measurement, Pt wires as both working electrode and counter electrode, and a freshly activated Ag wire as Ag/Ag^+ pseudoreference electrode calibrated versus the Fc/Fc^+ redox couple at the end of the measurements. A tetrabutylammonium hexafluorophosphate (Bu_4NPF_6) solution (0.1 M solution in anhydrous acetonitrile) was used as a supporting electrolyte, and N_2 gas was bubbled prior to each measurement. Two compounds were deposit onto the working electrode by drop-casting from solutions of 10 mg/mL in $CHCl_3$. HOMO and LUMO levels were estimated from the onset potentials by setting the oxidative onset potential of Fc/Fc^+ vs. the normal hydrogen electrode (NHE) to 0.63 V,[1] and the NHE vs. the vacuum level to 4.5 V.[2] The energy levels were calculated according to the formula LUMO = -(E_{onset}^{red} + 5.13) eV and HOMO = - (E_{onset}^{ox} + 5.13) eV. And E_{onset}^{red} and E_{onset}^{ox} were calculated from the equals of E_{onset}^{red} (or E_{onset}^{ox}) = E_{RE} (or E_{OX}) – $|Fc/Fc^+|$, where E_{RE} E_{OX} were determined from the reduction and oxidation onsets, respectively, and $|Fc/Fc^+|$ was the value of the calibration of the Fc/Fc^+ redox potential (located at 0.04 V) under the same experimental conditions.

1. Device Preparation and Measurement Methods

2.1 Device Fabrication

The OFETs were fabricated on heavily doped n-type silicon substrates covered by a 300 nm thermal oxide (SiO_2) dielectric layer. The Nochromix solution in sulfuric acid was used for cleaning silicon wafers and then washed in deionized water. And a thin layer of Au was thermally evaporated to ensure good electrical contact. The substrates were cleaned in ultrasonic bath with deionized water, acetone and isopropanol sequentially and then dried under nitrogen flow. Then, the substrates were treated in a UV-ozone cleaner for 20 minutes. Finally, the cleaned substrates were transferred to glovebox and the semiconductor layers (An-DPP and Br-An-DPP each dissolved as 10mg/mL in chloroform) was deposited on the substrates by using spin-coating at 2000 rpm for 60 sec.

2.2 Electrical Characterization

The electrical measurements were carried out using a custom-built, LabVIEW-based measurement system presented in **Figure 2**. Three XYZ-manipulators on a probe station are used to place tungsten tips on the contact pads of the sample. The gate voltage is supplied with a Falco Systems WMA-02 amplifier and the drain voltage is supplied with a Falco Systems WMA-300 amplifier, both controlled from the NI PCI6229 DAQ. The source current is measured with the SR570 current amplifier connected to the DAQ card.

In the saturation regime, the square root of the saturation current is directly proportional to the gate voltage,[3] and the equation (1) assumes that the mobility is gate voltage independent. Thence via transferring, the saturation mobility (μ_{sat}) was extracted from following equation (2):

$$I_{DS} = \frac{W}{2 \cdot L} \cdot \mu_{sat} \cdot C_i \cdot (V_G - V_{TH})^2 \qquad \text{(eq.1)}$$

$$\mu_{sat} = \left(\frac{d\sqrt{I_{DS}}}{d_{Vg}}\right)^2 \cdot \frac{2 \cdot L}{W \cdot C_i} \qquad \text{(eq.2)}$$

where I_{DS} is the drain-to-source saturated current; W and L is the channel width and length, respectively; C_i is the capacitance per unit area of the gate dielectric, and the V_G and V_{TH} are gate voltage and threshold voltage, respectively. A highly N-doped, single-side polished silicon (Si) wafer was used for a back gate electrode, which was covered with a 300 nm-thick thermally grown SiO_2 (C_i = 11.5 nF·m^{-2}) as the gate insulator. Channel length (L) and width (W) were 10 μm and 40 mm.

2. Synthesis of Materials

2,5-Bis(2-octyldodecyl)-3,6-di(thiophen-2-yl)pyrrolo[3,4-c]pyrrole-1,4-dione ***(2)***

Under nitrogen atmosphere, **1** (1.13 g, 3.76 mmol) and potassium carbonate (2.1 g, 15.22 mmol) were stirring in DMF (10 mL) at 145°C for 10 min. After turning deeper purple color. The three times overdose of brominated 2-octyldodecylbromide (6 mL, 16.10mmol) was added slowly. Then stirred overnight and cooled down to room temperature. An over amount of ice/water solution was added to quench the mixture. And extracted with DCM then washed with water, brine and dried over Na_2SO_4.

Purification by column chromatography on silica (CH_2Cl_2/petroleum ether = 1:1 as eluent) afforded **2** (1.02 g, 51.7%) as a purple solid.

2,5-Bis(2-octyldodecyl)-3,6-bis(5-(4,4,5,5-tetramethyl-1,3,2-dioxaborolan-2-yl)thiophen-2-yl)pyrrolo[3,4-c]pyrrole-1,4-dione ***(3)***

Under nitrogen atmosphere, compound **2** (0.53g, 1.0 mmol) was added into 2-isopropoxy-4,4,5,5-tetramethyl-1,3,2-dioxaborolane (0.6 mL, 3.0 mmol) of dry THF (15 mL) in two-necks flask at - 25°C. And keep stirring 1.5 hours at - 25°C after 2.0 M lithium diisopropylamide (1.2 mL, 2.4 mmol) in heptane was added dropwise. Then the mixture continued stirring for 2 hours at 0°C before the saturated aqueous of ammonium chloride (10 mL) was added into mixture to quench the reaction. And extracted with DCM then washed with brine and dried over Na_2SO_4. Purification by column chromatography on silica (CH_2Cl_2/petroleum ether = 1:1 as eluent) afforded **3** (0.81g, 72%).

2,5-Bis(2-octyldodecyl)-3,6-bis(5-(anthracene-9-yl)thiophen-2-yl)pyrrolo[3,4-c]pyrrole-1,4-dione ***(An-DPP)***

Compound **3** (0.41 g, 0.37 mmol), 9-bromoanthracene (0.24 g, 0.92 mmol), 2.0 M aqueous K_2CO_3 solution (3 mL) and toluene (9 mL) were added to a two-necked round bottom flask, and purged with nitrogen for 20 min. After $Pd(PPh_3)_4$ (43 mg, 0.037 mmol) was added under the protection of nitrogen, the mixture was heated at 110 °C under refluxed for 24 h. Then extracted with CH_2Cl_2, washed with brine and dried over anhydrous $MgSO_4$, then the solvent was evaporated under vacuum. The crude product was purified by chromatography on silica gel (eluent: CH_2Cl_2/petroleum ether, 2:1, v/v) to provide a dark red viscous solid (408 mg, 91%). ^{1}H NMR (600 MHz, $CDCl_3$, δ): 9.24 (d, J = 3.4 Hz, 2H), 8.59 (s, 2H), 8.07 (d, J = 8.4 Hz, 4H), 7.92 (d, J = 8.7 Hz, 4H), 7.51 (t, J = 11.1 Hz, 4H), 7.47 (t, J = 11.1 Hz, 4H), 7.40 (d, J = 3.8 Hz, 2H), 4.10 (d, J = 7.7 Hz, 4H), 2.08 (s, 2H), 1.37 (m, 8H), 1.20 (m, 24H), 0.86 (q, J = 7.0 Hz, 12H). ^{13}C NMR (151 MHz, $CDCl_3$, δ): 161.92, 145.11, 140.30, 136.11, 131.58, 131.18, 128.83, 128.48, 126.75, 126.44, 126.12, 125.44, 108.14, 46.52, 38.03, 31.91, 31.22, 30.03, 29.62, 29.54, 29.47, 29.33, 29.26, 26.26, 22.68, 14.11. HRMS: Calculated for $[C_{82}H_{104}N_2O_2S_2]^+$: 1213.8660; Found: 1213.8660.

2,5-Bis(R-group)-3,6-bis(5-(10-bromoanthracene-9-yl)thiophen-2-yl)pyrrolo[3,4-c]pyrrole-1,4-dione ***(Br-An-DPP)***

Under nitrogen atmosphere, the N-Bromosuccinimide (NBS, 71.2 mg, 0.4 mmol) was added into solution of **An-DPP** (200 mg, 0.16 mmol) with dry chloroform (10 mL) in single-necks flask at 0°C. Then the mixture moved to darkless place and stirred for 3 h at 60°C. Subsequently, the target product **Br-An-DPP** of 200 mg (yield: 92%) dark red solid was obtained after evaporating and purifying by chromatography on silica gel (eluent: CH_2Cl_2/petroleum ether, 1:1, v/v). ^{1}H NMR (600 MHz, $CDCl_3$, δ) 9.22 (d, *J* = 3.9 Hz, 2H), 8.64 (d, *J* = 8.9 Hz, 4H), 7.90 (d, *J* = 8.8 Hz, 4H), 7.64 (t, *J* = 11.3 Hz, 4H), 7.50 (t, *J* = 11.3 Hz, 4H), 7.39 (d, *J* = 3.9 Hz, 2H), 4.11 (d, *J* = 7.6 Hz, 4H), 2.09 (s, 2H), 1.37 (m, 8H), 1.20 (m, 24H), 0.84 (q, J = 7.0 Hz, 12H). ^{13}C NMR (151 MHz,

$CDCl_3$, δ): 161.88, 144.47, 140.22, 136.08, 132.24, 131.50, 131.41, 130.21, 128.11, 127.45, 127.24, 126.64, 125.49, 108.27, 46.51, 38.05, 31.91, 31.87, 31.25, 31.21, 30.01, 29.72, 29.62, 29.61, 29.54, 29.47, 29.33, 29.26, 26.25, 22.64, 14.11. HRMS: Calculated for $[C_{82}H_{102}Br_2N_2O_2S_2]^+$: 1371.6580; Found: 1371.6580.

3. Study of An-DPP and Br-An-DPP

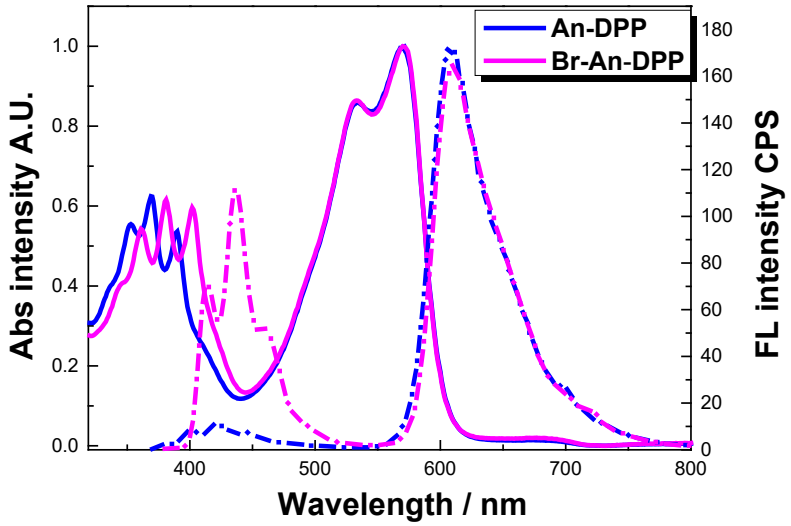

Figure S1. UV-vis absorption (Solid line) and fluorescent (Dot line, Ex = 360 nm) spectra of **An-DPP** (blue lines, 0.5 μM) and **Br-An-DPP** (magenta lines, 0.6 μM).

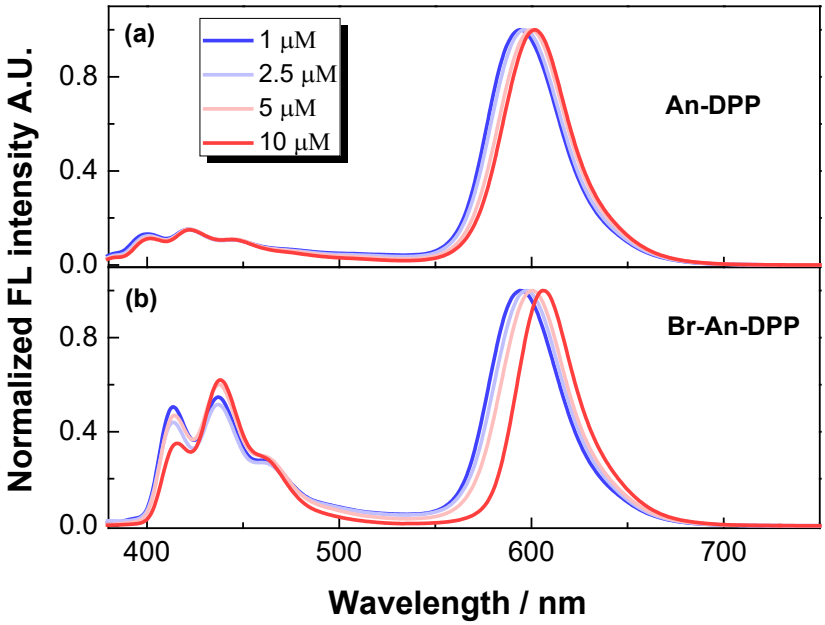

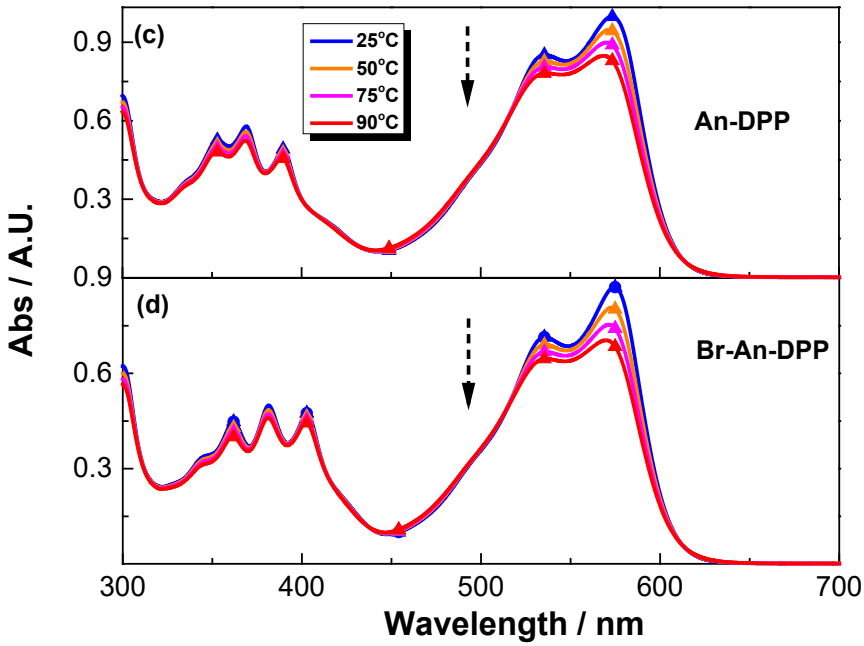

Figure S2. Concentration dependent fluorescence curves of **An-DPP** (**a**), **Br-An-DPP** (**b**), E_x = 350 nm, in Chloroform. Temperature dependent UV-vis absorption curves of **An-DPP** (**c**), **Br-An-DPP** (**d**) in Chlorobenzene, $C_{solution}$ = 5 μM.

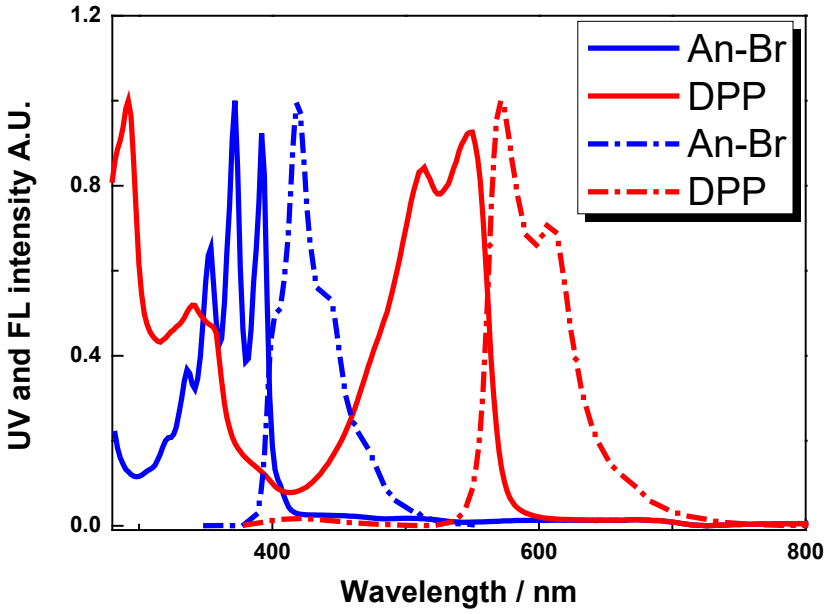

Figure S3. UV-vis absorption (solid line) and fluorescent (dot line, excited at 360 nm) spectra of 9-bromoanthracene (An-Br, red lines, 1 μM) and alkylated-DPP (compound **2**, blue lines, 1μM).

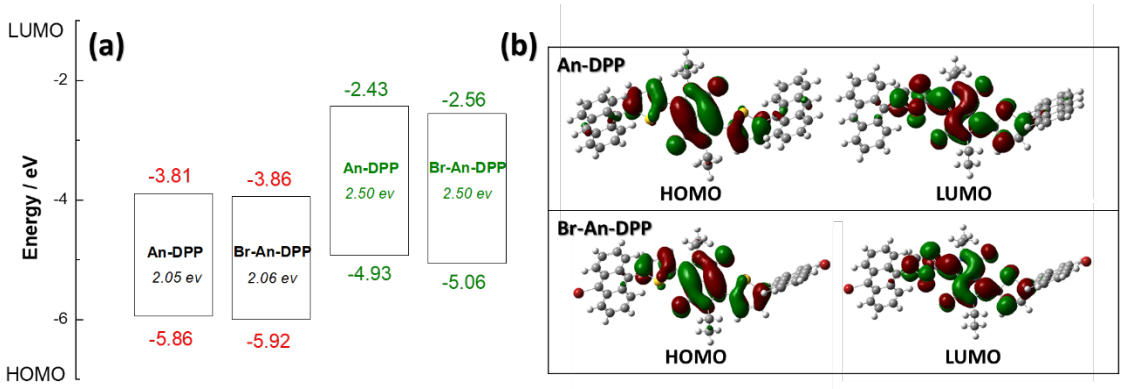

Figure S4. a) The experimental (black, CV) and calculated (green, DFT) HOMO/LUMO energy levels of **An-DPP** and **Br-An-DPP**. b) The calculated electron distributions at HOMO/LUMO orbitals of **An-DPP** and **Br-An-DPP,** performed at the level of B3LYP/6-31G(d, p) based on density functional theory (DFT) with Gaussian09 package[4].

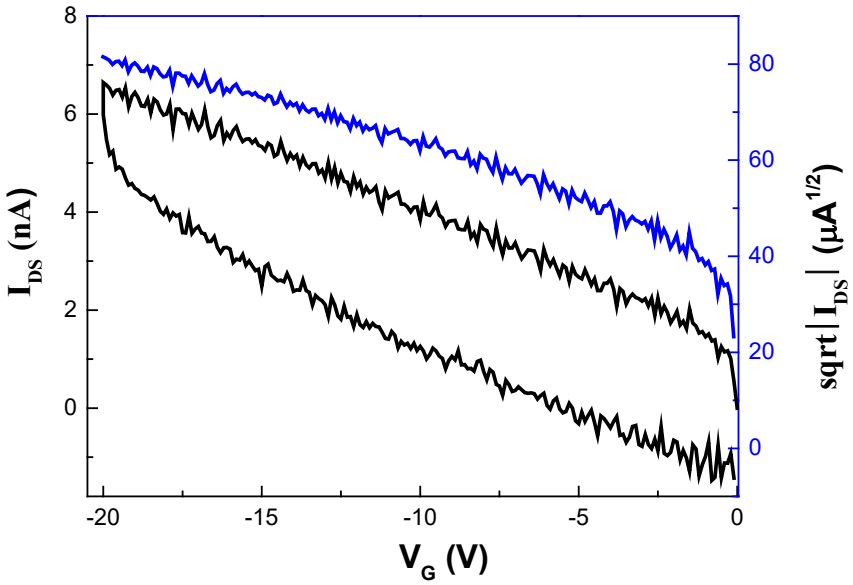

Figure S5. Transfer curves of Spin-coated thin-film OFET made using **An-DPP**.

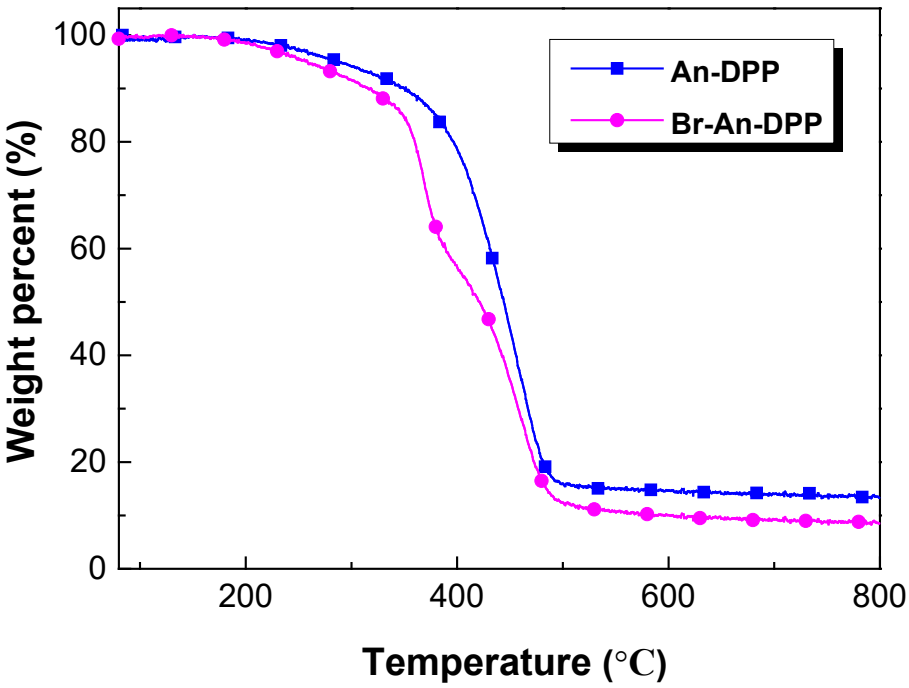

Figure S6. The thermogravimetric (TGA) curves of **An-DPP** and **Br-An-DPP**.

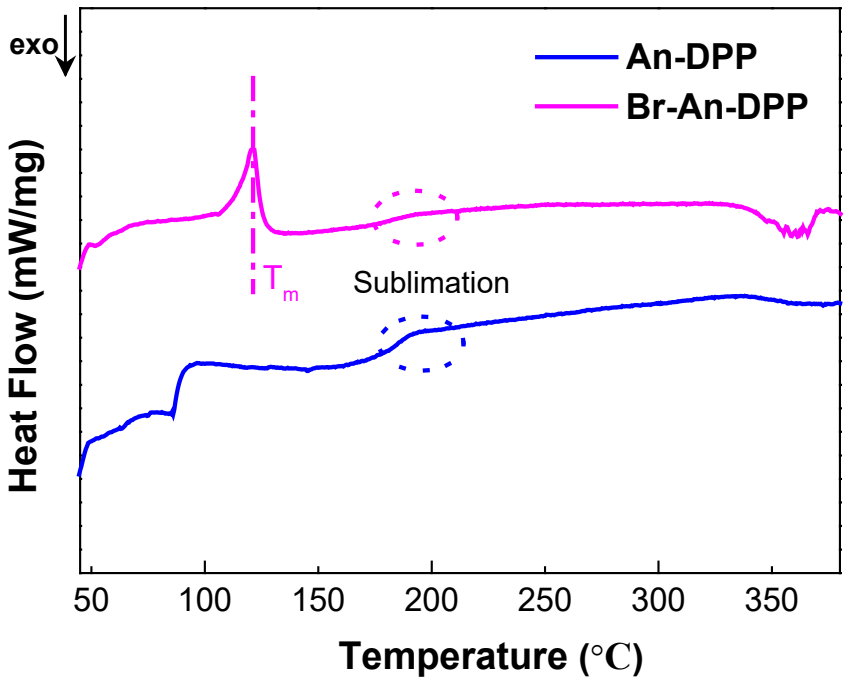

Figure S7. The differential scanning calorimetry (DSC) curves of **An-DPP** and **Br-An-DPP** .

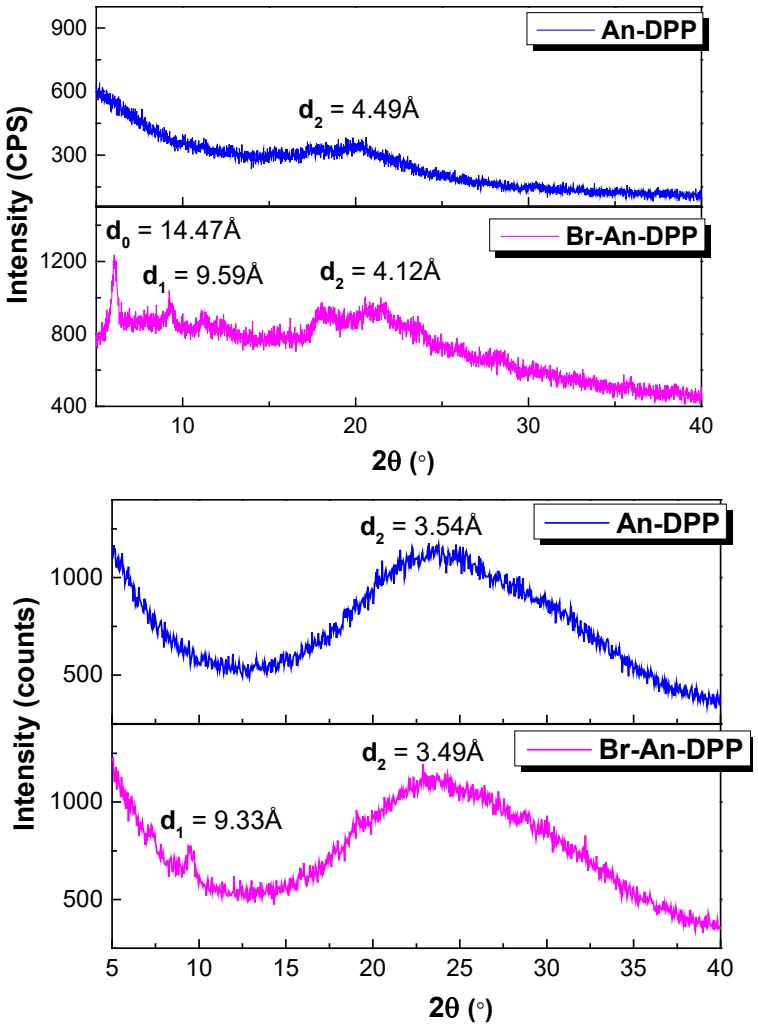

Figure S8. The out-of-plane (left) and in-plane (right) XRD patterns of the **An-DPP** (black) and **Br-An-DPP** (blue) in thin films.

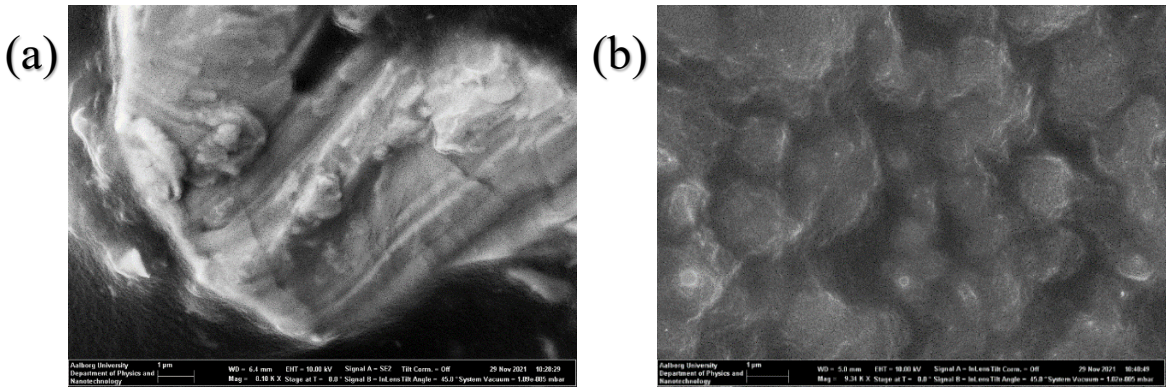

Figure S9. The SEM pictures of **An-DPP** (a) and **Br-An-DPP** (b) in scale of 12 ×10 μm area.

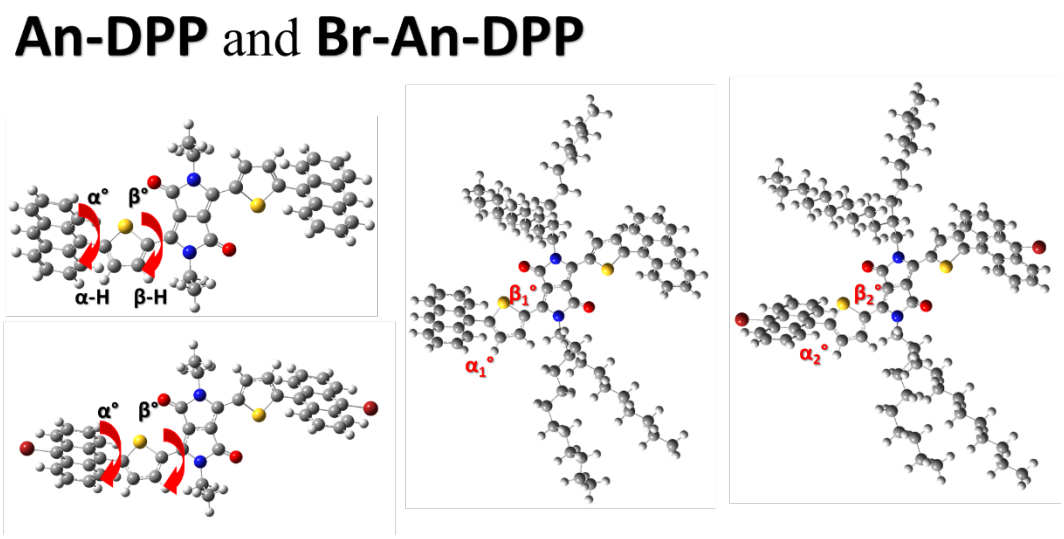

Figure S10. The optimized molecular geometry of **An-DPP** with ethyl substitute (or with octyldodecyl substitute) and **Br-An-DPP** with ethyl substitute (or with octyldodecyl substitute) at the B3LYP/6-31G(d,p) level.

Table S1. The corresponding value of α and β twisted angle at the B3LYP/6-31G(d,p) level.

Items (Substitute)	α	β
An-DPP	75.7°	30.6°
Br-An-DPP	81.3°	6.2°

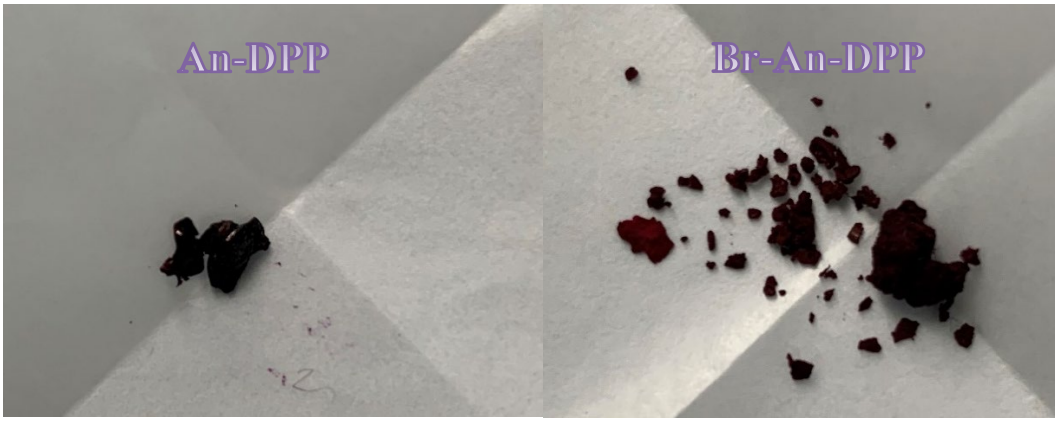

Figure S11. Photos of macroscopic morphology of **An-DPP** and **Br-An-DPP** at room temperature in air.

4. NMR and MS Spectra

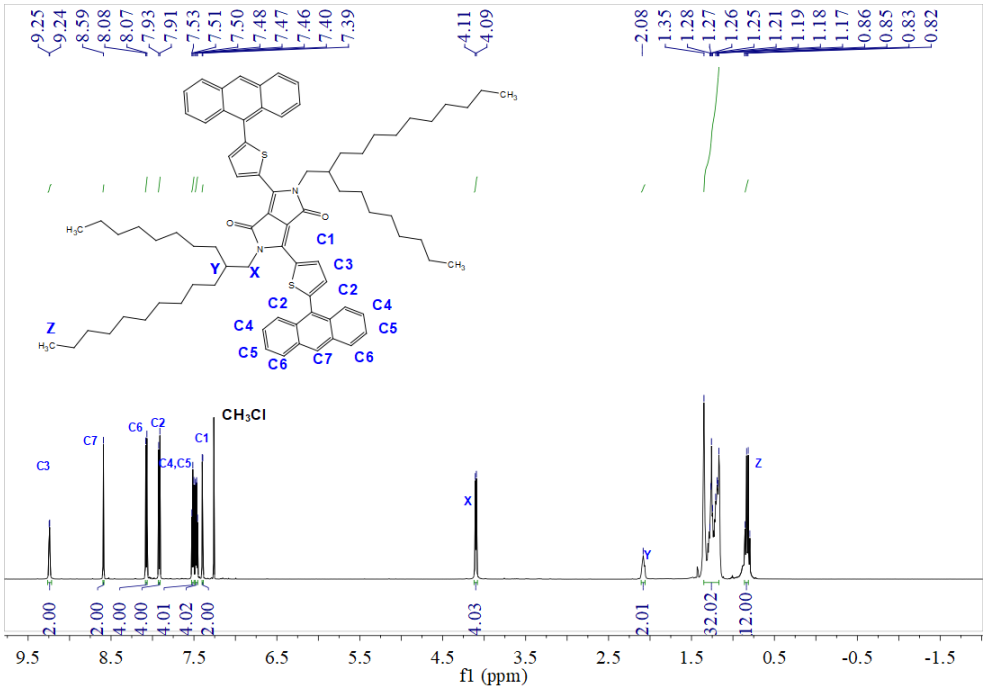

Figure S12. ^{1}H NMR spectra (600 MHz, d_6-$CDCl_3$) of **An-DPP**.

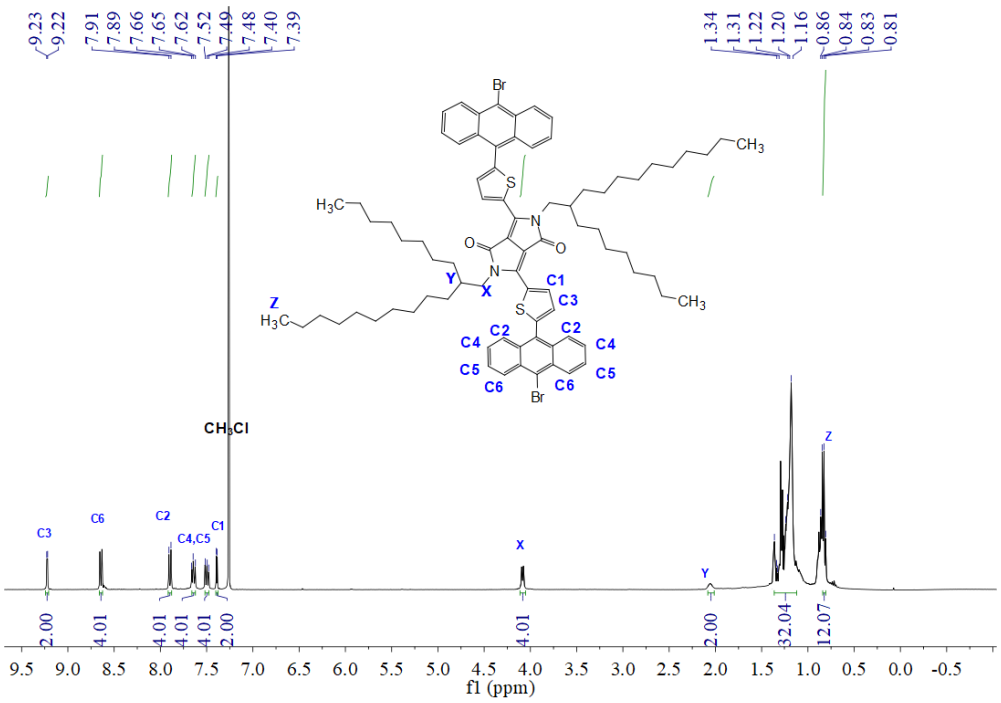

Figure S13. ^{1}H NMR spectra (600 MHz, d_6-$CDCl_3$) of **Br-An-DPP**.

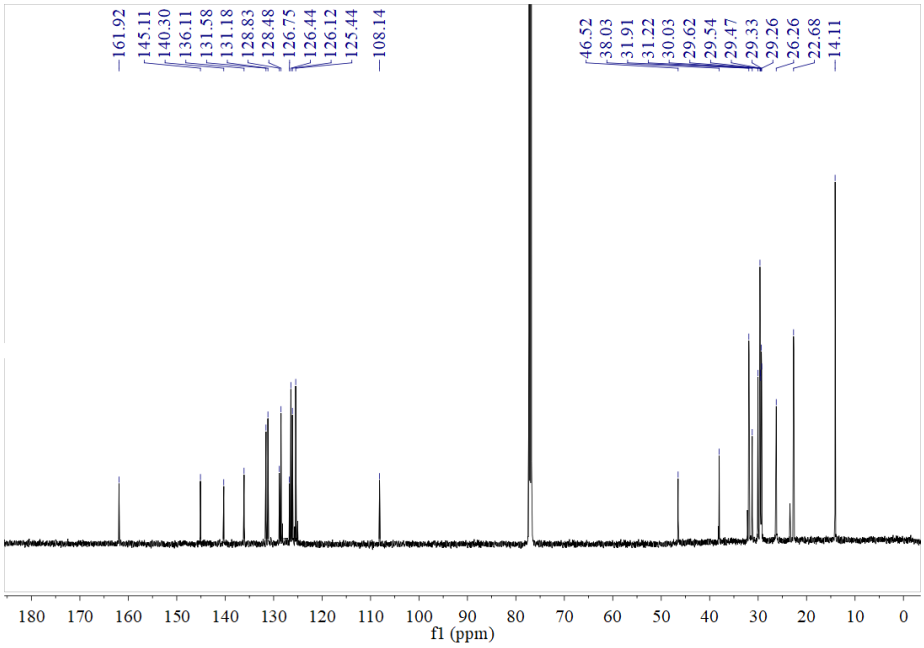

Figure S14. ^{13}C NMR spectra (600 MHz, d_6-$CDCl_3$) of **An-DPP**.

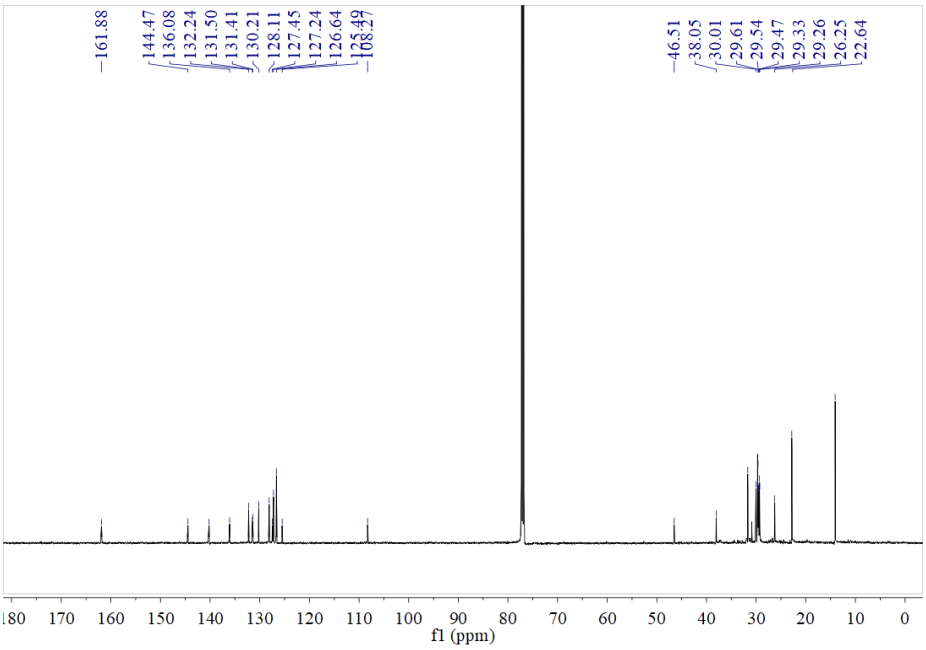

Figure S15. ^{13}C NMR spectra (600 MHz, d_6-$CDCl_3$) of **Br-An-DPP**.

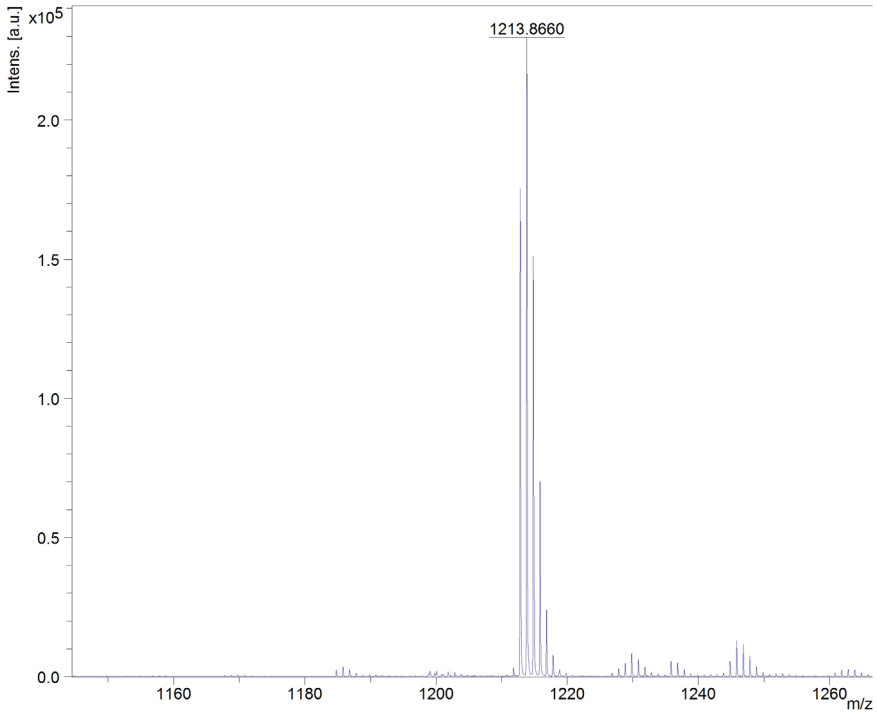

Figure S16. MALDI-TOF-HR-MS spectrum of **An-DPP**.

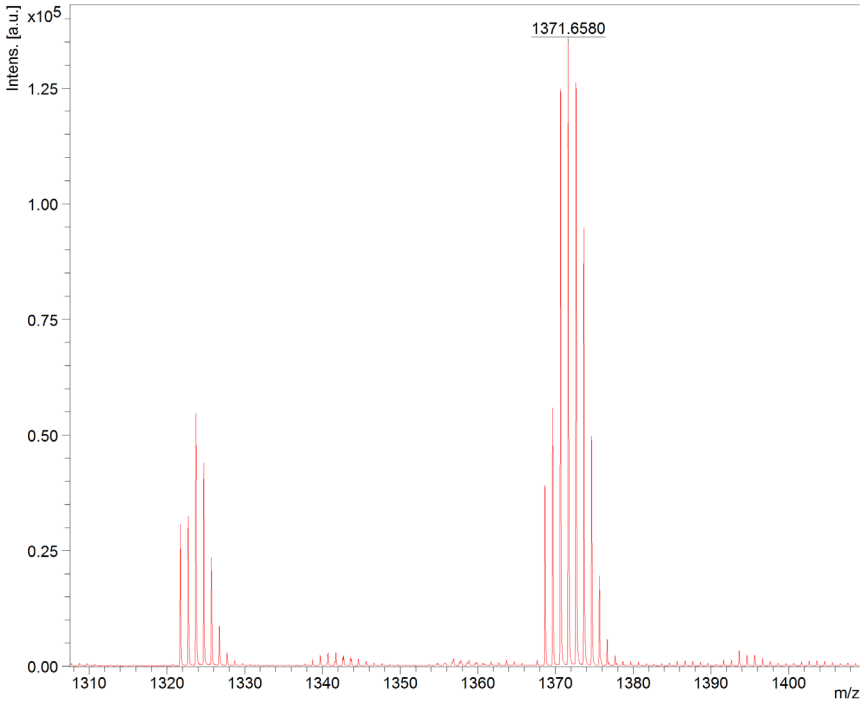

Figure S17. MALDI-TOF-HR-MS spectrum of **Br-An-DPP**.

5. Reference

[1]. (a) V. V. Pavlishchuk and A. W. Addison, Inorg. Chim. Acta, 2000, 298, 97–102; (b) N. G. Connelly and W. E. Geiger, Chem. Rev., 1996, 96, 877–910; (c) C. M. Cardona, W. Li, A. E. Kaifer, D. Stockdale and G. C. Bazan, Adv. Mater., 2011, 23, 2367–2371

[2]. L. R. F. Allen J. Bard, Electrochemical methods: fundamentals and applications, Wiley: New York, 2001.

[3]. Zaumseil J, Sirringhaus H. Electron and ambipolar transport in organic field-effect transistors. Chemical reviews, 2007, 107(4): 1296-1323.

[4]. Gaussian 16, Revision B.01, M. J. Frisch, G. W. Trucks, H. B. Schlegel, G. E. Scuseria, M. A. Robb, J. R. Cheeseman, G. Scalmani, V. Barone, G. A. Petersson, H. Nakatsuji, X. Li, M. Caricato, A. V. Marenich, J. Bloino, B. G. Janesko, R. Gomperts, B. Mennucci, H. P. Hratchian, J. V. Ortiz, A. F. Izmaylov, J. L. Sonnenberg, D. Williams-Young, F. Ding, F. Lipparini, F. Egidi, J. Goings, B. Peng, A. Petrone, T. Henderson, D. Ranasinghe, V. G. Zakrzewski, J. Gao, N. Rega, G. Zheng, W. Liang, M. Hada, M. Ehara, K. Toyota, R. Fukuda, J. Hasegawa, M. Ishida, T. Nakajima, Y. Honda, O. Kitao, H. Nakai, T. Vreven, K. Throssell, J. A. Montgomery, Jr., J. E. Peralta, F. Ogliaro, M. J. Bearpark, J. J. Heyd, E. N. Brothers, K. N. Kudin, V. N. Staroverov, T. A. Keith, R. Kobayashi, J. Normand, K. Raghavachari, A. P. Rendell, J. C. Burant, S. S. Iyengar, J. Tomasi, M. Cossi, J. M. Millam, M. Klene, C. Adamo, R. Cammi, J. W. Ochterski, R. L. Martin, K. Morokuma, O. Farkas, J. B. Foresman, and D. J. Fox, Gaussian, Inc., Wallingford CT, 2016.

PAPER II

PCCP
Physical Chemistry Chemical Physics

Accepted Manuscript

This article can be cited before page numbers have been issued, to do this please use: W. Xu, W. He, G. Li, J. Wu, C. Yang, Z. Cao, P. Cheng, H. Li, Z. Du and D. Yu, *Phys. Chem. Chem. Phys.*, 2022, DOI: 10.1039/D2CP05414K.

ROYAL SOCIETY OF CHEMISTRY

rsc.li/pccp

View Article Online
DOI: 10.1039/D2CP05414K

Challenging PM6-alike donor polymers for paring a Y-type state-of-art acceptor in binary blends for bulk heterojunction solar cells

Wei Xu,[a] Wei He,[b] Guojuan Li,[c] Jingnan Wu [a], Cheng Yang,[d] Zhong Cao,[e] Pei Cheng,[b] Hongxiang Li,[b*] Zhengkun Du,[f*] and Donghong Yu[a,g*]

[a.] Department of Chemistry and Bioscience, Aalborg University, Fredrik Bajers Vej 7H, Aalborg East, DK-9220, Demark

[b.] College of Polymer Science and Engineering, State Key Laboratory of Polymer Materials Engineering, Sichuan University, Chengdu, 610065 China

[c.] National Anti-Drug Laboratory Sichuan Regional Center, Chengdu, 610206 China

[d.] Key Laboratory of Green Chemistry & Technology of Ministry of Education, College of Chemistry, State Key Laboratory of Biotherapy, and Healthy Food Evaluation Research Center, Sichuan University, Chengdu 610064, Sichuan, China

[e.] Hunan Provincial Key Laboratory of Materials Protection for Electric Power and Transportation, and Hunan Provincial Key Laboratory of Cytochemistry, School of Chemistry and Biological Engineering, Changsha University of Science and Technology, Changsha 410114, China

[f.] College of Electrical Engineering and Automation, Shandong University of Science and Technology, Qingdao 266590, China

[g.] Sino-Danish Center for Education and Research, DK-8000, Aarhus, Denmark

* Corresponding authors, email: lihongxiang@scu.edu.cn, zhengkundu@163.com, yu@bio.aau.dk

Abstract

Being fluorine-free and a performance-star material as a small organic molecule acceptor, BTP-eC9 had been well mixed with BDT-based PM6 donor polymers for providing satisfactory photovoltaic properties, especially towards future large scale/large area solar cell production. However, as one of the key electrical outputs from such binary active layer materials, the open circuit voltage (V_{OC}) had been limited to ca. 0.84 V, which needs to be further improved for possible bright future of BTP-eC9. This paper focus on molecular design of alkylthio- and alkoxy-phenyl flanked benzo[1,2-b:4,5-b′]dithiophene-based conjugated polymers (PBDT-PS-ttTPD or shortly P10 and PBDT-PO-ttTPD or P11), which were successfully synthesized and applied as donor materials for pairing BTP-eC9 into organic photovoltaic (OPV) devices. Via fine-tuning side chains of the benzodithiophene (BDT)

View Article Online
DOI: 10.1039/D2CP05414K

moiety, such non-fullerene OPV devices with normal configuration demonstrate attractively high open circuit voltage (V_{OC}) of 0.89, and 0.87 V in P10(P11)/BTP-eC9 based binary single bulk hetero-junction OPV devices, while still maintaining an excellent J_{SC} of 22.7 and 20.0 mA cm^{-2} with their final power conversion efficiency (PCE) of 12.93% from 9.37%**,** respectively. The alkylthio-phenyl chain substituted BDT polymer exhibits better photovoltaic performance in all aspects than the alternatives with alkoxy chains due to the synergistic effect of the alkylthio-phenyl flanked BDT, TPD, and π-bridge (thieno[3,2-b]thiophene).

Introduction

Neither research nor developments of organic photovoltaics (OPVs) could be inspiringly continued worldwide until 2105 when "suddenly" a star molecule termed as ITIC was firstly reported by Lin and Zhan *et al.*, as a brand new family of small molecule non-fullerene acceptor (SM NFA) materials enabled power conversion efficiencies (PCEs) explored from its new start of 6.8% to a new plateau of ca. 13-14% when pairing with benzo[1,2-*b*:4,5-*b*'] dithiophene (BDT) based PBDB-T in the next two years.[1,2] Again just since 2019, based on the second renaissance of SM NFAs initiated by Yuan and Zou *et al.* until currently state-of-art hero Y-series compounds,[3,4] PCEs of organic solar cells (OSCs) have been furthermore boosted from 15.7% to nowadays close to or above 19%.[5–7] Among these, BTP-eC9 (a structural analogue to the popular BTP-4Cl (Y7)), being a more green candidate free from fluorine resources, features enhanced intermolecular ordering compared to Y6 or Y7 acceptor and chlorinated end groups which give the material synergistically deep HOMO and LUMO levels due to the modification of the alkyl chains.[8,9] Therefore, it has been recognized as one of most promising Y-acceptors which shows bright future for OSC production in large scale and large area.[10] As its counterpart, the donor materials that had been paired with them have been being dominated by or fluorinated PBDB-T (PM6) and polymers alike, claiming complimentary optical absorbance, matched energy level between the highest occupied molecular orbitals (HOMOs) of the donor PM6's and lowest unoccupied-molecular orbitals (LUMOs) of the Y-type acceptors, and controlled morphologies. Despite their breaking PCE values, these non-ideally high V_{OC} of below 0.84 V still reflect the imperfect molecular design of the PM6 or similar backbone structures for ideal control on their HOMO/LUMO levels.[7,9,11–18] As well known, the absorption bands, carrier mobility, crystallization, and morphology of bulk-heterojunction layers are closely related with the short circuit current (J_{SC}). While the energy levels difference between the HOMO of donor and the LUMO of acceptor corresponds to the open circuit voltage (V_{OC}). Both J_{SC} and V_{OC} are the vital parameters to

View Article Online
DOI: 10.1039/D2CP05414K

acquire the PCE of PSCs.[19–24] Comparing with J_{SC} and FF, V_{OC} is the more predictable photovoltaic performance of polymers when concepting the molecular structure. For donor-acceptor (D-A) copolymers, the choice of strong electron-withdrawing A units was the most efficient pathway to tune the HOMOs. However, there was a predicament that cannot be ignored, i.e., the high V_{OC} came at the expense of weak J_{SC}, which was extremely destructive for the PCE of the PSCs. The rational energy-level adjustment was the proper optimization mentality. To date, rational molecular designs for both high V_{OC} and large J_{SC} are still ambiguous. Based on the balance between weak electron pushing effect and moderate π-electron accepting ability of the 3d-orbitals at the aryl or allyl position,[25] alkylthiol group had been originally introduced into MEH-PPV by Hou *et al*.[26] for deeper HOMO levels. Followed by Ferraris *et al.* with alkylthiolation on 1-D BDT and on 2-D conjugated BDT moiety by Li *et al.* and Hou *et al.*, PBDTT-S-TT and PBDT-TS1 highlighted a useful design strategy on D-A polymer for lowering HOMO levels and therefore improved V_{OC} as 0.84 V and 0.80 V, resulting their PCE of 8.42% and 9.48%, respectively.[27–29] Recently, the thieno[3,4-c]pyrrole-4,6-dione (TPD) unit as the electron-acceptor moiety in D-A copolymers was reported to afford deeper HOMOs and more appropriate band gaps for absorption complementing typical low-bandgap small molecular non-fullerene acceptors (SM-NFAs) when coupled with benzo[1,2-b:4,5-b′]dithiophene (BDT).[30,31] Moreover, side chains modification on BDT moiety also could reach the same goal. And now a lot of work about thiophene-flanked modification on BDT had been reported that it successfully increased the V_{OC}, affording higher PCE.[29,32] Whereafter, the copolymers materials, containing BDT units with phenyl flanking, were demonstrated to be a deeper HOMO and a higher V_{OC} in corresponding photovoltaic devices than thiophene substitutes, because of the weaker electron-donor ability and the higher ionization potential of phenyl-flanked BDT moiety.[33–36] However, till now there were few papers to discuss the effect of alkyl side chains modification in phenyl-flanked BDT unit on the photovoltaic performance of NFAs PSCs.

In this work, we designed the BDT- and TPD-based conjugated polymer donors to afford high V_{OC} of PSCs. For avoiding the dilemma of the overregulated HOMOs, we inserted the thieno[3,2-b]thiophene as the π-bridge between BDT and TPD moieties, which could tune the absorption bandgap, HOMO/LUMO, crystallinity of active layers and π-π conjugated structure of the polymer backbone to improve charge carrier mobility, fill factor (FF) value and J_{SC}.[37] To investigate the effect of different side-chains alkyl-chalcogen on photovoltaic performance of BDT- and TPD-based PSCs. Thence, two copolymers with structure of PBDT-PX-ttTPD, where X were alkylthio or alkoxy side chains, were successfully synthesized and both exhibited excellent photovoltaic performance in

View Article Online
DOI: 10.1039/D2CP05414K

single-junction SM-NFAs PSCs when paired with BTP-eC9. As expected, the copolymers showed broad absorption both from 300-700 nm, and good hole mobilities of 3.84×10^{-4} cm^2 V^{-1} s^{-1} for PBDT-PS-ttTPD (P10) and 3.48×10^{-4} cm^2 V^{-1} s^{-1} for PBDT-PO-ttTPD (P11), respectively. Additionally, the PSCs based on P10 as donor and BTP-eC9 as acceptor demonstrated a PCE up to 12.93% with a V_{OC} of 0.89 V, a J_{SC} of 22.71 mA cm^{-2} and FF of 63.81% under 100 mW cm^{-2} illumination of AM1.5G.

1. Results and Discussion

Syntheses and Characterization

The alkylthio- and alkoxy-phenyl segments were introduced to the BDT backbone as the substituted conjugated side chains to rebuild such two-dimensional BDT-type polymers. As shown in the **Scheme 1**, the BDT-based copolymers, PBDT-PS-ttTPD and PBDT-PO-ttTPD which were above-named as P10 and P11, were obtained through the Stille Coupling reactions between monomers of bis-stannyl salts of alkythilated phenyl BDT (**M1**) or alkoxy-phenyl (**M2**) and dibrominated **TT-TPD**, respectively. All synthetic and structural details of monomers and copolymers were recorded in the Electronic Supplementary Information (**ESI**). The copolymer P11 was readily dissolved in chloroform (CF), chlorobenzene (CB), and *o*-dichlorobenzene (*o*-DCB), while P10 was mediocrely. The number-average molecular weight (M_n) and the polydispersity index (PDI) of 10.4 kDa and 2.01 for P10 and 7.7 kDa and 1.88 for P11 were measured by gel permeation chromatography (GPC), which were listed in the Table 1.

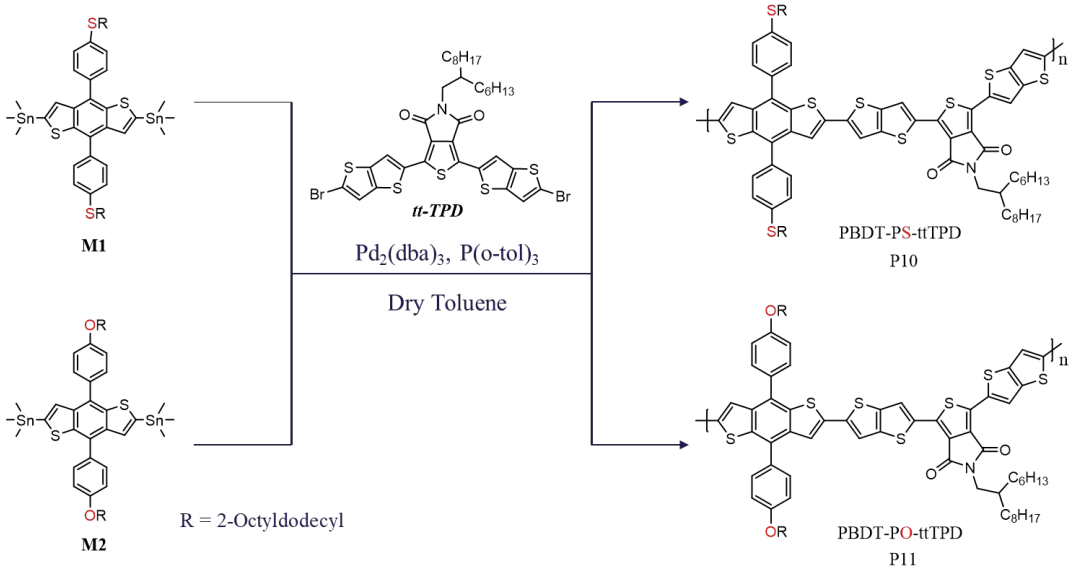

Scheme 1. The synthetic pathways of PBDT-PS-ttTPD (P10) and PBDT-PO-ttTPD (P11).

View Article Online
DOI: 10.1039/D2CP05414K

Thermal and Optical Properties

The thermal stability of the copolymers were measured by thermogravimetric analysis (TGA). As shown in **Figure S5b**, the decomposition temperatures (T_d) corresponding to 5% weight loss of P10 and P11 were 353 °C and 419 °C, respectively, exhibiting their reasonably good thermal stability for PSC applications. UV-vis absorption spectra of the two copolymers were acquired in both dilute CF solutions (0.01 mg/mL) and spin-coated films on quartz substrates at ambient and elevated temperatures as found in **Figure 1a**, **1c** and**1d**, respectively. The wavelengths *(λ_{edge})* at their absorption edge were found as 663 and 656 nm, corresponding to their optical band gaps (E_g^{opt}) of 1.87 and 1.89 eV, respectively, as summarized into **Table 1**, which are all comparable to the structurally analogous TPD-based polymers.[30,31,38] From solution to film, P10 and P11 both presented comparable strong and broad absorption in the region from ca. 300 to 660 nm, with no commonly visible bathochromic shifts of its maximum absorption, implying effective aggregation of these to polymer segments formed in their solution phase. This would be attributed to the strong intermolecular interactions caused by packing of alkylthiol- and alkoxy-phenyl side chains. Referring to their weak absorption for the π-π* transition below 400nm, the intense absorption peak at ca. 540 nm in solution, arising from the intramolecular charge transfer (ICT) between BDT (as a donor) and TPP (as an acceptor) moieties, indicates good electron push-pull effects between them. The strong intermolecular π-π stacking presented as the absorption peak at ca. 601 nm for P10 and 597 nm for P11 can be expected to facilitate intermolecular charge transport, which had been explored in many OSC polymers.[39–41] Such strong π-π stacking on P10 has been also experimentally evidenced by its relatively poor solubility in CF/CB or *o*-CB at ambient temperature. This is furthermore pronounced by the higher peak absorbance ratios between the absorption of π-π stacking band and ICT band for P10 and P11 when comparing them with well-known native- or modified PM6,[18,42] which again suggest the molecular aggregation effects of alkylthiolation and alkoxylation on the phenyl unit of the BDT sidechains. Subtle difference of 4 nm bathochromic shift of maximum absorption peak value for P10, was manifested in the shoulder absorption peaks, which demonstrated that the thiol-modified polymer had highly effective aggregation behavior. Considering the combined weak electron donating and moderate π-electron accepting capability as described in introduction, while alkoxy side chain is typically a strong electron-donating group, the electron cloud of alkoxy-phenyl flanking is denser than that of the alkylthio-phenyl flanking, which indicates the higher intermolecular repulsion potential between two π-conjugation planes of the copolymer backbone. This is in fact directly reflected by the chemical shifts of the two ortho-H in the NMR spectra of **M1** and **M2**, the former

View Article Online
DOI: 10.1039/D2CP05414K

with alkylthiol chains claims a higher chemical shift (7.52 ppm) than the latter (7.13 ppm), proving those protons are more de-shielded therefore resulting higher electron density on the aromatic moieties.[43,44] The temperature dependence on macromolecular aggregation via UV-vis absorption study on both P10 and P11 was investigated in dilute CB solution under different temperature as shown in **Figure 1**. These spectra demonstrate remarkable blue shifts, revealing their actual aggregates formation at ambient and their follow-up dissociation at elevated temperatures. In the meantime, we notice that, on one hand the intensity ratios between their peak- and shoulder-absorption for both P10 and P11 declined, indicating weaker agglomeration at elevated temperatures; on the other hand, such ratios for P10 are always higher than those for P11, proving stronger π-π stacking behavior for P10 in CB solution. On the contrast, the π-π stacking absorption of P11 (**Figure 1c** and **1d**) was gradually vanished along with the rising temperature, because the high-temperature heating provided sufficient potential energy for promoting disaggregation of π-π stacking under synergistic effect of the strong intermolecular repulsion potential. In spite of their different aggregation behavior between these two copolymers, their optical absorption bandgap in solution and thin film are all quite comparable, implying possible similar J_{SC}, due to their comparable abilities of harvesting solar photons.[45,46]

Table 1. Molecular, thermal, optical, and electrochemical properties of two copolymers

Sample	M_n (KDa) [a]	PDI [a]	T_d (°C) [b]	λ_{edge} [nm]	E_g^{opt} [eV] [c]	HOMO [eV] [d]	LUMO [eV] [e]	HOMO [eV] [f]	LUMO [eV] [f]
P10	10.4	2.01	353	663	1.87	-5.33	-3.46	-4.98	-2.65
P11	7.7	1.88	419	656	1.89	-5.30	-3.41	-4.92	-2.58

[a] M_n and PDI of the copolymers were determined by GPC using polystyrene standards in $CHCl_3$; [b] Temperature at 5% weight loss at a heating rate of 10 °C min^{-1} under N_2 atmosphere; [c] Evaluated from the absorption band edge of the polymer films and determined by the equation E_g^{opt} = 1240/(onset band edge of absorption); [d] Calculated from the CV equation E_{HOMO} = - (E_{OX} + 4.8 - |Fc/Fc^+|) eV; [e] $E_{LUMO} = E_{HOMO} + E_g^{opt}$; [f] Calculated via DTF simulations.

View Article Online
DOI: 10.1039/D2CP05414K

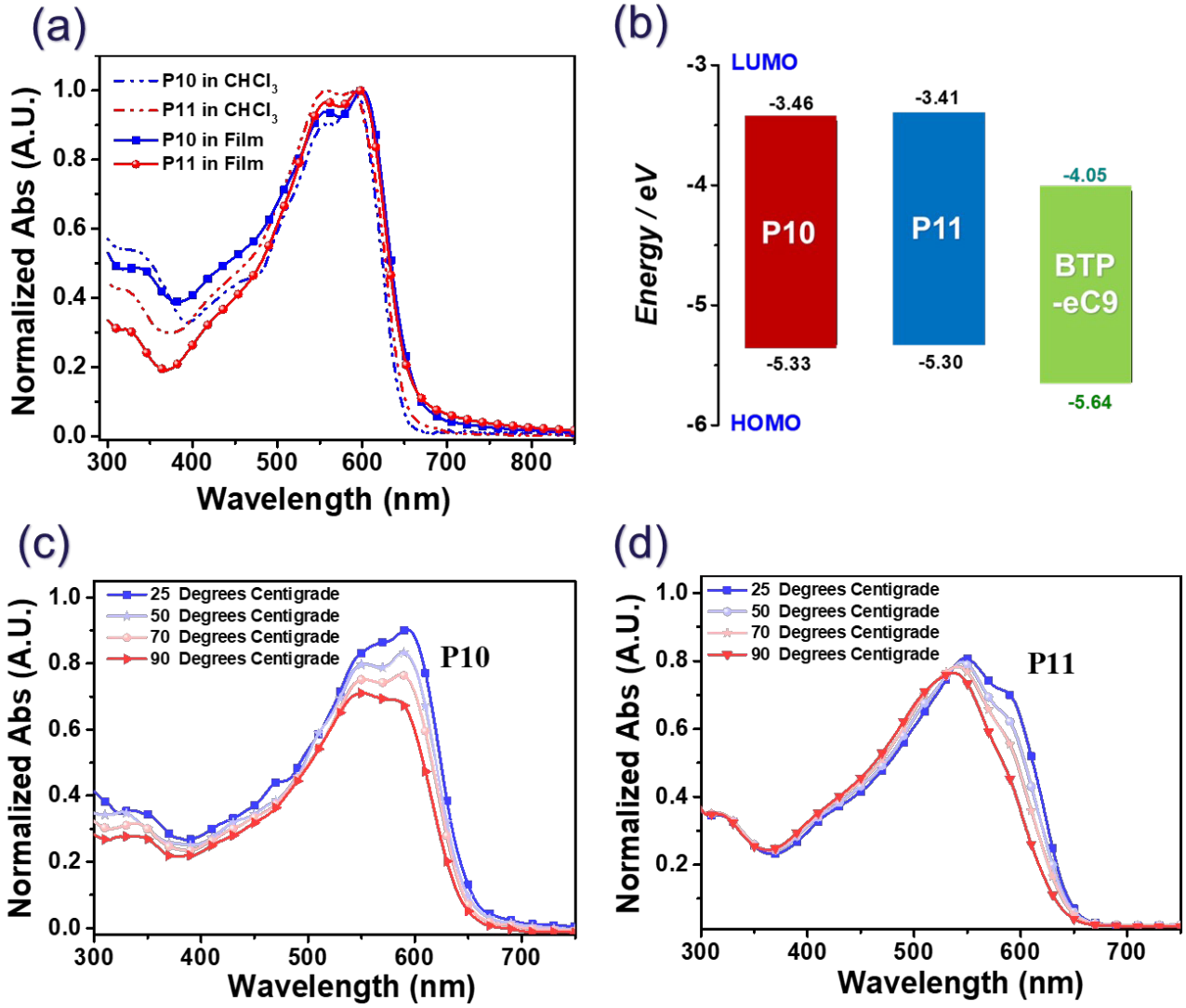

Figure 1. (a) Normalized UV-vis absorption spectra of two copolymers (P10 and P11) in CF and in film, respectively; (b) HOMO/LUMO energy levels schematic of copolymers and acceptor; Temperature dependent UV-vis absorption curves of (c) P10 and (d) P11 in Chlorobenzene.

Electrochemical Properties

To investigate the energy levels of the highest occupied molecular orbital (HOMO) of the two copolymers, the thin-film's electrochemical characteristics of P10 and P11 were studied by means of cyclic voltammetry (CV, **Figure S5a**) as detail-instructed in the **ESI**. The energy alignment of HOMO/LUMO levels of copolymers and SM-acceptor were illustrated in **Figure 1b** and with their optical band gaps listed together in **Table 1**. The onset oxidation potentials (E_{OX}) of P10 and P11 were 0.88 and 0.85 V, which corresponding to HOMO levels of -5.33 and -5.30 eV, respectively. The HOMO of P10 was ~0.03 eV deeper than P11, indicating that alkylthio-phenyl side chains had a more

View Article Online
DOI: 10.1039/D2CP05414K

electron-drawing effect than alkoxy-phenyl substituents for BDT-based copolymer. Thence, P10-based PSC device with lower lying HOMO energy level was expected to achieve higher V_{OC}. Because sulfur atom has an empty *d* orbital, it could generate π electron-withdrawing effect when coupling with phenyl (at the benzyl position), which is at the same time in accordance with its greater electronegativity of the sulfur atom than that of carbon, which induces σ electron-withdrawing effect. While alkoxy chain always pronounces stronger p-π conjugation electron-donating effect than its induced σ electron-withdrawing one, resulting relative less deep HOMO levels. Compared with the analogous copolymers with thienyl flanking,[33,37,47] copolymers with phenyl side chains reveal deeper HOMOs. Besides, the energy levels of lowest unoccupied molecular orbital (LUMO) of two copolymers were determined from the difference of E_{HOMO} and E_g^{opt}, which were found as -3.46 eV for P10 and -3.41 eV for P11, respectively. The LUMOs of P10, comparing with P11, was closer energetic proximity and higher-lying than that of the acceptor molecule BTP-eC9 (ca. -4.05 eV).[9] Thus, the higher efficient exciton dissociation could be expected in corresponding P10-based OPV devices than P11-based ones.

Molecular Simulations

To further investigate the structure-property difference between P10 and P11, density-functional theory (DFT) calculations on the dimer of two copolymers were performed by using Gaussian 16 program with B3LYP functional at the 6-31G(d,p) basis set level in the gas phase. For easing the computational load of server, all the 2-octyldodecyl side chains were substituted by the methylthiol and methyl groups for P10 and P11, respectively. As shown in Figure 2, the simulation results demonstrated that the LUMO of P10 and P11 centralized mainly on tt-TPD moieties, while the HOMOs were evenly distributed along the whole molecular π-conjugation backbone. Being different from BDTT-based copolymers,[37] there was little delocalization for the wave function on their phenyl flanking, which implied that it was little attribution to phenyl side chains to form the 2D π-conjugated structure. Due to the intense intramolecular repulsion among side-phenyl and benzodithiophene moieties, a large torsion angle (ca. ~58°) was formed between phenyl side chains and benzodithiophene moieties to hinder the expansion of π-conjugation on vertical orientation of polymer backbone. Despite the interference of electron-donating capabilities of alkoxy side chains, our structural modification still succeeded in deepening the HOMO/LUMO energy levels as expected. Dihedral angles were obtained from the optimal structure by the DFT and recorded in the **Table S1**. Those among BDT, tt π-bridge, and TPD motifs (A1 to A6) in ranges of from 0.01 to max 6.59 ° for P10 and max 5.89 ° for P11 evident their nice planarity along backbone, while much larger dihedral

View Article Online
DOI: 10.1039/D2CP05414K

angles like 58 or 59 ° between alkylthiol- or alkoxy-phenyl moieties with BDT units for both P10 and P11 confesses twisted and certain coil-like polymer conformation as a result of enhanced torsional relaxation along the backbone.[48] This can, to some extent, be indicated by the non-visible bathochromic shifts on the absorption maxima between the solutions and films for either P10 or P11 as already discussed above. This is furthermore expected to have a negative influence on the band gap properties, as the spatial steric effect will affect the π-π stacking. It is important to mention that all side-chain substituents were replaced with a methylthiol group in order to simplify the calculations; nevertheless, the side chains typically play an important role in modeling torsion angels of conjugated polymers.[49] Herein we used the same simplified side group for both moieties of alkylthiolated or alkoxylated-phenyl substituted BDT and tt-TPD, therefore the results regarding to the torsion angles between BDT and tt-TPD should be reasonable. When observing the orbital distribution (**Figure 2**), it non-surprisingly becomes evident that HOMO covers more in the BDT donor units while LUMO occupies more in tt-TPD acceptor motifs, strongly evidencing the synergetic effect of weak electron-pushing and -accepting capability by the 3d-orbitals of sulfur element on simultaneously lowering HOMO/LUMO level of P10 comparing to P11, which leads to high V_{OC} of 0.89 V (presented below) for solar cells made from P10.

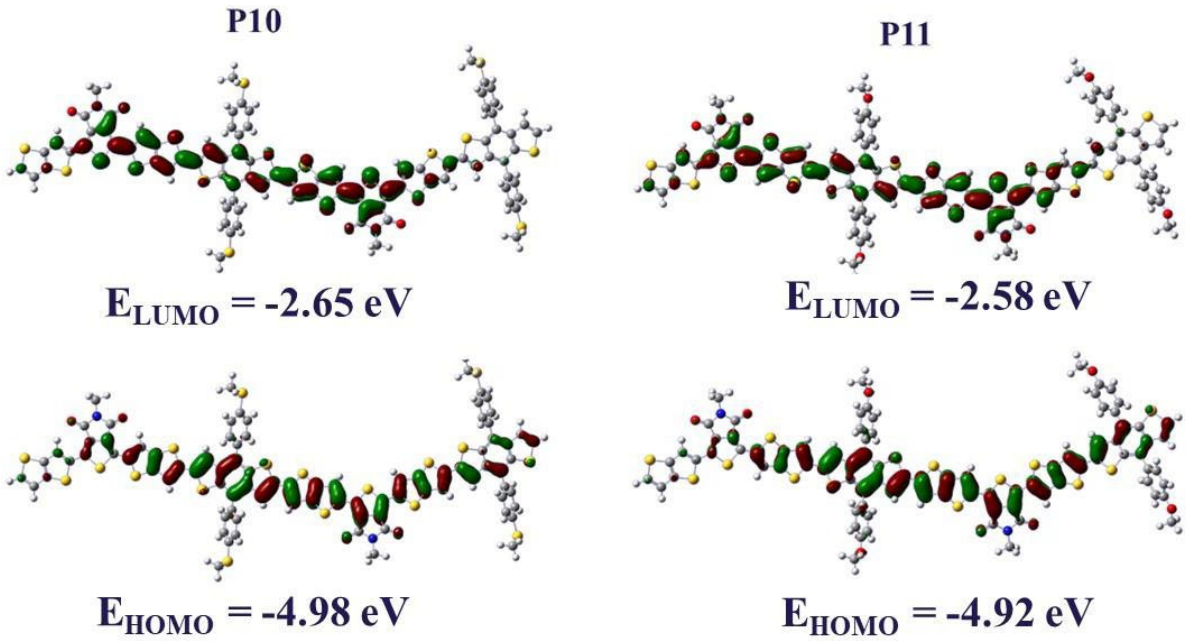

Figure 2. The calculated electron distributions at HOMO/LUMO orbitals of P10 and P11, performed at the level of B3LYP/6-31G(*d*, *p*) based on density functional theory (DFT).

View Article Online
DOI: 10.1039/D2CP05414K

Photovoltaic Performance of SM NFA-Based Solar Cells

To characterize the photovoltaic properties of two copolymers paired with small molecule non-fullerene acceptor (SM-NFA) for organic solar cells with an active area of 0.04 cm^2 were fabricated as detailly described in the **ESI**, with their corresponding current density-voltage (*J-V*) curves presented in **Figure 3a**. The device configuration was designed as ITO/PEDOT:PSS /polymer:BTP-eC9/PFN-Br/Ag, where ITO is indium tin oxide as the anode, PEDOT:PSS is poly(3,4-ethylenedioxythiophene):polystyrene sulfonate as the hole transport layer (HTL), PFN-Br as the electron transport layer (ETL) is poly(9,9-bis(3'-(N,N-dimethyl)-N-ethylammoinium-propyl-2,7-fluorene)-alt-2,7-(9,9-dioctylfluorene))-dibromide, Ag is silver as the cathode, and the active layer is the bulk-heterojunction structure of donor and acceptor with the thickness of 100 nm. In this work, the optimized photovoltaic performance of OPV devices were focused on varying donor/acceptor (D/A) ratios and different contents of DIO as the additive in the active layer. as listed in **Table S2** and **S3**, with D/A weight ratios of 1:1 (w/w) obtained as the optimized one. For P10, both J_{SC} and V_{OC} are persistent regarding less varying D/A ratio from 1:1 to 1:1.5, while FF decreased from 55.9% to 52.4% As for P11, it is the J_{SC} that claims relative larger D/A dependency, resulting to significant power conversion efficiency (PCE) drops from 8.40 to 8.05%. 1,8-Diiodooctane (DIO), as the additive, was adjusted with different volume ratios (*Vol* %) to solutions to optimize the morphology of the bulk-heterojunction BHJ based OSCs, as illustrated in **Table S3**. For P10-based and P11-based conventional devices, the content of DIO were adjusted from 0 to 0.5% and 0 to 1.0%, respectively, the most optimal dosage of DIO were found as 0.3% for P10 and 0.7% for P11, respectively. Shown in **Table 2 and S3**, the former reached both the highest FF of 63.81% and J_{SC} of 22.71 $mA \cdot cm^{-2}$, with its final highest PCE of 12.93% obtained. On the contrary, distinguished from highly DIO-sensitive D-A system of P10, the latter P11 reached the most optimal FF of 54.07% and J_{SC} of 19.96 $mA \cdot cm^{-2}$, gaining its hero PCE of 9.37% . The best performance for P10 (no DIO, see **Table S2**) was obtained with a V_{OC} of 0.89 V, a J_{SC} of 23.00 $mA \cdot cm^{-2}$, and an FF of 57.33%, affording the PCE of 11.75%. The increasement of experimental V_{OC} (~0.02 V) caused by alkylthio-phenyl flanking for P10 than P11 with alkoxy-phenyl side chain was consistent with the predicted results of the HOMOs difference. Comparing with PM6/BTP-eC9-based PSCs, the P10 showed the highest V_{OC} while maintaining a reasonably good J_{SC}.[9] In general cases, high V_{OC} and strong J_{SC} are always contradictory for OPV devices, which must be acceptable when considering the needs of either deepening the HOMO of donors and/or lifting the LUMO level of the acceptors. But the former will enlarge polymer's band gap energy, and the latter would result in loss of electron separation from donor to the acceptor, which

View Article Online
DOI: 10.1039/D2CP05414K

both are limiting the generation of J_{SC}. Therefore, when reading the J_{SC} values of 22.71 and 19,96 mA·cm^{-2} for P10 and P11 respectively (corresponding to their V_{OC} s), relative synergistical effect on high V_{OC} and strong J_{SC} was successfully gained via incorporating alkylthiolation instead of oxlyation on the thiophenyl sidechains. Furthermore, the external quantum efficiency (EQE, **Figure 3b**) curves under optimal conditions indicated that the integrated J_{SC} was calculated of 22.34 mA·cm^{-2} for P10 and 19.41 mA·cm^{-2} for P11, with calculated J_{SC} shown in Table 2. We can see that ca. 5% differences between the measured- and calculated- J_{SC} s are pronounced, which can be caused by two reasons: a.) the imperfect control of direction of incident light or beam-coverage on the supposed active areas; b.) non-ideal device stability when I-V and EQE measurements were performed in different days. These explanations are now added to the discussion of the PV performance part in our revised manuscript (red-highlighted). The former P10 based device showed a little higher EQE value in a much broader range (300-1000 nm) than latter one (P11). Besides, the middle wavelength (450-800 nm) confirmed that the excitons generated by the P10 domains were more efficiently separated at the P10/BTP-eC9 interfaces, and the holes are effectively collected through the BTP-eC9 domains.

Besides these, for better comparison, ITIC was used as the alternative electron acceptor for copolymers photovoltaic devices, with their performance shown in Figure S4 and data listed in **Table S4**, the simple optimization of P10- and P11-based devices had already reach to the average PCE of the structurally similar NFA photovoltaic modules.[47] Noticeably, high V_{OC} values of 1.04 and 1.00 V for P10- and P11-based PSCs were, which was non-surprisingly higher than the BTP-eC9-based OPVs, due to the higher LUMO level of ITIC than that of BTP-eC9. However, the slightly higher (4%) V_{OC} for P10:ITIC based device than that for P11 based on lies in a good agreement with their photovoltaic performance with BTP-eC9 paired OSCs, proving the same improvement of alkythiolation compared to alkoxy substitution on phenyl side chains of BDT.

Moreover, J_{SC} is affected by not only the optical absorption but also many other physical aspects such as charge carrier mobility, crystallinity, and morphology of the active layer. As shown in **Figure 3c**, the carrier mobilities were studied by space-charge-limited current (SCLC) method as detailed instructions in **ESI** and calculated from the linear fitting results in **Figure S7**, with their hole mobility found as 3.30×10^{-4} cm^2 V^{-1} s^{-1} for P10-based OPVs and 3.10×10^{-4} cm^2 V^{-1} s^{-1} for P11-based OPVs, respectively. While their electron mobility were obtained as 2.50×10^{-4} cm^2 V^{-1} s^{-1} for P10 and 1.71×10^{-4} cm^2 V^{-1} s^{-1} for P11, respectively. It can be seen that the higher and more balanced hole and electron mobilities (μ_h/μ_e) could facilitate enhanced J_{SC} and FF for the corresponding P10/BTP-eC9 cells (than P11 based cells) as mentioned above, which is caused by the alkylthiolation on its phenyl

View Article Online
DOI: 10.1039/D2CP05414K

unit. Such improved mobility can be attributed to its both previously discussed better co-planarity and π-π stacking, which can be furthermore reflected by the X-ray diffraction studies on them below-introduced. The charge recombination abilities were characterized following the described instructions in **ESI**, and the charge dissociation abilities (P_{diss}) of two NFA-based PSCs (see **Figure 3f**) were listed in the **Table 3** together with their charge carrier mobilities. Obviously, the P10-based device performed better charge carrier mobility and charge dissociation ability comparing with P11-based device, which afforded a higher J_{SC}. Furthermore, the function diagrams of the light intensity against J_{SC} and V_{OC} in two SM-NFA PSCs were presented of in **Figure 3d and 3e**, which could be used to describe the biomolecular recombination process inside the devices (see **ESI** for more details). P10-baesd devices pronounce its α value of 1.01 and slope of 1.24 *KT/q*, while P11-based devices reveal with α value of 0.98 and slope of 1.08 *KT/q*, indicating that little trap-assisted recombination was in two kinds of devices and the bimolecular recombination also could nearly be ignored.

In the meantime, considering that either energy- or voltage-loss ($E_{loss} = E_g - qV_{oc}$, $V_{loss} = E_g/q - V_{oc}$, q is the elemental charge) is indispensable for OSCs,[50–53] we confirmed Vlosss of 0.89V and 1.02V, corresponding to energy loss of 0.89 eV and 1.02 eV, for P10 and P11, respectively, which are far higher than those of 0.60 eV as energy loss described by Janssen *et al.* ,[54] suggesting plenty of room for further perceptive improvement on such molecular design for pairing this BTP-eC9 acceptor. We may also reasonably suspect that such big losses could be mainly caused by the radiative- and nonradiative-recombination of both P10 and P11, which is obviously much less pronounced for thioalkylated P10 than oxylated P11, leading to better PV performance as just above-discussed.

Meanwhile, the surface morphology of D-A blending thin films was characterized by utilized the means of atomic force microscopy (AFM) (**Figure S6**). The desirable root-mean-square (RMS) roughness values of 1.15 nm for P10:BTP-eC9 and 1.18 nm for P11:BTP-eC9 blending thin film, respectively, show in general low surfaces roughness. While P10 somehow exhibits small aggregates sizing in nanometer scale, proving that the phase separation of P10-based active layer was better than P11 in microscopic scale. In addition, to distinguish molecular crystallization, arranged orientation and π-stacking of these copolymers in their thin films (w/o BTP-eC9), grazing-incidence wide-angle X-ray scattering (GIWAXS) was applied. As shown in **Figure 4a**, P10 and P10:BTP-eC9 both preferentially formed face-on orientation, and obviously the blending thin films exhibited enhanced rigid conjugated backbone in higher degree of polymerization which induced the closer π-π stacking structure. Interestingly, when P11 was blended with BTP-eC9, the random arrangement of polymer

View Article Online
DOI: 10.1039/D2CP05414K

backbone turned to face on orientation immediately. The size of π-stacking polymer backbone region (q_z) indicated that the P11 only thin film demonstrated a loose copolymer backbone and far intermolecular distance. Nonetheless, the blending thin films were the same crystalline degree at the side chain stacking direction. The out-of-plane and in-plane cut pattern of all films were presented in the **Figure 4c**, a (010) diffraction peak along the q_z axis of 1.83, 1.76, 1.93 and 1.83 Å^{-1} for P10, P11, P10/BTP-eC9 and P11/BTP-eC9, respectively, which correspond to the d-spacing of 3.43, 3.58, 3.25 and 3.44 Å, respectively. This result revealed that BHJ films were induced the enhancement of π-π stacking along the polymer backbone after blending with acceptor molecule. Besides, in same figure there was an emerging signal of P10/BTP-eC9 at 1.54 Å^{-1}, corresponding to the d-spacing of 4.06 Å, which belonged to the π-stacking self-aggregation of acceptor molecules. It implied that the P10/BTP-eC9 blending BHJ films contained the obvious D-A phase separation. It was notably to discuss in **Figure 4b** that the diffraction peaks along the q_{xy} axis (next to the (100)) of all films demonstrated that the P10/BTP-eC9 emerged novel and closer ordered lamellar packing of side chains between different phase in thin films.

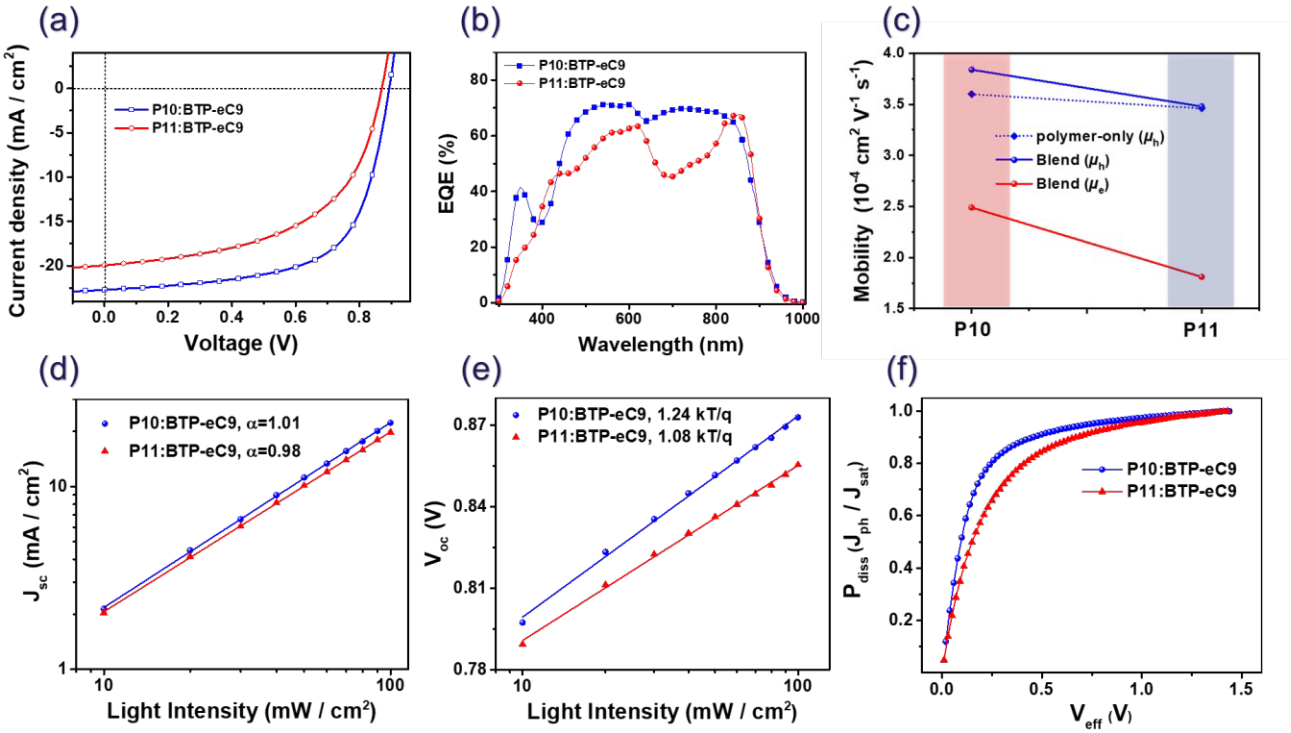

Figure 3. The (a) *J-V* characteristics and (b) external quantum efficiency curves of P10:BTP-eC9 and P11:BTP-eC9; (c) the carrier mobility in polymer-only and Polymers:BTP-eC9 blends films by the SCLC method; dependence diagram of J_{SC} (d) and V_{OC} (e) as a function of light intensity based on polymers:BTP-

View Article Online
DOI: 10.1039/D2CP05414K

eC9 devices; and (f) charge dissociation probabilities (P_{diss}) vs effective voltage (V_{eff}) of NFA-based OPVs.

Table 2. Performance of NFA-based polymer solar cells.

Polymer:BTP-eC9	DIO (vol%)	FF (%)	V_{OC} (V)	J_{SC} / J_{SC} [b] (mA cm^{-2})	PCE (%) Best/Ave [a]
PBDT-PS-ttTPD	0.3	63.81	0.89	22.71/22.34 [b]	12.93/12.24 ± 0.68 [a]
PBDT-PO-ttTPD	0.7	54.07	0.87	19.96/19.41 [b]	9.37/9.04 ± 0.34[a]

[a] Average PCE is calculated from 12 parallel devices. [b] Integrated by EQE.

Table 3. Charge mobility and dissociation properties of polymer-only and NFA-based OPVs

Items	μ_h (10^{-4} cm^2 V^{-1} s^{-1})	μ_e (10^{-4} cm^2 V^{-1} s^{-1})	μ_h/μ_e	P_{diss} [a]
P10:BTP-eC9	3.60 (3.84 [b])	2.49	1.32	0.97
P11:BTP-eC9	3.46 (3.48 [b])	1.81	1.71	0.95

[a] The charge dissociation probability (P_{diss}) is described by $P_{diss} = J_{ph}/J_{sat}$; [b] The hole mobilities of polymers-only devices and the corresponding $J^{0.5}$-V plots were present in ESI.

View Article Online
DOI: 10.1039/D2CP05414K

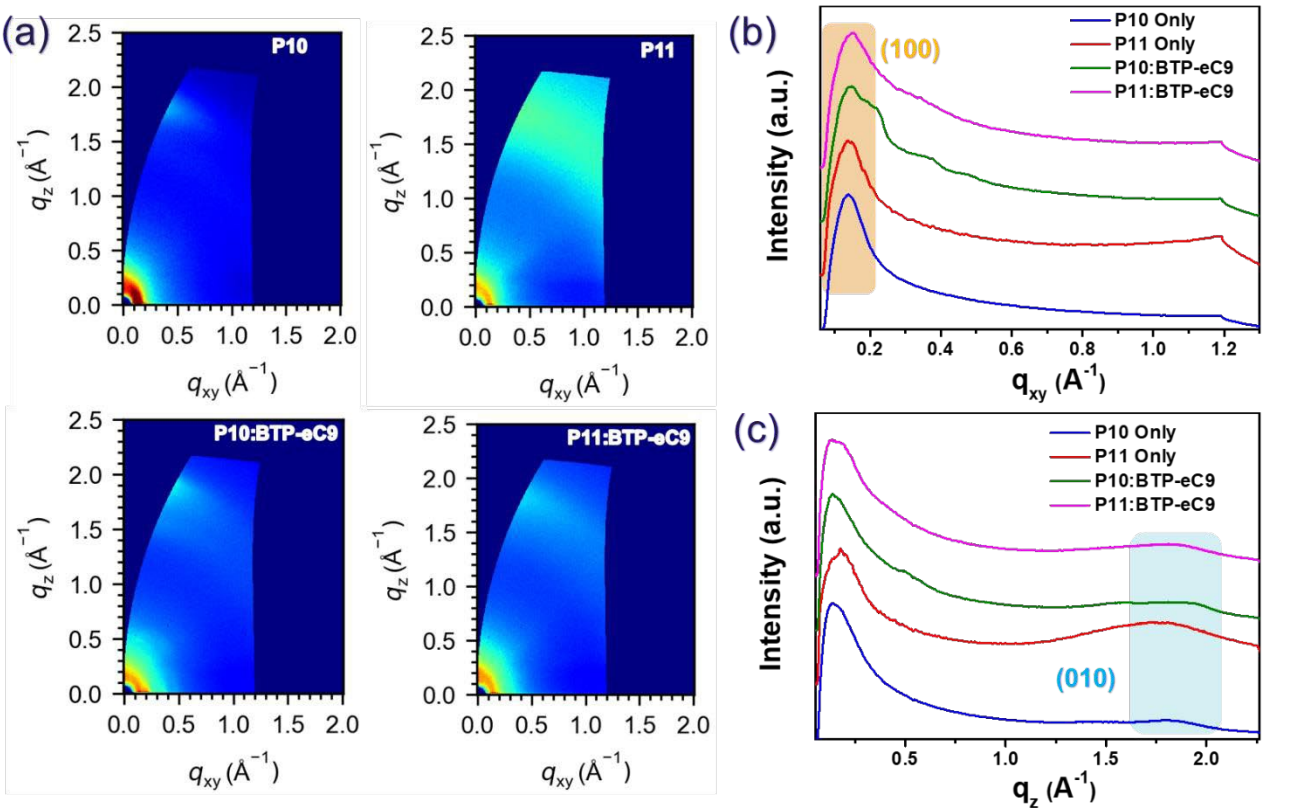

Figure 4. (a) Grazing incident wide-angle X-ray scattering (GI-WAXS) patterns of P10 , P11, P10/BTP-eC9 (1:1,w/w) and P11/BTP-eC9 (1:1,w/w), corresponding out-of-plane direction and in- plane direction as shown in (b) and (c).

Conclusion

In summary, two new benzo[1,2-*b*:4,5-*b*'] dithiophene based donor-acceptor copolymers, deriving from alkylthio- (for PBDT-PS-ttTPD) and alkoxy-phenyl (for PBDT-PO-ttTPD) flanked benzo[1,2-b:4,5-b']-dithiophene and 5-(2-hexyldecyl)-4H-thieno[3,4-c]pyrrole-4,6(5H)-dione units with π-bridge of thieno[3,2-b]thiophene were successfully designed, synthesized, and applied in SM-NFA PSCs. Well-followed our design idea, the alkylthio- and alkoxy-phenyl flanking substituted BDT-containing polymers present deeper HOMOs (-5.33 and -5.30 eV) in relation to the LUMO level of BTP-eC9, therefore both wide bandgap copolymers:BTP-eC9 based OSCs show excellent voltage output with their V_{OC} of 0.89 and 0.87V, respectively, which is attractively higher than that of PM6 based donor polymers when pairing with one of such state-of-art BTP-eC9 acceptor in single-heterojunction devices. Finally, their reasonably nice PCE of 12.93% and 9.37%, with J_{SC} of 22.71 mA cm^{-2} and 19.96 mA cm^{-2}, and FF of 63.81% and 54.07%, were achieved, respectively. Thus, we

View Article Online
DOI: 10.1039/D2CP05414K

develop two new and promising BDTP-PS-TPD- and BDTP-PO-TPD-based electron donors containing thieno[3,2-b]thiophene as π-bridge for constructing high efficiency photovoltaic materials for paring Y-series of state-of-art acceptors.

Conflicts of interest

There are no conflicts to declare.

Acknowledgements

This work received a financial support from China Scholarship Council (CSC No. 201908510136). The authors also thank Beijing Synchrotron Radiation Facility (BSRF) 1W1A for 2D GIWAXS measurements. Support from Sino-Danish Center (SDC) for Education and Research is fully acknowledged.

Reference

1 Y. Lin, J. Wang, Z. G. Zhang, H. Bai, Y. Li, D. Zhu and X. Zhan, An electron acceptor challenging fullerenes for efficient polymer solar cells, *Advanced Materials*, 2015, **27**, 1170–1174.

2 W. Zhao, D. Qian, S. Zhang, S. Li, O. Inganäs, F. Gao and J. Hou, Fullerene-Free Polymer Solar Cells with over 11% Efficiency and Excellent Thermal Stability, *Advanced Materials*, 2016, **28**, 4734–4739.

3 J. Yuan, Y. Zhang, L. Zhou, G. Zhang, H. L. Yip, T. K. Lau, X. Lu, C. Zhu, H. Peng, P. A. Johnson, M. Leclerc, Y. Cao, J. Ulanski, Y. Li and Y. Zou, Single-Junction Organic Solar Cell with over 15% Efficiency Using Fused-Ring Acceptor with Electron-Deficient Core, *Joule*, 2019, **3**, 1140–1151.

4 J. Yuan and Y. Zou, The history and development of Y6, *Org Electron*, 2022, **102**, 106436.

5 L. Zhu, M. Zhang, J. Xu, C. Li, J. Yan, G. Zhou, W. Zhong, T. Hao, J. Song, X. Xue, Z. Zhou, R. Zeng, H. Zhu, C. C. Chen, R. C. I. MacKenzie, Y. Zou, J. Nelson, Y. Zhang, Y. Sun and F. Liu, Single-junction organic solar cells with over 19% efficiency enabled by a refined double-fibril network morphology, *Nat Mater*, 2022, **21**, 656–663.

6 Y. Cui, Y. Xu, H. Yao, P. Bi, L. Hong, J. Zhang, Y. Zu, T. Zhang, J. Qin, J. Ren, Z. Chen, C. He, X. Hao, Z. Wei and J. Hou, Single-Junction Organic Photovoltaic Cell with 19% Efficiency, *Advanced Materials*, 2021, **33**, 2102420.

7 L. Zhan, S. Li, Y. Li, R. Sun, J. Min, Z. Bi, W. Ma, Z. Chen, G. Zhou, H. Zhu, M. Shi, L. Zuo and H. Chen, Desired open-circuit voltage increase enables efficiencies approaching 19% in symmetric-asymmetric molecule ternary organic photovoltaics, *Joule*, 2022, **6**, 662–675.

8 Y. Lin, Y. Firdaus, F. H. Isikgor, M. I. Nugraha, E. Yengel, G. T. Harrison, R. Hallani, A. El-Labban, H. Faber, C. Ma, X. Zheng, A. Subbiah, C. T. Howells, O. M. Bakr, I. McCulloch, S. de Wolf, L. Tsetseris and T. D. Anthopoulos, Self-assembled monolayer enables hole transport layer-free organic solar cells with 18% efficiency and improved operational stability, *ACS Energy Lett*, 2020, **5**, 2935–2944.

View Article Online
DOI: 10.1039/D2CP05414K

9 Y. Cui, H. Yao, J. Zhang, K. Xian, T. Zhang, L. Hong, Y. Wang, Y. Xu, K. Ma, C. An, C. He, Z. Wei, F. Gao and J. Hou, Single-Junction Organic Photovoltaic Cells with Approaching 18% Efficiency, *Advanced Materials*, 2020, **32**, 1908205.

10 X. Dong, Y. Jiang, L. Sun, F. Qin, X. Zhou, X. Lu, W. Wang and Y. Zhou, Large-Area Organic Solar Modules with Efficiency Over 14%, *Adv Funct Mater*, 2022, **32**, 2110209.

11 Y. Cai, Y. Li, R. Wang, H. Wu, Z. Chen, J. Zhang, Z. Ma, X. Hao, Y. Zhao, C. Zhang, F. Huang and Y. Sun, A Well-Mixed Phase Formed by Two Compatible Non-Fullerene Acceptors Enables Ternary Organic Solar Cells with Efficiency over 18.6%, *Advanced Materials*, 2021, **33**, 2101733.

12 C. Li, J. Zhou, J. Song, J. Xu, H. Zhang, X. Zhang, J. Guo, L. Zhu, D. Wei, G. Han, J. Min, Y. Zhang, Z. Xie, Y. Yi, H. Yan, F. Gao, F. Liu and Y. Sun, Non-fullerene acceptors with branched side chains and improved molecular packing to exceed 18% efficiency in organic solar cells, *Nat Energy*, 2021, **6**, 605–613.

13 Y. Li, Y. Guo, Z. Chen, L. Zhan, C. He, Z. Bi, N. Yao, S. Li, G. Zhou, Y. Yi, Y. M. Yang, H. Zhu, W. Ma, F. Gao, F. Zhang, L. Zuo and H. Chen, Mechanism study on organic ternary photovoltaics with 18.3% certified efficiency: From molecule to device, *Energy Environ Sci*, 2022, **15**, 855–865.

14 Y. Qin, Y. Chang, X. Zhu, X. Gu, L. Guo, Y. Zhang, Q. Wang, J. Zhang, X. Zhang, X. Liu, K. Lu, E. Zhou, Z. Wei and X. Sun, 18.4% efficiency achieved by the cathode interface engineering in non-fullerene polymer solar cells, *Nano Today*, 2021, **41**, 101289.

15 C. Yan, J. Yu, Y. Li, P. W. K. Fong, R. Ding, K. Liu, H. Xia, Z. Ren, X. Lu, J. Hao and G. Li, Ambipolar-transport wide-bandgap perovskite interlayer for organic photovoltaics with over 18% efficiency, *Matter*, 2022, **5**, 2238–2250.

16 T. Zhang, C. An, P. Bi, Q. Lv, J. Qin, L. Hong, Y. Cui, S. Zhang and J. Hou, A Thiadiazole-Based Conjugated Polymer with Ultradeep HOMO Level and Strong Electroluminescence Enables 18.6% Efficiency in Organic Solar Cell, *Adv Energy Mater*, 2021, **11**, 2101705.

17 J. Han, H. Xu, S. H. K. Paleti, Y. Wen, J. Wang, Y. Wu, F. Bao, C. Yang, X. Li, X. Jian, J. Wang, S. Karuthedath, J. Gorenflot, F. Laquai, D. Baran and X. Bao, Vertical Stratification Engineering of Insulating Poly(aryl ether)s Enables 18.6% Organic Solar Cells with Improved Stability, *ACS Energy Lett*, 2022, **7**, 2927–2936.

18 X. Duan, W. Song, J. Qiao, X. Li, Y. Cai, H. Wu, J. Zhang, X. Hao, Z. Tang, Z. Ge, F. Huang and Y. Sun, Ternary strategy enabling high-efficiency rigid and flexible organic solar cells with reduced non-radiative voltage loss, *Energy Environ Sci*, 2022, **15**, 1563–1572.

19 X. Xu, H. Wu, S. Liang, Z. Tang, M. Li, J. Wang, X. Wang, J. Wen, E. Zhou, W. Li and Z. Ma, Quantum Efficiency and Voltage Losses in P3HT:Non-fullerene Solar Cells, *Wuli Huaxue Xuebao/ Acta Physico - Chimica Sinica*, 2022, **38**, 2201039.

20 A. Tang, B. Xiao, Y. Wang, F. Gao, K. Tajima, H. Bin, Z. G. Zhang, Y. Li, Z. Wei and E. Zhou, Simultaneously Achieved High Open-Circuit Voltage and Efficient Charge Generation by Fine-Tuning Charge-Transfer Driving Force in Nonfullerene Polymer Solar Cells, *Adv Funct Mater*, 2018, **28**, 1704507.

21 P. Cheng, X. Zhao and X. Zhan, Perylene Diimide-Based Oligomers and Polymers for Organic Optoelectronics, *Acc Mater Res*, 2022, **3**, 309–318.

View Article Online
DOI: 10.1039/D2CP05414K

22 P. Cheng, G. Li, X. Zhan and Y. Yang, Next-generation organic photovoltaics based on non-fullerene acceptors, *Nat Photonics*, 2018, **12**, 131–142.

23 S. Guo, Y. Hu, M. Qin, J. Li, Y. Wang, J. Qin and P. Cheng, Toward high-performance organic photovoltaics: the new cooperation of sequential solution-processing and promising non-fullerene acceptors, *Mater Horiz*, 2022, **9**, 2097–2108.

24 C. Yan, J. Qin, Y. Wang, G. Li and P. Cheng, Emerging Strategies toward Mechanically Robust Organic Photovoltaics: Focus on Active Layer, *Adv Energy Mater*, 2022, **12**, 2201087.

25 Y. J. Cheng, J. Luo, S. Huang, X. Zhou, Z. Shi, T. D. Kim, D. H. Bale, S. Takahashi, A. Yick, B. M. Polishak, S. H. Jang, L. R. Dalton, P. J. Reid, W. H. Steier and A. K. Y. Jen, Donor - Acceptor thiolated polyenic chromophores exhibiting large optical nonlinearity and excellent photostability, *Chemistry of Materials*, 2008, **20**, 5047–5054.

26 J. Hou, B. Fan, L. Huo, H. E. Chang, C. Yang and Y. Li, Poly(alkylthio-p-phenylenevinylene): Synthesis and electroluminescent and photovoltaic properties, *J Polym Sci A Polym Chem*, 2006, **44**, 1279–1290.

27 D. Lee, S. W. Stone and J. P. Ferraris, A novel dialkylthio benzo[1,2-b:4,5-b′]dithiophene derivative for high open-circuit voltage in polymer solar cells, *Chemical Communications*, 2011, **47**, 10987–10989.

28 D. Lee, E. Hubijar, G. J. D. Kalaw and J. P. Ferraris, Enhanced and tunable open-circuit voltage using dialkylthio benzo[1,2-b:4,5-b′]dithiophene in polymer solar cells, *Chemistry of Materials*, 2012, **24**, 2534–2540.

29 C. Cui, W. Y. Wong and Y. Li, Improvement of open-circuit voltage and photovoltaic properties of 2D-conjugated polymers by alkylthio substitution, *Energy Environ Sci*, 2014, **7**, 2276–2284.

30 W. T. Hadmojo, F. T. A. Wibowo, D. Y. Ryu, I. H. Jung and S. Y. Jang, Fullerene-Free Organic Solar Cells with an Efficiency of 10.2% and an Energy Loss of 0.59 eV Based on a Thieno[3,4-c]Pyrrole-4,6-dione-Containing Wide Band Gap Polymer Donor, *ACS Appl Mater Interfaces*, 2017, **9**, 32939–32945.

31 C. Y. Liao, Y. Chen, C. C. Lee, G. Wang, N. W. Teng, C. H. Lee, W. L. Li, Y. K. Chen, C. H. Li, H. L. Ho, P. H. S. Tan, B. Wang, Y. C. Huang, R. M. Young, M. R. Wasielewski, T. J. Marks, Y. M. Chang and A. Facchetti, Processing Strategies for an Organic Photovoltaic Module with over 10% Efficiency, *Joule*, 2020, **4**, 189–206.

32 J. M. Jiang, P. Raghunath, Y. C. Lin, H. K. Lin, C. L. Ko, Y. W. Su, M. C. Lin and K. H. Wei, Linear solubilizing side chain substituents enhance the photovoltaic properties of two-dimensional conjugated benzodithiophene-based polymers, *Polymer (Guildf)*, 2015, **79**, 262–270.

33 L. Dou, J. Gao, E. Richard, J. You, C. C. Chen, K. C. Cha, Y. He, G. Li and Y. Yang, Systematic investigation of benzodithiophene- and diketopyrrolopyrrole- based low-bandgap polymers designed for single junction and tandem polymer solar cells, *J Am Chem Soc*, 2012, **134**, 10071–10079.

34 J. Yuan, L. Xiao, B. Liu, Y. Li, Y. He, C. Pan and Y. Zou, New alkoxylphenyl substituted benzo[1,2-b:4,5-b′] dithiophene-based polymers: Synthesis and application in solar cells, *J Mater Chem A Mater*, 2013, **1**, 10639–10645.

View Article Online
DOI: 10.1039/D2CP05414K

35 M. Fan, Z. Du, W. Chen, D. Liu, S. Wen, M. Sun and R. Yang, Benzodithiophene-Based Polymers Containing Alkylthiophenyl Side Chains with Lowered HOMO Energy Levels for Organic Solar Cells, *Asian J Org Chem*, 2016, **5**, 1273–1279.

36 W. Chen, G. Huang, X. Li, H. Wang, Y. Li, H. Jiang, N. Zheng and R. Yang, Side-Chain-Promoted Benzodithiophene-based Conjugated Polymers toward Striking Enhancement of Photovoltaic Properties for Polymer Solar Cells, *ACS Appl Mater Interfaces*, 2018, **10**, 42747–42755.

37 J. H. Kim, J. B. Park, F. Xu, D. Kim, J. Kwak, A. C. Grimsdale and D. H. Hwang, Effect of π-conjugated bridges of TPD-based medium bandgap conjugated copolymers for efficient tandem organic photovoltaic cells, *Energy Environ Sci*, 2014, **7**, 4118–4131.

38 J. Yuan, Z. Zhai, H. Dong, J. Li, Z. Jiang, Y. Li and W. Ma, Efficient polymer solar cells with a high open circuit voltage of 1 volt, *Adv Funct Mater*, 2013, **23**, 885–892.

39 W. Yue, X. Huang, J. Yuan, W. Ma, F. C. Krebs and D. Yu, A novel benzodipyrrolidone-based low band gap polymer for organic solar cells, *J Mater Chem A Mater*, 2013, **1**, 10116–10119.

40 Y. Liu, J. Zhao, Z. Li, C. Mu, W. Ma, H. Hu, K. Jiang, H. Lin, H. Ade and H. Yan, Aggregation and morphology control enables multiple cases of high-efficiency polymer solar cells, *Nat Commun*, 2014, **5**, 5293.

41 J. Wang, M. Xiao, W. Chen, M. Qiu, Z. Du, W. Zhu, S. Wen, N. Wang and R. Yang, Extending π-conjugation system with benzene: An effective method to improve the properties of benzodithiophene-based polymer for highly efficient organic solar cells, *Macromolecules*, 2014, **47**, 7823–7830.

42 H. Wang, H. Lu, Y. N. Chen, A. Zhang, Y. Liu, D. Li, Y. Liu, X. Xu and Z. Bo, A Versatile Planar Building Block with C2V Symmetry for High-Performance Non-Halogenated Solvent Processable Polymer Donors, *Adv Energy Mater*, 2022, **12**, 2104028.

43 A. D. Buckingham, CHEMICAL SHIFTS IN THE NUCLEAR MAGNETIC RESONANCE SPECTRA OF MOLECULES CONTAINING POLAR GROUPS, *Can J Chem*, 1960, **38**, 300–307.

44 K. BOCK and J. OE. DUUS, ChemInform Abstract: A Conformational Study of Hydroxymethyl Groups in Carbohydrates Investigated by 1H NMR Spectroscopy, *ChemInform*, 2010, **25**, 513–543.

45 S. C. Price, A. C. Stuart, L. Yang, H. Zhou and W. You, Fluorine substituted conjugated polymer of medium band gap yields 7% efficiency in polymer-fullerene solar cells, *J Am Chem Soc*, 2011, **133**, 4625–4631.

46 X. Wang, Y. Sun, S. Chen, X. Guo, M. Zhang, X. Li, Y. Li and H. Wang, Effects of π-conjugated bridges on photovoltaic properties of donor-π-acceptor conjugated copolymers, *Macromolecules*, 2012, **45**, 1208–1216.

47 J. B. Park, J. W. Ha, I. H. Jung and D. H. Hwang, High-Performance Nonfullerene Organic Photovoltaic Cells Using a TPD-Based Wide Bandgap Donor Polymer, *ACS Appl Energy Mater*, 2019, **2**, 5692–5697.

48 S. Zhang, H. Fan, Y. Liu, G. Zhao, Q. Li, Y. Li and X. Zhan, Soluble dithienothiophene polymers: Effect of link pattern, *J Polym Sci A Polym Chem*, 2009, **47**, 2843–2852.

49 S. B. Darling and M. Sternberg, Importance of side chains and backbone length in defect modeling of poly(3-alkylthiophenes), *Journal of Physical Chemistry B*, 2009, **113**, 6215–6218.

50 J. Wang, H. Yao, Y. Xu, L. Ma and J. Hou, *Mater Chem Front*, 2021, 5, 709–722.

View Article Online
DOI: 10.1039/D2CP05414K

51 C. Xu, X. Ma, Z. Zhao, M. Jiang, Z. Hu, J. Gao, Z. Deng, Z. Zhou, Q. An, J. Zhang and F. Zhang, Over 17.6% Efficiency Organic Photovoltaic Devices with Two Compatible Polymer Donors, *Solar RRL*, 2021, **5**, 2100175.

52 X. Ma, A. Zeng, J. Gao, Z. Hu, C. Xu, J. H. Son, S. Y. Jeong, C. Zhang, M. Li, K. Wang, H. Yan, Z. Ma, Y. Wang, H. Y. Woo and F. Zhang, Approaching 18% efficiency of ternary organic photovoltaics with wide bandgap polymer donor and well compatible Y6: Y6-1O as acceptor, *Natl Sci Rev*, 2021, **8**, nwaa305.

53 W. Xu, X. Zhu, X. Ma, H. Zhou, X. Li, S. Y. Jeong, H. Y. Woo, Z. Zhou, Q. Sun and F. Zhang, Achieving 15.81% and 15.29% efficiency of all-polymer solar cells based on layer-by-layer and bulk heterojunction structures, *J Mater Chem A Mater*, 2022, **10**, 13492–13499.

54 D. Veldman, S. C. J. Meskers and R. A. J. Janssen, The energy of charge-transfer states in electron donor-acceptor blends: insight into the energy losses in organic solar cells, *Adv Funct Mater*, 2009, **19**, 1939–1948.

Electronic Supplementary Information for

Challenging PM6-alike donor polymers for paring a Y-type state-of-art acceptor in binary blends for bulk heterojunction solar cells

Wei Xu,[a§] Li Du[b§], Guojuan Li,[c] Jingnan Wu [a], Wei He,[d] Cheng Yang,[e] Zhong Cao,[f] Pei Cheng,[d] Hongxiang Li,[d*] Zhengkun Du,[b*] and Donghong Yu[a,g*]

[a.] Department of Chemistry and Bioscience, Aalborg University, Fredrik Bajers Vej 7H, Aalborg East, DK-9220, Demark

[b.] Al-ion Battery Research Center, College of Energy Storage Technology, Shandong University of Science and Technology, Qingdao 266590, China

[c.] National Anti-Drug Laboratory Sichuan Regional Center, Chengdu, 610206 China

[d.] Department of College of Polymer Science and Engineering, State Key Laboratory of Polymer Materials Engineering, Sichuan University, Chengdu, 610065 China

[e.] Key Laboratory of Green Chemistry & Technology of Ministry of Education, College of Chemistry, and State Key Laboratory of Biotherapy, Sichuan University, Chengdu 610064, Sichuan, China

[f.] Hunan Provincial Key Laboratory of Materials Protection for Electric Power and Transportation, and Hunan Provincial Key Laboratory of Cytochemistry, School of Chemistry and Biological Engineering, Changsha University of Science and Technology, Changsha 410114, China

[g.] Sino-Danish Center for Education and Research, DK-8000, Aarhus, Denmark

* Corresponding authors, email: lihongxiang@scu.edu.cn，zhengkundu@163.com，yu@bio.aau.dk

§ W. Xu and L. Du contributed equally to this work.

1. General information

All solvents and reagents were of reagent quality, purchased commercially, and used without further purification. NMR spectra were recorded at room temperature on Bruker Avance III^{TM} HD-600 (operating at 600 MHz for ^{1}H NMR and ^{13}C NMR). Elemental analysis was measured by Euro Vector EA3000. The UV-visible spectra were obtained on a JASCO V-650 UV-vis spectrometer. And thermogravimetric analysis (TGA) are measured by STA 449 F3 Jupiter®. Atomic Force Microscope (AFM) were acquired by Smart SPM. Photovoltaic performance was characterized under illumination with an AM 1.5G (100 mW cm^{-2}), and the *J-V* curves were recorded using a Keithley 2400 source meter. The EQE of solar cells were analyzed using a certified Newport incident photon conversion efficiency measurement system. 2D GIWAXS patterns of films prepared at different temperatures were obtained at 1W1A Diffuse X-ray Scattering Station, Beijing Synchrotron Radiation Facility (BSRF-1W1A). The monochromatic wavelength of the light source was 1.54 Å. The data was recorded by Pilatus 100 K from DECTRIS, Switzerland. The grazing incidence angles were 0.2°.

The CV (cyclic voltammetry) of the two polymers were recorded on a CH-Instruments Model 650A Electrochemical Workstation. Three-electrode configuration were using in measurement, Pt wires as both working electrode and counter electrode, and a freshly activated Ag wire as Ag/Ag^{+} pseudoreference electrode. To obtain the oxidation potentials, the reference electrode was calibrated by using the ferrocene/ferrocenium (Fc/Fc^{+}), which has an absolutely potential of 4.8 eV versus the vacuum level. And the redox potential of Fc/Fc^{+} was obtained for calibration of 0.35 eV vs Ag/Ag^{+} electrode under the same conditions. A tetrabutylammonium hexafluorophosphate (Bu_4NPF_6) solution (0.1 M solution in anhydrous acetonitrile) was used as a supporting electrolyte, and N_2 gas was bubbled prior to each measurement. Two polymers were deposit onto the working electrode by drop-casting from solutions of 10 mg/mL in $CHCl_3$. And ferrocene was used as an external standard vs Ag/Ag^{+} under these conditions. The HOMO and LUMO levels were calculated according to the formula E_{HOMO} = - (E_{OX} + 4.8 - |Fc/Fc^{+}|) eV and $E_{LUMO} = E_{HOMO} - E_g^{opt}$, where the E_{OX}, E_g^{opt} and |Fc/Fc^{+}| was determined from the oxidation onsets in the CV curves, the 1240/(onset absorption band edge of the polymer films) and the half-wave potential of ferrocene in CV curves, respectively.

2. Synthesis of Materials

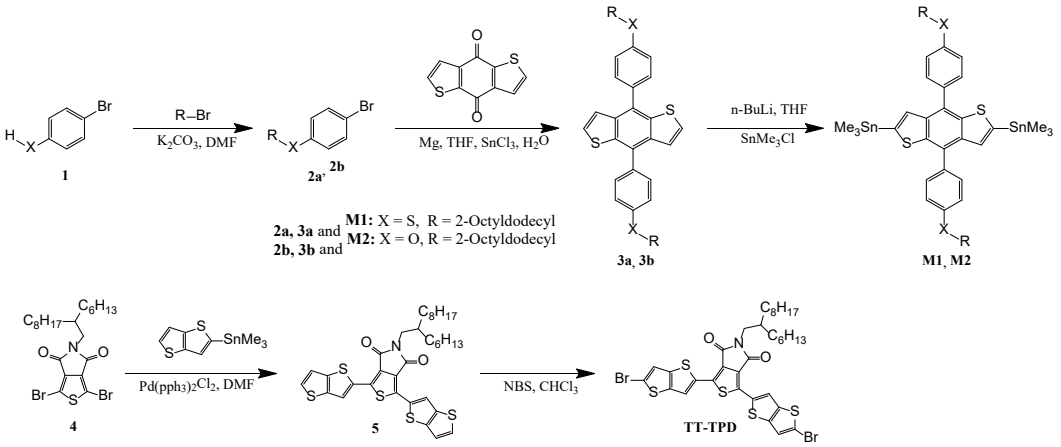

Scheme S1. The synthetic pathway of **M1**, **M2** and **tt-TPD**.

1-Bromo-4-(2-octyldodecxyl)X-benzene ***(X: thiol for 2a, and X: oxy for 2b)***

Under nitrogen atmosphere, 4-bromophenol or 4-bromo-1-thiol-benzene (reagent **1**) (25 mmol), K_2CO_3 (4.1 g, 30 mmol) and were dissolved into 120 mL DMF. Then 1-bromo-2-ethyl-hexane (4.8 g, 25 mmol) was added dropwise into the mixture. And the reaction solution was kept stirring overnight at 150 °C in darkness. After cooling to room temperature, the mixture was quenched with water and extracted three times with ethyl acetate. Then the crude product was purified on a silica gel column eluting with petroleum ether. And purified compound **2** (yellow oil) was obtained for 2a with a yield of 71% and 2b with 68% yielded. **^{1}H NMR** (600 MHz, $CDCl_3$, ppm) δ (***2a***) 7.46 (d, 2H), 6.96 (d, 2H), 3.28 (d, 2H), 1.72 (m, 1H), 1.38 (m, 32H), 0.91 (m, 6H); δ (***2b***) 7.36 (d, 2H), 7.16 (d, 2H), 3.05 (d, 2H), 1.60 (m, 1H), 1.35 (m, 32H), 0.89 (m, 6H).

4,8-Bis((2-octyldodecxyl)X-1-phenyl)-benzo[1,2-b:4,5-b']-dithiophene ***(X: thiol for 3a, and X: oxy for 3b)***

Magnesium spalls (0.73 g, 30.5 mmol) and few I_2 were put into a dried three necked round-bottom flask under nitrogen. The compounds **2a or 2b** (24.2 mmol) in THF (40 mL) was added dropwise by using syringe. Then the mixture was refluxed until all magnesium consumed. Benzo[1,2-b:4,5-b']dithiophene- 4,8-dione (1.34 g, 6.1 mmol) in THF (40 mL) was added slowly into the flask and kept reflux for 12 h. Then, $SnCl_2 \cdot 2H_2O$ (10.95 g, 48.5 mmol) and 10% aqueous HCl was added dropwise into the mixture and stirred for another 2 h at 80°C. After cooling to room temperature, the mixture was quenched with water, and extracted with dichloromethane three times, then dried, concentrated, and purified by column chromatography, the final products were obtained for 3a(39%) and 3b (45%). **^{1}H NMR** (600 MHz, $CDCl_3$, ppm) δ (***3a***) 7.67 (d, 4H), 7.42 (d, 2H), 7.35 (d, 2H), 7.09 (d, 4H), 3.08 (d, 4H), 1.73 (m, 2H), 1.54 (m, 64H), 0.91 (m, 12H); δ (***3b***) 7.65 (d, 4H), 7.50 (d, 2H), 7.40 (d, 2H), 7.33 (d, 4H), 3.04 (d, 4H), 1.74 (m, 2H), 1.33 (m, 64H), 0.89 (m, 12H).

2,6-Bis(trimethyltin)-4,8-bis((2-octyldodecxyl)X-1-phenyl)-benzo[1,2-b:4,5-b′]-dithiophene ***(M1: X is thiol** and **M2: X is oxy)***

Dry THF (50 mL) solution of compound **3a** or **3b** (0.50 mmol) was cooled to -78°C in a round-bottom flask under argon, and *n*-butyllithium in *n*-hexane (8.65 mL, 13.84 mmol) was added dropwise. After warming up to room temperature, the mixture was stirred for 3 h. Then trimethyltin chloride solution in THF (16.4 mL) was added at 0°C and the reaction mixture was stirred at ambient temperature overnight. After quenching with water, extracting with dichloromethane (three times), drying over anhydrous sodium sulfate, and concentrating with a rotary evaporator, the residue was recrystallized from isopropanol to yield the target monomer as a light white (**M1**, 54%) and a pale-yellow (**M2**, 50%) solid.

M1: **^{1}H NMR** (600 MHz, $CDCl_3$) δ 7.66 (d, 4H), 7.52 (d, 4H), 7.38 (s, 2H), 3.07 (d，4H), 1.82-1.74 (m, 2H), 1.55-1.42 (m, 8H), 1.40-1.22 (m, 56H), 0.90 (dt, 12H), 0.39 (t, 18H). **^{13}C NMR** (600 MHz, $CDCl_3$, ppm) δ 138.22, 138.14, 136.22, 136.13, 129.90, 129.75, 128.44, 127.30, 122.88, 38.11, 37.62, 33.31, 31.94, 31.93, 29.97, 29.96, 29.71, 29.67, 29.63, 29.38, 29.37, 26.60, 22.70, 14.13.

M2: **^{1}H NMR** (600 MHz, $CDCl_3$) δ 7.67 (d, 4H), 7.41 (t, 2H), 7.13 (d, 4H), 3.98 (d, 4H), 1.91-1.84 (m, 2H), 1.57-1.50 (m, 4H), 1.47-1.26 (m, 60H), 0.92 (dt, 12H), 0.38 (t, 18H). **^{13}C NMR** (600 MHz, $CDCl_3$, ppm) δ 158.52, 138.22, 136.22, 136.13, 132.14, 128.12, 127.30, 122.88, 116.38, 71.20, 37.90, 31.93, 31.91, 31.32, 30.01, 30.00, 29.67, 29.65, 29.62, 29.59, 29.36, 29.33, 26.83, 22.70, 14.13.

1,3-di(thenio[3,2-b]thiophen-2-yl)-5-(2-hexyldecyl)-4H-thieno[3,4-c]pyrrole-4,6(5H)-dione ***(5)***

Compound **4** (1.2 g, 2.84 mmol) and 2-trimethyltin-thieno[3,2-b]thiophen (2.4g, 6.3 mmol) were dissolved in 12 mL of dry toluene under nitrogen atmosphere. Then after adding $Pd_2(dba)_3$ (0.094 g, 0.01 mmol) and $P(o\text{-}tol)_3$ (0.061 g, 0.02 mmol), the mixture was refluxed for 24h at 100°C. When cooling to room temperature, the product was extracted with 100 mL DCM for 3 times. After removing the solvent, the target product was obtained by purifying with silica gel column chromatography (1.56 g, 83% yield). **^{1}H NMR** (600 MHz, $CDCl_3$, ppm) δ 7.58 (d, 2H), 7.44 (d, 2H), 7.29 (s, 2H), 3.35 (d, 2H), 1.81 (m, 1H), 1.31 (m, 24H), 0.92 (m, 6H).

1,3-bis(5-bromo-thenio[3,2-b]thiophen-2-yl)-5-(2-hexyldecyl)-4H-thieno[3,4-c]pyrrole-4,6(5H)-dione ***(tt-TPD)***

N-bromosuccinimide was added into the 25 mL DMF solution of compound **5** (1.56 g, 2.38mmol) under N_2 atmosphere and darkness. Then the mixture was stirred at room temperature for 4 h and filtered to obtain the precipitates. After thoroughly washing with methanol for 2 times and cold diethyl ether for once, the target product was purified by column chromatography to give 1.58 g (82% yield). **^{1}H NMR** (600 MHz, $CDCl_3$, ppm) δ 7.17 (s, 2H), 6. 92 (s, 2H), 3.34 (d, 2H), 1.80 (m, 1H), 1.30 (m, 24H), 0.91 (m, 6H).

*Synthesis of PBDT-PS-ttTPD (**P10**) and PBDT-PO-ttTPD (**P11**)*

Under Ar_2 atmosphere, **M1** or **M2** (0.15 mmol), $Pd_2(dba)_3$ (2 mg, 0.002 mmol), P(o-tol)$_3$ (4 mg, 0.013 mmol) and **tt-TPD** (0.15 mmol) were introduced into a 20 mL round-bottom flask. Then, 6 mL dry toluene was added, and the solution was heated to 110°C for 24 h. After cooling to room temperature, the mixture was poured into methanol, then filtered. The precipitate was extracted by using hexane, acetone, and chloroform, respectively with Soxhlet extraction. Then, the chloroform fraction was collected and dried overnight under vacuum. Finally, the target copolymers were obtained.

P10 (115 mg, yield 59.8 %). Elemental analysis calculated (%) for [$C_{72}H_{81}NO_2S_9$]: C, 71.44%; H, 8.26%; N, 0.85%; O, 1.94%; S, 17.51%; found: C 71.25%; H 8.13 %; N 0.83%; S 17.30 %.

P11 (106 mg, yield 56.4 %). Elemental analysis calculated (%) for [$C_{72}H_{81}NO_4S_7$]: C, 72.86%; H, 8.42%; N, 0.87%; O, 3.96%; S, 13.89%; found: C 72.66%; H 8.32%; N 0.85%; S 13.69 %.

3. Dihedral angle of the two polymers

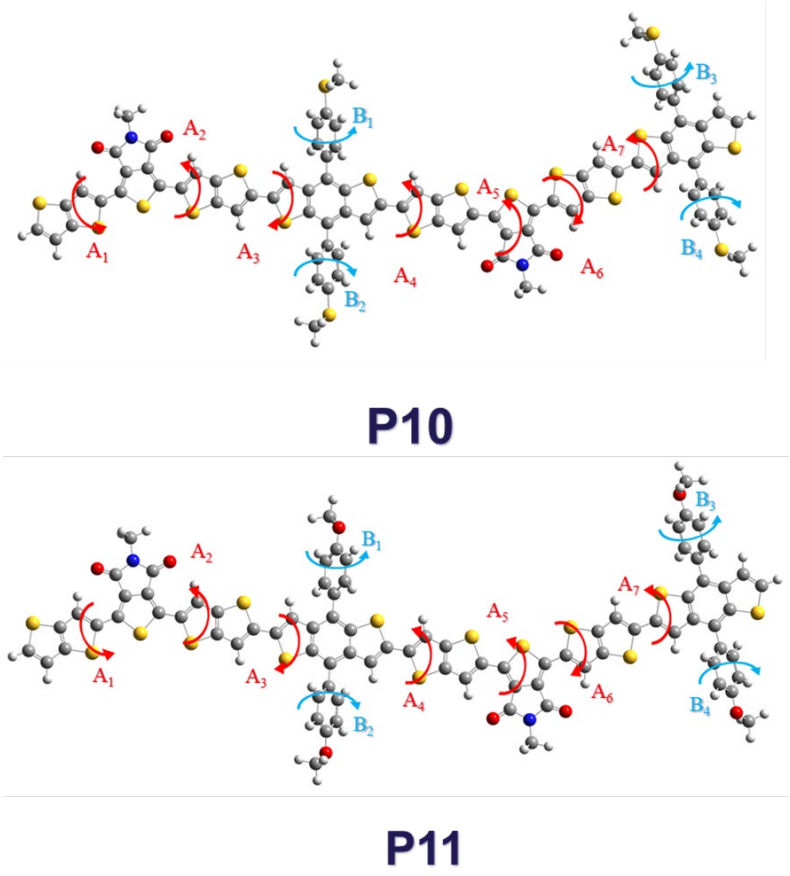

Figure S1. The optimized molecular structure of dimers, representing segments of two polymers.

Table S1. The dihedral angels of the optimal-structured molecules calculated by the density functional theory (DFT).

Polymers	Dihedral angels (°)										
	A_1	A_2	A_3	A_4	A_5	A_6	A_7	B_1	B_2	B_3	B_4
P10	0.01	0.01	0.28	6.23	0.25	0.21	6.59	58.9	58.9	58.9	58.3
P11	0.01	0.25	0.29	5.34	0.21	0.11	5.84	59.0	59.0	59.3	58.6

4. Fabrication and Optimization of OPV devices

The SM-NFA OPV devices were fabricated on top of a pre-patterned ITO substrate with the conventional structure of ITO/PEDOT:PSS/Active layers/PFN-Br/Ag. After cleaning the ITO with aqueous detergent, deionized water, acetone, and 2-propanol, UV-ozone treatment was applied for 15 min. Filtered PEDOT:PSS (CLEVIOS™ P VP AI 4083) was spin-coated on the ITO substrate to form a 30 nm-thick layer. Then the coated substrates were annealed on the thermal plate at 150 °C for 20 min. After annealing, the chlorobenzene (CB) solution of the blending active substances was spin-cast on top of the PEDOT:PSS layer to produce the active layer with a thickness of 100 nm under 2000 rpm in glovebox under N_2 atmosphere, and the coated substrates with active layer were annealed for 10 min at 100 °C. Then PNF-Br was spin-coated under 3000 rpm to form a 10 nm-thickness layer. Finally, the device fabrication was completed by thermal evaporation of 100 nm Ag as the anode in high vacuum (< 10^{-6} mbar). All the experimental details were summarized in the below tables. And for exhibiting better reproducibility of these devices, all data in the tables was average value calculated from 6 parallel devices.

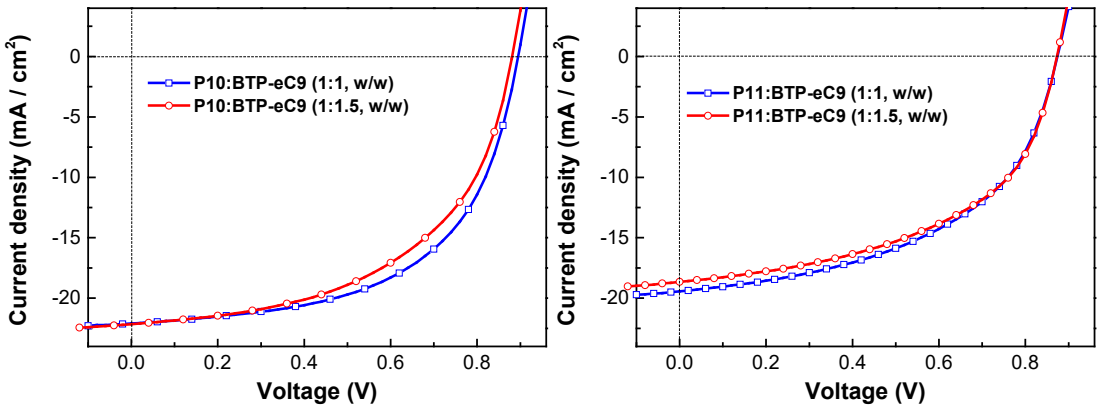

Figure S2. The *J-V* curves of polymers/BTP-eC9-based PSCs with different D-A weight ratios (1:1 and 1:1.5) under an illumination of AM 1.5 G, 100 mW cm^{-2}

Table S2. Photovoltaic properties of the OPVs based on Polymers/BTP-eC9 with different weight ratio of donor and acceptor under an illumination of AM 1.5 G, 100 mW cm^{-2}

Polymer/ BTP-eC9	D:A (w/w)	FF (%) [a]	V_{OC} (V) [a]	J_{SC} (mA cm^{-2}) [a]	PCE (%) [a]
P10	1:1	55.94	0.89	22.47	11.19
	1:1.5	52.40	0.88	22.46	10.34
P11	1:1	49.51	0.87	19.51	8.40
	1:1.5	50.66	0.87	18.33	8.05

[a] The experimental data was average obtained from 6 parallel devices.

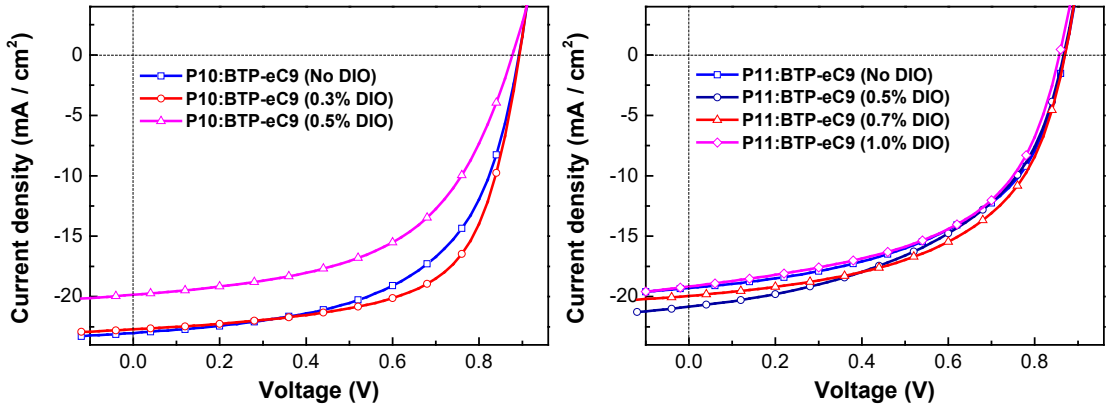

Figure S3. The *J-V* curves of polymers/BTP-eC9-based PSCs with and without additive volume ratios under an illumination of AM 1.5 G, 100 mW cm^{-2}

Table S3. Photovoltaic properties of the OPVs based on Polymers/BTP-eC9 (1:1, w/w) with different content of DIO under an illumination of AM 1.5 G, 100 mW cm^{-2}

Polymer/ BTP-eC9	DIO (vol%)	FF (%) [a]	V_{OC} (V) [a]	J_{SC} (mA cm^{-2}) [a]	PCE (%) [a]
P10	0	55.62	0.89	22.54	11.16
	0.3	61.58	0.89	22.94	12.53
	0.5	52.31	0.88	20.04	9.20
P11	0	50.37	0.87	19.33	8.49
	0.5	49.19	0.86	20.84	8.88
	0.7	52.83	0.87	20.01	9.20
	1	54.72	0.86	18.53	8.74

[a] The experimental data was average obtained from 6 parallel devices.

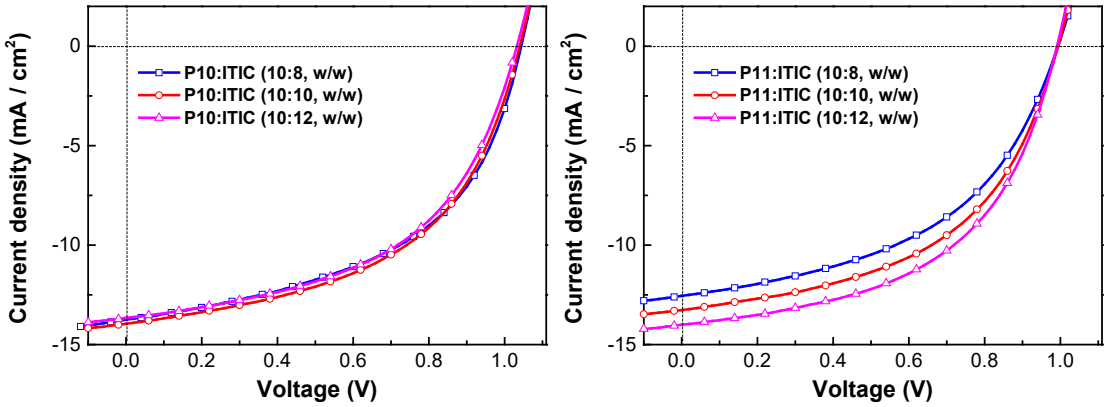

Figure S4. The *J-V* curves of polymers/ITIC-based PSCs with different D-A weight ratio under an illumination of AM 1.5 G, 100 mW cm^{-2}

Table S4. Photovoltaic properties of the OPVs based on Polymers (10 mg/mL)/ITIC under an illumination of AM 1.5 G, 100 mW cm^{-2}

Polymer/ ITIC	D:A (w/w)	FF (%) [a]	V_{OC} (V) [a]	J_{SC} (mA cm^{-2}) [a]	PCE (%) [a]
P10	1:0.8	50.50	1.04	13.56	7.15
	1:1	50.81	1.04	13.60	7.17
	1:1.2	50.29	1.03	13.33	6.93
P11	1: 0.8	47.53	1.00	12.37	5.85
	1:1	50.16	0.99	13.25	6.59
	1:1.2	51.16	0.99	13.69	6.95

[a] The experimental data was average obtained from 6 parallel devices.

5. Properties of charge transfer and recombination

The mobility properties of the active layer were determined by applying the space charge limited current (SCLC) method to the *J-V* measurements of the devices. The hole-only and electron-only polymers devices were designed as the vertical diodes with the structure of ITO/PEDOT:PSS/Active layers/Au and Ag/ZnO/Active layers/Ag, respectively, where the active layer were made of P10:BTP-eC9 with 1:1 w/w (CB 0.3% DIO, 2000 rpm) and P11:BTP-eC9 with 1:1 w/w (CB 0.7% DIO, 2000 rpm), respectively. And the mobilities were calculated from the SCLC using the following equation[1]:

$$J_{SCLC} = (9/8)\varepsilon_r\varepsilon_0\mu(V^2/L^3)$$

where J is the current density, ε_r is the dielectric constant of the polymers, ε_0 is the permittivity of the vacuum, μ is the hole mobility, L is the thickness of the blend films, $V = V_{appl} - V_{bi}$, where V_{appl} is the applied potential, and V_{bi} is the built-in voltage which results from the difference in the work function of the anode and cathode.

Charge dissociation probability was characterized by the function of photogenerated current density (J_{ph}) *versus* effective applied voltage (V_{eff}). The J_{ph} is defined as the difference between

J_L and J_D, where J_L and J_D are the current density of devices under light (100 mW cm^{-2}) and dark, respectively. $V_{eff} = V_0 - V$, where V_0 is the voltage when $J_{ph} = 0$ and V is the applied voltage during the measurement. When the reverse voltage is greater than 2 V, the recombination is suppressed by a high internal electric field. Thus, J_{ph} will reach the saturated current density (J_{sat}). Consequently, $P_{diss} = J_{ph}/J_{sat}$ could be used to describe the charge dissociation probability.[2,3] A higher P_{diss} is indicated the more effective charge dissociation. Besides, the relationship of J_{SC} and the light intensity (I) is $J_{SC} \propto I^{\alpha}$, where α is the degree of biomolecular recombination. When $\alpha = 1$, dissociated free charges do not recombine during the movement process, and are all collected by the electrode, implying the recombination can be ignored. If α is less than 1, the bimolecular recombination will be present in the devices, and the smaller the value of α indicates the stronger bimolecular recombination. Meanwhile, $V_{OC} \propto n(kT/q)\cdot\ln(I)$, where K represents the Boltzmann constant, T is the Kelvin temperature, and q is the elementary charge. If the slope is close to 2 kT/q, the trap-assisted recombination will occur inside the devices.[4,5]

6. Other Supplemental Figures

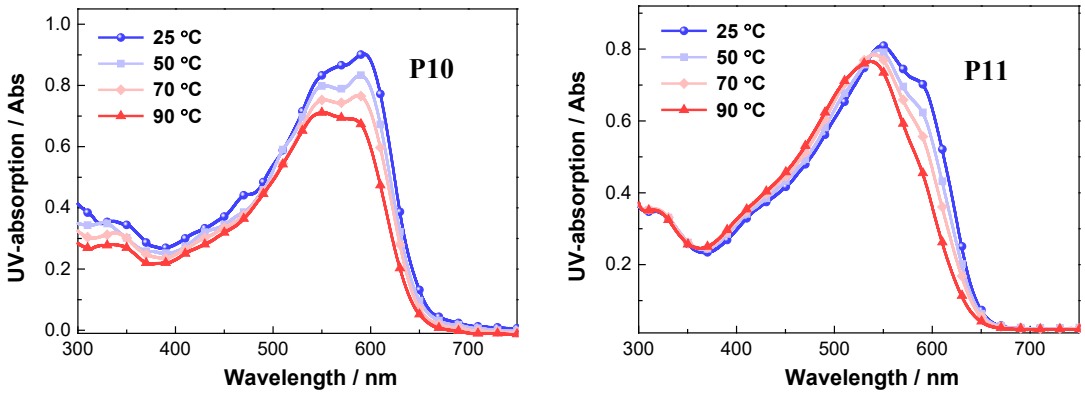

Figure S5. Temperature dependent UV-vis absorption curves of P10 (left) and P11 (right) in Chlorobenzene.

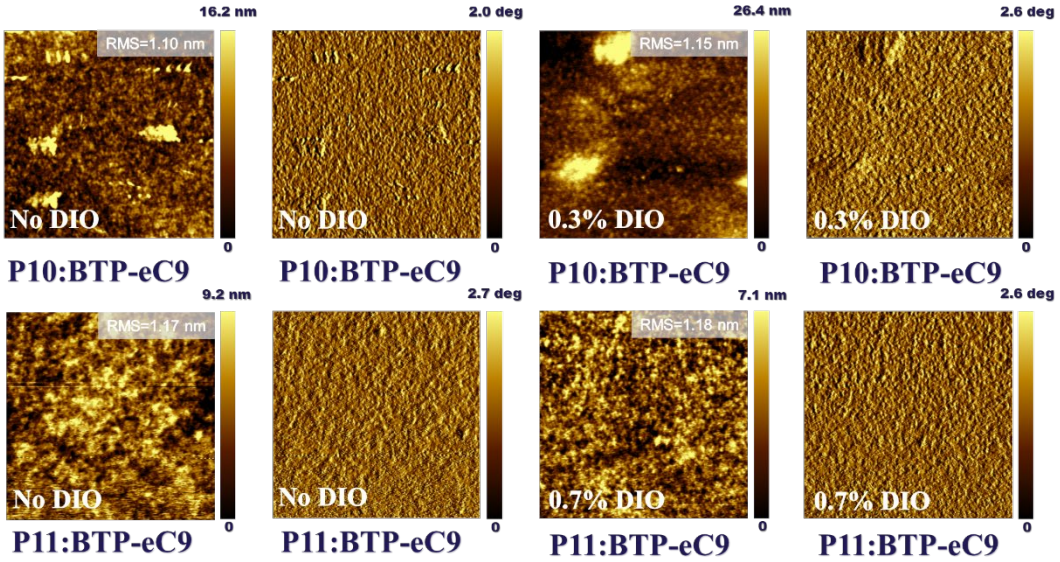

Figure S6. Atomic force microscopy height (a, c, e, and g) and phase (b, d, f, and h) diagrams of P10:BTP-eC9 (with/without DIO) and P11:BTP-eC9 (with/without DIO) thin films, 4 μm × 4 μm.

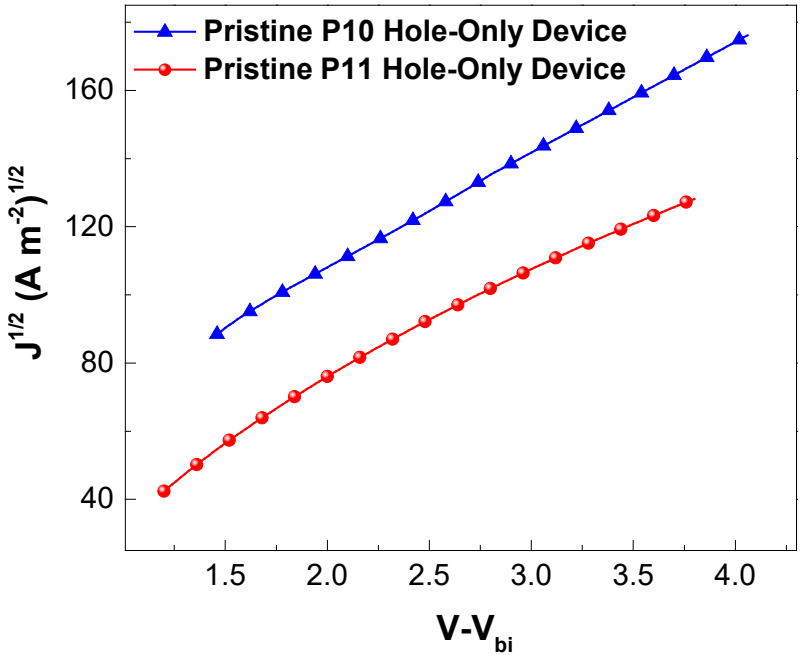

Figure S7. $J^{1/2}$-V plots for the measurement of the hole mobility in pristine polymer hole-only devices by the SCLC method.

Reference

[1] C. Melzer, E. J. Koop, V. D. Mihailetchi, P. W. M. Blom, Hole Transport in Poly(phenylene vinylene)/Methanofullerene Bulk-Heterojunction Solar Cells, Advanced Functional Materials, 14 (2004), 865-870

[2] P. W. M. Blom, V. D. Mihailetchi, L. J. A. Koster, D. E. Markov, Device Physics of Polymer:Fullerene Bulk Heterojunction Solar Cells, Advanced Materials, 19 (2007), 1551-1566

[3] L. Huo, T. Liu, X. Sun, Y. Cai, A. J. Heeger, Y. Sun, Single-Junction Organic Solar Cells Based on a Novel Wide-Bandgap Polymer with Efficiency of 9.7%, Advanced Materials, 27 (2015), 2938-2944

[4] L. J. A. Koster, V. D. Mihailetchi, R. Ramaker, P. W. M. Blom, Light intensity dependence of open-circuit voltage of polymer:fullerene solar cells, Applied Physics Letters, 86 (2005), 123509

[5] A. K. K. Kyaw, D. H. Wang, D. Wynands, J. Zhang, T.-Q. Nguyen, G. C. Bazan, A. J. Heeger, Improved Light Harvesting and Improved Efficiency by Insertion of an Optical Spacer (ZnO) in Solution-Processed Small-Molecule Solar Cells, Nano Letters, 13 (2013), 3796-3801

PAPER III

Revisiting benzodithiophene-based donor polymers via thiolalkylation for enhanced photovoltaic performance

Wei Xu,[a§] Li Du [b§], Guojuan Li,[c] Wei He,[d] Cheng Yang,[e] Hongxiang Li,[d] Zhong Cao,[f] Zhengkun Du,[b*] Pei Cheng, [d*] and Donghong Yu[a,g*]

[a.] Department of Chemistry and Bioscience, Aalborg University, Fredrik Bajers Vej 7H, Aalborg East, DK-9220, Denmark

[b.] Al-ion Battery Research Center, College of Energy Storage Technology, Shandong University of Science and Technology, Qingdao, Shandong 266590, China

[c.] National Anti-Drug Laboratory Sichuan Regional Center, Chengdu, 610206 China

[d.] Department of College of Polymer Science and Engineering, State Key Laboratory of Polymer Materials Engineering, Sichuan University, Chengdu, 610065 China

[e.] Key Laboratory of Green Chemistry and Technology of Ministry of Education, College of Chemistry, and State Key Laboratory of Biotherapy, Sichuan University Chengdu, 610064, China

[f.] Hunan Provincial Key Laboratory of Materials Protection for Electric Power and Transportation, and Hunan Provincial Key Laboratory of Cytochemistry, School of Chemistry and Biological Engineering, Changsha University of Science and Technology, Changsha 410114, China

[g.] Sino-Danish Center for Education and Research, DK-8000, Aarhus, Denmark

§ equal contributions to this work

Abstract

In this study, we explore the effect of the asymmetric structure in homopolymer organic solar cells (OSCs) based on benzo[1,2-b;4,5-b′]dithiophene (BDT) monomers by comparing the BDTT-S-*alt*-BDTT-Cl asymmetric homopolymer (P13), BDTT-*alt*-BDTT-S asymmetric homopolymer (P15) and BDTT-S homopolymer (P14) in terms of polymer chemical structure , physical, electrochemical, optical, photovoltaic, semiconductor and film-morphology properties. The asymmetric homopolymer, P15, with most significant push-pull electron effect had the best photovoltaic performance in non-fullerene photovoltaic device (BTP-eC9 as electron acceptor), which was found of 65.87% for FF, 22.04 mA/cm^{-2} for J_{SC} and 11.5% for PCE, respectively. This PCE value is the highest values reported for homopolymer donor-based OPVs. And we also believe that the homopolymer with asymmetric structure has more promising photovoltaic performance.

Introduction

The structure design of polymer donor materials plays an important role in improving the energy conversion efficiency of polymer solar cells (PSCs). Recently, the copolymers with the molecular structure of electron-donor (D) and electron-accepter (A) alternating units have attracted a considerable attention as the potential donor materials in PSCs. However, the copolymer naturally demands multiple synthetic steps to produce two or more different types of monomers, which costs more time and raw materials. Although the prices of the popular polymer donor materials are affordable for scientific studies in laboratory, their costs remain high as the commercial product. In order to solve this dilemma, the homopolymers could serve as the ideal alternative electron-donor materials, which have simpler molecular structures and shorter synthetic pathways. Actually, the investigations of homopolymers had already commenced over a decade ago, and one of the most successful homopolymer donor materials was poly(3-hexylthiophene) (P3HT) till now. Nonetheless, the potential limitations and the structure-modified difficulties of P3HT restricted the further development. Because P3HT had a narrow absorption in the visible region, weak light-harvesting capability and the relatively higher laying HOMO energy level, the PSC devices based on P3HT usually had lower short current density (J_{SC}) and open circuit voltage (V_{OC}). Thus, the homopolymers with novel electron-donating units are required to overcome the predicament.

So far, extensive efforts had been made for seeking the alternative homopolymer with the advantages of simple structures and high performance. In 2015, J. Kim and his colleagues reported a potential homopolymer based on alkyl-thienyl benzodithiophene (BDT) units (PBDTT), which obtained a nice PCE of 6.1% in $PC_{71}BM$-based PSCs. Comparing with P3HT, BDT-based homopolymer had broader optical bandgap, higher absorption coefficient, lower lying HOMO levels and better thermal stability. Then, besides the novel BDT-based homopolymer with alkylthio-thienyl side chains, Hwang et al. also firstly reported the asymmetrical BDT-based homopolymer with different flanks. They found that alkylthio side chains substituted BDT-based homopolymer (PBDTT-S) performed a higher PCE of 7.05% with a higher V_{OC} of 0.99 V and a better J_{SC} of

13.92 mA/cm^{-2} than PBDTT. And the asymmetrical homopolymer (PBDTT-BDTT-S) exhibited the moderate photovoltaic performance among three homopolymers in fullerene-based PSCs. Subsequently, Wong and co-workers synthesized the fluorine-flanks substituted asymmetrical BDT-based homopolymer (PBBF) and applied it into the IDIC-based PSCs to achieve a higher PCE of 8.5%. Obviously, the photovoltaic performance of PBBF-based PSCs was better than PBDTT in all aspects. In addition to the optical absorption enhancement and HOMO level deepening brought about by fluorination, which increased the J_{SC} and V_{OC}, the asymmetrical homopolymer also had the better film morphology inducing the improvement FF. These results demonstrated that one future bright structure design idea was asymmetrical homopolymer donor materials that could achieve better photovoltaic performance. And nowadays there are no articles reported on the study of asymmetric homopolymers. Accordingly, further efforts should be aimed to: (1) deepen the HOMO energy level under the balance of the trade-offs between V_{OC} and J_{SC}; (2) increase the light absorption coefficient and improve the charge mobility to maximize the J_{SC} and FF.

In this study, we designed and synthesized two asymmetric homopolymers based on BDT with the properly selected flanks via Still Coupling reactions, i.e., poly{4,8-bis(5-((2-ethylhexyl)thio)thiophen-2-yl)-benzo[1,2-b:4,5-b′]dithiophene-alt-4,8-bis(4-chloro-5-(2-ethylhexyl))thiophen-2-yl)-benzo[1,2-b:4,5-b′]-dithiophene} (P13 or PBDTT-S-BDTT-Cl) and poly{4,8-bis(5-((2-ethylhexyl)thio)thiophen-2-yl)-benzo[1,2-b:4,5-b′]dithiophene-alt-4,8-bis(5-(2-ethylhexyl))thiophen-2-yl)-benzo[1,2-b:4,5-b′]dithiophene} (P15 or PBDTT-BDTT-S). Besides, we also prepared contrastive homopolymer, poly{4,8-bis(5-((2-ethylhexyl)thio)thiophen-2-yl)benzo[1,2-b:4,5-b′]-dithiophene} (P14 or PBDTT-S), for highlighting the advantages of asymmetric homopolymers. Interestingly, the asymmetric homopolymers (P13 and P15) exhibited better photovoltaic performance than homopolymer (P14), and the asymmetric homopolymers (P15) showed notably improved charge dissociation, charge recombination and hole mobilities, affording an astonishing PCE of 11.5%, which is the highest value reported for devices with homopolymers.

Results and Discussion

The chemical structures of BDT-based homopolymers were shown in Fig. 1, and the synthetic pathway of them was outlined in the Scheme. 1 of Supplemental Electric Information (ESI), copolymerizing with 4,8-bis(5-((2-ethylhexyl)thio)thiophen-2-yl)benzo[1,2-b:4,5-b′]-dithiophene (BDTT-S), 4,8-bis(4-chloro-5-(2-ethylhexyl))thiophen-2-yl)benzo[1,2-b:4,5-b′]-dithiophene (BDTT-Cl) or 4,8-bis(5-(2-ethylhexyl))thiophen-2-yl)benzo[1,2-b:4,5-b′]-dithiophene (BDTT) monomers via using $Pd(PPh_3)_4$ catalyst. Furthermore, the crude homopolymers were further purified successively with methanol, acetone, *n*-hexane, and chloroform by using Soxhlet extraction. The homopolymers are readily dissolving in most organic solvents, such as chloroform (CF), chlorobenzene (CB), and o-dichlorobenzene (o-DCB), which indicated that they all are easily solution processable. Through gel permeation chromatography (GPC), the number-average molecular weight (M_n) and the polydispersity index (PDI) of the homopolymers were measured with calibration against polystyrene standards, which were found of 3.43 KDa with PDI 2.58 for P13, 2.89 KDa with PDI 2.20 for P14 and 2.79 KDa with PDI 2.16 for P15, respectively. As the organic semiconductor materials (Fig. S1), all polymer

materials were thermally stable with the decomposition temperatures for 5% weight loss of 348 °C for P13, 315 °C for P14 and 341 °C for P15, respectively.

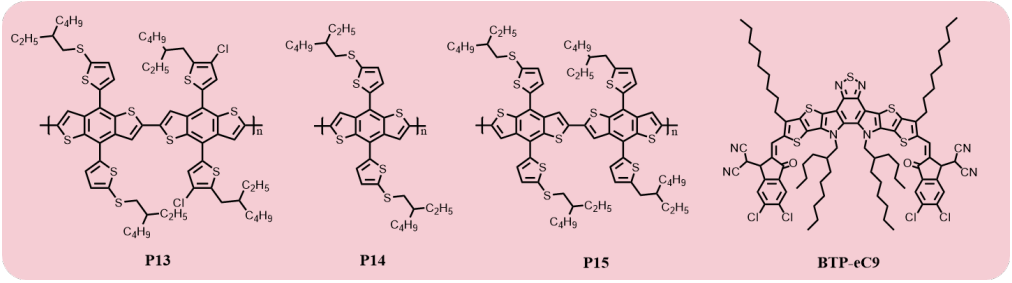

Figure 1. Schematic diagram of the molecular structures of synthetic polymers and acceptor

Then, the optical property was charactered by ultraviolet-visible spectroscopy, as shown in Fig. 2A, the UV-vis absorption spectrum of three polymers in thin films indicated that P15 exhibited the best optical property with broadest absorption edge. And the optical absorption edges of these homopolymers were found of 630 nm for P13, 635 nm for P14 and 640 nm for P15, which corresponded the optical bandgaps of 1.97 eV for P13, 1.95 eV for P14 and 1.94 eV for P15, respectively. And three polymers were complementary to the absorbance of acceptor BTP-eC9 in the visible light region. Besides, the thin-films electrochemical characteristics of three were studied by CV (Fig. 2B), whose onset oxidation potentials (E_{OX}) were found of 1.13 V for P13, 1.15 V for P14, and 1.10 V for P15, corresponding to HOMO energy levels of -5.51 eV for P13, -5.53 eV for P14 and -5.48 eV for P15, respectively. The HOMO level of P14 was undoubtably lowest lying than others, and we attributed it to the strongest electron-withdrawing effect of alkylthio side chains. And the LUMO energy levels of these homopolymers were obtained by the same mean exhibiting in Table 1. Thus, the electronic bandgaps E_g of three could be calculated, which approximated to their optical bandgaps E_g^{opt}. And the optimization and calculation by DTF, energy-levels schematic diagram these homopolymers were present in Fig. 2D. It was obviously that the electron clouds in HOMO energy levels of P13 and P14 were almost evenly distributed along the polymer backbone, while that of P15 was favorably centered in BDTT monomers. The optimized result revealed that the electron push-pull effect of P15 was significant between BDTT-S and BDTT units causing by the huge difference of inductive effect between alkyl-thienyl side chains and alkylthio-thienyl side chains, which was similar to D-A alternating copolymers.

Table 1. The electronic and optical properties of P13-P15.

Sample	HOMO [eV][a]	LUMO [eV][a]	E_g [eV][b]	λ_{edge} [nm]	E_g^{opt} [eV][c]	HOMO [eV][d]	LUMO [eV][d]
P13	-5.51	-3.63	1.88	630	1.97	-5.23	-2.18
P14	-5.53	-3.60	1.91	635	1.95	-5.27	-2.14
P15	-5.48	-3.61	1.87	640	1.94	-5.15	-2.05

[a] Calculated from the equation E_{HOMO} / E_{LUMO} = - (E_{OX} / E_{RED} + 4.8 - |Fc/Fc$^+$|) eV; [b] $E_g^{opt} = E_{LUMO} - E_{HOMO}$; [c] Evaluated from the absorption band edge of the polymer films and determined by the equation E_g^{opt} = 1240/(onset band edge of absorption); [d] Calculated via DTF

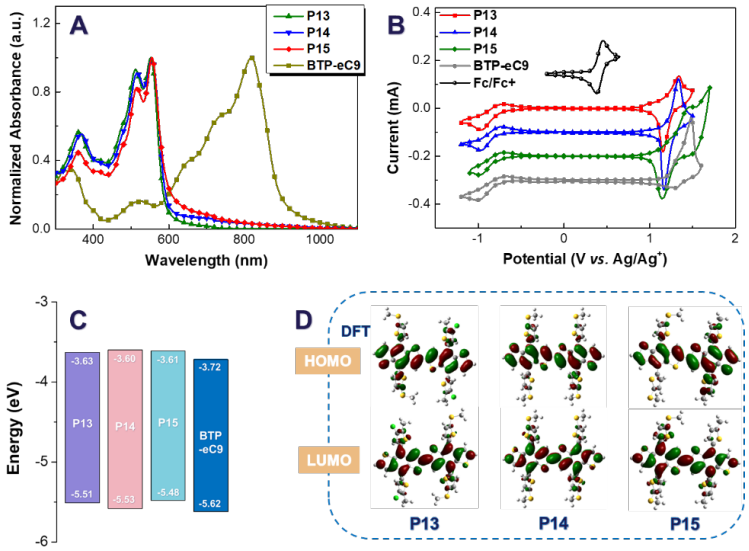

Figure 2. UV-vis absorption spectrum (A), CV chart (B), molecular energy levels (C) and the calculated electron distributions at HOMO/LUMO orbitals (D) of polymers and acceptor.

For further investigating the thin-film properties of the organic active layers based on three homopolymers, DFT method was used to simulate the optimal thermodynamic structure of three homopolymers. And the dihedral angles of the polymer backbones were calculated and present in Fig. S2. These homopolymers had the similar dihedral angles between thienyl side chain and BDT core. However, P14 exhibited the minimum dihedral angle between two adjacent BDT units, which was attributed to the symmetrical structure of the polymer backbone. And another result also proved above inference, P13 substituted with chloride thienyl side chains had the largest dihedral angle due to its most asymmetrical structure. As far as the theoretical results are concerned, the smaller the dihedral angle corresponded the flatter conjugated backbones, which could indicate that P14 and P15 would form closer π-π stacking than P13 in thin films.

To study the PV performance of these homopolymer donor materials, we applied them into practical OPV devices with the conventional structure as mentioned in ESI. Through many-times attempts in blending weight ratio of donor and acceptor, we confirmed the optimal blending weight ratio (1:1, w/w) of active layer based on these homopolymers. And on the basis of the optimal weight ratio, we went further optimization by tuning the content of solvent additive, DIO. The optimal processes of the content of solvent additive in active layers based on three homopolymers were present in following Fig. S3. Both P13 and P15 had the same optimal content of solvent additive of 0.1% volume ratio, and P14-based OPV devices performed optimally at the pristine blending condition, which means that P14-based OPV devices were strongly negatively sensitive to DIO. For P13, the content of solvent additive in active layer increased from 0 to 0.1%, FF had an increasement of 7.9%, J_{SC} had a decrease of 4.8% and V_{OC} kept content. When from 0 to 0.3%, FF had an increasement of 10.0%, while J_{SC} had a decrease of 13.9%, which indicated that DIO had a moderate effect on P13-based active layers. For P15, content of additive increased from 0 to 0.1%, FF had an increasement of 6.8%, J_{SC} had an increasement of 0.3% and V_{OC} had an increasement of 1.3%. And from 0 to 0.3%, FF had an increasement of 4.5%, J_{SC} had an increasement of 0.6%, and V_{OC} maintained the increasement of 1.3%. This result implied that DIO only exhibited the positive effect in P15-based active layer.

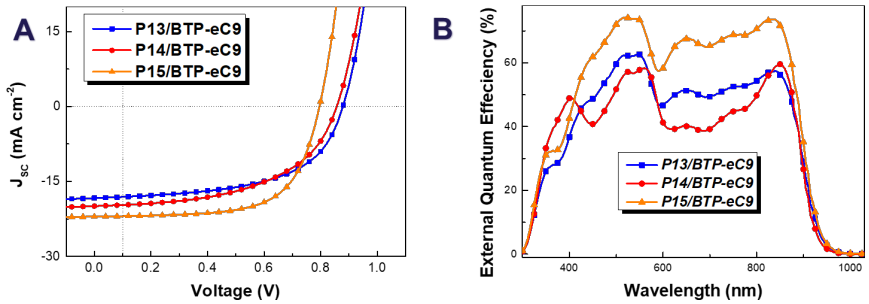

Polymer/ BTP-eC9	PCE (%) [a]	FF (%)	V_{oc} (V)	J_{sc} (mA cm^{-2}) [b]
P13	9.18 (8.63)	57.10	0.88	18.33 (17.68)
P14	9.07 (8.49)	53.15	0.86	19.94 (19.33)
P15	11.53 (11.08)	65.87	0.79	22.04 (21.44)

[a] Average PCE is calculated from 10 parallel devices. [b] Calculated by the EQE.

Figure 3. J-V curves (A), EQE plots (B) and Table (bottom) of the optimal OPV devices based on three homopolymers.

Thence, we obtained the optimal PV performance in OPV devices based on these homopolymers. As shown in Fig. 3A, although the V_{OC} was the lowest among three, P15-based OPV devices performed the best PCE of 11.53% (the average PCE was 11.08%, obtaining from 10 parallel devices), which had the highest FF of 65.87% and the highest J_{SC} of 22.04 mA/cm^{-2}. It was no doubt that P15-based devices had the lowest V_{OC} due to the highest lying HOMO level among three. Compared with P14, P13-based OPV devices occupied the higher FF of 57.1% and V_{OC} of 0.88 V, resulting them to perform a higher PCE of 9.18% (Ave. 8.63%). P14-based OPV devices performed the worst PCE of 9.07% (Ave. 8.49%) owing to its lowest FF although they had moderate the J_{SC} and V_{OC}. According to external quantum efficiency (EQE) plots (Fig. 3B), the integrated J_{SC} of the optimal homopolymer-based OPV devices were calculated of 17.68 mA·cm^{-2} for P13, 19.33 mA·cm^{-2} for P14 and 21.44 mA·cm^{-2} for P15, which were consistent to their J-V experimental results. Interestingly, P14 had the lowest lying HOMO energy levels but the corresponding OPV devices did not exhibited highest V_{OC} due to their higher voltage loss. Overall, three homopolymers had the excellent J_{SC} than these homopolymers reported, and also achieved the best PCE. Especially, the P15-based OPV devices had an astonishing PCE of 11.53%, which had surpassed the current most efficient homopolymer-based OPV devices with a 20% improvement in PCE. In generally, when coupling with BTP-eC9, the OPV devices based on P13, P14 and P15 all had the excellent PV performance.

Table 2. The hole mobilities, charge recombination and charge dissociation properties of P13-P15.

Items	μ_h ($cm^2 V^{-1} s^{-1}$)	α	KT/q	P_{diss} [a]
P13:BTP-eC9	5.03×10^{-5}	0.99	1.45	0.97
P13:BTP-eC9, 0.1% DIO	3.65×10^{-5}	0.98	1.25	0.97
P14:BTP-eC9	1.26×10^{-5}	0.98	1.97	0.99
P14:BTP-eC9, 0.1% DIO	7.86×10^{-6}	0.97	1.83	0.98
P15:BTP-eC9	4.88×10^{-5}	0.99	1.45	0.99
P15:BTP-eC9, 0.1% DIO	2.30×10^{-4}	0.98	1.25	0.98

[a] The charge dissociation probability (P_{diss}) is described by $P_{diss} = J_{ph}/J_{sat}$.

For further investigating the difference among three homopolymer materials in PSCs, their semiconductor characteristics (Table 2) were characterized following the described instructions in ESI. The hole mobilities of homopolymer-based PSCs without DIO were found of 5.03×10^{-5} cm^2 V^{-1} s^{-1} for P13, 1.26×10^{-5} cm^2 V^{-1} s^{-1} for P14 and 4.88×10^{-5} cm^2 V^{-1} s^{-1} for P15, respectively. After adding the additive of DIO, the hole mobilities of three were found of 3.65×10^{-5} cm^2 V^{-1} s^{-1} for P13, 7.86×10^{-6} cm^2 V^{-1} s^{-1} for P14 and 2.30×10^{-4} cm^2 V^{-1} s^{-1} for P15, respectively. And the P_{diss} (see ESI for details) of P13-, P14- and P15-based OPVs (with or without DIO) was listed in the Table 2. Besides, the charge recombination were characterized by the function diagrams of the light intensity against J_{SC} and V_{OC} in OPVs. All homopolymers had the excellent α values (0.97~0.99) in corresponding PSC devices with or without DIO, which indicated that the bimolecular recombination of two could all nearly be ignored. But it was notably that the slopes of KT/q decreased when adding the DIO additive, which indicated that the DIO additive induced the reductions of the trap-assisted recombination inside homopolymer-based OPV devices. Obviously, the optimal PSC devices based on P15 performed highest hole mobility, best charge dissociation ability and smallest charge recombination among three, and next was P13.

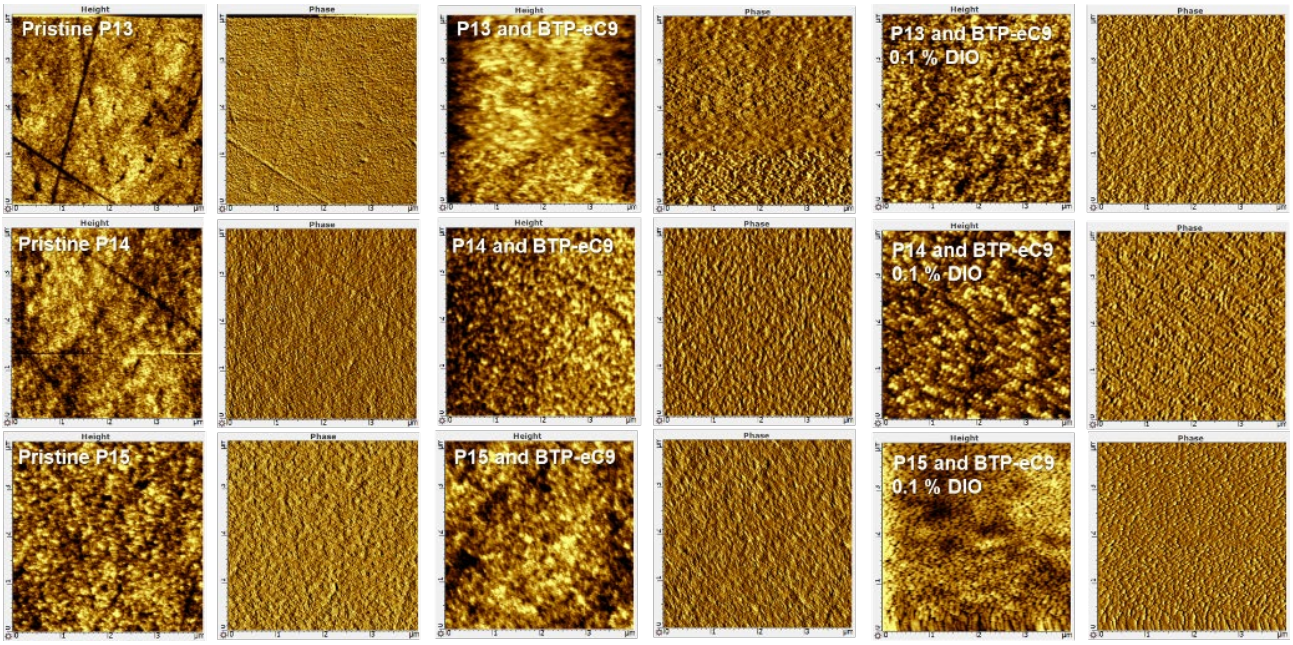

Figure 4. AFM height and phase diagrams of the thin films of pristine P13, pristine P14, pristine P15, P13:BTP-eC9, P14:BTP-eC9, P15:BTP-eC9, P13:BTP-eC9 with 0.1% DIO, P14:BTP-eC9 with 0.1% DIO and P15:BTP-eC9 with 0.1% DIO, 4 μm × 4 μm.

And the actual morphology of these thin films still required more characterizations to investigate by atomic force microscopy (AFM) or grazing-incidence wide-angle X-ray scattering (GIWAXs). Therefore, we firstly charactered the morphologies of three homopolymer thin films and their corresponding blending thin films by AFM (see Fig. 4). Totally, the surface morphologies of these thin films were less roughness, uniform particles and good miscibility. And all pristine homopolymer thin films showed oriented, parallel and thin-lines like fibers in the phase diagrams, which demonstrated that all the homopolymer chains were ordered and closed arrangement by π-π stacking along the polymer backbone. After blending with BTP-eC9, the size of the particles of three in thin films were bigger, and all the oriented and parallel arrangement of polymer backbones became a well-developed nanoscale bicontinuous interpenetrating network fibrous structure. We attributed this to the assistance of the acceptor BTP-eC9, which enhanced the crystalline of polymer/BTP-eC9 particles and stimulate the dense π-π stacking interaction between donors and acceptors. Besides, according to the height and phase diagrams of blending thin films, three homopolymers all exhibited the excellent surface phase separation, which was beneficial for the charge separation and recombination. Obviously, the blending thin films of P13 and P14 both changed from the densely arranged morphology to the loose and porous morphology, although they formed the larger crystalline particles, which indicated that intense aggregation effect and strong crystallinity resulted the unfavorable factors for corresponding OPVs such as excessive phase separation and unbalanced charge transport. Thence, these blending OPV devices with DIO additive had higher FF and lower J_{SC}, comparing with pristine blending OPVs. While P15-based blending OPV device present contrary results, because its thin-film morphology became smaller crystalline morphology and denser morphology. These results of the surface morphologies in active layers all conformed to the variation of PV performance when the DIO was incorporated into the organic active layers.

Furthermore, to investigate in-plane morphologies of the thin films based on three homopolymers, GIWAXs analysis was used to characterized, which revealed more detailed information of molecular arrangement in active layers. Shown in Fig. 5, three homopolymer-only thin films mainly formed in the face-on orientation stacking arrangement, while they also had part edge-on orientation molecular arrangement. After blending with BTP-eC9, all homopolymers had undergone significant changes. For P13 and P14, the blending thin films both showed an obvious enhancement of face-on orientation stacking arrangement. And P15-based blending thin film had a significant increasement of edge-on orientation stacking arrangement, and the face-on orientation stacking arrangement of it also had a slight enhancement. After incorporating with 0.1% DIO, the blending thin films of three all changed to dominate by edge-on orientation stacking arrangement. Except for P15, the face-on orientation arrangements of others almost totally disappeared, which indicated the increase of electron transport properties and the decrease of hole transport properties in their OPV. However, an excellent organic semiconductor device demanded a balance of hole and electron transport properties. Obviously, P13 and P14 blending thin films had the worse balances and the practical J_{SC} of their corresponding OPV devices decreased after adding the additive. While P15-based blending thin film showed a better balance, so that the J_{SC} of its OPV device exhibited a slight increasement with the incorporation of DIO.

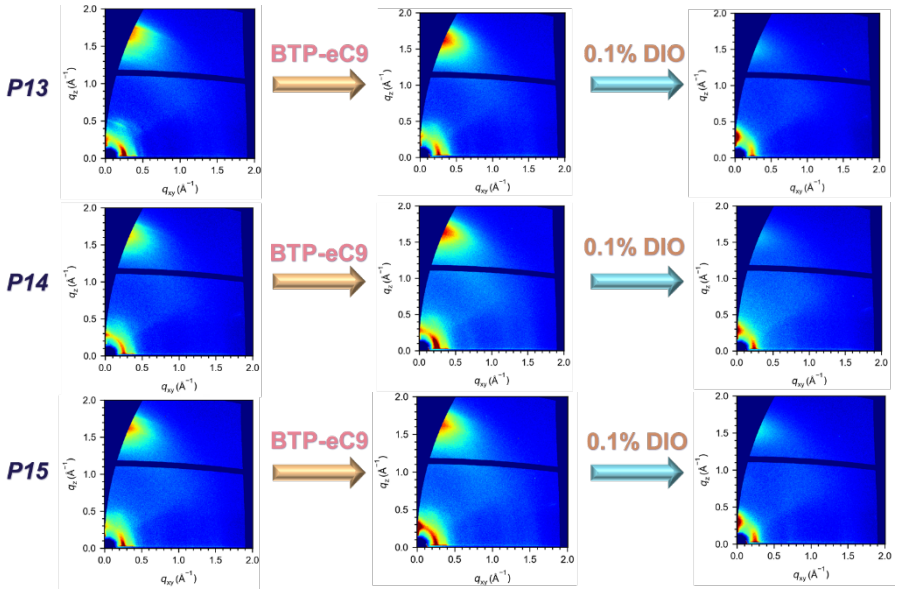

Figure 5. GIWAXs diagrams of the homopolymers-only (left), blending homopolymers/BTP-eC9 (middle) and blending homopolymers/BTP-eC9 with 0.1% DIO (right) thin films.

Conclusion

In this work, we successfully designed and synthesized high performance BDT-based homopolymer donor materials, named P13, P14 and P15, which achieved the highest PCE reported for analogous homopolymer donor materials recently. Meanwhile, we found that the solvent additive, DIO, induced the variation of three homopolymers of the surface and in-plane morphologies in NFA-based blending thin films, such as crystallinity, phase separation and arrangement orientation. And the asymmetrical structure of homopolymer P15 exhibited best PCE of 11.5% with an astonishing J_{SC} in corresponding OPV devices, which indicated that

the asymmetric strategy had its unique advantages in controlling the energy level and morphology of polymer molecular donor materials (reducing the unfavorable factors such as excessive phase separation and unbalanced carrier transport, caused by strong crystallinity and strong aggregation effect). P13-based symmetrical homopolymer had a moderate PV performance owing to its large steric hindrance caused by the large-size chloroform atoms. Besides, we also develop a design idea of homopolymer structure based on BDT units to improve the PV performance in their NFA-based OPVs. Thence, we believe that the future BDT-based homopolymer could achieve higher PV performance through suitable modulation of polymer structure.

Conflicts of interest

There are no conflicts to declare.

Acknowledgements

This work received a financial support from China Scholarship Council (CSC No. 201908510136). The authors also thank Beijing Synchrotron Radiation Facility (BSRF) 1W1A for 2D GIWAXS measurements.

Electronic Supplementary Information

Revisiting benzodithiophene-based donor polymers via thiolalkylation for enhanced photovoltaic performance

Wei Xu,[a§] Li Du [b§], Guojuan Li,[c] Wei He,[d] Cheng Yang,[e] Hongxiang Li,[d] Zhong Cao,[f] Zhengkun Du,[b*] Pei Cheng, [d*] and Donghong Yu[a,g*]

[a.] Department of Chemistry and Bioscience, Aalborg University, Fredrik Bajers Vej 7H, Aalborg East, DK-9220, Denmark

[b.] Al-ion Battery Research Center, College of Energy Storage Technology, Shandong University of Science and Technology, Qingdao, Shandong 266590, China

[c.] National Anti-Drug Laboratory Sichuan Regional Center, Chengdu, 610206 China

[d.] Department of College of Polymer Science and Engineering, State Key Laboratory of Polymer Materials Engineering, Sichuan University, Chengdu, 610065 China

[e.] Key Laboratory of Green Chemistry and Technology of Ministry of Education, College of Chemistry, and State Key Laboratory of Biotherapy, Sichuan University Chengdu, 610064, China

[f.] Hunan Provincial Key Laboratory of Materials Protection for Electric Power and Transportation, and Hunan Provincial Key Laboratory of Cytochemistry, School of Chemistry and Biological Engineering, Changsha University of Science and Technology, Changsha 410114, China

[g.] Sino-Danish Center for Education and Research, DK-8000, Aarhus, Denmark

§ equal contributions to this work

1. General information

All solvents and reagents were of reagent quality, purchased commercially, and used without further purification. NMR spectra were recorded at room temperature on Bruker Avance III^{TM} HD-600 (operating at 600 MHz for ^{1}H NMR). Elemental analysis was measured by Euro Vector EA3000. The UV-visible spectra were obtained on a JASCO V-650 UV-vis spectrometer. Besides, thermo-gravimetric analysis (TGA) both are measured by STA 449 F3 Jupiter®. Atomic Force Microscope (AFM) were acquired by Smart SPM. Photovoltaic performance was characterized under illumination with an AM 1.5G (100 mW cm^{-2}), and the J-V curves were recorded using a Keithley 2400 source meter. The EQE of solar cells were analyzed using Enlitech QE-R Quantum Efficiency Analyzer. 2D GIWAXS patterns of films prepared at different temperatures were obtained at 1W1A Diffuse X-ray Scattering Station, Beijing Synchrotron Radiation Facility (BSRF-1W1A). The monochromatic wavelength of the light source was 1.54 Å. The data was recorded by Pilatus 100 K from DECTRIS, Switzerland. The grazing incidence angles were 0.2°.

The CV (cyclic voltammetry) of the two polymers were recorded on a CH-Instruments Model 650A Electrochemical Workstation. Three-electrode configuration were using in measurement, Pt wires as both working electrode and counter electrode, and a freshly activated Ag wire as Ag/Ag^{+} pseudoreference electrode. To obtain the oxidation potentials, the reference electrode was calibrated by using the ferrocene/ferrocenium (Fc/Fc^{+}), which has an absolutely potential of 4.8 eV versus the vacuum level. And the redox potential of Fc/Fc^{+} was obtained for calibration of 0.418 eV vs Ag/Ag^{+} electrode under the same conditions. And a tetrabutylammonium hexafluorophosphate (Bu_4NPF_6) solution (0.1 M solution in anhydrous acetonitrile) was used as a supporting electrolyte, and N_2 gas was bubbled prior to each measurement. The homopolymers were deposit onto the working electrode by drop-casting from solutions of 10 mg/mL in $CHCl_3$. The HOMO and LUMO levels were calculated from the formulas of E_{HOMO} / E_{LUMO}= -(E_{OX} / E_{RED} + 4.8 - |Fc/Fc^{+}|) eV and $E_g = E_{LUMO} - E_{HOMO}$, where the E_{OX}, E_{RED}, E_g^{opt} and |Fc/Fc^{+}| was determined from the oxidation/reduction onsets in the CV curves, the 1240/(onset absorption band edge of the polymer films) and the half-wave potential of ferrocene in CV curves, respectively.

2. Synthesis of Materials

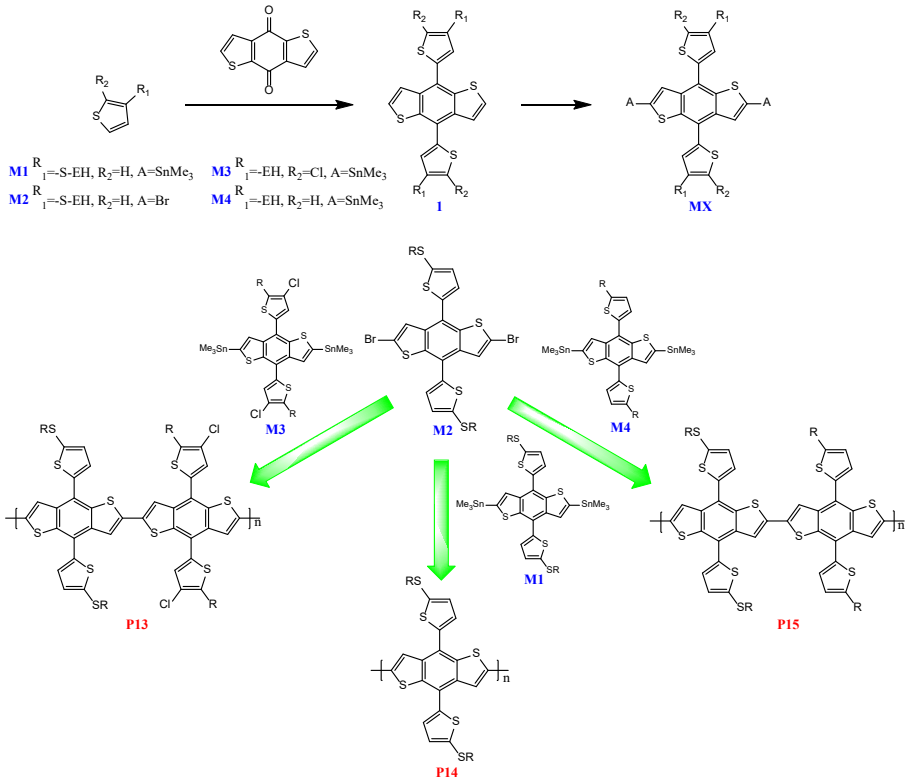

Scheme S1. *The synthetic pathway of* ***P13, P14*** *and* ***P15****.*

(4,8-Bis(4-chloro-5-(2-ethylhexyl)-2-thienyl)-benzo[1,2-b:4,5-b']dithiophene-2,6-diyl)-bis(trimethylstannane) ***(M1)***

Step 1: Under N_2 atmosphere, LDA solution (25.4 mmol) was added dropwise into an anhydrous THF solution (25 mL) of 2-(2′-ethylhexylthio)-thiophene (5.7 g, 25 mmol) at -78 °C. The mixture was stirred for 1.5h, and then the THF solution (25 mL) of benzo[1,2-b:4,5-b']-dithiophene (2.6 g, 12 mmol) was added drop by drop and kept stirring for 3h at -78 °C. Subsequently, the mixture slowly warmed to r.t for another stirring of 12h. Then Tin (II) chloride dihydrate (9.05 g, 37.9 mmol) in 10% HCl (20 mL) was added slowly and stirred for an additional 2h. And the raw material **1** was gotten after quenching with water and extracting with diethyl ether.

Step 2: Compound **1** (2.1 g, 3.2 mmol) of dry THF (30 mL) solution was cooled to -78°C in the round-bottom flask under argon, and n-butyllithium solution in 2.5 M n-hexane (2.56 mL, 6.4 mmol) was added dropwise. After warming up to room temperature, the mixture was stirred for 3 h. Then trimethyl tin chloride solution in 1.0 M THF (6.4 mL, 6.4 mmol) was added at 0°C and the reaction mixture was stirred at ambient temperature overnight. After quenching with water, extracting with dichloromethane (three times), drying over anhydrous sodium sulfate, and concentrating with rotary evaporator, the residue was recrystallized from isopropanol to obtain the target monomer (**M1**) (2.2 g, 70%). **^{1}H NMR** (600 MHz, $CDCl_3$, ppm) δ 7.67 (S, 2H); 7.36 (d, 2H); 7.25 (d, 2H); 2.97 (d, 4H); 1.71-1.67 (m, 2H); 1.59-1.41 (m, 8H); 1.35-1.32 (m, 8H); 0.96-0.92 (dd, 12H); 0.43 (t, 18H).

2,6-dibromo-4,8-bis(5-((2-ethylhexyl)thio)thiophen-2-yl)-benzo[1,2-b:4,5-b']-dithiophene ***(M2)***

A solution of compound **1** (4.2 g, 6.5 mmol) and N-bromosuccinimide (2.35 g, 13.2 mmol) in 30 mL $CHCl_3$, was stirred for 8 h at room temperature under dark atmosphere. Then removed the solvent and purified by the silica gel column chromatography with the eluent (hexane) to obtain monomer **M2** (5.12 g, 98 % yield). **^{1}H NMR** (600 MHz, $CDCl_3$, ppm) δ 7.57 (s, 2H), 7.27 (d, 2H), 7.21 (d, 2H), 2.97 (d, 4H), 1.68-1.64 (m, 2H), 1.55-1.43 (m, 8H), 1.37-1.30 (m, 8H), 0.94 (t, 12H).

(4,8-bis(5-((2-ethylhexyl)thio)thiophen-2-yl)-benzo[1,2-b:4,5-b']dithiophene-2,6-diyl)-bis(trimethylstannane) ***(M3)*** *and (4,8-bis(5-(2-ethylhexyl)thiophen-2-yl)-benzo[1,2-b:4,5-b']dithiophene-2,6-diyl)-bis(trimethylstannane)* ***(M4)***

Following the abovementioned synthesis route of **M1**, the monomers **M3** (2.04 g, 68%) and **M4** (2.34 g, 65%) were obtained, respectively.
M3: **^{1}H NMR** (600 MHz, $CDCl_3$, ppm) δ 7.61 (S, 2H); 7.17 (S, 2H); 2.87 (d, 4H); 1.75-1.68 (m, 2H); 1.60-1.43 (m, 8H); 1.35-1.32 (m, 8H); 0.96-0.92 (dd, 12H); 0.43 (t, 18H).
M4: **^{1}H NMR** (600 MHz, $CDCl_3$, ppm) δ 7.65 (S, 2H); 7.28 (d, 2H); 6.87 (d, 2H); 2.86 (d, 4H); 1.74-1.67 (m, 2H); 1.60-1.43 (m, 8H); 1.34-1.32 (m, 8H); 0.96-0.92 (dd, 12H); 0.43 (t, 18H).

*Synthesis of PBDTT-S-BDTT-Cl (**P13**), PBDTT-S (**P14**) and PBDTT-BDTT-S (**P15**)*

Under argon atmosphere, **M1** (360 mg, 0.37 mmol), **M2** (298 mg, 0.37 mmol), $Pd_2(PPh_3)_4$ (18 mg, 3.0 μmol) and DMF (1 mL) were dissolved in 6 mL dry toluene, and then the mixture was refluxed at 110°C for 24 h. After cooling to room temperature, the reaction was filtered in methanol. Then the precipitate was extracted by using acetone, hexane and DCM with Soxhlet extraction. The crude product was dissolved in 100 mL hot chlorobenzene, and purified via silica gel flash column with a column length of about 3 cm after cooling to r.t, using chlorobenzene as the eluent. Then the concentrated chlorobenzene phase was filtrated in methanol, and vacuum-dried at 45 degrees overnight to obtain the target homopolymer **P13**. Besides, asymmetric homopolymers, **P14** and **P15**, were synthesized via the same ways.

3. Thermal properties and dihedral angles of the homopolymers

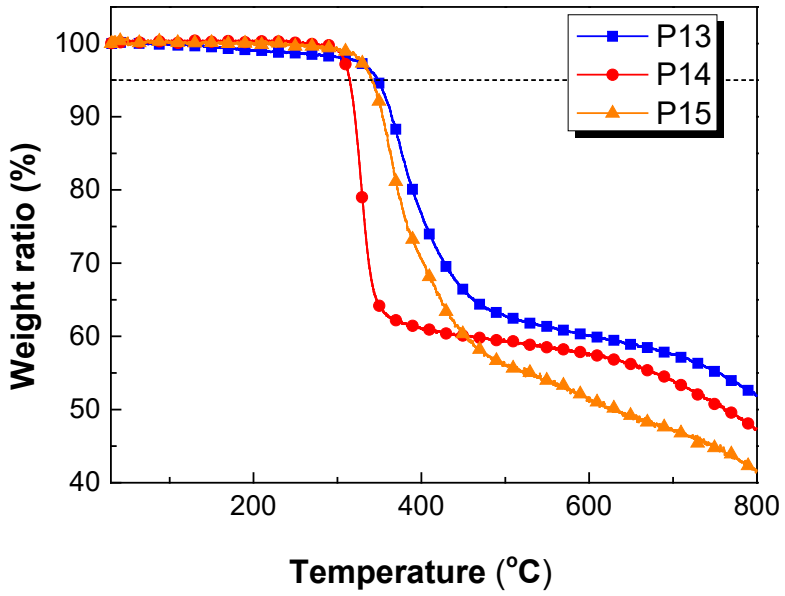

Figure S1. TGA curves of three homopolymers.

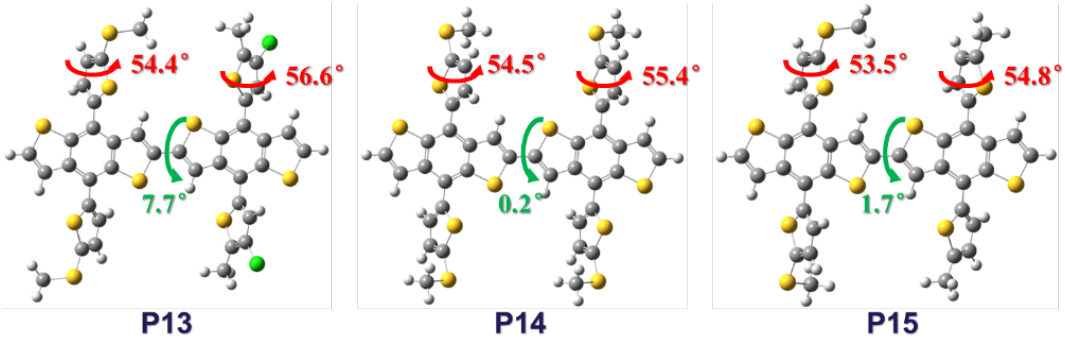

Figure S2. The optimized dimer-moieties structure of the homopolymers by DFT.

4. Fabrication and Optimization of OPV devices

The SM-NFA OPV devices were fabricated on top of a pre-patterned ITO substrate with the conventional structure of ITO/PEDOT:PSS/Active layers/PFN-Br/Ag. After cleaning the ITO with aqueous detergent, deionized water, acetone, and 2-propanol, UV-ozone treatment was applied for 15 min. Filtered PEDOT:PSS (CLEVIOS™ P VP AI 4083) was spin-coated on the ITO substrate to form a 30 nm-thick layer. Then the coated substrates were annealed on the thermal plate at 150 °C for 20 min. After annealing, the chlorobenzene (CB) solution of the blending active substances was spin-cast on top of the PEDOT:PSS layer to produce the active layer with a thickness of 100 nm under 2000 rpm in glovebox, and the coated substrates with active layer were annealed for 5 min at 100 °C. Then PNF-Br were spin-coated on the active layer substrates under 3000 rpm. Finally, the device fabrication was completed by thermal evaporation of 100 nm Ag as the anode in high vacuum (< 10^{-6} mbar).

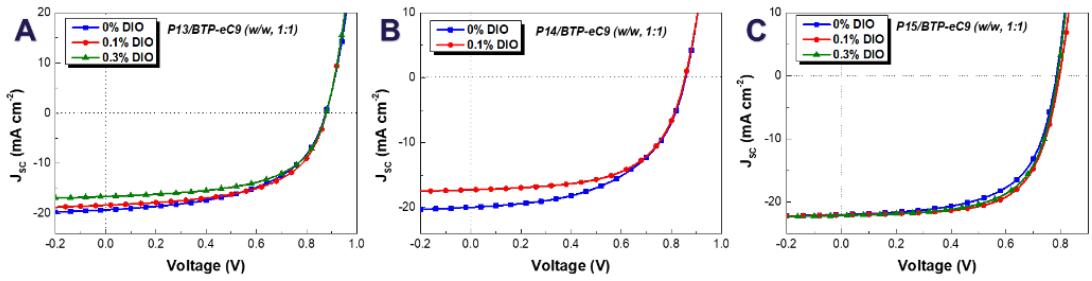

Polymer/ BTP-eC9	D:A	DIO (vol%)	PCE (%)	FF (%)	V_{oc} (V)	J_{sc} (mA cm^{-2})
P13	1:1	0	8.92	52.90	0.88	19.25
		0.1	9.18	57.10	0.88	18.33
		0.3	8.46	58.24	0.88	16.58
P14	1:1	0	9.07	53.15	0.86	19.94
		0.1	8.76	59.54	0.85	17.26
P15	1:1	0	10.61	61.69	0.78	21.97
		0.1	11.53	65.87	0.79	22.04
		0.3	11.20	64.46	0.79	22.10

Figure S3. J-V curves of P13- (A), P14- (B) and P15-based (C) OPV devices with different content of DIO at spin-coating speed of 2000 rpm under an illumination of AM 1.5 G, 100 mW cm^{-2}. Corresponding table (bottom) of Photovoltaic performance.

5. Properties of charge transfer, dissociation and recombination

The hole mobilities of the active layer were measured by applying the space charge limited current (SCLC) method to the J-V measurements of the devices. The hole-only homopolymer devices were designed as the semiconductor diodes with the structure of ITO/PEDOT:PSS/Active layer/Au, and calculated from the following equation[1]:

$$J_{SCLC} = (9/8)\varepsilon_r\varepsilon_0\mu(V^2/L^3)\exp(0.89r\sqrt{V/L})$$

where J is the current density, ε_r is the dielectric constant of the polymers, ε_0 is the permittivity of the vacuum, μ is the hole mobility, L is the thickness of the blend films, $V = V_{appl} - V_{bi}$, where V_{appl} is the applied potential, and V_{bi} is the built-in voltage which results from the difference in the work function of the anode and cathode.

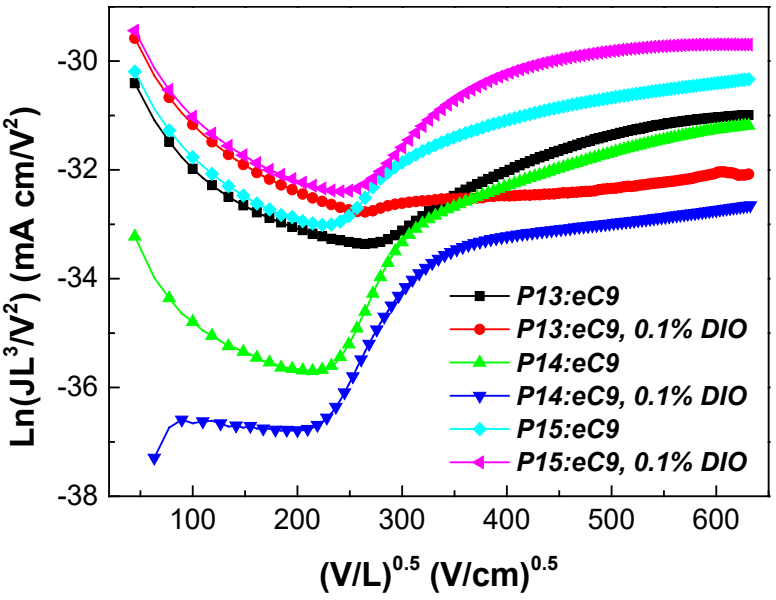

Figure S4. Ln(JL^2/L^3)-$(V/L)^{0.5}$ plots of hole-only devices based on P13:BTP-eC9, P13:BTP-eC9 (0.1% DIO), P14:BTP-eC9, P14:BTP-eC9 (0.1% DIO), P15:BTP-eC9, P15:BTP-eC9 (0.1% DIO).

Charge dissociation probability was characterized by the function of photogenerated current density (J_{ph}) *versus* effective applied voltage (V_{eff}). The J_{ph} is defined as the difference between J_L and J_D, where J_L and J_D are the current density of devices under light (100 mW cm^{-2}) and dark, respectively. $V_{eff} = V_0 - V$, where V_0 is the voltage when $J_{ph} = 0$ and V is the applied voltage during the measurement. When the reverse voltage is greater than 2 V, the recombination is suppressed by a high internal electric field. Thus, J_{ph} will reach the saturated current density (J_{sat}). Consequently, $P_{diss} = J_{ph}/J_{sat}$ could be used to describe the charge dissociation probability.[2, 3] And the higher P_{diss} is indicated the more effective charge dissociation. Besides, the relationship of J_{SC} and the light intensity (I) is $J_{SC} \propto I^{\alpha}$, where α is the degree of biomolecular recombination. When $\alpha = 1$, dissociated free charges don´t recombine during the movement process, and are all collected by the electrode, implying the recombination can be ignored. If α is less than 1, the bimolecular recombination will be present in the devices, and the smaller the value of α indicates the stronger bimolecular recombination. Meanwhile, $V_{OC} \propto (nkT/q)\cdot\ln(I)$, where K represents the Boltzmann constant, T is the Kelvin temperature, and q is the elementary charge. If the slope is close to 2kT/q, the trap-assisted recombination will be inside the devices.[4, 5]

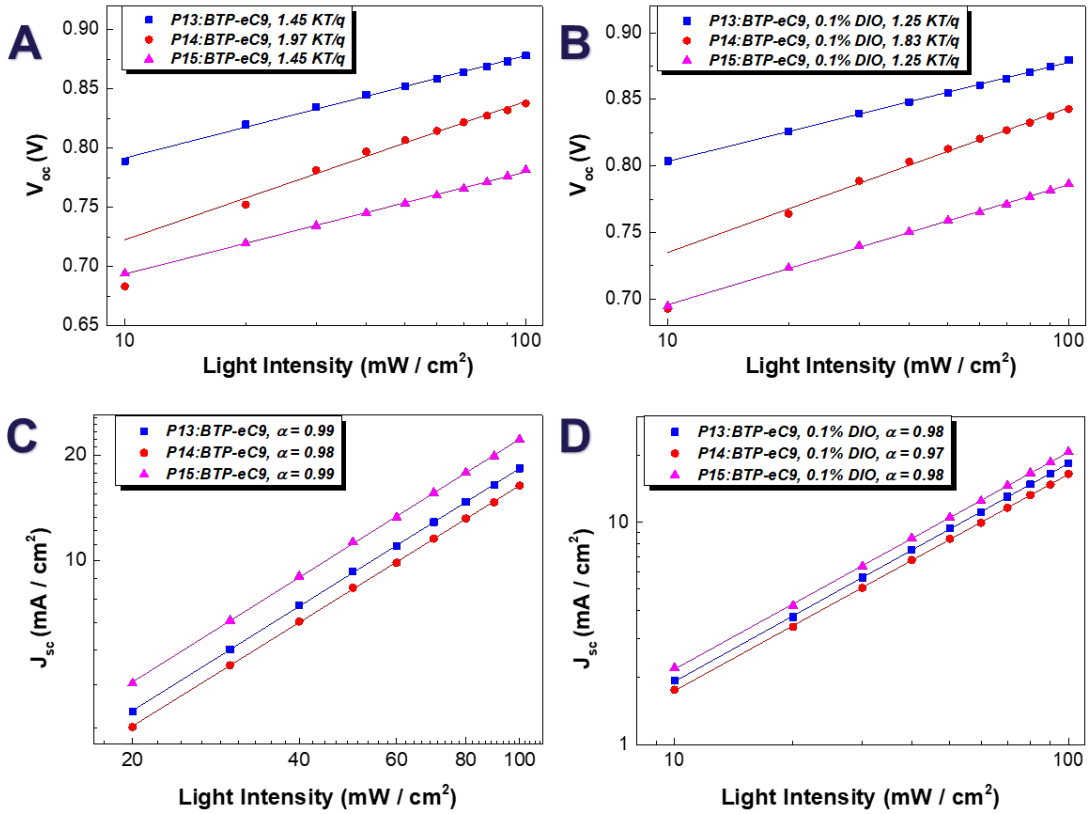

Figure S5. Dependence diagram of V_{OC} (A, B) and J_{SC} (C, D) as a function of light intensity in OPV devices based on three homopolymers.

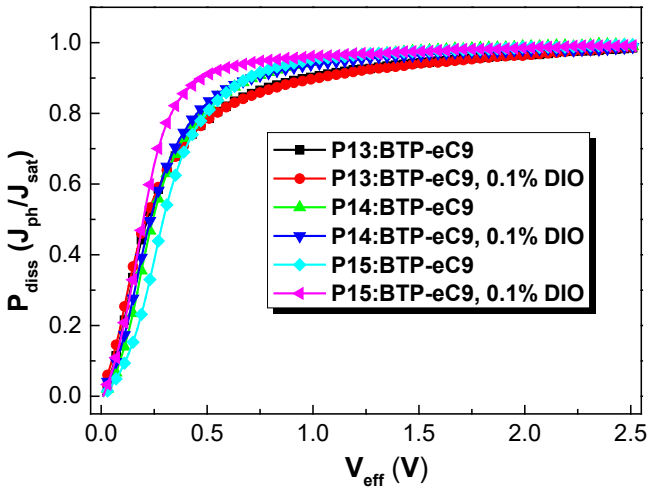

Figure S6. P_{diss} vs V_{eff} Plots of OPV devices based on P13:BTP-eC9, P13:BTP-eC9 (0.1% DIO), P14:BTP-eC9, P14:BTP-eC9 (0.1% DIO), P15:BTP-eC9, P15:BTP-eC9 (0.1% DIO).

6. Reference

[1] C. Melzer, E. J. Koop, V. D. Mihailetchi, P. W. M. Blom, Hole Transport in Poly(phenylene vinylene)/Methanofullerene Bulk-Heterojunction Solar Cells, Advanced Functional Materials, 14 (2004), 865-870

[2] P. W. M. Blom, V. D. Mihailetchi, L. J. A. Koster, D. E. Markov, Device Physics of Polymer:Fullerene Bulk Heterojunction Solar Cells, Advanced Materials, 19 (2007), 1551-1566

[3] L. Huo, T. Liu, X. Sun, Y. Cai, A. J. Heeger, Y. Sun, Single-Junction Organic Solar Cells Based on a Novel Wide-Bandgap Polymer with Efficiency of 9.7%, Advanced Materials, 27 (2015), 2938-2944

[4] L. J. A. Koster, V. D. Mihailetchi, R. Ramaker, P. W. M. Blom, Light intensity dependence of open-circuit voltage of polymer:fullerene solar cells, Applied Physics Letters, 86 (2005), 123509

[5] A. K. K. Kyaw, D. H. Wang, D. Wynands, J. Zhang, T.-Q. Nguyen, G. C. Bazan, A. J. Heeger, Improved Light Harvesting and Improved Efficiency by Insertion of an Optical Spacer (ZnO) in Solution-Processed Small-Molecule Solar Cells, Nano Letters, 13 (2013), 3796-3801

PAPER IV

The impact of position-sensitive fluorination on photovoltaic performance of donor-acceptor polymer/Y-type small molecule based organic solar cells

Wei Xu,[a§] Wei He,[b§] Guojuan Li,[c] Cheng Yang,[d] Hongxiang Li,[c] Zhong Cao,[e] Zhengkun Du,[f*] Pei Cheng,[c] and Donghong Yu[a,g*]

[a.] Department of Chemistry and Bioscience, Aalborg University, Fredrik Bajers Vej 7H, Aalborg East, DK-9220, Demark

[b.] College of Polymer Science and Engineering, State Key Laboratory of Polymer Materials Engineering, Sichuan University, Chengdu, 610065 China

[c.] National Anti-Drug Laboratory Sichuan Regional Center, Chengdu, 610206 China

[d.] Key Laboratory of Green Chemistry & Technology of Ministry of Education, College of Chemistry, Sichuan University, Chengdu 610064, Sichuan, China

[e.] Hunan Provincial Key Laboratory of Materials Protection for Electric Power and Transportation, and Hunan Provincial Key Laboratory of Cytochemistry, School of Chemistry and Biological Engineering, Changsha University of Science and Technology, Changsha 410114, China

[f.] Al-ion Battery Research Center, College of Energy Storage Technology, Shandong University of Science and Technology, Qingdao, Shandong 266590, China

[g.] Sino-Danish Center for Education and Research, DK-8000, Aarhus, Denmark

§ equal contributions to this work

Abstract

This work, the novel copolymers PBDT-DTBT and PBDT-DFDTBT with 4-alkoxy-3,5-difluorophenyl flanking were synthesized as the donor materials for non-fullerene acceptor (NFA) polymer solar cells (PSCs). Both two materials showed excellent open circuit voltage (V_{OC}) in PSCs blending with of polymer:BTP-eC9, where were PBDT-DFDTBT-based PSCs of 0.90 V and PBDT-DTBT-based PSCs of 0.87 V, respectively. Astonishingly, PBDT-DTBT-based devices exhibited superior power conversion efficiency (PCE) of 12.56%, which was almost two times of PBDT-DFDTBT-based devices. Interestingly, we found that photovoltaic performance of two copolymer materials are completely different between fullerene and non-fullerene PSCs, i.e., the PBDT-DFDTBT has better PCE than PBDT-DTBT in fullerene-based PSCs owing to the higher V_{OC}. And we attribute this case to the excessive fluorine atoms in polymer donor materials, which obstructed the charge separation and hole mobility process and occurred more charge recombination in NFA

PSCs. These results indicate that a promising strategy of improving the photovoltaic efficiencies by controlling fluorine modification could be valid for NFA-PSCs.

1. Introduction

The copolymer donor materials have drawn a huge attention in organic photovoltaic (OPV) devices nowadays due to their specific advantages of lightweight, flexible and solution processable manufacturing. Many remarkable achievements have been gotten in improving the photovoltaic performance through architecting the molecular structure of activity layer in polymer solar cells (PSCs). Up to now, dramatical elevation of power conversion efficiency (PCE) in PSCs has been achieved since the small molecular (SM) non-fullerene acceptor (NFA) materials were widely and further studied. The D-A strategy of PSCs adopting p-type copolymers as the donor (D) and n-type SM NFAs as the acceptor (A) have achieved the astonish PCE of over 15%, far exceeding PCBM-based fullerene solar cells. Despite this, the study of NFA solar cells still face many challenges such as improvement of the devices stability, open circuit voltage (V_{OC}) loss and charge separation and recombination, etc. As well known, most among these characterizations of the devices could be attributed to the pronounced impact of ordering molecular arrangement and aggregate morphology of the active layers. Therefore, much attempt has been made to optimize the structure of the bulk heterojunction (BHJ) in PSCs by chemical modification of the structure of the copolymer donor materials, which possess more processable potential on morphology optimization. Recently, benzo[1,2-b:4,5-b']dithiophene (BDT) unit with fluorinated phenyl flanking was demonstrated that fluorine-modification polymer exhibited wider optical bandgap and lower lying highest occupied molecular orbital (HOMO). Meanwhile, fluorinated copolymer as a promising candidate of electron-rich donor materials, the inter- or intramolecular strong C−F···H interaction leads to smaller backbone chain distance and more face-on orientation, which could improve the charge mobility, resulting in a higher short circuit current (Jsc) and fill factor (FF).

In this work, the BDT monomer, the D moiety containing two fluorine atoms (BDT-PDF), was copolymerized with 4,7-di(4-(2-ethylhexyl)-2-thienyl)-2,1,3-benzothiadiazole (DTBT) unit or 5,6-difluoro-4,7-di(4-(2-ethylhexyl)-2-thienyl)-2,1,3-benzothiadiazole (DFDTBT), the A moieties, to obtain two novel polymers named PBDT-PDF-DFDTBT (P16) and PBDT-PDF-DTBT (P17), respectively, by Pd-catalyzed Stille coupling reaction. Two polymers both exhibited good thermal stabilities and medium wide optical bandgap. Although two copolymer-based photovoltaic devices showed similarly superior V_{OC} when blending with NFA acceptor, other photovoltaic performances,

such as PCE, J_{SC}, charge mobilities or charge recombination properties, were tremendously different. Under the illumination of AM 1.5, 100 mW cm^{-2}, the J_{SC} and PCE of PBDT-PDF-DTBT-based PSCs were 20.8 mA/cm^{-2} and 12.56%, respectively, which was much higher than ones in PBDT-PDF-DFDTBT-based PSCs. Especially, the hole mobility of PBDT-PDF-DTBT-based solar cell was 3.5×10^{-4} cm^2 V^{-1} s^{-1}, which was 3 times the order of magnitude higher than PBDT-PDF-DFDTBT-based device. Interestingly, the photovoltaic performance of two polymers were practically identical in fullerene solar cells, which was markedly different from NFA-based PSCs. Through a comprehensive investigation, we attribute the consequence to the exceed fluorine content of polymer donor, which obstructs the charge separation and hole mobility properties and generates more charge recombination in NFA PSCs.

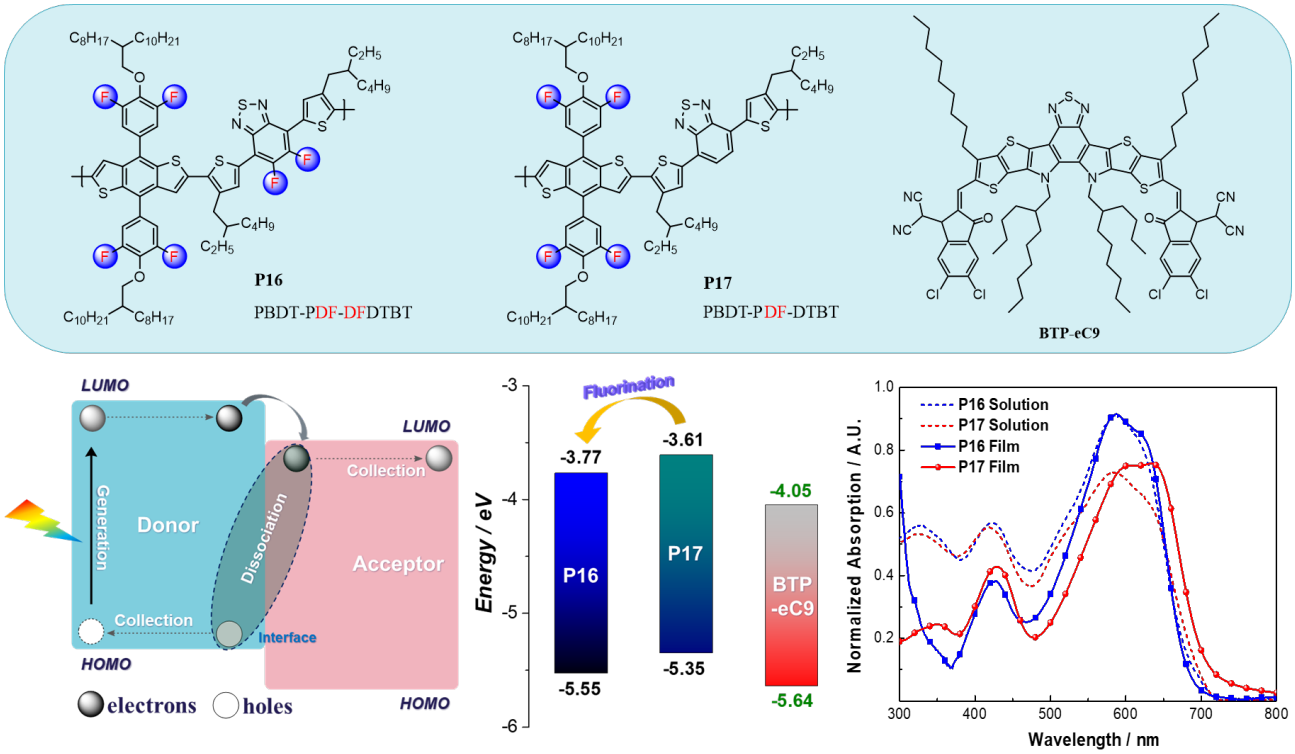

Figure 1. The molecular structure of PBDT-Pff-DFDTBT (**P16**) and PBDT-Pff-DTBT (**P17**). Schematic showing photogeneration, charge separation process and charge collection across the D:A heterojunction in polymer solar cells. HOMO/LUMO energy levels schematic of copolymers and acceptor. Normalized UV-vis absorption curves of two copolymers in chloroform and films.

2. Results and Discussion

Syntheses and characterization

The synthesis route for D-A strategy donor materials, the BDT-PDF unit 4,8-bis(3,5-difluro-4-(2-octyldodecyl)phenyl)-benzo[1,2-b:4,5-b']dithiophene as the D moiety and DTBT unit 4,7-di(4-(2-ethylhexyl)-2-thienyl)-2,1,3-benzothiadiazole as the A moiety, were shown in Scheme S1 of Electronic Supplementary Information (ESI). To increase the C−F···H band interaction, we designed another difluorinated A moiety, which was modified with two more fluorine on DTBT. Herein, the donor copolymers, **PBDT-PDF-DFDTBT** (P16) and **PBDT-PDF-DTBT** (P17), were obtained after further purifying with methanol, acetone, n-hexane, and chloroform by using Soxhlet extraction. All details of the synthetic pathway were recorded in ESI. Two polymers were readily dissolving in most organic solvent, such as chloroform (CF), chlorobenzene (CB), and o-dichlorobenzene (o-DCB), which indicated that they were better for solution process. Through gel permeation chromatography (GPC), the number-average molecular weight (M_n) and the polydispersity index (PDI) of two polymers were measured with calibration against polystyrene standards and listed in the Table 1. The number average molecular weights (M_n) of P16 and P17 were found to be 12.1 and 15.3 KDa with PDI of 1.77 and 1.92, respectively. Despite the polymerization of two polymers were on same conditions, the difference of M_n and PDI still existed, which was attributed to the polymerization kinetics or the polymers' solubility. Obviously, two copolymer materials both exhibited good thermal stability according to measurement results of thermogravimetric analysis (TGA). As shown in Table 1, the decomposition temperatures (T_d) for 5% weight loss of P16 and P17 were 406 °C and 420 °C, respectively, and the weight loss versus temperature curves were exhibited in Figure S2.

Optical and electrochemical properties

The normalized UV-vis absorption spectra of two polymers in chloroform solution and thin films was exhibited in Figure 1. The UV absorption spectrum of P16 and P17 in solution was similar, meaning that the introducing of fluorine in A moiety infected little on optical bandgap. Whereas, in thin film P17 showed 17 nm bathochromic shift of maximum absorption peak comparing with P16, which indicated that P17 had a tighter intermolecular π-π stacking behavior along the polymer backbone. Furthermore, demonstrated as the temperature dependent UV absorption curves (Figure S3), the hypsochromic shift of P17 along with the increased temperature was more distinct and sensitive than P16, which indicated π-π stacking disaggregation degree of P17 was higher than P16. On the other hand, P16 still maintained shoulder peak next to the maximum absorption even under such high temperature in DCB, which indicated that C−F···H band interaction of P16 was stronger than P17. There are less π-π conjugated interaction and more hydrogen bond interaction are in P16, because the fluorine atoms generate strong inductive effect which impairs electron delocalization area of delocalized π bond in A moiety. Obviously, more fluorine atoms hinder the better formation of

conjugation effect, instead. Moreover, in thin films, the absorption edge wavelengths (λ_{edge}) and the optical band gaps (E_g^{opt}) could be clearly distinguished in the UV absorption spectrum, which were summarized into Table 1.

Table 1. Molecular, thermal, optical, and electrochemical properties of two copolymers

Sample	M_n (KDa) [a]	PDI [a]	T_d (°C) [b]	λ_{edge} [nm]	E_g^{opt} [eV] [c]	HOMO [eV] [d]	LUMO [eV] [e]	HOMO [eV] [f]	LUMO [eV] [f]
P16	12.1	1.77	405	698	1.78	-5.55	-3.77	-5.16	-2.79
P17	15.3	1.92	421	712	1.74	-5.35	-3.61	-5.09	-2.70

[a] M_n and PDI of the copolymers were determined by GPC using polystyrene standards in $CHCl_3$; [b] Temperature at 5% weight loss at a heating rate of 10 °C min^{-1} under N_2 atmosphere; [c] Evaluated from the absorption band edge of the polymer films and determined by the equation E_g^{opt} = 1240/(onset band edge of absorption); [d] Calculated from the CV equation E_{HOMO} = - (E_{OX} + 4.8 - |Fc/Fc^+|) eV; [e] E_{LUMO} = E_{HOMO} + E_g^{opt}; [f] Calculated via DTF

The thin-films electrochemical characteristics of P16 and P17 were studied by cyclic voltammetry (CV, Figure S2) as detail-instructed in the ESI. According to the instruction of ESI, the onset oxidation potentials (E_{OX}) of P16 and P17 were 1.1 and 0.9 V, which corresponding to highest occupied molecular orbital (HOMO) of -5.55 and -5.35 eV, respectively. The HOMO level of fluor-substituted DTBT-containing polymer was ~0.2 eV lower than one of non-fluoridated DTBT-containing polymer, indicating that fluorine atoms had a significant electron-withdrawing effect on the molecular backbone of polymers to induce the deepener HOMOs. A lower lying HOMO energy level corresponds to a higher open circuit voltage (V_{OC}), which means that P16-based PSC will have larger V_{OC} than P17. And lower unoccupied molecular orbital (LUMO) was determined from the difference of E_{HOMO} and E_g^{opt}, which were found of -3.77 eV for P16 and -3.61 eV for P17, respectively. Shown in Figure 1, comparing to the LUMO of BTP-eC9, P16 was closer lying than P17, which indicated the higher efficient exciton dissociation could be expected in P16-based OPV devices. All the optical and electrochemical characters were recorded together in Table 1.

Molecular Simulations

For further investigation of molecular structure property of two polymers, density-functional theory (DFT) was used to simulate and calculate the thermodynamically optimal structure and corresponding energy levels on the base of Gaussian 16 program with B3LYP functional at the 6-31G(d,p) basis set

level in the gas phase. To reduce the computational burden on the server, all alternative side alkyl chains were substituted with methyl groups. As shown in the Figure 3, the simulated consequence with electron cloud density distribution demonstrated that LUMOs of P16 and P17 centralized on the DTBT moieties, and HOMOs of ones evenly distributed along the molecular π-conjugation backbone. Obviously, owing to existing of the highly electronegative fluorine atoms, neighboring DTBT unit presented a phenomenon of reducing electron cloud density. Besides, intramolecular intense repulsion between side-phenyl o-Hydron and benzodithiophene 3-b-Hydron induced a large torsion angle between phenyl side chains and benzodithiophene moiety, which implied that polymer molecular backbone preferred 3D three-dimensional structure rather than 2D π-conjugated planar structures in thermodynamics. Comparing with the planar structure, 3D structure was more beneficial for forming of C−F···H band interaction between the neighboring polymer backbones. Dihedral angles were also obtained from the optimal structure by the DFT (Figure S1) and recorded in the Table S1. Although A moiety of P16 represent better rigid plane structure owing to the C−F···H interaction between fluorine atoms on benzothiadiazole and hydron atoms on thiophene, bigger included angle between D moiety and A moiety weaken overall rigidity flatness. And a stereoscopic structure between the phenyl flanking and polymer backbone made the polymer made the A_3 more influential in the conjugated plane of the polymer backbone. Hence, P17 could be better in generation of π-π stacking behavior.

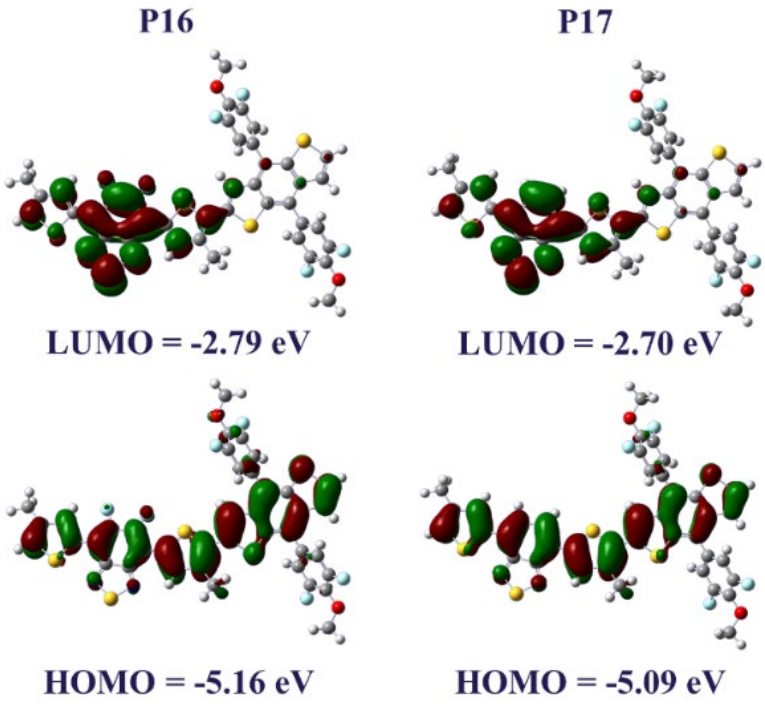

Figure 3. The calculated electron distributions at HOMO/LUMO orbitals of **P16** and **P17**, performed at the level of B3LYP/6-31G(d, p) based on density functional theory (DFT).

Photovoltaic Performance and morphology of SM NFA-Based Solar Cells

To evaluate the photovoltaic potentials of two novel donor polymer materials, a series of polymer solar cells with conventional structure, BTP-eC9 as an electron acceptor, were fabricated as describing in the **ESI**. The PSC device configuration is ITO/PEDOT:PSS/polymer:BTP-eC9/PFN-Br/Ag, where ITO is indium tin oxide as the anode, PEDOT:PSS is poly(3,4-ethylenedioxythiophene):polystyrene sulfonate as the hole transport layer (HTL), PFN-Br as the electron transport layer (ETL) is poly(9,9-bis(3'-(N,N-dimethyl)-N-ethylammoinium-propyl-2,7-fluorene)-alt-2,7-(9,9-dioctylfluorene))-dibromide, Ag is silver as the cathode, and the active layer is the bulk-heterojunction structure of donor and acceptor with 100 nm thickness. Through optimizing the fabrication conditions, e.g., weight ratio of donor and acceptor, content of solvent additive and spin-coating speed of active layer, the best photovoltaic performance of PSC devices were obtained. As shown in Table 2, P17-based PSC presented the best PCE of 12.71% with FF of 69.9%, J_{SC} of 21.08 $mA \cdot cm^{-2}$ and V_{OC} of 0.86 V, under conditions of 10:12 (w/w) of donor-to-acceptor weight ratio, non-additive and spin-coating of 2000 rpm (see Table S2, S3 and S4 for details). And corresponding current density-voltage (J-V) curves and external quantum efficiency (EQE) spectra of the solar cells are illustrated in Figure 4. Interestingly, although the manufacture condition was most optimized, P16-based device showed a lower PCE of 6.46% with FF of 51.83%, J_{SC} of 13.78 $mA \cdot cm^{-2}$ and V_{OC} of 0.90 V. Obviously, the PCE of P16-based device was much lower than P17, in spite of the higher V_{OC} of P16-based device. The EQE curves under optimal conditions indicated that the integrated J_{SC} was calculated of 13.58 $mA \cdot cm^{-2}$ for P16 and 20.82 $mA \cdot cm^{-2}$ for P17, which were consistent to their J-V experimental results.

For further investigating the difference between two polymer materials in PSCs, the charge mobilities and charge dissociation abilities were characterized as the described instructions in ESI. As shown in Figure 5, the carrier mobilities of two materials were studied by Space-Charge-Limited Current (SCLC) method. Both of them were fabricated to hole-only and electron-only devices, respectively, where the structure of hole-only device was ITO/PEDOT:PSS/Donor: Acceptor(10:12, w/w)/Au and the structure of electron-only device was Ag/ZnO/ Donor: Acceptor (10:12, w/w)/Ag. Besides, hole-

only device with only donor material was also made for reference as above. According to the formula of SCLC method, the hole mobility properties were found of 2.12×10^{-7} cm^2 V^{-1} s^{-1} for P16-based OPVs and 3.50×10^{-4} cm^2 V^{-1} s^{-1} for P17-based OPVs, respectively. Comparing with donor only devices, the hole mobility of P17-based NFA device was approximate, while mobility of P16-based device was unexpectedly much lower. And the electron mobility properties were obtained of 3.80×10^{-5} cm^2 V^{-1} s^{-1} for P16 and 8.89×10^{-5} cm^2 V^{-1} s^{-1} for P17, respectively. The P_{diss} (charge dissociation abilities, see ESI for details) of P16- and P17-based OPVs (see **Figure 5c**) was listed in the Table 3 together with the charge carrier mobilities. Obviously, the P17-based device performed better charge mobility and charge dissociation ability than P16. Besides, the charge recombination were characterized by the function diagrams of the light intensity against J_{SC} and V_{OC} in OPVs, (see Figure 4) P16-baesd device was found of α value of 0.95 and slope of 1.40 KT/q and P17-based device was found of α value of 0.96 and slope of 1.02 KT/q, which indicated that the bimolecular recombination of two could nearly be ignored and there was more trap-assisted recombination inside of P16-based device. Interestingly, the photovoltaic performance of two polymer materials were opposite when they were applied into the fullerene PSCs. As shown in Table S5, P16-based devices exhibited better PCE of 4.42% with FF of 62.87%, J_{SC} of 6.83 $mA \cdot cm^{-2}$ and V_{OC} of 1.02 V than P17, affording a PCE of 3.92% with FF of 63.01%, J_{SC} of 6.89 $mA \cdot cm^{-2}$ and V_{OC} of 0.90 V, in OPVs blending with $PC_{71}BM$. Except for the higher V_{OC}, other characterizations of P16-based PSC were similar to P17, and finally affording higher PCE. Moreover, two donor materials presented identical charge recombination and charge dissociation ability, where the α and KT/q value of two polymers were almost equal. But other different SM-NFAs were paired with P16 and P17 in PSCs, as illustrated in the Table S5, the result indicated that photovoltaic performance of P17-based solar cells were more excellent than P16-based devices, which was in accord with former result in BTP-eC9-blending OPVs. Obviously, donor materials modifying with fluorine atoms on A moiety performed worse charge separation, weaker charge mobility ability and more charge recombination in SM-NFA PSCs.

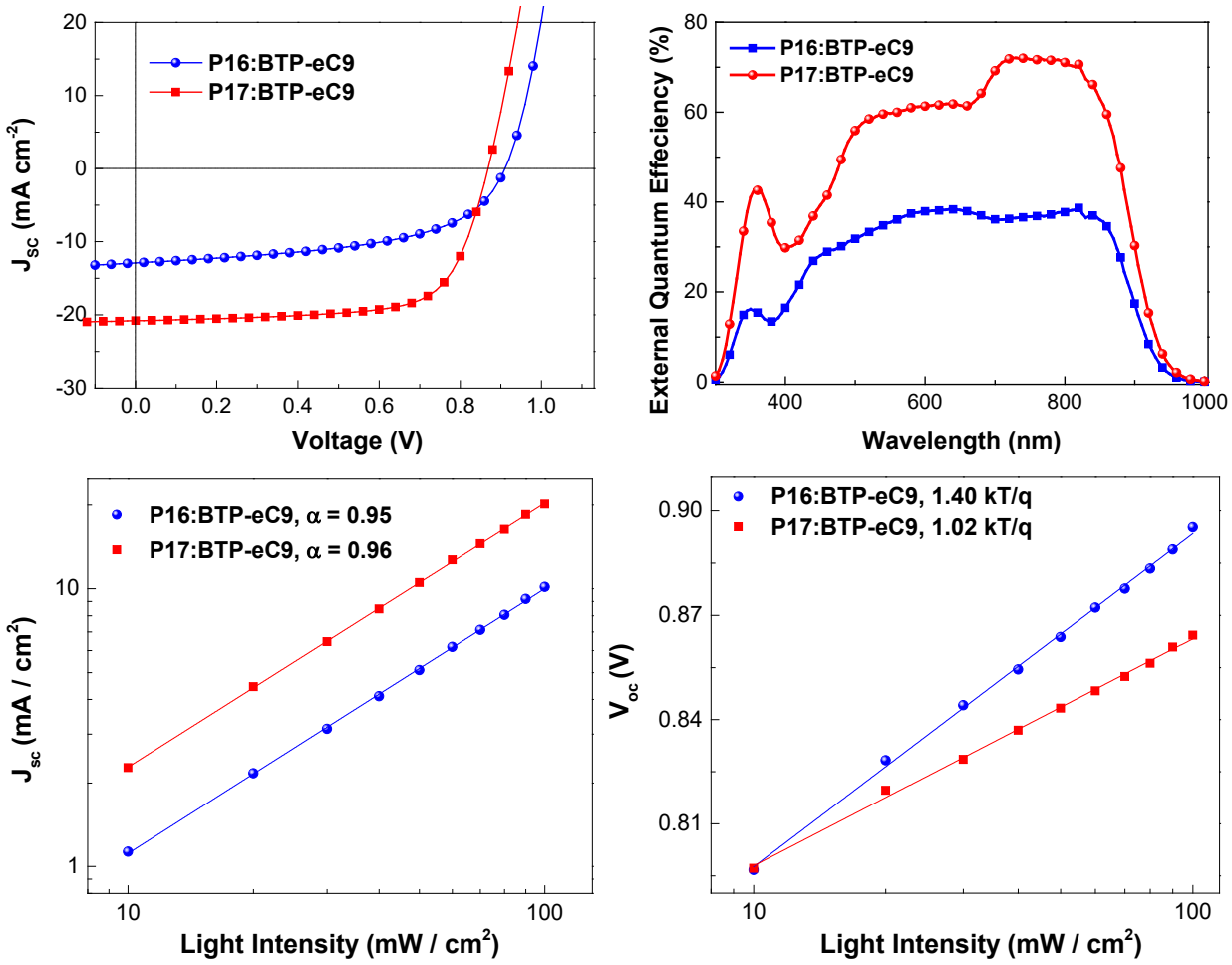

Figure 4. The J-V characteristics and EQE curves of P16:BTP-eC9 and P17:BTP-eC9. Dependence diagram of J_{SC} (a) and V_{OC} (b) as a function of light intensity in P16:BTP-eC9 and P17:BTP-eC9 devices.

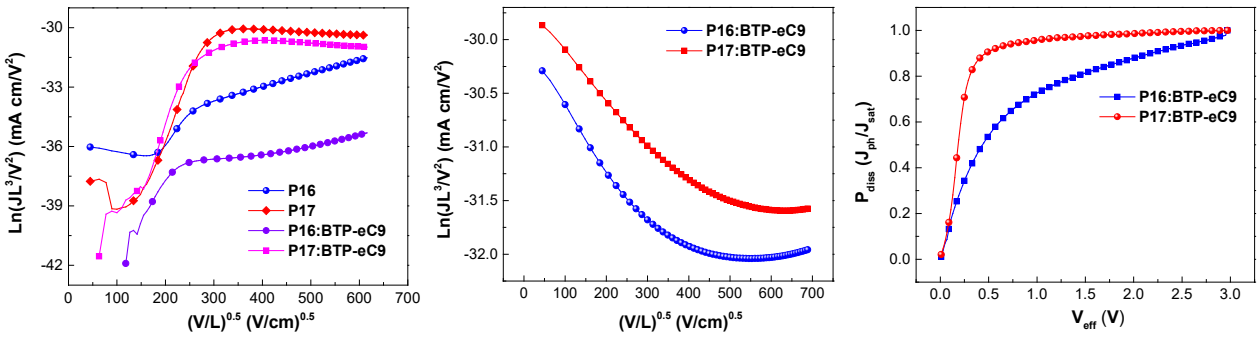

Figure 5. $Ln(JL^3/V^2)$ vs $(V/L)^{0.5}$ plots for the measurement of the carrier mobility in Polymers:BTP-eC9 blends by the SCLC method: (a) hole-only devices and (b) electron-only devices; and (c) charge dissociation probabilities (P_{diss}) vs effective voltage (V_{eff}) curves of NFA-based OPVs.

Table 2. Photovoltaic performance of NFA-based polymer solar cells.

Polymer/ BTP-eC9	D:A (w/w)	FF (%)	V_{OC} (V)	J_{SC} (mA cm^{-2})	J_{SC} [a] (mA cm^{-2})	PCE (%) Best/Ave [b]
P16	10:12	51.83	0.90	13.78	12.53	6.46/6.08
P17	10:12	69.90	0.86	21.08	20.42	12.71/12.26

[a] Calculated from EQE integrated short circuit density, [b] Average PCE is calculated from 15 parallel devices.

Table 3. Charge mobility and dissociation properties of P16- and P17-based OPVs

Items	μ_h (cm^2 V^{-1} s^{-1})	μ_e (cm^2 V^{-1} s^{-1})	μ_h/μ_e	P_{diss} [a]
P16:BTP-eC9	2.12×10^{-7} /1.11×10^{-6} [b]	3.80×10^{-5}	5.58×10^{-3}	0.88
P17:BTP-eC9	3.5×10^{-4} /5.01×10^{-4} [b]	8.89×10^{-5}	3.94	0.99

[a] The charge dissociation probability (P_{diss}) is described by $P_{diss} = J_{ph}/J_{sat}$; [b] Corresponding polymers-only $Ln(JL^3/V^2)$ vs $(V/L)^{0.5}$ plots were present in ESI.

In order to obtain further understanding of the photovoltaic performance difference between two donor materials in NFA PSCs, the most notable devices with BTP-eC9 as acceptor, atomic force microscopy (AFM), transmission electron microscope (TEM) and grazing-incidence wide-angle X-ray scattering (GIWAXs) were used to investigate the nanoscale morphologies and molecular arrangement. As shown in Figure 7a, it could be seen that the heterojunction morphologies of pristine P16 and P17 films were face-on orientation, and it was obvious that the morphology orientation of P17 film was more ordered. Interestingly, the AFM image showed that the main chain entanglement of the two polymer donors seemed to have a certain orientation. By contrast, P16 had more C-F···H bonds, which made the cross-linked polymer chains more closely stacked, so that the overall arrangement was more regular and had more obvious orientation. P17 due to less binding of C-F···H bonds made the staggering between chains more disordered and more closely arranged. When blended with the NFA acceptor BTP-eC9, P16-based blend film showed same smooth surface topographies and domain sizes as P17-based blend film (Figure 6), which indicated the good

miscibility and desirable phase separation of all D-A blending thin films. As shown in Figure 7a, the orientation of the face-on morphology in P16- and P17-based blend films were enhanced comparing with pristine films, and the AFM images showed that the planar stacking of the blended heterojunction was enhanced. In addition, P16-based blend film also had obviously partly edge-on morphology orientation leading to its more impure phase morphology, which indicated that P16 blended film exhibited worse rigid conjugated structure along the polymer backbone and had weaker π-π stacking structure. And according to the AFM and TEM images of Figure 6, although the surface roughness of the blended film of P16 was slightly better than P17, former blended phase separation was far worse than latter one. Moreover, P17 blend films exhibited better polymer phase separation and are characterized by a well-developed nanoscale bicontinuous interpenetrating network fibrous structure. The out-of-plane and in-plane cut pattern of blended films were presented in the Figure 7b and 7c, a (010) diffraction peak along the q_z axis of 1.82 and 1.85 $Å^{-1}$ for P16/BTP-eC9 and P17/BTP-eC9, respectively, which correspond to the d-spacing of 3.45 and 3.40 Å, respectively, which revealed that P17 BHJ film had closer π-π stacking structure along the polymer backbone.

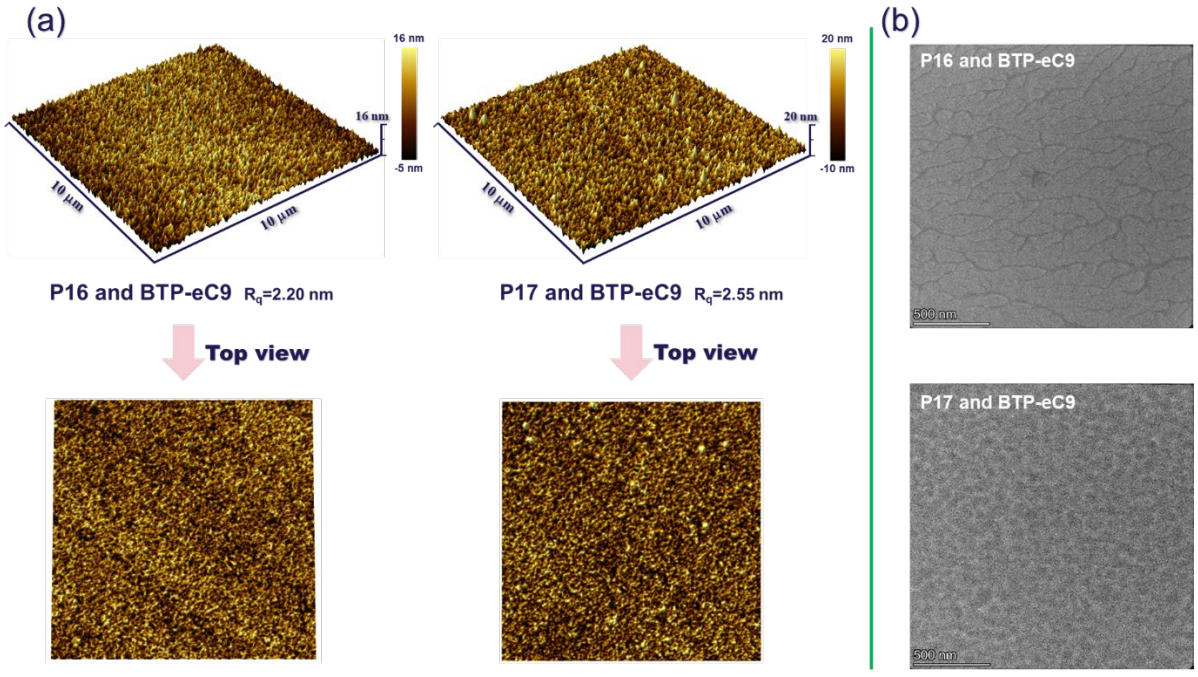

Figure 6. Atomic force microscopy 3D and top view diagrams (a) and transmission electron microscope pictures (b) of P16:BTP-eC9 and P17:BTP-eC9 thin films.

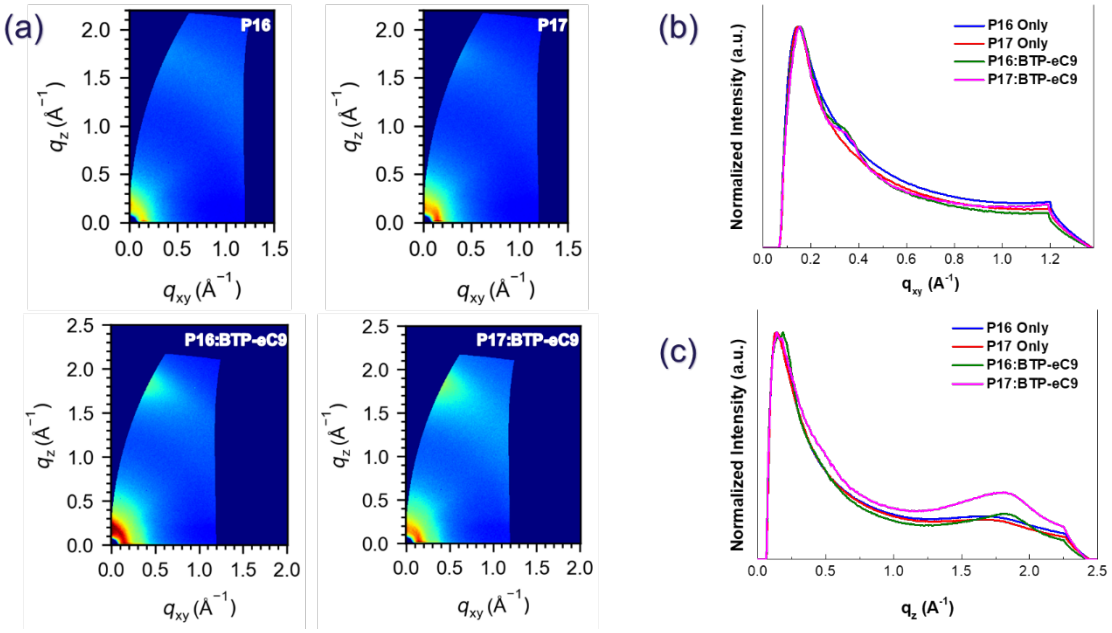

Figure 7. (a) Wide-angle X-ray scattering (GIWAXs) images of P16, P17, P16/BTP-eC9 (1:1.2,w/w) and P17/BTP-eC9 (1:1.2,w/w), corresponding out-of-plane direction (b) and in-plane direction (c)

3. Conclusion

In conclusion, two novel D-A strategy of copolymers, PBDT-PDF-DTBT and PBDT-PDF-DFDTBT, were designed, synthesized and applied in SM-NFA PSCs. As medium wide bandgap copolymers, P17-based single-heterojunction NFA OPVs, blending with BTP-eC9, showed excellent photovoltaic performance, which afforded a high PCE of 12.71% with FF of 69.9%, J_{SC} of 21.08 mA·cm^{-2} and V_{OC} of 0.86 V. On the contrary, P16-based device showed worse PCE of 6.46% with FF of 51.83% and J_{SC} of 13.78 mA·cm^{-2}, in spite of the higher V_{OC} of 0.90 V. Interestingly, when two donor materials were applied into fullerene PSCs, P16-based devices showed better photovoltaic performance than P17. We attributed this consequence to the excess fluorine atoms, which could obstruct the charge separation and charge mobility process and increased the probability of charge recombination in SM-NFA PSCs.

Conflicts of interest

There are no conflicts to declare.

Acknowledgements

This work received a financial support from China Scholarship Council (CSC No. 201908510136). And the authors thank Beijing Synchrotron Radiation Facility (BSRF) 1W1A for 2D GIWAXS measurements.

Electronic Supplementary Information

The impact of position-sensitive fluorination on photovoltaic performance of donor-acceptor polymer/Y-type small molecule based organic solar cells

Wei Xu,[a§] Wei He,[b§] Guojuan Li,[c] Cheng Yang,[d] Hongxiang Li,[c] Zhong Cao,[e] Zhengkun Du,[f*] Pei Cheng,[c] and Donghong Yu[a,g*]

[a.] Department of Chemistry and Bioscience, Aalborg University, Fredrik Bajers Vej 7H, Aalborg East, DK-9220, Demark

[b.] College of Polymer Science and Engineering, State Key Laboratory of Polymer Materials Engineering, Sichuan University, Chengdu, 610065 China

[c.] National Anti-Drug Laboratory Sichuan Regional Center, Chengdu, 610206 China

[d.] Key Laboratory of Green Chemistry & Technology of Ministry of Education, College of Chemistry, Sichuan University, Chengdu 610064, Sichuan, China

[e.] Hunan Provincial Key Laboratory of Materials Protection for Electric Power and Transportation, and Hunan Provincial Key Laboratory of Cytochemistry, School of Chemistry and Biological Engineering, Changsha University of Science and Technology, Changsha 410114, China

[f.] Al-ion Battery Research Center, College of Energy Storage Technology, Shandong University of Science and Technology, Qingdao, Shandong 266590, China

[g.] Sino-Danish Center for Education and Research, DK-8000, Aarhus, Denmark

§ equal contributions to this work

1. General information

All solvents and reagents were of reagent quality, purchased commercially, and used without further purification. NMR spectra were recorded at room temperature on Bruker Avance III^{TM} HD-600 (operating at 600 MHz for ^{1}H NMR and ^{13}C NMR). Elemental analysis was measured by Euro Vector EA3000. The UV-visible spectra were obtained on a JASCO V-650 UV-vis spectrometer. And thermo-gravimetric analysis (TGA) both are measured by STA 449 F3 Jupiter®. Atomic Force Microscope (AFM) were acquired by Smart SPM. Photovoltaic performance was characterized under illumination with an AM 1.5G (100 mW cm^{-2}), and the J-V curves were recorded using a Keithley 2400 source meter. The EQE of solar cells were analyzed using a certified Newport incident photon conversion efficiency measurement system. 2D GIWAXS patterns of films prepared at different temperatures were obtained at 1W1A Diffuse X-ray Scattering Station, Beijing Synchrotron Radiation Facility (BSRF-1W1A). The monochromatic wavelength of the light source was 1.54 Å. The data was recorded by Pilatus 100K from DECTRIS, Switzerland. The grazing incidence angles were 0.2°.

The CV (cyclic voltammetry) of the two polymers were recorded on a CH-Instruments Model 650A Electrochemical Workstation. Three-electrode configuration were using in measurement, Pt wires as both working electrode and counter electrode, and a freshly activated Ag wire as Ag/Ag^{+} pseudoreference electrode. To obtain the oxidation potentials, the reference electrode was calibrated by using the ferrocene/ferrocenium (Fc/Fc^{+}), which has an absolutely potential of 4.8 eV versus the vacuum level. And the redox potential of Fc/Fc^{+} was obtained for calibration of 0.35 eV vs Ag/Ag^{+} electrode under the same conditions. A tetrabutylammonium hexafluorophosphate (Bu_4NPF_6) solution (0.1 M solution in anhydrous acetonitrile) was used as a supporting electrolyte, and N_2 gas was bubbled prior to each measurement. Two polymers were deposit onto the working electrode by drop-casting from solutions of 10 mg/mL in $CHCl_3$. And ferrocene was used as an external standard vs Ag/Ag^{+} under these conditions. The HOMO and LUMO levels were calculated according to the formula $E_{HOMO} = -(E_{OX} + 4.8 - |Fc/Fc^{+}|)$ eV and $E_{LUMO} = E_{HOMO} - E_g^{opt}$, where the E_{OX}, E_g^{opt} and $|Fc/Fc^{+}|$ was determined from the oxidation onsets in the CV curves, the 1240/(onset absorption band edge of the polymer films) and the half-wave potential of ferrocene in CV curves, respectively.

2. Synthesis of Materials

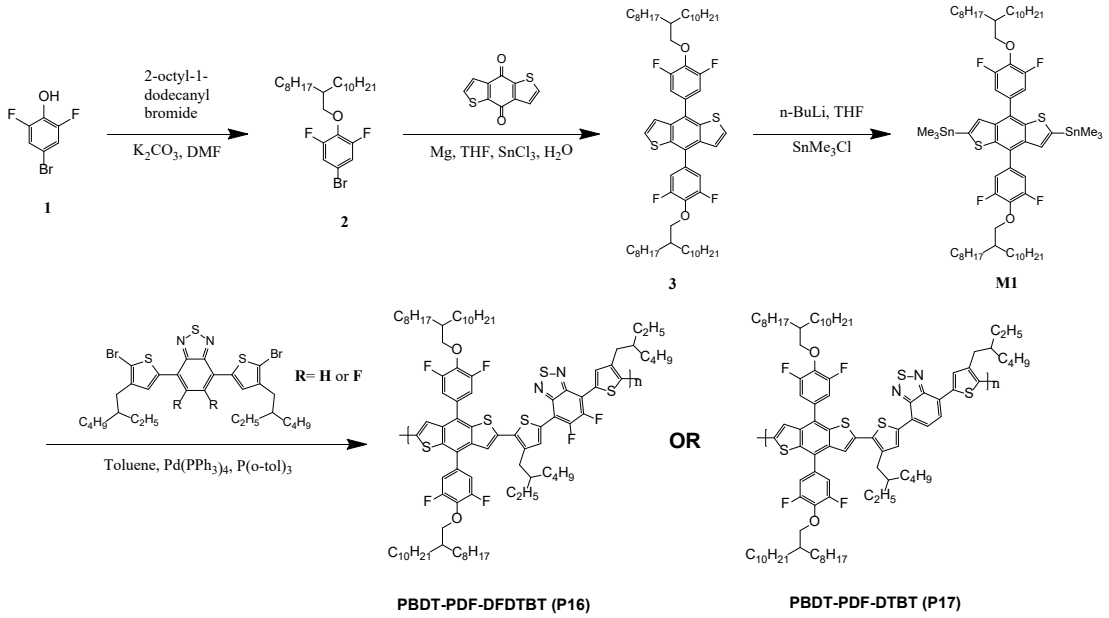

Scheme S1. The synthetic pathway of **M1**, **P16** and **P17**.

*1-bromo-3,5-difluoro-4-(2-octyldodecanyl)oxy-benzene **(2)***

Under the nitrogen atmosphere, 4-bromo-2,6-difluorophenol (**1**) (5.2 g, 25 mmol), K_2CO_3 (3.9 g, 28 mmol) and were dissolved into 150 mL DMF. Then 1-bromo-2-octyldodecane (9.1 g, 25 mmol) was added dropwise into the mixture. And the reaction solution kept stirring overnight at 150 °C in the dark. After cooling to room temperature, the mixture was quenched with water and extracted three times with ethyl acetate. Then the crude product was purified on a silica gel column eluting with petroleum ether. Pale-yellow oil was obtained (10.56 g, 87% yield). **^{1}H NMR** (600 MHz, $CDCl_3$, ppm) δ 7.07 (d, 2H), 3.98 (d, 2H), 1.72-1.70(m, 1H), 1.47-1.27 (m, 32H), 0.88 (t, 6H).

*4,8-Bis(3,5-difluoro-4-(2-octyldodecanyl)oxy-phenyl)-benzo[1,2-b:4,5-b']-dithiophene **(3)***

Magnesium spalls (0.48 g, 20 mmol) and slight I_2 were put into a dried three necked round-bottom flask under nitrogen. The compounds 2 (7.0 g, 15 mmol) in THF (80 mL) was added dropwise by using syringe. Then the mixture was refluxed until the magnesium consumed. Benzo[1,2-b:4,5-b']dithiophene-4,8-dione (1.54 g, 7 mmol) in THF (30 mL) was added slowly into the flask and kept reflux for 12 h. Then, $SnCl_2{\cdot}2H_2O$ (5.48 g, 24 mmol) 10% aqueous HCl was added dropwise into the mixture and stirred for another 2 h at 80°C. After cooling to room temperature, the mixture was quenched with water, and extracted with dichloromethane three times. And then dried, concentrated, and purified by column chromatography, the final products were obtained (6.04 g, 40%). **^{1}H NMR** (600 MHz, $CDCl_3$, ppm) δ 7.45 (d, 2H), 7.32 (d, 2H), 7.23 (d, 4H), 4.15 (d, 4H), 1.83-1.80 (m, 2H), 1.58-1.53 (m, 4H), 1.44-1.26 (m, 60H), 0.90-0.87 (m, 12H). **^{13}C NMR** (600 MHz, $CDCl_3$, ppm) δ 157.04, 156.99, 155.38, 155.38, 138.06, 136.22, 136.13, 136.04, 135.95, 133.40, 133.34, 128.47, 128.01, 122.48, 113.42, 113.39, 133.31, 133.27, 77.00, 38.92, 31.94, 31.00, 30.05, 29.67, 29.37, 26.80, 22.71, 14.14.

*2,6-Bis(trimethyltin)-4,8-bis(3,5-difluoro-4-(2-octyldodecanyl)oxy-phenyl)-benzo[1,2-b:4,5-b′]-dithiophene **(M1)***

Compound **3** (6.04 g, 6 mmol) of dry THF (50 mL) solution was cooled to -78°C in the round-bottom flask under argon, and n-butyllithium solution in n-hexane (7.4 mL, 12 mmol) was added dropwise. After warming up to room temperature, the mixture was stirred for 3 h. Then trimethyltin chloride solution in THF (14 mL) was added at 0°C and the reaction mixture was stirred at ambient temperature overnight. After quenching with water, extracting with dichloromethane (three times), drying over anhydrous sodium sulfate, and concentrating with rotary evaporator, the residue was recrystallized from isopropanol to yield the target monomer (**M1**) (4 g, 50%). **^{1}H NMR** (600 MHz, $CDCl_3$, ppm) δ 7.35 (S, 2H), 7.29 (s, 2H), 7.28 (S, 2H), 4.20 (d, 4H), 1.89-1.85 (m, 2H), 1.62-1.58 (m, 4H), 1.50-1.42 (m, 12H), 1.36-1.32 (m, 48H), 0.93-0.90 (m, 12H), 0.43 (t, 18H). **^{13}C NMR** (600 MHz, $CDCl_3$, ppm) δ 157.04, 155.34, 143.25, 142.34, 136.78, 135.89, 134.17, 129.98, 126.84, 113.45, 113.34, 77.60, 38.96, 31.95, 31.05, 30.08, 29.72, 29.68, 29.64, 29.38, 26.83, 22.72, 14.15.

*Synthesis of PBDT-PDF-DFDTBT (**P16**) and PBDT-PDF-DTBT (**P17**)*

Under argon atmosphere, **M1** (0.2 mmol), **DTBT** (0.2 mmol), $Pd_2(dba)_3$ (2.6 mg, 2.8 μmol) and P(o-tol)$_3$ (3.8 mg, 12.5 μmol) were put into a 20 mL round-bottom flask. Then, 8 mL dry toluene was added, and the solution was heated to 110°C for 24 h. After cooling to room temperature, the mixture was poured into methanol, then filtered. The precipitate was extracted by using hexane, acetone, and chloroform with Soxhlet extraction. Then, the chloroform fraction was collected and dried overnight under vacuum. Finally, the target copolymers were obtained. Elem. Anal. Calculated for $C_{94}H_{130}F_6N_2O_2S_5$ (**P16**): C, 70.81; H, 8.22; N, 1.76. Found: C, 70.32; H, 8.03; N, 1.73; $C_{94}H_{132}F_4N_2O_2S_5$ (**P17**): C, 72.45; H, 8.54; N, 1.80. Found: C, 72.57; H, 8.33; N, 1.76.

3. Dihedral angle of the two polymers

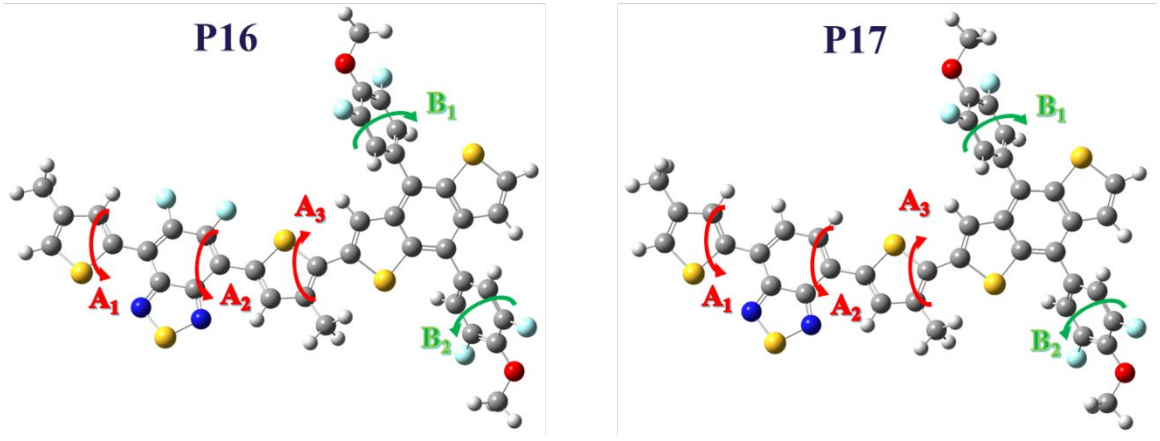

Figure S1. The optimized molecular structure of dimer moieties of two polymers.

Table S1. The dihedral angels of the optimal-structure molecules calculated by the density functional theory (DFT).

Polymers	Dihedral angels (°)				
	A_1	A_2	A_3	B_1	B_2
P16	0.10	0.49	25.63	58.70	58.41
P17	11.29	5.67	18.98	58.63	58.75

4. Fabrication and Optimization of OPV devices

The SM-NFA OPV devices were fabricated on top of a pre-patterned ITO substrate with the conventional structure of ITO/PEDOT:PSS/Active layers/PFN-Br/Ag. After cleaning the ITO with aqueous detergent, deionized water, acetone, and 2-propanol, UV-ozone treatment was applied for 15 min. Filtered PEDOT:PSS (CLEVIOS™ P VP AI 4083) was spin-coated on the ITO substrate to form a 30 nm-thick layer. Then the coated substrates were annealed on the thermal plate at 150 °C for 20 min. After annealing, the chlorobenzene (CB) solution of the blending active substances was spin-cast on top of the PEDOT:PSS layer to produce the active layer with a thickness of 100 nm under 2000 rpm in glovebox, and the coated substrates with active layer were annealed for 10 min at 100 °C. Then PNF-Br were spin-coated under 3000 rpm to form a 10 nm-thickness layer. Finally, the device fabrication was completed by thermal evaporation of 100 nm Ag as the anode in high vacuum (< 10^{-6} mbar). To optimal the corresponding OPV devices, the weight ratio of D/A or the content of additives were studied in following tables. Besides, the OPV devices blending with other non-fullerene acceptors were fabricated to study the difference of their photovoltaic performance in common NFA-based PSCs. All the experimental details were summarized in the below tables. And all data shown in the tables was collected from 8 parallel devices for better reproducibility.

Table S2. Photovoltaic properties of the OPVs based on Polymers/BTP-eC9 with different weight ratio of donor and acceptor at spin-coating speed of 2000 rpm under an illumination of AM 1.5 G, 100 mW cm^{-2}

Polymer/ BTP-eC9	D:A (w/w) [a]	FF (%)	V_{OC} (V)	J_{SC} (mA cm^{-2})	PCE (%) Best/Ave [b]
P16	10:10	51.27	0.90	10.75	4.98/4.80
	10:12	51.83	0.90	13.78	6.46/6.15
	8:12	51.70	0.91	12.16	5.72/5.34
P17	10:10	67.51	0.86	20.22	11.77/11.23
	10:12	69.90	0.86	21.08	12.71/12.37
	8:12	69.70	0.86	18.75	11.31/10.91

[a] D:A(w/w), 10:10 equals to 10 mg/mL:10 mg/mL, [b] The average is obtained from 8 parallel devices.

Table S3. Photovoltaic properties of the OPVs based on Polymers/BTP-eC9 (10:12, w/w) with different content of DIO at spin-coating speed of 2000 rpm under an illumination of AM 1.5 G, 100 mW cm^{-2}

Polymer/ BTP-eC9	DIO (vol%)	FF (%)	V_{OC} (V)	J_{SC} (mA cm^{-2})	PCE (%) Best/Ave [a]
P16	0	51.83	0.90	13.78	6.46/6.15
	0.15	51.96	0.91	12.33	5.83/5.48
	0.3	47.20	0.89	12.23	5.12/5.01
P17	0	69.90	0.86	21.08	12.71/12.37
	0.15	69.58	0.87	20.80	12.56/12.18
	0.3	69.53	0.86	20.83	12.39/12.05

[a] The average is obtained from 8 parallel devices.

Table S4. Photovoltaic properties of the OPVs based on Polymers/BTP-eC9 (10:12, w/w) in different spin-coating speed under an illumination of AM 1.5 G, 100 mW cm^{-2}

Polymer/ ITIC	Spin-coating speed (rpm)	FF (%)	V_{OC} (V)	J_{SC} (mA cm^{-2})	PCE (%) **Best/Ave** [a]
P16	1800	49.08	0.90	13.79	6.11/5.93
	2000	51.83	0.90	13.78	6.46/6.15
	2200	51.96	0.91	12.33	5.83/5.61
P17	1800	69.88	0.86	20.52	12.32/12.13
	2000	69.90	0.86	21.08	12.71/12.37
	2200	68.81	0.86	20.47	12.09/11.97

[a] The average is obtained from 8 parallel devices.

5. Properties of charge transfer and recombination

The mobility properties of the active layer were determined by applying the space charge limited current (SCLC) method to the J-V measurements of the devices. The hole-only and electron-only polymers devices were designed as the diodes with the structure of ITO/PEDOT:PSS/Active layers (copolymers:BTP-eC9, 10:10 w/w, 2000 rpm)/Au and Ag/ZnO/Active layers(same conditions as above)/Ag, respectively. And the mobilities were calculated from the SCLC using the following equation[1]:

$$J_{SCLC} = (9/8)\varepsilon_r\varepsilon_0\mu(V^2/L^3)\exp(0.89r\sqrt{V/L})$$

where J is the current density, ε_r is the dielectric constant of the polymers, ε_0 is the permittivity of the vacuum, μ is the hole mobility, L is the thickness of the blend films, $V = V_{appl} - V_{bi}$, where V_{appl} is the applied potential, and V_{bi} is the built-in voltage which results from the difference in the work function of the anode and cathode.

Charge dissociation probability was characterized by the function of photogenerated current density (J_{ph}) *versus* effective applied voltage (V_{eff}). The J_{ph} is defined as the difference between J_L and J_D, where J_L and J_D are the current density of devices under light (100 mW cm^{-2}) and dark, respectively. $V_{eff} = V_0 - V$, where V_0 is the voltage when $J_{ph} = 0$ and V is the applied voltage during the measurement. When the reverse voltage is greater than 2 V, the recombination is suppressed by a

high internal electric field. Thus, J_{ph} will reach the saturated current density (J_{sat}). Consequently, P_{diss} = J_{ph}/J_{sat} could be used to describe the charge dissociation probability.[2, 3] And the higher P_{diss} is indicated the more effective charge dissociation. Besides, the relationship of J_{SC} and the light intensity (I) is $J_{SC} \propto I^{\alpha}$, where α is the degree of biomolecular recombination. When α = 1, dissociated free charges don´t recombine during the movement process, and are all collected by the electrode, implying the recombination can be ignored. If α is less than 1, the bimolecular recombination will be present in the devices, and the smaller the value of α indicates the stronger bimolecular recombination. Meanwhile, $V_{OC} \propto (nkT/q)\cdot\ln(I)$, where K represents the Boltzmann constant, T is the Kelvin temperature, and q is the elementary charge. If the slope is close to 2kT/q, the trap-assisted recombination will be inside the devices.[4, 5]

6. Other Supplemental Figures

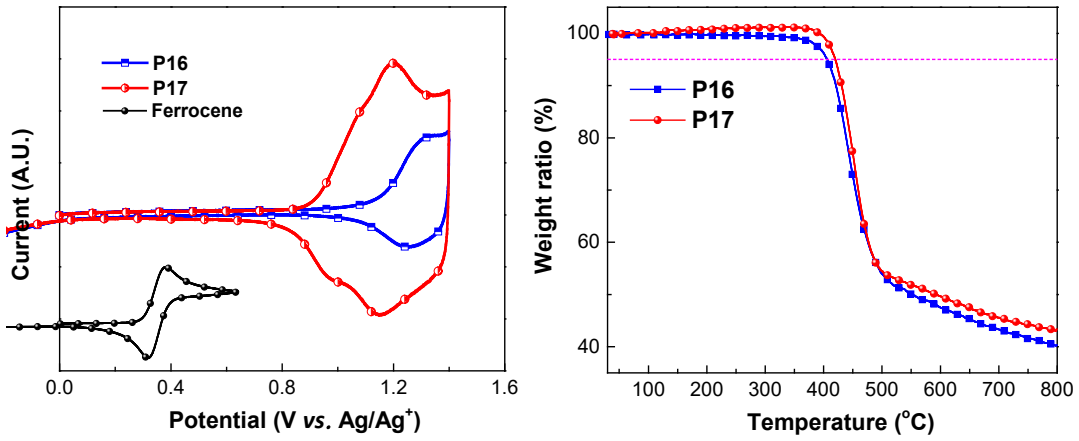

Figure S2. Cyclic voltammetry curves (A) and TGA curves (B) of two copolymers (P16 and P17) in film, respectively.

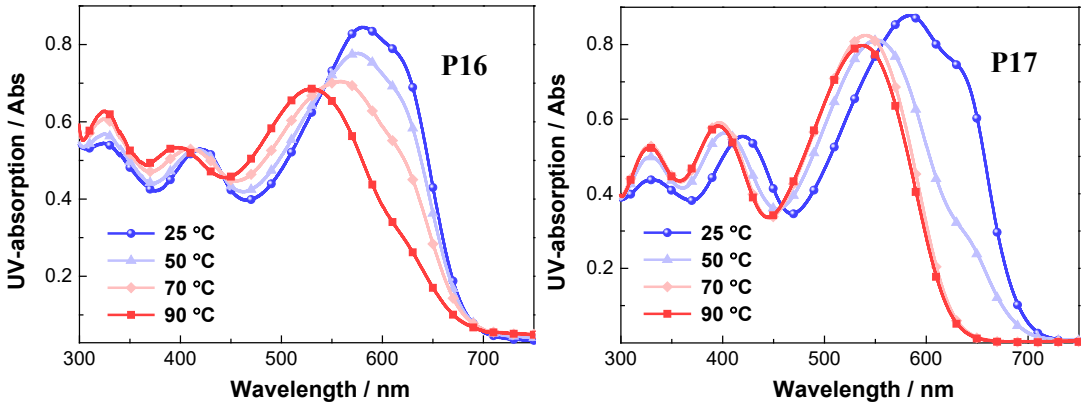

Figure S3. Temperature dependent UV-vis absorption curves of P16 and P17 (both 0.01 mg/mL) in Chlorobenzene.

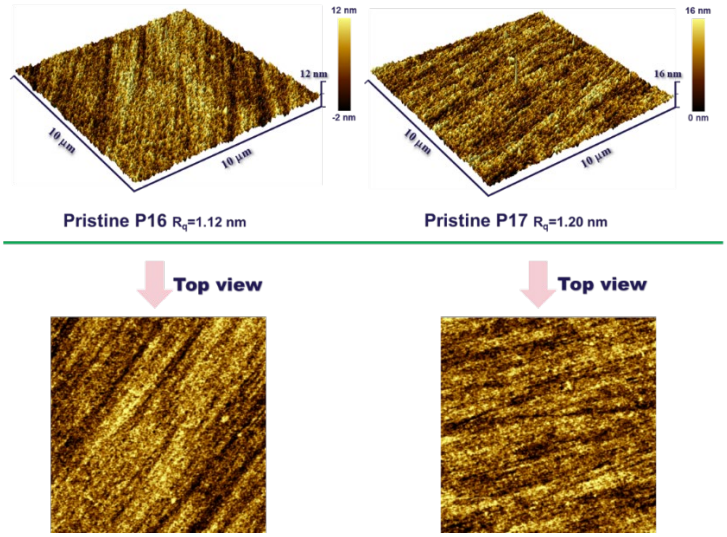

Figure S4. Atomic force microscopy 3D and top view diagrams of pristine P16 and P17 thin films.

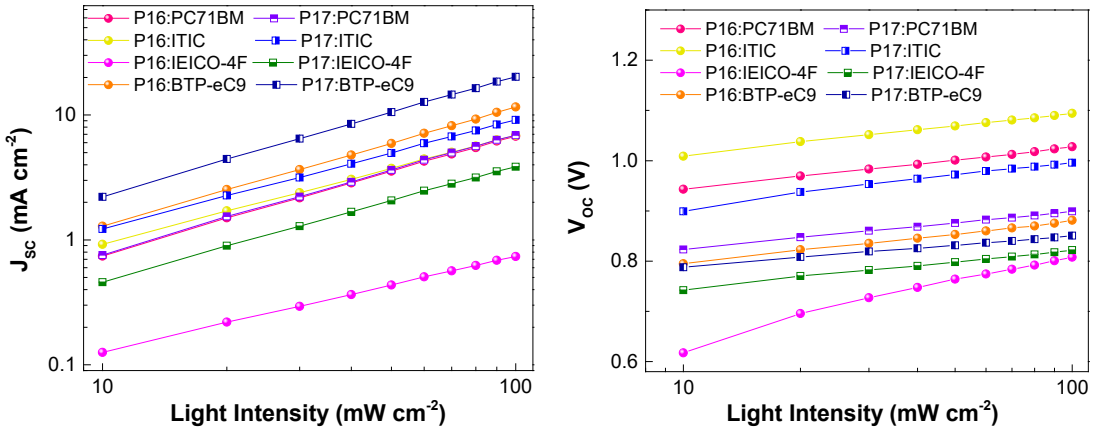

Figure S5. Dependence diagram of J_{SC} (a) and V_{OC} (b) as a function of light power in D/A-based devices.

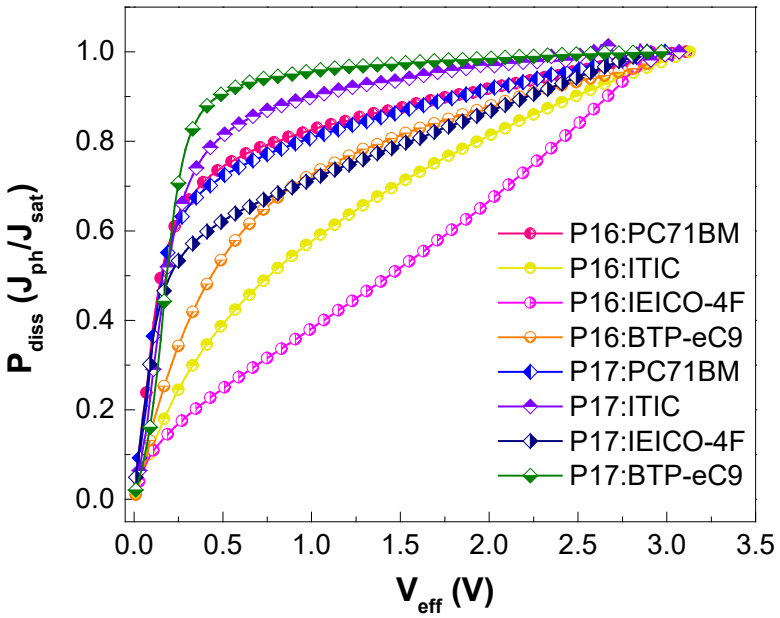

Figure S6. Charge dissociation probabilities (P_{diss}) vs. effective voltage (V_{eff}) curves of D/A-based OPVs.

Table S5. Photovoltaic performance of non-additive D/A-based polymer solar cells.

Polymer / NFAs	D:A (w/w) [a]	PCE Best/Ave(%) [b]	FF (%)	V_{OC} (V)	J_{SC} (mA cm^{-2})	J_{SC} (mA cm^{-2}) [c]	α	KT/q	P_{diss} (J_{ph}/J_{sat})
P16:PC71BM	1:1.5	4.42/4.22	62.87	1.03	6.83	6.21	0.96	1.39	0.92
P16:ITIC	1:1.2	3.21/3.04	46.05	1.10	6.31	5.12	0.87	1.39	0.81
P16:IEICO-4F	1:1.2	0.22/0.20	35.39	0.81	0.75	0.58	0.77	3.04	0.67
P16:BTP-eC9	10:12	6.46/6.15	51.83	0.90	13.78	12.58	0.95	1.40	0.88
P17:PC71BM	1:1.5	3.92/3.83	63.01	0.90	6.89	6.68	0.96	1.35	0.92
P17:ITIC	1:1.2	6.51/6.27	60.06	0.99	10.91	10.73	0.87	1.38	0.97
P17:IEICO-4F	1:1.2	1.87/1.81	59.64	0.83	3.77	2.96	0.92	1.29	0.87
P17:BTP-eC9	10:12	12.71/12.37	69.90	0.86	21.08	20.42	0.96	1.02	0.99

[a] Blend solution of BTP-eC9-based devices are concentration of 22 mg/mL, others are concentration of 20 mg/mL, [b]Average PCE is calculated from 8 parallel devices, [c] Calculated from EQE integrated short circuit density.

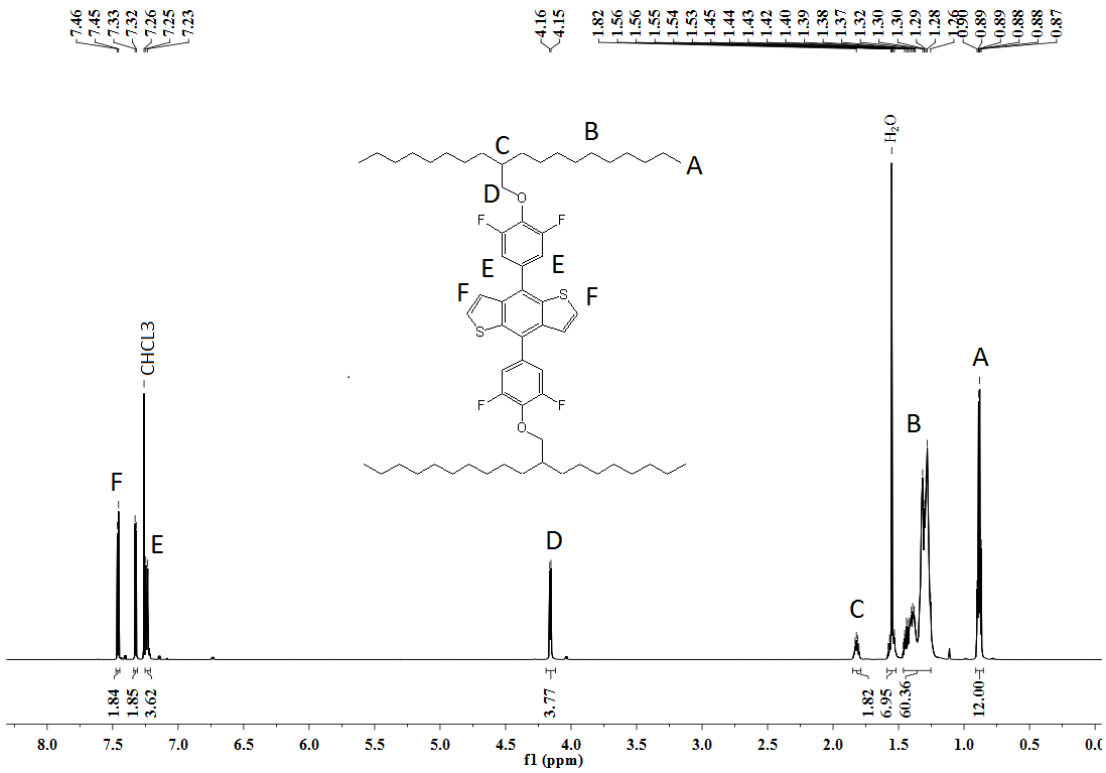

Figure S7: ^{1}H NMR spectrum of compound **3**.

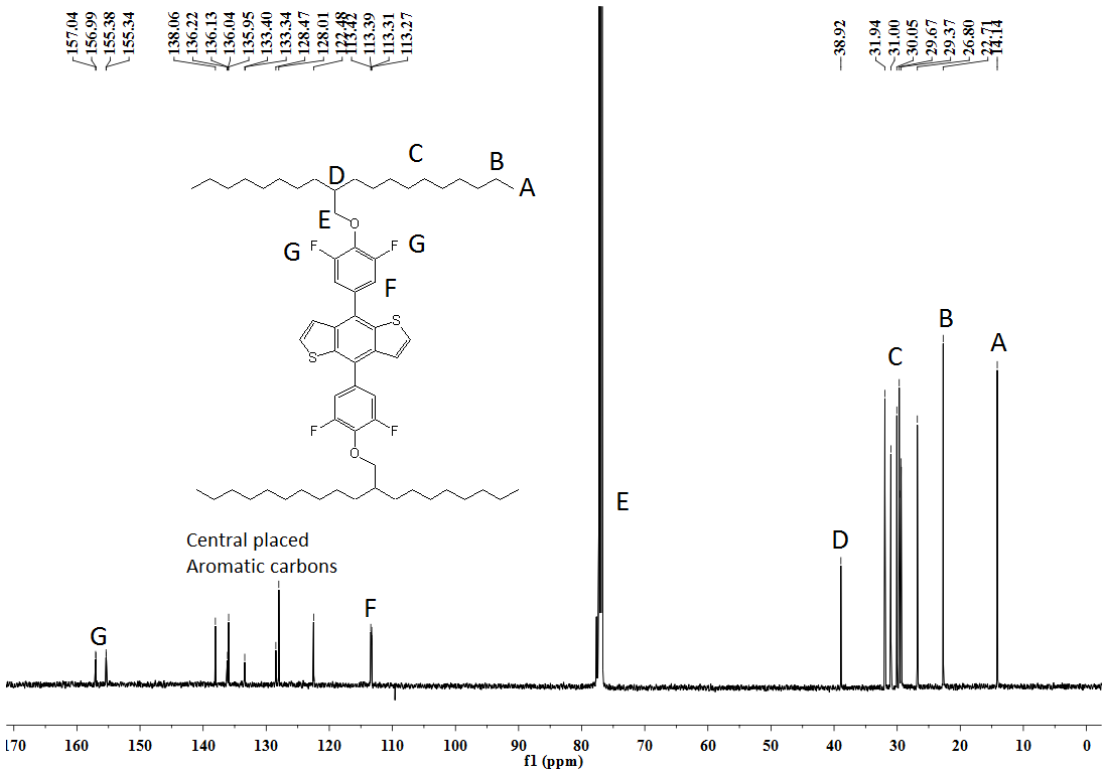

Figure S8: ^{13}C NMR spectrum of compound **3**.

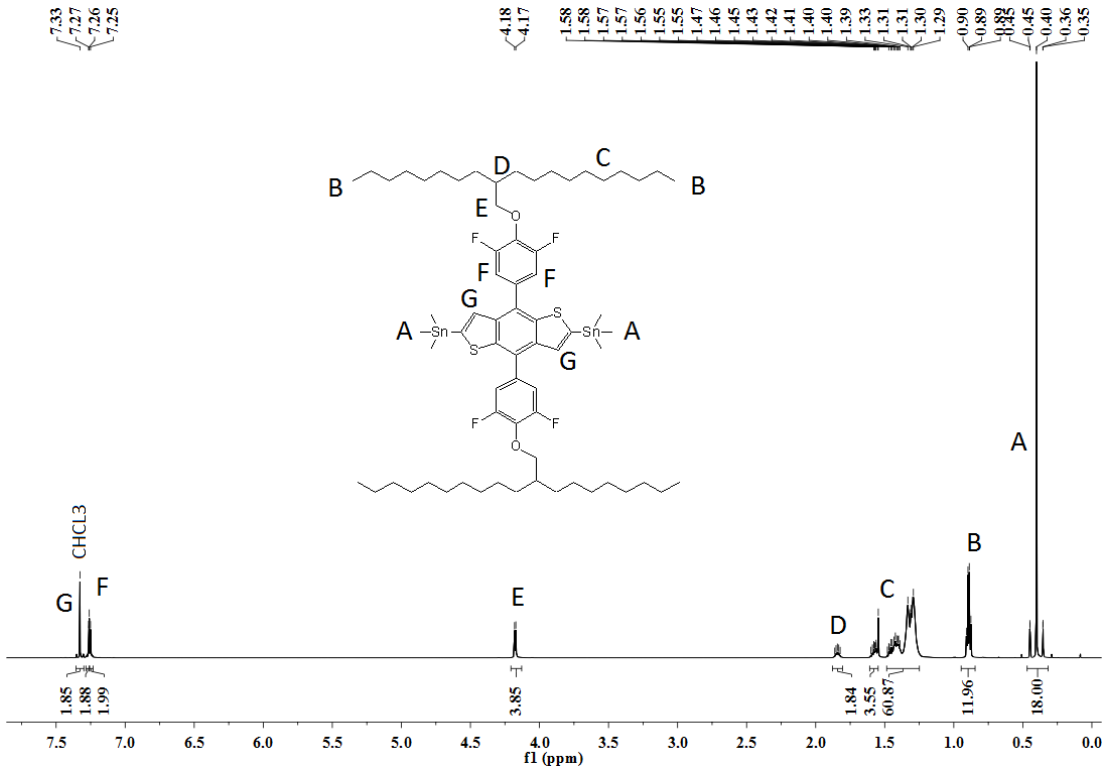

Figure S9: ^{1}H NMR spectrum of compound **M1**.

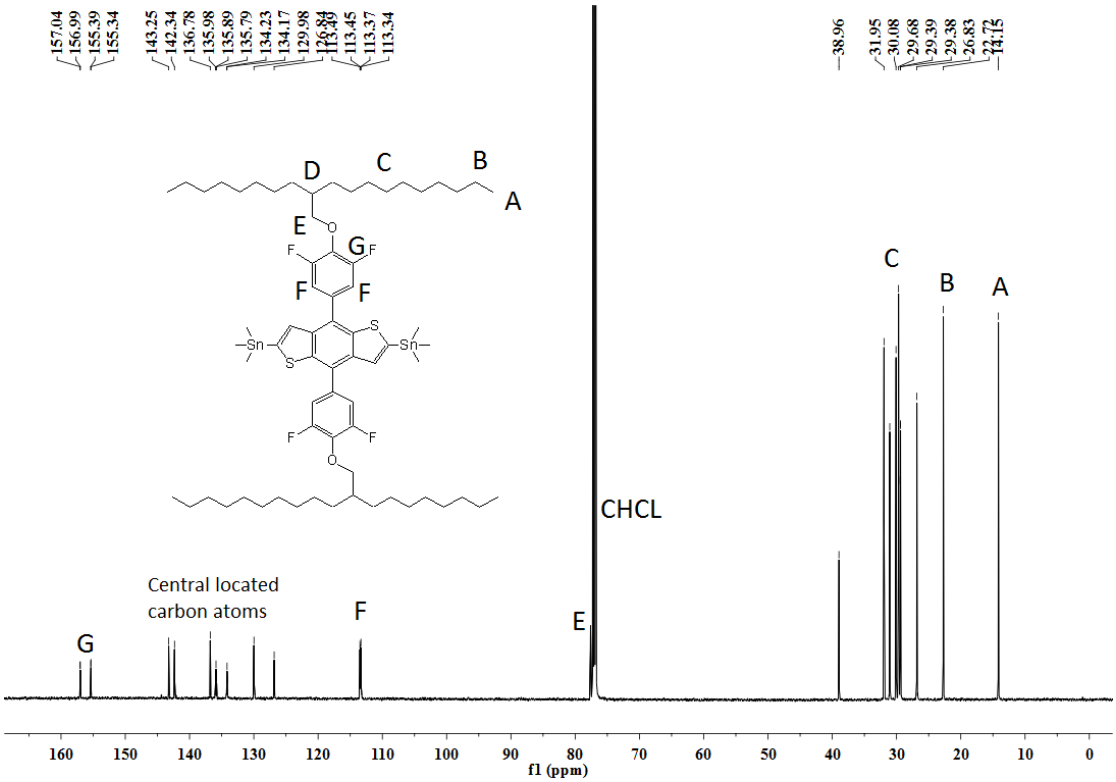

Figure S10: ^{13}C NMR spectrum of compound **M1**.

Reference

[1] C. Melzer, E. J. Koop, V. D. Mihailetchi, P. W. M. Blom, Hole Transport in Poly(phenylene vinylene)/Methanofullerene Bulk-Heterojunction Solar Cells, Advanced Functional Materials, 14 (2004), 865-870

[2] P. W. M. Blom, V. D. Mihailetchi, L. J. A. Koster, D. E. Markov, Device Physics of Polymer:Fullerene Bulk Heterojunction Solar Cells, Advanced Materials, 19 (2007), 1551-1566

[3] L. Huo, T. Liu, X. Sun, Y. Cai, A. J. Heeger, Y. Sun, Single-Junction Organic Solar Cells Based on a Novel Wide-Bandgap Polymer with Efficiency of 9.7%, Advanced Materials, 27 (2015), 2938-2944

[4] L. J. A. Koster, V. D. Mihailetchi, R. Ramaker, P. W. M. Blom, Light intensity dependence of open-circuit voltage of polymer:fullerene solar cells, Applied Physics Letters, 86 (2005), 123509

[5] A. K. K. Kyaw, D. H. Wang, D. Wynands, J. Zhang, T.-Q. Nguyen, G. C. Bazan, A. J. Heeger, Improved Light Harvesting and Improved Efficiency by Insertion of an Optical Spacer (ZnO) in Solution-Processed Small-Molecule Solar Cells, Nano Letters, 13 (2013), 3796-3801

ISSN (online): 2446-1636
ISBN (online): 978-87-7573-766-6

AALBORG UNIVERSITY PRESS